Experimental and Modeling Investigations on Local Performance and Local Degradation in Solid Oxide Fuel Cells

THÈSE N^{O} 4525 (2009)

PRÉSENTÉE LE 4 DÉCEMBRE 2009

À LA FACULTÉ SCIENCES ET TECHNIQUES DE L'INGÉNIEUR
LABORATOIRE D'ÉNERGÉTIQUE INDUSTRIELLE
PROGRAMME DOCTORAL EN ENERGIE

ÉCOLE POLYTECHNIQUE FÉDÉRALE DE LAUSANNE

POUR L'OBTENTION DU GRADE DE DOCTEUR ÈS SCIENCES

PAR

Zacharie WUILLEMIN

acceptée sur proposition du jury:

Prof. J. R. Thome, président du jury
Prof. D. Favrat, Dr J. Van Herle, directeurs de thèse
Prof. Y. Bultel, rapporteur
Prof. C. Comninellis, rapporteur
Prof. H. Yokokawa, rapporteur

ÉCOLE POLYTECHNIQUE
FÉDÉRALE DE LAUSANNE

Suisse
2009

Acknowledgment

First of all, I would like to gratefully thank Prof. Daniel Favrat and Dr. Jan Van herle for having offered me the possibility to join the fuel cell group at LENI and work on this thesis in a highly stimulating environment. I have really appreciated the opportunity to join this project and thank them for their support and lasting trust and confidence during all these years, even when the fuel cells didn't perform as well as they do today...

This thesis has been financially supported by the Swiss National Science Foundation (Project n°: 200021-100 721-1 and n°: 200020-109 643-1), the Swiss Commission for Technology and Innovation (project 6649.3 IWS-IW), as well as the European Projects *RealSOFC* and *FlameSOFC* and partners which are gratefully thanked for having made this work possible. A special acknowledgement is due to the *FlameSOFC* project and to all involved partners for giving me a unique opportunity to develop from scratch the completely new *F-design* stack, as well as the diagnostic testing station which both represent the major achievement of this thesis. Many thanks also go to HTceramix SA (Yverdon, CH) and SOFCpower Srl. (Trento, I) for the joined collaboration on these projects and the providing of experimental material. In particular, thanks are due to Michele Molinelli, former colleague from LENI, who supported the development of the *F-design* stack, to Massimo Bertoldi for his very constructive approach, and to the management teams in Yverdon and Trento.

Concerning everyday work, many thanks go especially to Jan and all the colleagues of the LENI fuel cell group, Diego, Nordhal, Michele, Stefan, Arata, Antonin, Andreas, Henning, Pietro, Leonidas, for the good working atmosphere, for the interesting discussions and many hours spent behind the test benches or the microscope, and also for our creative workshops in the mountains.

To Diego, Nordahl, Michele and Stefan, who were there before me and shared their knowledge with me, and also to Arata who joined later on, for the long times spent together to make things work, for the good atmosphere -even in more difficult times-, for the moments spent in Satellite, and for the fact that we finally achieved at least part of what we had worked for. Many thanks especially to Nordahl and Diego who have set up the production procedure, carefully assembled and successfully tested the *F-design* stack a few weeks ago, which enables me to present its validation, with efficiencies reaching 53%. A special thanks also goes to those having sent results to include in this work and reviewed the chapters ahead.

There are many persons without whom this work would not have been possible. A great thank you goes to:

- Arata Nakajo for his very valuable work on the diagnostic test station for the F-design stack and his outstanding work on the electrochemical model
- Andres Müller, Pierre Oberholzer and Minh-Tam Luong, master thesis students having, during the months spent with me, successfully contributed to this work by designing and making work the different experimental tools, and by bringing in new ideas and enthusiasm
- Thierry Cornu and the other students having contributed to the development of the model
- Andreas J. Schuler, Antonin Faes, Caroline Calderone and Stefan Diethelm for the long hours spent under the microscope analyzing and preparing samples for me
- Marc Salle, Roger Mottier, Bernard Savary and Freddy Thomas from the mechanical workshop (ATSE), who spent lots of effort to build the equipment and prototypes, contributing by their experience to find the right technical solutions
- Luis Quina, who assembled and tested the designed electronic loads and who cares of the lab
- Nicolas Badel, Christophe Fournier and Alexandre Chainho at HTCeramix SA for the careful preparation of stacks and cells and their readiness to adapt production and quality control procedures to latest ideas
- The administration team, who ensures that everything works well
- Céline, Damien, Arata and Luc for the many discussions on technical (and many non-technical !) issues between Lausanne and Geneva

Last but not least, I would like to give special thanks to all LENI colleagues for the time spent with them and the great working (and after-work) atmosphere, and, of course, to family and friends for their support all along this time, with a special thought for my mother who didn't imagine that giving me a an electronics experimenting set as a present would be of such use twenty years later! Finally, I would like to thank Dominique for everything, and even more, that she gave me during this time. Many, many thanks!

Abstract

This thesis focuses on performance, reliability and degradation in solid oxide fuel cells (SOFC), which currently represent the three key technical challenges for the deployment of this technology. By its development of dedicated modeling and experimental tools, this thesis offers a new access to, and comprehension of, ***local*** electrochemical performance, degradation and reliability.

The experimental tools developed have, for the first time, allowed ***in-situ measurements of local performance degradation*** with time, and this in a real SOFC prototype. Giving access to local electrochemistry on 18 measurement points in a repeat-element of 200 cm^2 active area, the spatial distribution of the electrochemical reaction, as well as its degradation with time, could be monitored and analyzed. The *intrinsically local character of degradation* could clearly be revealed, a point of central importance for future investigations on stack degradation and for the interpretation of post-experiment analyses. Using impedance spectroscopy, it was possible to *identify the affected electrochemical processes* and to study the *spatial distribution of their degradation.* The result was put in relation with post-experiment analyses, allowing to *identify pollutants on the air side as major source of degradation.*

To understand the highly coupled phenomena leading to performance, degradation and reliability issues, a ***3D computational fluid dynamic model*** (CFD) was developed. Based on the key idea to include the *non-ideal properties of the used components and materials*in the model, it was possible to obtain an excellent match between experimental observations and modeling outputs. Besides the *identification of performance limitations*, one result of crucial importance was in addition obtained by the ***identification of the principal cause of failure for the prototypes tested in the laboratory***. The model revealed the presence of detrimental local redox-cycling of the cells upon changes of the operating point, as a result from an inadequate combination of slightly porous seal materials and certain aspects of the stack construction. This analysis, *validated by experimental observations*, led to ***solutions permitting an important gain in efficiency and reliability***.

Based on the ***identified and analyzed performance limitation, degradation and failure sources*** obtained from the tools developed in this thesis, ***two stack prototypes*** were successively ***designed, manufactured and tested*** in collaboration with the industrial partner HTceramix-SOFCpower. Starting from a predecessor design limited at 250 W_{el} and an electrical efficiency (LHV) inferior to 40%, the first of the designed prototypes attained a power output of 1.1 kW_{el} (72 cells of 50 cm^2), as well as a maximal efficiency of 53% in short stack configuration. The *second designed stack*, which represents the *major achievement of this thesis*, had, at the time of writing, reached a power output of 1.84 kW_{el} and a maximal efficiency of 53% in a 20-cell stack configuration (200 cm^2 cells). Both results were obtained using dilute hydrogen as fuel; in other words, future operation on reformed natural

gas should lead to an electrical efficiency exceeding 60% (LHV).

With the successful resolution of the main failure source and a demonstrated gain in efficiency, the chosen design iterations confirmed the *predicting capabilities* and the *accuracy of the CFD model* for a design towards the *mandatory reliability and the high performance* expected from SOFC stacks.

Finally, the degradation issue, which was found to be strongly correlated with pollution from different sources, was addressed in a prospective study showing the capability of the CFD model to predict the ***internal generation, transport and deposition of pollutants*** inside of a stack. The *good match obtained with experimental observations* supports therefore the development of such types of models, both for *model-based diagnostics and for future design iterations.*

Keywords: solid oxide fuel cell, in-situ measurements, local characteristics, performance, degradation, reliability, oxidation, sealing, diffusion, pollutant, impedance spectroscopy, computational fluid dynamics, CFD, modeling

Résumé

Cette thèse traite de trois domaines clés dans le développement de piles à combustible à oxide solide (SOFC): ***le rendement, la fiabilité et les phénomènes de dégradation interne***. Par l'utilisation conjointe de modèles numériques et d'outils expérimentaux spécialement créés et développés dans le cadre de cette thèse, ce travail fournit un accès et une compréhension novateurs en ce qui concerne le ***caractère local*** de la performance électrochimique, des phénomènes de dégradation et des problèmes de fiabilité.

Les outils expérimentaux développés ont permis d'effectuer, pour la première fois, ***des mesures in-situ des phénomènes de dégradation locale*** au sein d'un véritable prototype. Offrant un accès à l'électrochimie locale de 18 points de mesure disposés sur une cellule, cette technique de mesure a permis de suivre et d'analyser la répartition spatiale de la réaction électrochimique et d'en suivre l'évolution avec le temps. Ceci a permis de révéler la *nature intrinsèquement locale des phénomènes de dégradation*, un point clé remettant en question l'analyse de données de dégradation obtenues sur des stacks, ainsi que l'interprétation des analyses post-expérience. A l'aide de la spectroscopie d'impédance, il a en outre été possible d'*identifer le niveau de dégradation pour différents processus électrochimiques* ainsi que d'en *étudier la distribution spatiale*. Finalement, des analyses faites sur les composants ont permis, en relation avec les données spatiales, d'identifier la *principale source de dégradation sous la forme de polluants*.

Afin de comprendre les nombreuses interactions entre les différents paramètres ayant un impact sur la performance, la dégradation et la fiabilité, un ***modèle numérique*** de dynamique des fluides (CFD) a été développé. Celui-ci comporte un modèle électrochimique créé spécifiquement et validé sur des données expérimentales. Développé avec l'idée-clé d'*inclure dans le modèle les propriétés non-idéales de certains composants*, et en particulier une porosité résiduelle des joints utilisés, le modèle a permis de reproduire avec précision de nombreux phénomènes observés expérimentalements et jusqu'alors inexpliqués. Hormis *l'identification de certaines causes de limitations en performance*, le modèle a permis d'***identifier la principale cause de défaillance observée sur les prototypes*** testés au laboratoire. Le modèle a ainsi permis de révéler l'existence de cycles redox locaux endommageant les cellules lors de changements de points de fonctionnement, un phénomène résultant d'une inadéquation entre des joints présentant une porosité résiduelle et certains aspects de la construction de la pile. Cette analyse, *validée par des observations expérimentales*, a mené à des ***solutions apportant un important gain en rendement et en fiabilité***.

Sur la base de l'*observation et de l'analyse des limitations en performance, de la dégradation et des sources de défaillances* obtenues à l'aide des *outils développés dans le cadre de ce travail*, ***deux prototypes de pile à combustible*** ont été successivement ***dessinés, réalisés et***

testés avec succès, en collaboration avec le partenaire industriel HTceramix-SOFCpower. Partant du design d'origine limité à 250W$_{el}$ et présentant un rendement (PCI) inférieur à 40%, le premier prototype conçu a atteint une puissance de 1,1kW$_{el}$ (72 cellules de 50 cm^2) et un rendement maximal de 53% (PCI) avec une pile de 6 éléments. Le *second design, qui constitue la principale réalisation de cette thèse*, avait atteint, au moment de mettre le point final à cet écrit, une puissance de 1,84 kW$_{el}$ ainsi qu'un rendement maximal de 53%, ceci avec une pile de 20 éléments (cellules de 200 cm^2). Dans les deux cas, ces résultats ont été obtenus avec de l'hydrogène dilué. En d'autres termes, une opération future sous gaz naturel réformé permettrait avec ces piles d'atteindre des rendements électriques excédant les 60% (PCI).

Avec la résolution du principal point faible des prototypes étudiés, et avec les importants gains en performance obtenus avec les prototypes conçus, les capacités prédictives et la précision du modèle CFD ont pu ainsi être vérifiées, permettant de tendre vers la fiabilité requise et vers les hauts rendement attendus de la part des piles à combustible SOFC.

Pour terminer, une étude prospective a été menée pour étudier la possibilité de ***modéliser les phénomènes de génération, de transport et de déposition de pollutants***, polluants qui représentent l'une des principales causes de dégradation observée dans ce projet. La *capacité du modèle CFD ainsi complété à prédire certaines sources importantes de polluants a pu être vérifiée* sur la base d'observations expérimentales, illustrant ainsi une possible application de la modélisation pour d'autres types de diagnostiques ainsi que pour d'éventuels nouveaux designs de stacks.

Mots-clés: pile à combustible à oxyde solide, mesure in-situ, propriétés locales, performance, rendement, dégradation, fiabilité, oxydation, joint, diffusion, polluant, spectroscopie d'impédance, mécanique des fluides numérique, CFD, modélisation

Contents

List of Figures

List of Tables

Abbreviations and symbols

Abbreviations

ASC	anode supported cell
ASR	area specific resistance
CFD	computational fluid dynamics
CHP	combined heat and power generation
DLR	Deutschen Zentrum für Luft- und Raumfahrt
EIS	electrochemical impedance spectroscopy
LENI	Laboratoire d'Energétique Industrielle
LSC	strontium doped lanthanum cobaltite
LSF	strontium doped lanthanum ferrite
LSM	strontium doped lanthanum manganite
OCV	open circuit voltage
SOFC	solid oxide fuel cell
TEC	thermal expansion coefficient
YSZ	Yttria Stabilized Zirconia
3YSZ	3% molar Yttria Stabilized Zirconia
8YSZ	8% molar Yttria Stabilized Zirconia

Constants

$\mathcal{R}$	Universal gas constant
k_b	Boltzmann constant
σ	Stefan-Boltzmann constant

Adimensional numbers

Gr_L	Grashof number (characteristic length L)	–
K_n	Knudsen number	–
Nu_L	Nusslet number (characteristic length L)	–
Pr	Prandtl Number	–
Ra_L	Rayleigh number	–
Re_L	Reynolds number (characteristic length L)	–
Sc	Schmidt number (characteristic length L)	–
Sh	Sherwood number (characteristic length L)	–

Variables of state

$C_,i$	Molar concentration of specie i	$\mathrm{mol\,m^{-3}}$
$M_{w,i}$	Molar mass	kg/kmol
P	Pressure	K
T	Temperature	K
p_i	Partial pressure of specie i	atm
x_i	Mole fraction of specie i	$-$
α	Thermal diffusivity	$\mathrm{m^2s^{-1}}$
β	Volumetric thermal expansion coefficient	K^{-1}
ρ	Density	$\mathrm{kgm^{-3}}$
ρ_i	Density of specie i	$\mathrm{kgm^{-3}}$
$[i]$	Concentration of gas specie i (alternative)	$\mathrm{kmol\,m^{-3}}$

Mass transfer

h_m	Mass-transfer coefficient	$\mathrm{m\,s^{-1}}$
$\dot{N}$	Molar flux	$\mathrm{mol\,s^{-1}}$
$\dot{N}''$	Surface-specific molar flux	$\mathrm{mol\,m^{-2}s^{-1}}$

Diffusion

D_{ij}	Binary diffusion coefficient of specie i in j	
J_i	Diffusive mass fluxes	$\mathrm{kgm^{-2}s^{-1}}$
$D_{binary,i-j}$	Binary diff. coeff. for specie i in specie j	$\mathrm{m^2s^{-1}}$
$D_{i,m}$	Multicomponent diffusion coefficient for specie i	$\mathrm{m^2s^{-1}}$
$D_{Kn,i}$	Knudsen diffusion coefficient	$\mathrm{m^2s^{-1}}$
$D_{i,eff}^{por,Kn<1}$	Effective diff. coeff. without Knudsen correction	$\mathrm{m^2s^{-1}}$
$D_{eff,i}^{por,1<Kn<10}$	Effective diff. coeff., with Knudsen-term correction	$\mathrm{m^2s^{-1}}$
l	Mean free path of molecules	m
$\overline{d}_p$	Average pore diameter	m
ε	Porosity	$-$
τ	Tortuosity	$-$
σ_{ii}	Collision diameter of diffusive species	m

Viscous flow

$\overline{\overline{D}}$	Permeability tensor	$\mathrm{m^2}$
$\overrightarrow{g}$	Gravitationnal acceleration	$\mathrm{ms^{-2}}$
$\overrightarrow{v}$	Velocity	$\mathrm{ms^{-1}}$
v_x	j component of velocity vector	$\mathrm{ms^{-1}}$
$1/\alpha$	Darcy cofficient (FLUENT notation)	$\mathrm{m^{-2}}$
μ	Viscosity	$\mathrm{kg\,s^{-1}m^{-1}}$

ν	Kinematic viscosity	$\mathrm{m^2\,s^{-1}}$
$\overline{\overline{\tau}}$	Stress tensor	

Heat transfer

a_i	Planck absorption coefficient for specie i	$\mathrm{m^{-1}\,atm^{-1}}$
$\overline{a}$	Planck mean absorption coefficient for specie	$\mathrm{m^{-1}}$
h_{rad}	Radiative heat transfer coefficient	$\mathrm{Wm^{-2}K^{-1}}$
$h_{freeconv}$	Free convection heat transfer coefficient	$\mathrm{Wm^{-2}K^{-1}}$
$\overline{h}$	Average heat transfer coefficient	$\mathrm{Wm^{-2}K^{-1}}$
$\overline{\overline{K}}$	Anistropic thermal conductivity tensor	$\mathrm{Wm^{-1}K^{-1}}$
k	Thermal conductivity	$\mathrm{Wm^{-1}K^{-1}}$
k_{eff}	Effective thermal conductivity in porous media	$\mathrm{Wm^{-1}K^{-1}}$
$\dot{Q}_k^-$	Surface heat flux	$\mathrm{Wm^{-2}s^{-1}}$
$\overrightarrow{q}$	Heat flux	$\mathrm{Wm^{-2}s^{-1}}$
$\overline{T}$	Average temperature	K
ϵ_i	Emissivity of surface i	–

Chemical reactions

r_{SMR}	Surface reaction rate for the SMR reaction	$\mathrm{kmol\ m^{-2}\ s^{-1}}$
r_k	Volumetric reaction rate for reaction k	$\mathrm{kmol\ m^{-3}\ s^{-1}}$
A^*_{SMR}	Ratio of catalyst surface to geometric surface for SMR	-
r_{H_2}	Volumetric reaction rate for hydrogen combustion	$\mathrm{kmol\ m^{-3}\ s^{-1}}$
$r_{CO,f}$	Forward volumetric reaction rate for CO combustion	$\mathrm{kmol\ m^{-3}\ s^{-1}}$
$r_{CO,b}$	Backward volumetric reaction rate for CO combustion	$\mathrm{kmol\ m^{-3}\ s^{-1}}$
K_{eq}	Equilibrium constant	

Fuel cell operation parameters

I	Current	A
ϵ_t	Fuel thermodynamic efficiency	–
ϵ_{el}	Electrical efficiency	–
λ	Air excess factor	–

Electrochemical model

j_{loss}	Electrolyte leakage current density	$\mathrm{Acm^{-2}}$
j_{tot}	Total current density	$\mathrm{Acm^{-2}}$
j_{utile}	Utile current density	$\mathrm{Acm^{-2}}$
R	Resistance (area-specific)	$\Omega\mathrm{cm^2}$
R_{Ionic}	Ionic resistance of electrolyte	$\Omega\mathrm{cm^2}$

R_{Pol}	Polarization resistance (area-specific)	Ωcm^2
R_{diff}^{an}	Anode diffusion resistance (area-specific)	Ωcm^2
R_{ct}^{an}	Anode charge-transfer resistance (area-specific)	Ωcm^2
R_{ct}^{cat}	Cathode charge-transfer resistance (area-specific)	Ωcm^2
R_{Coll}	Collection resistance (area-specific)	Ωcm^2
$R_{\Omega}^{electrode}$	Ohmic resistance (electrode)	Ωcm^2
R_{Ω}^{GDL}	Ohmic resistance (GDL)	Ωcm^2
R_{Ω}^{MIC}	Ohmic resistance (MIC)	Ωcm^2
$R_{Leakage}$	Electrolyte leakage resistance	Ωcm^2
$U_{collection}$	Local collection potential	V
U_{cell}	Cell potential	V
U_{Nernst}	Local Nernst potential	V
E_a^k	Activation energy for reaction k	kJ/mol
η_k	Overpotential	V
σ_{ionic}	Ionic conductivity	Scm^{-1}
σ_k	Electronic conductivity	Scm^{-1}

Variables of the electrochemical model can be found in Table 6.2, pp. 99.

Chapter 1

Introduction

1.1 Introduction

This thesis focuses on the study and solving of reliability and degradation issues in solid oxide fuel cells (SOFC), with a combined application of modeling and experimental tools.
A **CFD model** was developed that enables the simulation of SOFC repeat-units and short stacks including locally-resolved electrochemistry, with additional modules allowing the simulation of degradation and failure sources. The degradation models include parasitic diffusion in seals and interfaces, parasitic combustion, local damage of electrodes by reoxidation or reduction and associated cycling effects, and generation and transport of pollutant species from different components. By opposition to usual CFD models which often consider ideal component behavior, this work shows that the introduction of imperfect component properties -which corresponds to experimental reality- opens up new perspectives in the use of simulation. A much better match is obtained between simulation and experiments, which offers the possibility to perform model-based diagnostics. More important, the model allows to design new prototypes while taking into account the possible imperfections of components, which enables to study different design alternatives in order to overcome potential reliability or degradation issues.
While degradation of individual components has been studied intensively, the dynamics of degradation of SOFC stacks and repeat-units and their major underlying mechanisms are not fully identified and understood, although of crucial importance. The principal cause for this fact is the difficulty to extract direct information from experiments. To meet this demand, a diagnostic testing station was developed to perform **in-situ measurements** of local electrochemistry in an operating repeat-element. For the first time, the evolution of local degradation was studied in a SOFC repeat-element. This experiment allowed to identify major degradation sources and to study their effect, some of which were found to be linked to the design of the prototype, and other to the testing conditions. For this purpose, specific methodologies were developed to identify the degradation of the different electrochemical

processes from impedance spectroscopy measurements.
Based on the identified and analyzed degradation and failure sources obtained from the herein developed tools, two stack **prototypes** were successively designed and tested in collaboration with HTceramix-SOFCpower. With the successful solving of the main failure source and an important gain in efficiency, these design iterations proved the predicting capabilities and the accuracy of the CFD model for a design of SOfCs towards better reliability and performance.

1.2 Context and motivation

In the context of high energy prices and need to reduce greenhouse gas (GHG) emissions, fuel cells are considered as a promising technology for clean and efficient generation of electricity. This in particular in the case of combined heat and power (CHP) applications where the released heat can be used for heating purposes, hence avoiding loss of unused energy into the atmosphere.

Different types of fuel cells have been developed, reaching power ranges from a few watts to several megawatts. Each type of fuel cell presents advantages and drawbacks in the flexibility of use, in the type of fuels used, in the tolerance to impurities in fuels and air, in lifetime and cost.
Among the different types, solid oxide fuel cells are considered of high interest for small-scale power generation and CHP applications. Based on ceramic and ceramic-metal (cermet) components and operated at high temperatures (600°C-1000°C), they can be operated with different fuels such as hydrogen, methane, natural gas or bio gas, and reformed liquid fuels, with higher tolerance to fuel impurities than other fuel cell types. By reducing the cost of fuel pre-processing, the cost of SOFC-based CHP units can be lowered which could promote the use of this technology in both private and commercial buildings.
The major challenges for the deployment of this technology remain the achievement of long lifetimes (over 40'000 hours) at high efficiencies and the mastering of the risk of failure. The operation at high temperatures represents tough requirements for the materials which can suffer from chemical reactions (interaction between materials or materials and gases, generation of pollutants that degrade the electrochemical performance), from thermal ageing or thermomechanical issues. Failures of SOFCs occur principally due to the rupture of one or several cells, either induced by inappropriate mechanical constraints or mechanical weakness of the components, or by the later described reoxidation of the fuel electrode.
Part of these issues can be solved by appropriate design of the components, material selection, and operating conditions. As a high degree of interaction exists between components, between operating conditions and performance, between choice of materials and possible degradation issues, integrated modeling tools are required to address the complexity of the studied object, with the final objective to design enhanced prototypes. The development of a model addressing this task is the ***first objective of the present thesis***.

The knowledge about ageing, degradation processes and failure of SOFCs is in continuous evolution. While certain mechanisms have been clarified, others have been identified recently and are under investigation. Moreover, as soon as the stack and system levels are attained, prototype-specific, producer-specific and laboratory-specific issues [7] appear, depending on the applied materials and techniques, on the design of the prototype and on the testing conditions. These differences complicate the comparison and interpretation of results provided by different research groups.
Experimental investigations on degradation processes are usually performed at two different scales. Experiments on fundamental degradation mechanisms are performed on different components, at a small scale and in controlled conditions to ensure well-determined operating conditions and to prevent unwanted degradation sources. On the other hand, degradation is also tested at the scale of a stack or even in a full system. In this configuration, the components are exposed to operating conditions varying locally in the fuel cell. In most cases, degradation is only measured as the global loss of performance with time of one cell or stack, in particular due to the fact that local information is hard to obtain in an SOFC operating at high temperatures. At this scale of investigation, the identification of degradation sources becomes difficult, requiring a large number of experiments. Moreover, the link between the small-scale experiments and large-scale ones is not always easily established and the reasons for the observed discrepancies are not easily identified. In particular, the design of the prototype can cause specific degradation patterns which add to other mechanisms.
To overcome the gap between small scale experiments and stack-level, we propose to study experimentally the local operating conditions and the resulting local degradation in a real SOFC prototype. This represents the ***second objective of this work***. As in-situ measurements remain hardly feasible at certain locations in a fuel cell, we propose in such cases to use the developed modeling tool instead of measurements, by using dedicated submodels, in combination with experimental observations.
With the combined tool of dedicated models and a diagnostic testing station allowing specially resolved in-situ measurements, the efficiency, the performance limitations, the degradation and its sources, and risk of failure of different SOFC prototypes can be assessed and compared to analyze the effect of stack design, choice of materials, operating point or system integration on performance and degradation. Based on the acquired knowledge,the purpose is to provide a tool for the design and operation of more reliable and performing SOFC stacks. This last point represents the ***finality of this thesis***.
In the frame of the collaboration between EPFL and its spin-off company HTceramix S.A. (now HTceramix-SOFCpower), this approach was applied for the development and testing of stack prototypes, resulting in the assessment an development of three stack prototypes, and in particular the design of a second- and third-generation stack.

1.3 State of the art

Degradation and in-situ measurements Different types of in-situ measurements in Solid Oxide Fuel Cell repeat-units are reported in literature. The most accessible measure-

ment is the mapping of temperature, which can be performed without excessively invasive techniques [8]. Another type of measurement, considerably more complex, is the analysis of local fuel composition by sampling of gas and analysis in a gas chromatograph or mass spectrometer [9]. This type of measurement is principally made to investigate the kinetics of internal steam reforming of methane and the resulting electrochemistry.

Locally-resolved measurements of the electrochemical reaction are rarely performed in the case of SOFCs, contrarily to the case of PEMFCs or DMFCs where this technique has been employed several times owing an easier implementation of the instrumentation at lower operating temperatures [10–15]. For PEMFC and DMFC, this technique was principally used to investigate the effect of the gas distribution channels on performance and on water management [14, 15]. Other locally-resolved measurements were performed at a smaller scale by Reum et al. [13] to investigate the current distribution in the catalytic layer itself.
In the case of SOFCs, mappings of current densities were performed by Metzger et al. [9] at the German Aerospace Center (DLR, Stuttgart, Germany), and by Ravussin et al. [16] in our laboratory. Both experiments were performed by a segmentation of the active layer and interconnection into electrically-independant areas. At DLR, measurements are performed in a dedicated test configuration, allowing local measurements on 16 equiareal segments disposed on a $100cm^2$ cell. Local temperature measurements are also performed, as well as sampling of gas for analysis. In the frame of a collaboration between our laboratory and P.Metzger at DLR, local measurements were performed on different cells, allowing to establish an electrochemical model presented hereafter in this thesis.
The experiment of Ravussin et al. [16] differed from the experiment at DLR, as it was performed in a real stack prototype. The segmentation was performed into 8 electrically-independent segments on a small active area of $50cm^2$. Mappings of Nernst potential and current densities were obtained, showing important variations over the active area. The electrochemical performance was analyzed by electrochemical impedance spectroscopy (EIS). The results were compared with modeling results by D. Larrain [8] for analysis and model validation. This experiment showed among others the limitations of the investigated prototype in terms of flow distribution.
From literature, it appears that the degradation with time of **local** electrochemical performance has until now not been investigated experimentally. Different modeling studies and experimental results indicate that degradation is probably not homogeneously distributed over the active surface of the cell in a repeat-element, but with different conclusions depending on the considered mechanisms. In the general effort towards an understanding of degradation, this prediction is of importance as it possibly changes the way degradation results obtained experimentally on a stack have to be interpreted. Therefore, it is of large interest to overcome the existing lack of experimental verification.
By performing locally-resolved measurements of degradation in a repeat-unit, our work contributes therefore to the exploration and understanding of degradation mechanisms at the scale of a repeat-element, as well as to the development of this specific diagnostic and measurement technique.

Modeling tools To understand and develop SOFC systems, a large number of modeling tools has been developed across the different length- and time-scales, from micromodeling of electrodes to dynamics and control of complete systems. The main topics of interest are fundamental electrochemistry, stack and system performance, and thermomechanics. The first class of models is based on electrochemistry coupled with mass and heat transfer, while the second is oriented on thermomechanics of cells and assemblies.

In the first class of models, different types of tools are proposed:

- electrochemical micro-models considering fundamental electrochemistry in typical SOFC electrodes [1, 17–32]
- 'channel models' considering the interaction between cell, current collectors and gas streams [33, 34]
- 'repeat-unit models' considering mass and heat transfer in a repeat-unit, including local electrochemical reactions [8, 35–37]
- 'stack models' that describe the global behavior of a stack under different operating points. Such models are implemented in system modeling tools [38].
- 'system models' describing the interaction between the stack and the balance-of-plant (BOP) components [38, 39]

For these different length and time scales, different modeling tools have been developed. Electrode models are mainly written in equation solvers (Simulink [18],LIMEX [21],gPROMS [40], etc.), allowing to test different hypotheses concerning the reaction kinetics. In such models, mass transport is generally considered in the form of diffusion across the electrodes. While certain models focus on steady-state predictions, one specific class of models deals with the simulation of electrochemical impedance spectra [18, 21, 41, 42]. Measured experimentally, AC impedance spectra are used to identify electrochemical processes [43, 44] and to analyze their sensitivity to operating parameters or their evolution with time [45, 46].
From 'channel models' to 'stack models', CFD packages serve as a base for the modeling of mass and heat transfer, with eventual addition of supplemental chemical reactions. Upon the different scales, the major differences concern the level of detail in terms of geometric description as well as in the complexity of the electrochemical model. Electrochemical models are understood here in a broad sense, including internal fuel processing, i.e. steam-reforming and water-gas-shift reactions. Stack and system models address the dimensioning of stacks and their integration in systems. The electrochemistry is reduced to a fast and essentially descriptive zero-dimensional or one-dimensional model for integration in system modeling and system optimization tools [38, 39]. A detailed review on different modeling approaches can be found in [47] by Kakaç et al.

Another important modeling effort is set on thermomechanics and fracture mechanics, which is traditionally more oriented towards analysis of the risk of failure of components. A large

attention is paid to the evaluation of mechanical stresses in cells, with study of the subsequent possible failure modes. Other authors focus on the calculation of stresses in glass-ceramic seal materials, with particular attention to the risk of fracture and delamination. Combination of materials and components are also studied, with specific focus on design issues. For example, a study of design alternatives is presented by Weil and Koeppel [48] (Pacific Northwest National Laboratory, USA), which considers the effect of seal geometry and choice of materials on the resulting mechanical stress on the cells. Reaching the level of a complete repeat-unit, several authors import results from CFD or electrochemical models to analyze the effect of operating conditions on thermal stress and risk of failure. One complete study concerns directly the 2.5kW$_{el}$ stack prototype developed in this thesis. Developed by A. Nakajo from our laboratory, the model considers the risk of failure during different operating phases, including first operation, polarization or thermal cycling. The results of this study can be found in references [40, 49].

Degradation and failure models At the micro-scale, degradation is studied at two different levels. First, physico-chemical models are used to investigate ageing processes of the electrodes microstructure [50]. One major difficulty in this case is the important differences among materials, microstructure, cell types, operating temperatures, etc. which complicate the establishment of generic models. Second, the above-mentioned electrochemical models are used to predict the effect of different degradation patterns (loss of contact, modification of diffusive properties, change in TPB length...) on the expected electrochemical performance. Therefore, this approach offers the possibility of model-based diagnostics [51]. A review of this technique is given by Huang in [41].
At the repeat-element level, different degradation studies have been proposed. Larrain [8] and Van herle [52] from our laboratory introduced degradation submodels into a repeat-element model. The growth of oxide scale was implemented as a function of time and operating temperature, affecting the conductivity of the internal current collection. In addition, the risk of cell reoxidation due to fuel starvation was investigated. Other examples can be found with other research groups. Kulikovsky et al. [53] studied the effect of current-free spots (i.e. loss of contact) on the distribution of current densities over the active area, as well as the degradation of electrochemical performance due to local exceeding of a threshold current density.
In the majority of cases, the primary goal is to perform benchmark tests and parametric studies, in order to evaluate the effect of different operating points or design parameters on the expected degradation or risk of failure. Consequently, such models are principally applied on generic or simplified repeat-unit and stack geometries, but they don't consider real prototypes in detail. The probable reason for this is that degradation is principally assumed to be a matter of materials and operating conditions, and less as an issue linked to the design of the prototype (including geometry, materials and assembly). For a researcher facing degradation or failure of a real stack prototype, such models therefore may fail to explain the observed phenomena, which limits their relevance for this type of diagnostics.

A complementary approach In a context where several CFD models for SOFCs exist, even commercial ones, one can ask whether there is a real need for new developments in this field. However, the capabilities of such models are not completely exploited so far, and could well contribute to the understanding of SOFC systems. In particular, the application of CFD models for diagnostic purposes can be developed. This work contributes to the development of this type of applications.
To permit this development, we propose a novel approach which consists in modeling not only complete repeat-units in geometrically detailed manner, but foremost by considering the non-ideal properties of real materials or components, in order to reproduce experimental conditions with accuracy.

1.4 Structure of the present work

The present thesis is articulated around the modeling and experimental tools developed for the design and analysis of stack prototypes. The emphasis is put on the investigation of different failure and degradation sources. The diagnostics obtained from modeling or experiments on different stacks are detailed, and the subsequent corrective actions are presented.

In a first part, the modeling tool is presented, including the establishment of an electrochemical model from experiments, and the implementation of degradation submodels. By modeling, the effect of stack design and choice of materials on performance and degradation is studied, with particular focus on three different topics:

- performance limitations resulting from sub-optimal gas distribution
- effect of stack assembly and design options on degradation and risk of failure in the vicinity of seal gaskets
- topology of degradation resulting from the generation of pollutant species in, and upstream of, the stack

In a second part, the diagnostic test station developed for local in-situ measurements is presented, accompanied by the description of dedicated analysis techniques for the identification of degradation effects. The results of a degradation test performed during 1900 hours is presented, giving insight in a complex and non-homogeneous degradation sequence of a real repeat-element. In addition, the locally-resolved characterization of the prototype is detailed, allowing to assess the quality of the design.

For the characterization, the following aspects are treated:

- kinetics of reduction of the repeat-unit
- verification of assembly
- electrochemical performance map
- spatial distribution of operating parameters under polarization

In the degradation study, the following topics are treated:

- evolution of local electrochemical performance
- spatial reorganization of the electrochemical reaction with time
- assessment of the state of degradation by impedance spectroscopy
- identification of electrochemical processes and their level of degradation
- analysis of the spatial distribution of degradation for different reaction steps
- identification of possible degradation sources: endogenous and exogenous pollutants
- spatial distribution of pollutants over the active area
- effect of pollutants on the electrodes and their performance

1.5 Confidential issues

Throughout this work, different stack prototypes of HTceramix-SOFCpower are described and analyzed, showing part of their limitations. For confidentiality reasons, it is not possible to describe in all detail their proprietary technology, as well as all the corrective actions and solutions found to tackle the issues revealed in this study.
Nevertheless, HTceramix-SOFCpower authorized to publish in this study a large number of elements, allowing an open presentation of the methodology developed in this work and experimental results obtained from their technology. They are gratefully acknowledged for this. In addition, their core stacking technology based on their proprietary material SOFConnex^{TM} enabled in a flexible manner the design of second- and third-generation stacks developed from the herein developed tools, an opportunity for which they are also acknowledged.

Chapter 2

The solid oxide fuel cell

2.1 Operating principle

Solid oxide fuel cells convert in direct manner the reaction enthalpy of a fuel and air in electrical power by electrochemical reactions. They are based on a gas-tight ceramic ionic conductor (and electrical insulator) in contact with two electrically conductive electrodes, constituting a cell. The electrochemical reactions occur at the interface between the porous electrodes, the electrolyte material and the gas phase, called the triple-phase boundary (TPB). Different reaction sites and mass transport paths exist depending on the used materials and the operating conditions.

The operating principle of an SOFC is detailed in Fig. 2.1. Oxygen from air is reduced to oxygen ions (O^{2-}) at the cathode which delivers the necessary electrons. The oxygen ions are transported through the electrolyte to the anode where they react with species from the fuel. On anode side, fuel species (usually hydrogen or carbon monoxide) react with the oxygen ions at the surface of the electrode, to which the electrons are transferred. The reaction of fuel and oxygen on anode side results in a low partial pressure of oxygen. The difference in oxygen partial pressure between cathode and anode side creates the electrical potential which can be exploited.

The overall electrochemical reaction can be written as two half reactions occurring on each electrode (equation 2.2 and 2.1). In the case of the use of hydrogen as fuel, the half reactions are:

$$\frac{1}{2}O_2 + 2e^- \leftrightarrow O^{2-} \tag{2.1}$$

$$H_2 + O^{2-} \leftrightarrow H_2O + 2e^- \tag{2.2}$$

These reactions are in fact a simplification of the real reaction steps which imply different gaseous and adsorbed species (see Fig. 2.1), as well as different possible reaction pathways both on anode and cathode side [1, 17, 18, 24, 42].

The electrochemical reactions on anode and cathode side are controlled by the electrical

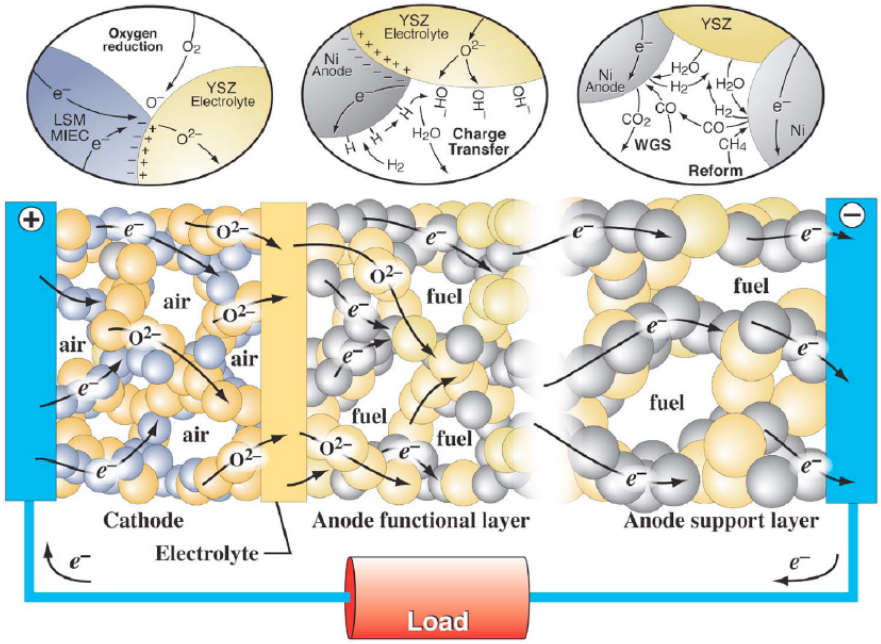

Figure 2.1: Elementary reaction steps in SOFC electrodes (taken from Zhu and Kee [1]).

current entering / leaving the electrodes. With the created electrical potential, an electrical current appears between anode and cathode side as soon as a conducting external circuit is connected to the fuel cell. To increase the delivered power, cells are connected in series through metallic interconnectors (MIC), providing a higher total potential for a common constant current.
Other fuels than hydrogen and carbon monoxide can be converted in SOFCs, whereas not by direct conversion. Methane from natural or bio-gas, methanol and other liquid fuels can be used, but require a fuel processing step (reforming). The reforming step can be performed either externally to the stack or internally. For methane reforming, either steam or carbon dioxide are mixed with the fuel, followed by a processing over a catalyst at high temperature. The steam methane reforming (SMR) and dry-reforming reactions are:

$$\begin{aligned} CH_4 + H_2O &\leftrightarrow CO + 3H_2 \\ &\quad \Delta_R H^0_{298K} = +206.2 kJ/mol \end{aligned} \tag{2.3}$$

$$\begin{aligned} CH_4 + CO_2 &\leftrightarrow 2CO + 2H_2 \\ &\quad \Delta_R H^0_{298K} = +247.9 kJ/mol \end{aligned} \tag{2.4}$$

As the nickel used in SOFC anodes is a catalyst for these reactions, their strong endothermic property can be used for cooling purposes, which is advantageous for system efficiency. In addition, as explained hereafter, the maximum reachable electrical efficiency is higher for methane (99%) than for hydrogen (78%), showing the interest of this fuel.
In the combined presence of H_2,CO,H_2O and CO_2 and at SOFCs operating temperatures, the *water gas shift reaction (WGS)* (Eqn. (2.5)) is close to equilibrium. As hydrogen is

supposed to be more easily converted electrochemically in the anode, carbon monoxide is consumed indirectly through this reaction.

$$CO + H_2O \leftrightarrow CO_2 + H_2 \tag{2.5}$$

2.2 Cells and stacks

Cells are constituted of one fuel and one air electrode sintered on either side of a solid electrolyte. One of the three layers is used for mechanical support, giving its name to the type of cell (anode-supported, cathode-supported or electrolyte-supported cells). Other support types were developed in addition to the already mentioned ones, such as metal-supported [54–57] or foil-supported cells (CeresPower, UK).
In addition to the type of support, SOFCs can be classified by their geometry. Planar and tubular cells are the mostly employed geometries, besides other types such as segmented-in-series (SIS) concepts. In the planar case, the cell is associated with a planar interconnect which enables the current collection from the cathode of one cell to the anode of another, while allowing the distribution of air and fuel on the reaction surface in a *gas diffusion layer* (GDL).

2.2.1 Electrolytes

SOFC electrolytes are made of a solid oxide material that is conductive for oxygen ions and electronically insulating. The mostly used electrolyte material is Yttria-Stabilized Zirconia (YSZ), with an yttrium doping in the range from 3% to 12%. The yttrium doping affects both the ionic conductivity and the mechanical strength of the material. The usual compositions are 8% mol Y_2O_3 - 92% ZrO_2 (referred to as 8YSZ) for its high conductivity, and 3% mol Y_2O_3 (3YSZ) for mechanical strength.
To limit losses, the thickness of the electrolyte is minimized. As the ionic conductivity increases with temperature, thicknesses in the range of 100μm are possible at high temperatures (850°C-950°C), allowing the use of electrolyte-supported cells. In the range of 700°C to 850°C, the electrolyte thickness is kept in a range of 3 to 20 μm for sufficient conduction. In this temperature range, anode-supported cells are mostly used. At lower temperatures, other materials are preferred to YSZ, such as doped ceria.

2.2.2 Electrodes and current collection

Anode The fuel electrode (anode) is usually constituted of a composite of metal and ionic-conductive oxide particles (cermet). The most common composition is a composite of nickel

and yttria-stabilized zirconia (Ni-YSZ). The production of the anode cermet is made by co-sintering of a mixture of micron-sized powder of nickel oxide (NiO) and YSZ, possibly accompanied by an additional pore-former material. During the first exposition to the fuel, the nickel oxide in the dense layer is reduced, forming interconnected metallic nickel particles. Due to the volume reduction during this process, an open porosity network is created, allowing diffusion of gases through the electrode. The interleaved structure of electronic conductive metal and ionic conductive YSZ provides a high reactivity for the transfer of charge at the triple phase boundary. Nevertheless, due to the finite ionic conductivity of YSZ, the electrochemical reaction takes place preferably in the vicinity of the electrolyte. Modeling results by Zhu and Kee [1] predict a distributed reaction occurring up to a few dozens of microns away from the electrolyte.
Despite their high performance, anode-supported cells based on nickel present a major drawback. Due to the large volume change of nickel to nickel oxide upon reoxidation and due to the stiff YSZ backbone, a complete reoxidation of the electrode leads to important internal mechanical stresses . Fracture of the YSZ backbone and propagation to the electrolyte is a frequent consequence of reoxidation, hence representing a major cause of cell failure.

Cathodes and cathode current collection layers Air electrodes (cathode) are made of a sintered porous structure possessing electronic as well as ionic conductivity. This mixed conductivity is either obtained by mixed conducting materials or by a composite of electronic conductive and ionic conductive materials. The use of metals as electronic conductors is not possible due to the oxidizing atmosphere, with exception of noble metals that have been considered in the past as potential cathode materials. Due to their high cost, they have been replaced by ionic and electronic conductive oxides, and principally by perovskite materials. The most common cathode materials are a composite of *strontium doped lanthanum manganite* $(\mathrm{La,Sr})\mathrm{MnO_3}$ (LSM) and YSZ, or the mixed ionic/electronic conductor *lanthanum strontium cobaltite ferrite* $(\mathrm{La,Sr})(\mathrm{Co,Fe})\mathrm{O_3}$ (LSCF). Oxygen is transported in the gas phase to the reaction sites in the vicinity of the electrolyte. If a composite electrode is used, the incorporation of the oxygen ions in the ionic conductor takes place preferably at the triple phase boundary (TPB), at the interface between the ionic and electronic conductor. The reactivity is then highly dependant of the length of the TPB per unit volume and on its morphology. Therefore, any physico-chemical process affecting the TPB can have an effect on the activity of the electrode and therefore on the losses occurring for this reaction step. In the case of a mixed electronic/ionic conductor such as LSCF, oxygen can be incorporated in the cathode material over its whole surface.
To limit mass transport losses, the thickness of cathode layers is minimized (with exception of cathode-supported cells). Standard thicknesses are in the range of 10 to 50 μm. From the cathode layer, the electronic current has to be collected to the interconnection. Current collectors are usually shaped as ribs providing channels for the supplied air and contacts on the air electrode. The usual spacing between ribs is in the range of a few millimeters to limit pressure drop in air channels. For 20μm thick cathodes, this spacing would induce unacceptable ohmic losses to the areas that are away from the contact areas. Therefore, an additional current collection layer (CCC) with coarser microstructure is placed on top of the

cathode layer.

2.2.3 Interconnects

In planar designs, cells are separated using interconnecting plates (interconnects). On each face of them, gas-diffusion layers (GDL) ensure gas distribution and contacting with the cell. While certain ceramic-type interconnects have been considered, metallic ones are the preponderant type in actual prototypes. To accommodate the thermal expansion of the cell, ferritic stainless steel with high chromium content is usually used. The protection against oxidation is obtained by a chromia layer, or by duplex oxide layers [58].

2.2.4 Sealing

To avoid gas cross-over from the anode to cathode and inversely, sealing materials are used. Different types of sealing gaskets have been developed, an overview of which is given by Fergus et al. in [59]. They can be classified as rigid or compressive seals, with in each category the presence of metal-based solutions or glass/ceramic and mica-based ones. A more detailed description of seal properties is given in the following paragraphs.

2.3 Efficiency and losses

By directly converting the available reaction enthalpy in electrical power, fuel cells overcome the intrinsic limitation of thermodynamic cycle engines defined by the temperature levels of the hot and cold sources, allowing to reach high efficiencies which make the attractiveness of this technology.

Thermodynamic efficiency From thermodynamics, it is known that the maximum achievable work from a given reaction is given by the change in standard Gibbs free energy $\Delta G^0 = \Delta H^0 - T\Delta S^0$. For the same reaction, the maximum released heat is given by the change in standard enthalpy ΔH^0. Therefore, it is possible to define a maximum achievable thermodynamic efficiency for a given fuel:

$$\epsilon_t = \frac{\Delta G^0}{\Delta H^0} \tag{2.6}$$

At a temperature of 1000K, the maximum thermodynamic efficiency obtained for hydrogen is $\epsilon_{t,H_2} = 78\%$ while it is $\epsilon_{t,CH_4} = 99.6\%$ for methane. Consequently, higher electrical effi-

ciencies are attainable with methane than with hydrogen.

The maximal work can be expressed as an electrical equivalent for a molar reaction rate $\dot{N}$ (mol/s) and a number of exchanged electrons z (F is the Faraday constant):

$$\Delta G^0 \dot{N} = U^0 I \tag{2.7}$$

$$I = \dot{N} z F \tag{2.8}$$

$$U^0 = \frac{\Delta G^0}{zF} \tag{2.9}$$

U^0 is the reversible potential at standard state. For situations differing from standard state, the maximum achievable work for the reaction is given by

$$\Delta G = \Delta G^0 + \sum_{react-prod} RTln\frac{P_j}{P_{atm}} \tag{2.10}$$

Expressed as electrical potential, one obtains the expression of the reversible (Nernst) potential. For the case of hydrogen, it is given by:

$$U_N = U^0 + \frac{RT}{2F} ln \frac{p_{O_2}^{1/2} p_{H_2}}{p_{H_2O}} \tag{2.11}$$

with the partial pressures p_j of gases given in *atm*. This potential corresponds to the maximum electrical potential achievable locally on a fuel cell where the gas compositions are given by the partial pressures p_j on either face of the cell. Due to the consumption of fuel species and generation of reaction products, the partial pressures of gases evolve along the flow path in the fuel cell, resulting in a variation of Nernst potential. As air is usually supplied in excess to the required stoichiometry for complete conversion, the oxygen partial pressure varies in a limited range over the reaction surface. For this reason, the Nernst potential decreases principally along the fuel stream.

Electrochemical losses The efficiency of the electrochemical reaction is limited by several losses. The kinetics of the elementary reactions on each electrode (dissociation, charge transfer, incorporation, surface diffusion, etc.) depend on the used materials and operating conditions, on the thickness, morphology and microstructure of the electrodes, and in particular on the length of the triple-phase boundaries. While certain reactions are at equilibrium and therefore don't cause efficiency losses, other ones represent *rate-limiting reaction steps* and are accompanied by losses. In addition, mass transport by diffusion through the electrodes results in losses due to the resulting concentration gradients that lower the partial pressure of the reactive species at the electrolyte, and consequently lower the Nernst potential precisely at the reaction zone (see Eq. 2.11).
Finally, electronic current through electrodes and connectors is accompanied by ohmic losses due to the finite conductivity of the materials. In the same way, the transfer of oxygen ions through the electrolyte causes losses of ohmic type.

Available power and losses Due to the losses, the effective electrical power differs from the maximum achievable power from equation 2.10:

$$P_{el} = U \cdot I = \Delta G \dot{N} - P_{loss} \tag{2.12}$$

where P_{el} is the electrical power and P_{loss} represents the losses. Consequently, the available electrical potential U differs from the Nernst potential by a sum of potential losses (overpotentials) η_i:

$$U(j, T, p_1..p_k) = U_N(T, p_1..p_k) - \sum_i \eta_i(j, T, p_1..p_k) \tag{2.13}$$

The overpotentials are functions of the current density j (i.e the current per unit of active area), the temperature T and gas partial pressures $p_1..p_k$. The losses can be expressed as an *area-specific resistance (ASR)* (see Eqn. (2.15)).

$$U(j, T, p_1..p_k) = U_N(T, p_1..p_k) - ASR \cdot j \tag{2.14}$$

$$ASR(j, T, p_1..p_k) = \frac{U_N(T, p_1..p_k) - U}{j} \tag{2.15}$$

Cell potential The available potential U corresponds to the ***local*** electrical potential at which the electrical power is collected. We denote it therefore as ***collection potential*** U_{coll}.The difference between the collection potential U_{coll} and the Nernst potential can be considered as the driving force for the delivery of current. In a repeat-element, the collection potential is fixed by the way the current collection is made, while the Nernst potential is a local property given by local gas compositions. In a planar-type repeat-unit, the collection potential is almost constant over the active surface, due to the important in-plane conduction in the interconnects. By abuse of language, this common delivery potential is often called the *cell potential* U_{cell}. In the planar case, collection and cell potentials are therefore very close and in numerous models considered as equal.
For tubular designs, the collection of current is in most cases performed on one strip along the tube (Siemens-Westinghouse) or at the end of the tube. In those cases, the local collection potential differs from the cell potential due to the ohmic losses in the current collection.
The local power loss corresponds to the difference between local Nernst potential and local collection potential multiplied by the local current density (Eqn. (2.16)). To compute the overall losses, ohmic losses in the current collection have to be added.

$$P''_{loss} = (U_N - U_{coll}) \cdot j \tag{2.16}$$

Fuel utilization To extract current from the cell, the local collection potential has to be inferior to the local Nernst potential. As mentioned earlier, the latter decreases along the fuel stream, as reactive species are converted electrochemically. The conversion rate (denoted as *fuel utilization*) determines therefore the minimum Nernst potential existing on the reactive surface, and consequently the maximum achievable cell potential. As they depend

on the difference between Nernst and collection potential, the overall losses increase therefore rapidly at high fuel conversion rates. This problem is analogous to *pinch problems* observed for heat transfer in exchangers.
Moreover, at such operating points, the depleted gases induce increasing losses in the electrochemical reaction. For these reasons, fuel cells are not operated at 100% of fuel utilization, which limits the electrical efficiency. This situation can be considered as system losses if the heat from the residual fuel is not exploited.

Segmented-in-series concepts, cascaded stacks and recirculation loops To limit this type of losses, some system options have been studied and implemented. First, fuel recirculation loops have been proposed, where one part of the converted fuel is reintroduced at the inlet of the anode and mixed with non-converted fuel. This lowers the difference in Nernst potential over the reacting surface and helps to maximize fuel utilization and efficiency. In other systems, cells are ordered in series on a common substrate, with the fuel being successively converted from one to the other. This way, the variation in Nernst potential over one single cell is minimized. Such segmented-in-series arrangements are developed principally by Rolls-Royce (UK) or Tokyo Gas and Kyocera (JP). Finally, it is possible to arrange several stacks in a cascade where the gases are progressively converted.

2.4 Degradation and Failure Mechanisms

The degradation of performance with time is principally caused by ageing or pollution of the electrodes, and by an increase of the ohmic resistance in the current collection. In addition, thermomechanical issues are supposed to possibly alter the electrical contact between cell and interconnect. Other degradation sources don't alter the electrochemical performance in a direct manner, but affect other components with possible consequences on the reliability of the stack.
In the following paragraphs, the main degradation mechanisms are presented in a non exhaustive manner to provide an overview and situate the topics addressed in the present work.

2.4.1 Anode

Coarsening The microstructure of the anode evolves with time due to the operation at high temperature. Nickel particles are subject to coarsening phenomena by coalescence or Ostwald ripening, which results in a loss of percolation and a decrease in electronic conductivity, as well as in a reduction of the number of active sites for the electrochemical reaction.

This phenomenon can be accelerated in presence of steam due to the high mobility of volatile nickel hydroxide species [60].

Pollutants Anode materials are sensitive to pollutants species, in particular to H_2S which is often found as impurity in fuels. Haga, Sasaki and co-authors studied different anode pollutants [61], such as sulfur, chlorine, siloxane, phosphorus or boron. The poisoning mechanisms differ for the different volatile species. Sulfur is adsorbed on the nickel particles, affecting the electrochemical reaction and altering severely the kinetics of steam methane reforming. Formation of low-melting Ni_3S_2 is also possible at low H_2 content. It has to be noted that the complete mechanism of sulfur poisoning remains intensively investigated, due to its important consequences on fuel processing. Chlorine poisoning results in formation of $NiCl_2$ particles at the surface of nickel, while siloxane poisoning leads to deposition of silica. Differing from the other pollutants, boron is reported to promote particle coarsening.
While these pollutants are mostly impurities in the fuel, other pollutants can be generated inside the system. For example, $CaSO_4$ or Na(OH)(g) can be generated from water used for the steam-reforming reaction (Eqn. (2.3)). Other pollutants, such as boron or silicon can be released from sealing materials.
Besides exogenous pollutant sources, Mogensen et al. found that impurities in raw materials strongly affect the electrochemical performance, but also might explain the observed discrepancies among results from different cell developers [7, 62, 63]. In particular, Mogensen claims that traces of silica are always present even in almost pure YSZ, in sufficient amounts to form ultrathin amorphous layers on its surface by segregation, which strongly determines the electrochemistry.

Redox-cycling Nevertheless, the most damaging situation for the anode is the partial or complete reoxidation of the nickel matrix. Accompanied by a strong expansion of the nickel particles, the reoxidation induces important mechanical stress in the anode layer. In the case of electrolyte-supported cells, delamination of the electrode is the most probable consequence of a reoxidation-cycle (redox-cycle). For anode-supported cells, redox-cycles are accompanied in most cases by cracking of the anode-supporting layer, with possible propagation through the electrolyte [64, 65]. This effect is amplified by the fact that successive redox-cycles result in an increasing expansion [4]. Such repeated redox cycles are consequently a major source of cell failure for anode-supported cells. Due to the serial arrangement of cells in a stack, the failure of one single cell results in the complete failure of the device.

2.4.2 Cathode

Chemical reactions Cathode materials experience different types of degradation. First, not all cathode materials (such as $(La, Sr)CoO_3$)) are intrinsically stable, but some tend also

to react with other materials spontaneously. For example, depending on its stoichiometry, the commonly used cathode material $(La, Sr)MnO_3$ reacts spontaneously with YSZ, forming a highly resistive phase of lanthanum zirconate $La_2Zr_2O_7$ (LZO) [66]. Similarly, LSCF cathodes are very reactive with YSZ, requiring the co-sintering of a less reactive intermediate layer of ceria between a LSCF cathode and an YSZ electrolyte. A review on materials interactions for cathode materials is given by Yokokawa in [67].
Besides materials interactions, cathode materials can experience morphological changes due to sintering, which have been found to be related to a degradation of performance [42].

Current-induced activation and degradation In addition to these spontaneous degradation mechanisms, the performance of cathode materials is durably affected by the passage of current. In the first period of polarization, a current-induced activation of the electrodes performance is reported. The mechanisms leading to this activation remain not completely clarified. In the case of LSM, this activation is attributed to a change of morphology of the interface with YSZ [66], to dissolution of LZO phases [68], modification of the surface improving oxygen dissociative adsorption or surface diffusion [42, 69], or to formation of nanoporous LZO increasing the length of the triple-phase boundary [70]. Current-induced degradation is also reported by several authors for LSM. Hagen et al. report increasing degradation rates at increasing current densities [45], with more pronounced effect at lower (750°C) than higher temperatures (>850°C). Moreover, this type of degradation is found to be limited by an increase in oxygen partial pressure, with very low degradation under pure oxygen [68]. This degradation is accompanied by an alteration of the interface between LSM and YSZ particles, resulting in a decrease of the TPB and of the contact area [68]. A comprehensive review on LSM performance and degradation is given by Adler in [42].

Pollutants While spontaneous degradation by material interactions can be limited by an appropriate choice of materials and current-induced degradation can be limited by appropriate operating points, other degradation sources are not primarily related to the electrode itself. This is notably the case of pollutant species that alter the electrodes performance. The most studied pollutants are the chromium-containing volatile species CrO_3 and $CrO_2(OH)_2$, which originate from chromium-containing metallic parts. While CrO_3 is the most abundant specie in dry air, $CrO_2(OH)_2$ predominates even at low levels of humidity [71]. Metallic interconnects have been considered as principal chromium source. To avoid chromium evaporation, protective layers were developed and successfully applied. In addition to the metallic interconnects, system components and in particular heat exchangers are potential chromium sources.
Chromium-containing volatile species deposit in the cathode layers following different mechanisms. For certain cathode materials such as $(La, Sr)CoO_3$, a spontaneous reaction occurs, with formation of $SrCrO_4$. In the case of LSM-YSZ, deposition of chromium occurs by electrochemical reduction of the pollutant in the vicinity of the triple-phase boundary, forming

solid Cr_2O_3. Another possible path of deposition is by reaction with Mn segregated in zirconia [72]. The deposition of chromia results in a blocking of active sites near to the TPB and a degradation of electrochemical performance. Finally, as LSCF is a mixed conductor and consequently presents a large reaction surface, the same amount of chromium poisoning is supposed to result in a lower degradation than for LSM-YSZ.
Other pollutant species have been identified, such as silica [7][73][74], alkaline species [73], or the more recently investigated sulfur [75]. From gaseous species or from segregating impurities in the bulk materials, silica forms amorphous phases on particle surfaces [7]. Exogenous sources of silica are silicone tubes, residues from compressor lubricants in the supplied air [7], and seal materials. Silica is known to possess an important poisoning effect, as only a thin amorphous layer on the electrode can alter considerably the electrochemical reaction [74, 76]. Despite this important poisoning effect, it remains difficult to identify the exact nature of volatile silicon-containing species. One possible candidate could be $Si(OH)_4$ which is known to evaporate from SiO_2 under humid conditions, even in oxidizing atmospheres [6, 77–79].
The poisoning effect of alkaline species was investigated experimentally among others by Jiang and co-authors [80]. A LSM cathode was placed downstream of a borosilicate glass of composition $A_2O - Al_2O_3 - B_2O_3 - SiO_2$ (A=Na,K). The expected volatile species were Na_2O ,K_2O and B_2O_3 . In particular when exposed to Na_2O -containing glass, an important grain growth was observed in the LSM, as well as a reduction of its electrochemical activity. The presence or not of alkaline materials on the electrode after testing was not reported.
Sulfur poisoning has received more attention recently for cathode materials. Xiong and co-authors [75] investigated the effect of sulfur poisoning originating from the atmospheric SO_2. They showed an important reactivity with $(SmSr)CoO_3$ (SSC), but less with LSM. As SO_2 does not react with the cathode material electrochemically, it doesn't deposit preferably at the TPB, contrarily to chromium species.
As shown in this brief and partial overview, cathode materials are sensitive to a large number of pollutants. Still, more knowledge about pollutant species is required, in terms of thermodynamic data and kinetics. From this overview, two principal pollutant sources can be identified: metallic parts and sealing materials. While the first have been investigated in reducing and oxidizing atmospheres, both under dry and humid conditions, seal materials have been principally studied in humid and reducing conditions or in dry and oxidizing atmospheres. Consequently, there is a lack of data on humid air conditions, despite the fact that hydroxide formation often results in increased evaporation rates, such as in the case of chromium.

2.4.3 Seal materials

Chemical interactions Seal materials are known to react with the metallic interconnects they are in contact with. The reaction of usual seal compounds (Si, Al, Mg, Ba, Ca, Na, K, B...) with ferritic interconnect materials can cause an anomalous oxidation of the alloy [58, 81–83]. This anomalous oxidation is accompanied among others by a release of volatile chromium-containing species which are pollutants for the cathode materials. In addition, as

already mentioned, numerous volatile species can be released from sealant materials in the gas phase, causing possible degradation.

Loss of gas tightness One important issue for seal materials is the loss of gas tightness with time. The mode of degradation is strongly dependant on the raw material and its form. Silver rings were investigated as possible sealing materials. It was found that silver becomes porous with time when exposed to dual atmospheres, due to diffusion and reaction of oxygen and hydrogen. Concerning other types of metallic seals, corrugated metallic gaskets were found to undergo plastic deformation and creep, possibly resulting in leaks. In the case of rigid glass-ceramic seals, losses of gas tightness occur principally during thermal cycling, where small mismatches in thermal expansion coefficient between seal and metallic parts can lead to increased mechanical stresses and delamination.
For mica-based compressive seals, a decrease of gas tightness was observed by Chou et al. [84] during long-term operation and repeated thermal cycling, possibly caused by losses of material by reaction and evaporation, and by delamination of glass interfaces from the interconnect material.

Insulating properties In a large number of fuel cell designs, seals have to be electrically insulating. Degradation of these insulating properties were reported for glass-ceramic seals due to migration of conducting species in the bulk of the material. In addition, in the cases where glass-ceramic sealants are supposed to provide mechanical support, local overheating over the glass transition can lead to catastrophic loss of support and short-circuiting [83].

2.4.4 Metallic interconnects

Oxidation Growth of oxide scales on metallic interconnects has been studied and correlated with an increase of ohmic resistance, as well with a release of pollutant species. The interaction between chromium evaporation from the interconnects and pollution of the cathode layer has been discussed above, as well as a possible anomalous oxidation in presence of seal materials.

Creep and loss of contact Exposed to high temperatures as well as to important temperature gradients, interconnects are subjected to thermal stresses and to the resulting creep. The resulting deformations can lead among others to loss of contact between the GDL and the cell, with consequent effects on the electrochemical reaction due to a reduction of the active area. Moreover, plastic deformation can lead to increased deformations, especially during thermal cycling, which can be accompanied to excessive stresses in cells and seals.

2.4.5 System components

SOFC systems include an important number of additional components. The balance-of-plant (BOP) components consist mainly of heat exchangers, afterburners and fuel reformers. All components suffer from specific degradation issues, which are not described in detail here. Nevertheless, some degradation modes can have an impact on the stack, which is the most sensitive system component. In particular, emissions of pollutants have to be considered, with additional attention when recirculation loops are used for better energy recovery. In this case, not only pollutants might be recirculated, but also steam or other species which in turn induce increased evaporation of pollutants.
The locally-resolved experiment presented in Part 10 demonstrates the importance of this external source of degradation.

2.5 Investigated topics

Performance The first aspect studied in this work is the influence of stack design on efficiency and power output. The principal requirement for this task is an accurate description of the electrochemical reaction over a wide range of operating conditions. In order to reach high efficiencies, it is necessary to convert a maximum amount of fuel, which implies important variations of fuel compositions over the active area. Several losses increase rapidly with polarization in depleted areas, accompanied by an additional loss of local Nernst potential. These local operating conditions are consequently determining the maximum reachable efficiencies, and therefore, an accurate description of such effects is mandatory for accurate predictions. Consequently, an electrochemical model was developed from experimental results and implemented in a CFD model.

Degradation This work deals principally with degradation and failure issues linked to design options. Among the different degradation sources listed in the preceding paragraphs, several ones are directly or indirectly influenced by the design of the fuel cell. Among them, certain sources and mechanisms are directly linked to mass transport, chemical reactions and electrochemistry, and can therefore be addressed by CFD modeling.
The principal failure mechanism was investigated by studying the local risk of oxidation of the anode support in operation. The effect of stack construction, choice of materials and operating conditions was investigated and compared to experimental results. Corrective actions were subsequently implemented in second-generation stacks.
Another topic of importance for degradation is the generation and transport of pollutants, which is not often studied for detailed stack designs. This was done both numerically as well as experimentally, in an experiment where in-situ measurements allowed to attribute the principal degradation sources to pollutants.

Chapter 3

Investigated stack technology

The different prototypes on which modeling, design and experimental work were performed are briefly presented in the following paragraphs, in order to provide an overview.

3.1 Three different stack prototypes

Three different stack designs were studied in the present work: R-design, S-design and F-design, in chronological order. The R-design was the reference prototype at the beginning of the developments presented here. Both *S-design* and *F-design* stacks were designed and analyzed using the tools presented hereafter.
The *S-design* stack was developed to be integrated in an integrated system sub-component (HoTbox^{TM}) consisting of a high-temperature heat exchanger for fuel and air preheating, a catalytic partial oxidation (CPOX) reformer, and an afterburner. The *F-design* stack was developed in the framework of the FP6 European Project *FlameSOFC*, for integration in a 2.5kW$_{el}$ CHP system based on a thermal partial oxidation (TPOX) reformer. The stacks are presented in the following paragraphs. Their principal characteristics can be found in table 3.1.

3.2 HTceramix-SOFCpower stack technology

The stacks developed in collaboration between LENI and HTceramix-SOFCpower are based on planar, anode supported cells (ASE) pressed between two gas diffusion layers (GDL) made of HTceramix S.A. 's proprietary material called SOFConnex^{TM} . This material ensures electrical contact and flow distribution over the active area.

	R-design	*S-design*	*F-design*
Active area	50 cm^2	50 cm^2	200 cm^2
Flow arrangement	counter-flow	co- and counter-flow	co- and counter-flow
Fuel distribution type	internal	internal	internal
Air distribution type	internal	external	external
Fuel recovery	no	internal	internal
Air recovery	no	external	external
Cell type	ASE	ASE	ASE
GDL	SOFConnex^{TM}	SOFConnex^{TM}	SOFConnex^{TM}
Nominal power density	0.4 Wcm^{-2}	0.4 Wcm^{-2}	0.4 Wcm^{-2}
Nominal fuel utilization	40%	75%	85%
Max. electrical power in 5-elements stacks (tested)	135 W_{el}	164 W_{el}	384 W_{el}
Max. electrical power (tested)	250 W_{el}	1.1 kW_{el}	1.84 kW_{el}
Number of repeat-units	29	72	20
Max. achieved lifetime (1 RE)	5000 hours	5000 hours	2000 hours

Table 3.1: Overview of the stacks developed and tested for HTceramix-SOFCpower

Metallic interconnects Metallic separator plates (metallic interconnects, MICs) made of plane ferritic stainless steel ensure the separation of the air (cathode) and fuel (anode) volumes and the electrical connection from one repeat-element to the other. Different alloys are used as metallic interconnects: *Crofer 22 APU* (ThyssenKrupp VDM, Werdohl, D), *UGINOX F17TNb and F18TNb* (UGINE & ALZ, La Plaine St. Denis, F), *IT10* (Plansee, Reutte, A).

Cell type The anode-supported cells are based on a nickel / yttria-stabilized-zirconia (Ni-YSZ) cermet. The standard thickness of the anode support varies between 200 and 550μm. The air electrode consists of one active layer (referred to as 'cathode') and a current-collection layer (CCC). The standard cathode materials are a composite of strontium-doped lanthanum manganite $(La, Sr)MnO_3$ (LSM) and YSZ, and $(La, Sr)(Co, Fe)O_3$ (LSCF). Numerous experiments were also performed using strontium-doped lanthanum ferrite ($(La, Sr)FeO_3$). Finally, nickelate cathodes Nd_2NiO_4 were also studied for operation at low temperatures [85]. The cathode current collection layers are principally composed of strontium-doped lanthanum cobaltite $(La, Sr)CoO_3$ (LSC). In some experiments, LSC is replaced by LSM for current collection.
The different prototypes are not restricted to the use of anode-supported cells, but the latter are preferred to electrolyte-supported cells for their performance at lower temperatures.

Operating temperature Depending on the cathode material, the stack operating temperature is varied. Typical temperature ranges are shown in Table 3.2.

Cathode Material	Operating temperature
LSM/YSZ	750°C- 850°C
LSCF	700°C- 800°C
LSF	700°C- 800°C
Nickelate	700°C

Table 3.2: Operating temperatures for different cathode materials

Stack cooling To limit thermal gradients inside of the stack, the maximum temperature difference is kept in a range of max. 100°C. The generated heat is removed by convection (internal air flow), by radiation with the surroundings or by internal steam reforming. To avoid cold zones at the boundaries of the stack, convection cooling or steam-reforming are preferred and the radiative heat exchange is limited. Consequently, the air flow rate is varied depending on the operating point. Expressed as air excess factor λ (Eqn. (3.1)), typical values of $\lambda = 2$ to 10 are necessary to ensure cooling. These high values however don't necessary represent the net air flow entering the system, as the air can be recirculated internally to ensure appropriate cooling while keeping system heat losses low [38].

$$\lambda = \frac{\text{air flux}}{\text{air flux for complete fuel conversion}} \tag{3.1}$$

Mechanical loading To ensure gas tightness in the stack, compressive sealing gaskets are employed. Consequently, a mechanical load is applied on the stack by an external system in order to guarantee proper electrical contact and sealing. Typical loads are in the range 4-6 Ncm^{-2}

3.3 Sealing technology

HTceramix S.A. 's standard sealing technology is based on compressive seal materials such as mica paper, by opposition to rigid bonding technologies mostly based on glass or glass-ceramic sealant materials. While the latter present in most cases an excellent gas tightness, they suffer from thermomechanical issues resulting from the rigid bonding between parts. Cracks and delamination can occur, principally during thermal cycling due to mismatches in thermal expansion coefficients (TEC) between components. In addition, the use of glass sealants requires a heat treatment of the stack at high temperatures before operation, in order to ensure the bonding of parts.

Compressive seal materials, on the other hand, are mostly based on materials with residual porosity to enable compression. Mica papers used for SOFCs presents a structure of pressed plate-like crystals, usually consisting of muscovite or phlogopite [2, 59]. Different mica-based materials are available in different forms [59, 86] such as mica powder or paper, or in composite forms with addition of talc. Such seal gaskets are of particular interest due to the ease of use in production processes. However, they suffer from some drawbacks:

- a residual leakage resulting from the porosity of the material which, as we show hereafter, can contribute to severe reliability issues.
- the need for a loading system to maintain the gaskets in compression in the stack.
- the inadequacy of the required compressive loads with typical mechanical loads that can be applied in SOFC stacks
- inadequate sealing at the interfaces due to surface roughness and production tolerances.

To overcome these issues, composites of such sealing materials are proposed to ensure better gas tightness. As examples, Chou et al. propose the use of mica paper infiltrated with glass [87], while Bram et al. [86] propose composites made of compressive seal materials and embossed metallic profiles.
Besides these classes of seal materials, other technologies are available such as metallic brazes, or compressive seals based on deformable metallic shapes. An overview on the available seal technologies for SOFCs is given by Fergus et al. in [59].
For both glass sealants and compressive seals, the exposure to air and fuel at high temperatures can lead to detrimental chemical reactions with other components. The resulting implications on the degradation of stacks is studied in Chapter 12.
In the stacks developed in this work, different sealing options were tested. Raw mica paper was principally used for the *R-design* stack. For the *S-design* and *F-design* stacks, mica papers of different forms were used.

3.4 R-design

HTceramix S.A. 's first stack prototype (R-design) was developed until 2005 and intensively tested in the frame of the European project *RealSOFC* which addressed the study of degradation issues in SOFCs.

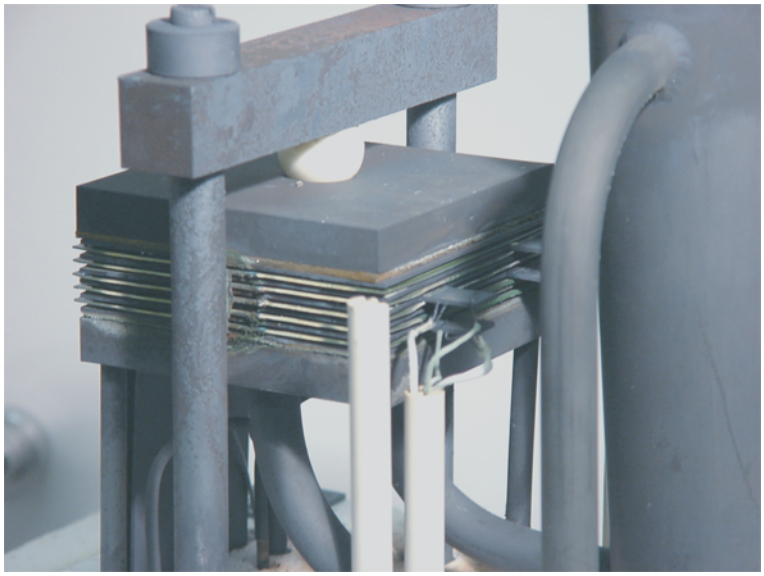

Figure 3.1: HTceramix S.A. 's *R-design* short stack.

The *R-design* stack is based on square anode-supported cells of 50cm^2 active area (Fig. 3.1). Air and fuel distribution are supplied to each element through internal manifolds requiring feeding holes in the cells. The resulting flow arrangement is a counterflow arrangement (Fig. 3.2). The excess air and fuel are not recovered in the stack, and the latter is consequently burnt at the stack's periphery.
The fuel and air manifolds are made by a succession of mica seal gaskets pressed between cell and MIC (see Fig. 3.3). These internal seals are therefore placed in a dual atmosphere. On the sides of the stack, gaskets of the same composition are placed to prevent leakage to the surroundings. The stack is placed in an insulation or an oven, and is therefore surrounded by stagnant air.
In the development period of this stack, the cell edges were not laser-cut for production purposes. They present therefore a more pronounced warpage along the edges (Fig. 3.3), which cannot be compressed between seal gaskets due to a risk of mechanical failure. Therefore, in this design, the cell edges are placed outside of the seals and are consequently exposed to stagnant air. This type of construction was found in the present work to induce redox-cycling of the cell edges on the sides and in the air manifold, leading to rupture of the cells and failure of the stack.
The maximum power output of this type of stack was 250W in a 29-element configuration.

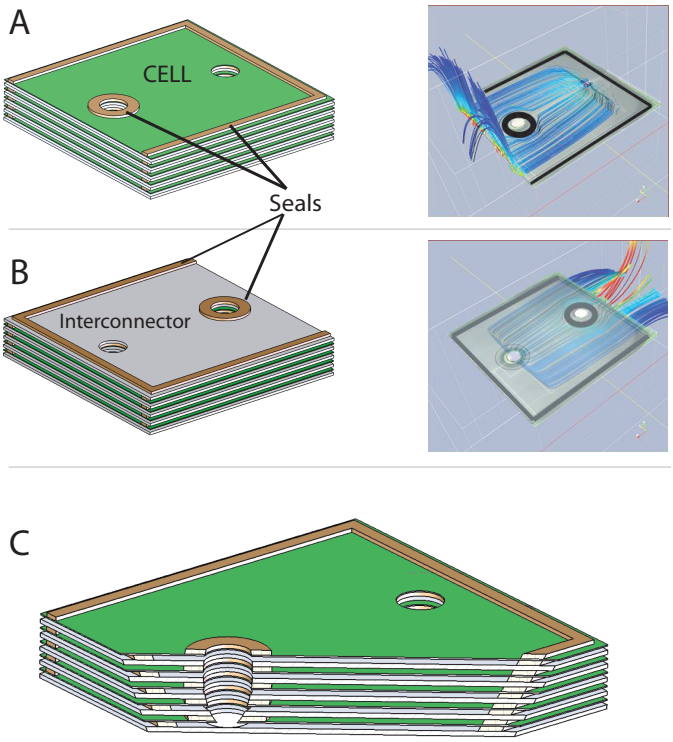

Figure 3.2: Gas manifolds. (A) Fuel manifold and corresponding simulated flowfield. (B) Air manifold and corresponding simulated flowfield. (C) Detail of the stack manifold.

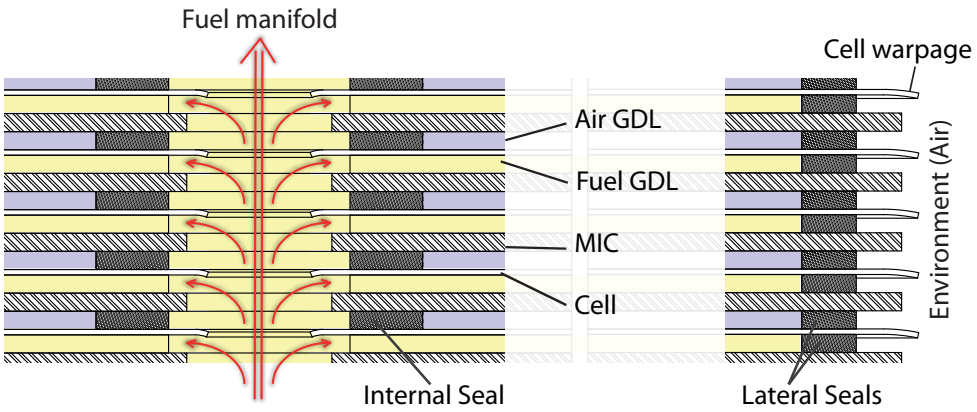

Figure 3.3: Detail of the seal construction in the *R-design* stack.

3.5 S-design

The S-design stack was developed to overcome two major limitations of the R-design. First, the open post-combustion was removed to limit the resulting degradation effects, as well as to allow easier system integration. Second, the fuel distribution was modified to increase the performance of the stack. This stack is a combined development involving three different modeling tools. The stack-dimensioning tool developed by D. Larrain [8] was used to test and optimize the performance and reliability of different flow configurations, operating points and design parameters. In addition, system design tools developed by N. Autissier [88] were used to determine the optimal size of the stack as well as its integration in a system. Finally, the tools presented in this thesis were used to make the detailed design of the stack, with particular focus on an adequate fuel distribution and on reliability aspects.

The *S-design* stack is based on cells of oblong and rounded shape, including holes for fuel

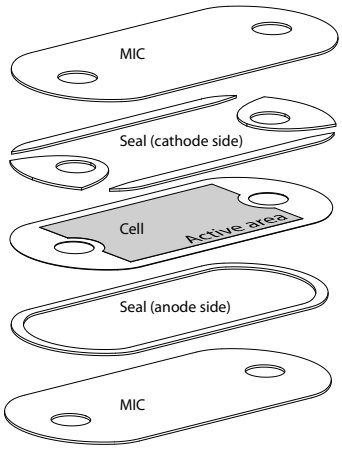

Figure 3.4: Detail of the assembly of the *S-design* stack.

supply and retrieval (Fig. 3.4 to Fig. 3.6). The fuel manifold consists of repeat sealing rings placed between cell and interconnectors, in a similar manner to the R-design stack. Contrarily to the R-design, air is supplied through external manifolds to the stack (Fig. 3.5). The air manifolds are made by a metallic band tightened on the top and bottom flanges. The flow arrangement is either in co- or counter-flow configuration. The cross-flow arrangement was skipped due to predicted lower performance.

With its 50cm^2 active area, the S-design replaces its predecessor, allowing to reach higher power outputs by increasing the number of repeat-units.

The sealing of the sides of the stack is performed in a similar way to the R-design stack, but with additional constraints due to the insulated metallic band surrounding the stack. A detailed view is given in Fig. 3.6. Due to the warpage of the cell edges at the time the stack was developed, the lateral anode seal was made shorter than the one on cathode side, allowing the cell to be pressed between both layers. This construction leaves a small gap

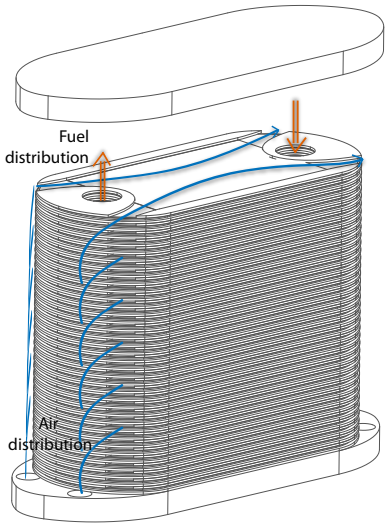

Figure 3.5: Air and fuel distribution for a 36-element *S-design* stack.

between stack and metallic band through which some air bypasses the stack. Similarly, this construction exposes the cell edges to flowing air, resulting in a similar redox-problem issue than in the R-design. This fact was found after the first design iterations, and corrective actions were consequently taken, which cannot be presented here.

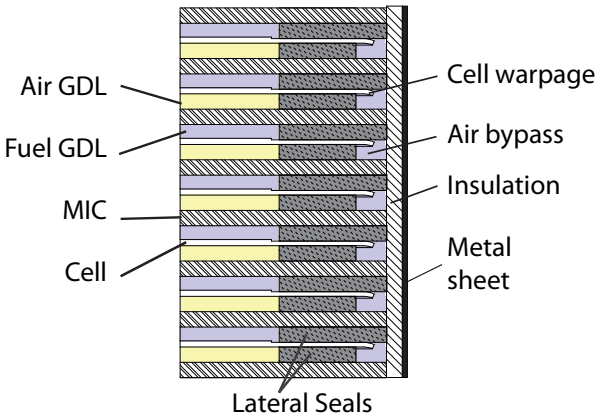

Figure 3.6: Detail of the lateral seal for the *S-design* stack.

The S-design stack was tested up to a 72-element configuration, allowing to reach a power output of 1.1kW$_{el}$ (0.3 Wcm^{-2}), shown in Fig. 3.8. In short stack configuration, a maximum power output of 164W was attained in a 5 element configuration. The best achieved efficiency was 53% using hydrogen as fuel, at a fuel utilization of 85%.

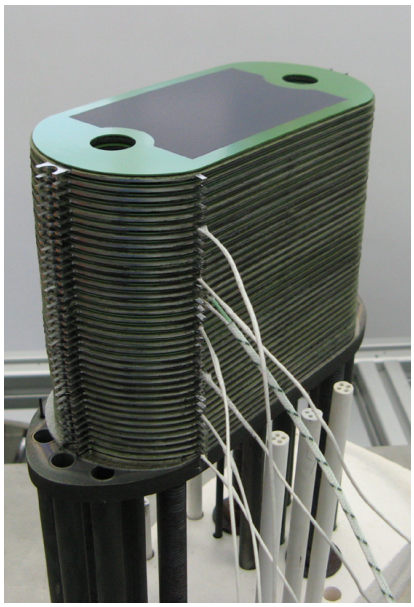

Figure 3.7: Assembly of a 1-kW class *S-design* stack.

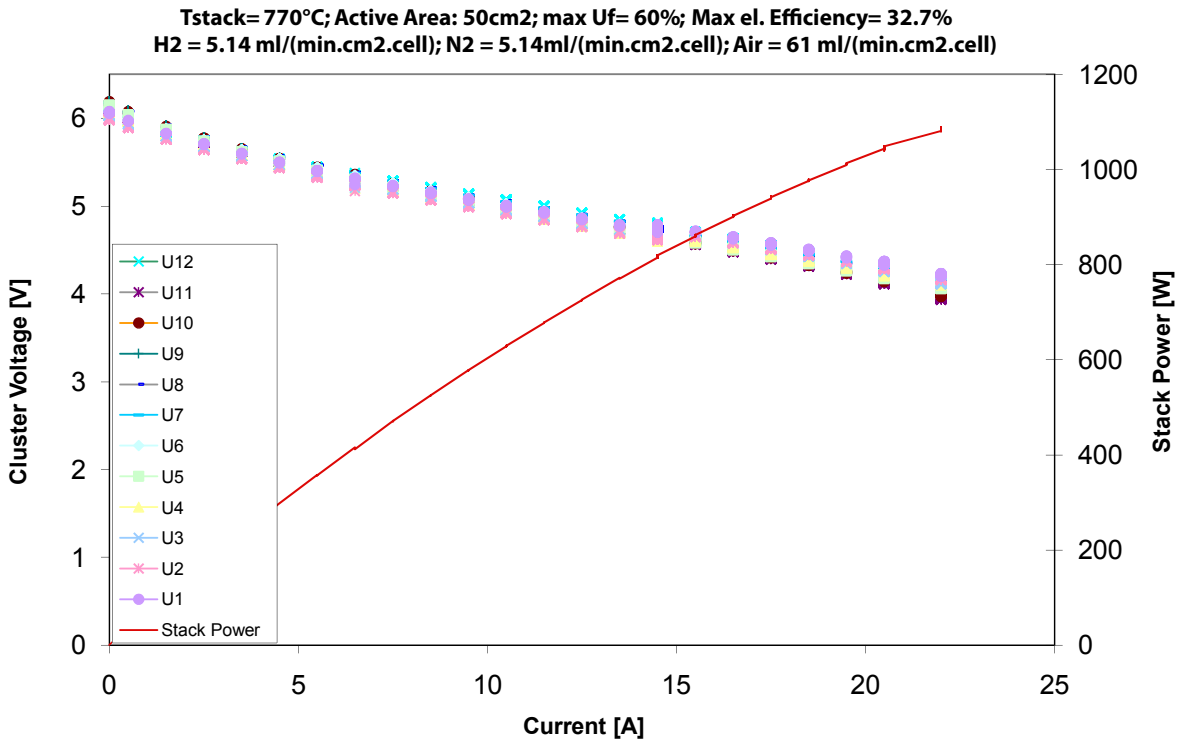

Figure 3.8: i-V characterization of a 72-element *S-design* stack. Potentials are given for clusters of 6 cells. (*Courtesy of M. Molinelli, HTceramix S.A.*)

3.6 F-design

The F-design stack is the most recent stack design and the principal achievement of this thesis. It was designed in the frame of the FP6 European Project *FlameSOFC* . With an active area of 200cm^2, it is developed to provide a nominal power output of 2.5kW$_{el}$ in a 50 element configuration, with possible extensions to higher power outputs. This stack was designed using the herein developed CFD model and its extensions. Different configurations and construction options were studied to prevent *ab initio* failure modes linked to anode reoxidation. A specific effort was made to design a seal system based on compressive seal materials that avoids any redox issues for the cell, hence overcoming the limitations of both *R-design* and *S-design* stacks. These issues are described in detail hereafter.

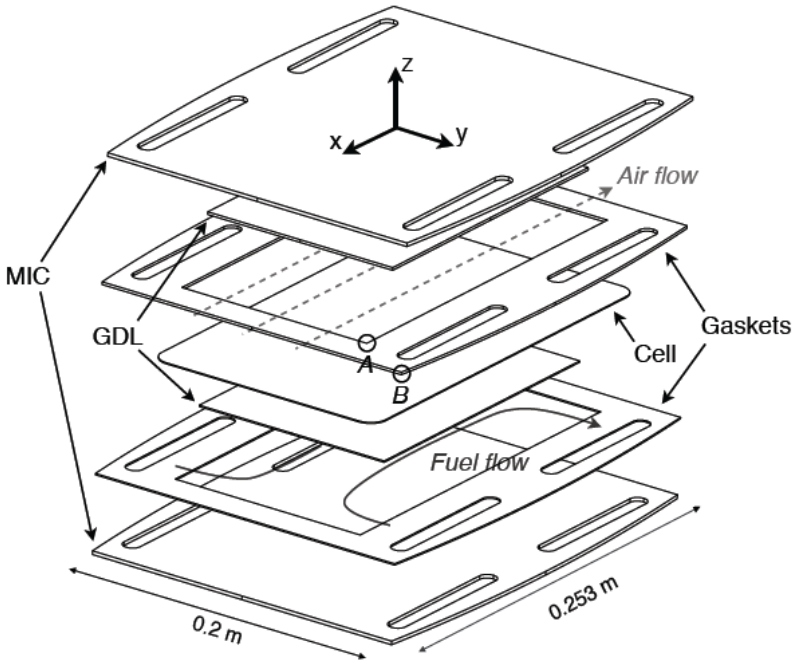

Figure 3.9: Construction of a *F-design* repeat-element.

The *F-design* stack is based on a cell of rectangular shape pressed between seals and GDLs (Fig. 3.9). Contrarily to the *S-design* stack, the fuel manifold is not passing through the cells, in order to optimize the ratio of active area to total area and to prevent rupture of cells in the vicinity of holes. Air and fuel are flowing either in co- or counter-flow arrangement. Fuel is provided internally from the repeat-element's sides. The fuel manifolds are made similarly to the *S-design* case by successive layers of metal (MICs) and seal materials. Air is provided through external manifolds, in a similar way to the *S-design* .

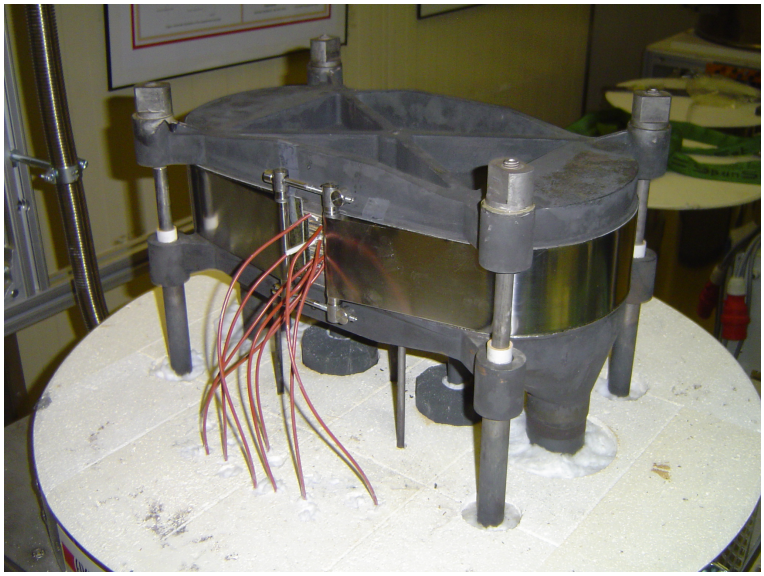

Figure 3.10: *F-design* 5-element stack on the developed diagnostic station.

Specifically designed for integration in a CHP system, thermal losses had to be minimized to enhance system efficiency. The number of thermal bridges between the hot stack and colder system areas was consequently minimized. The stack is pressed between multi-functional flanges, which not only provide mechanical loading, but also allow gas distribution and current collection. A picture of a short stack is shown in Fig. 3.10.

The performance and degradation of this stack prototype was studied in detail by in-situ measurements. Detailed results are presented in Chapters 7.6.2 and 10 of this work.

Despite the fact that the production and assembly of this stack is still ongoing at the moment of editing this thesis, rapidly improving results were obtained with the tested prototypes. In a first short stack, a power of 380W was attained in a 5-element configuration ($0.38 \mathrm{Wcm}^{-2}$). In a first experiment in a $1\mathrm{kW}_{el}$ configuration, a power output of $1.1\mathrm{kW}_{el}$ was attained with a 17-element stack, at a fuel utilization of 78% and an efficiency of 40%.

Finally, in a 20-element configuration (shown in Fig. 3.11), this stack was capable to reach a maximum power output of $1.84\mathrm{kW}_{el}$ with an efficiency of 43% and a fuel utilization of 70%. At lower power densities, both fuel utilization and efficiency increased, reaching 50% of efficiency at $1.43\mathrm{kW}_{el}$ (80% of fuel utilization), and 53% at $780\mathrm{W}_{el}$, attaining a fuel utilization of 85%. The results are shown in Fig. 3.12 and Fig. 3.13.

These results are far beyond the expectations existing at the beginning of this thesis. With

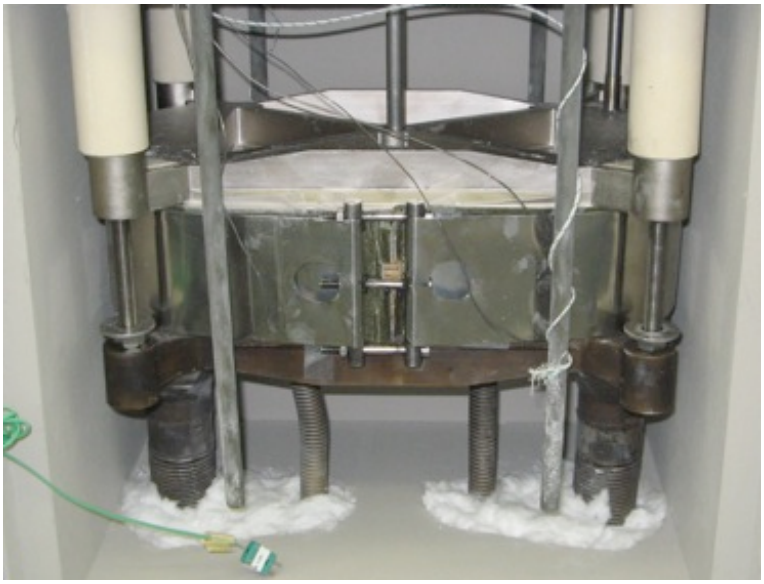

Figure 3.11: *F-design* 1kW prototype assembled in its insulation.

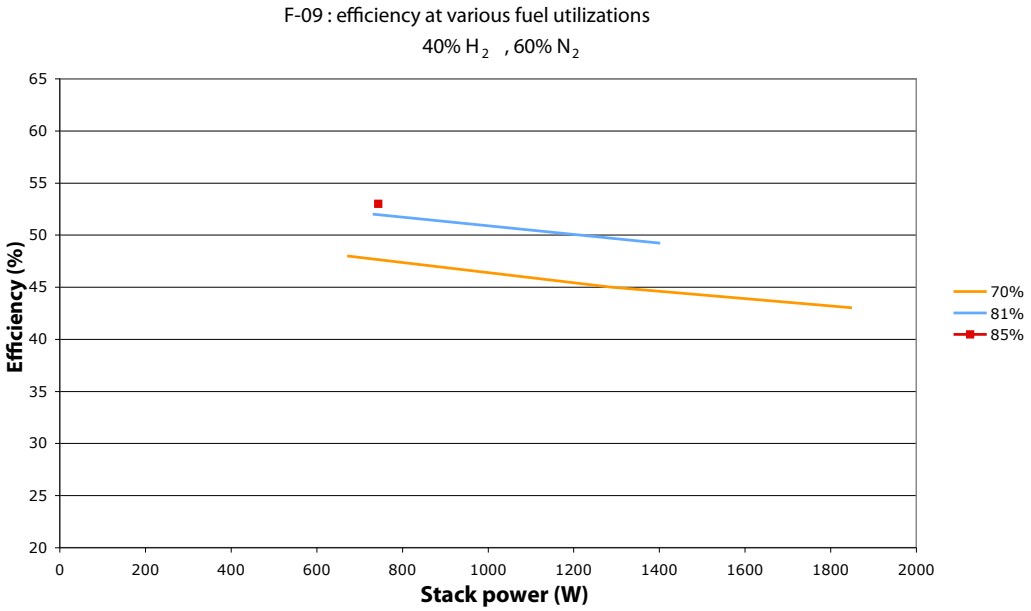

Figure 3.12: Efficiencies attained by a 20-element *F-design* prototype at different fuel utilizations. Operation under dilute fuel (40% hydrogen, 60% nitrogen). Courtesy of N. Autissier, HTceramix S.A.

this stack design, not only higher efficiencies are attained with, as shown in the following chapters, a performance close to an ideal repeat-element (in terms of gas distribution). Even more important, the resolution of the main source of failure affecting the older designs (see Chapter 8) enables a more reliable operation over the whole range of operating conditions.

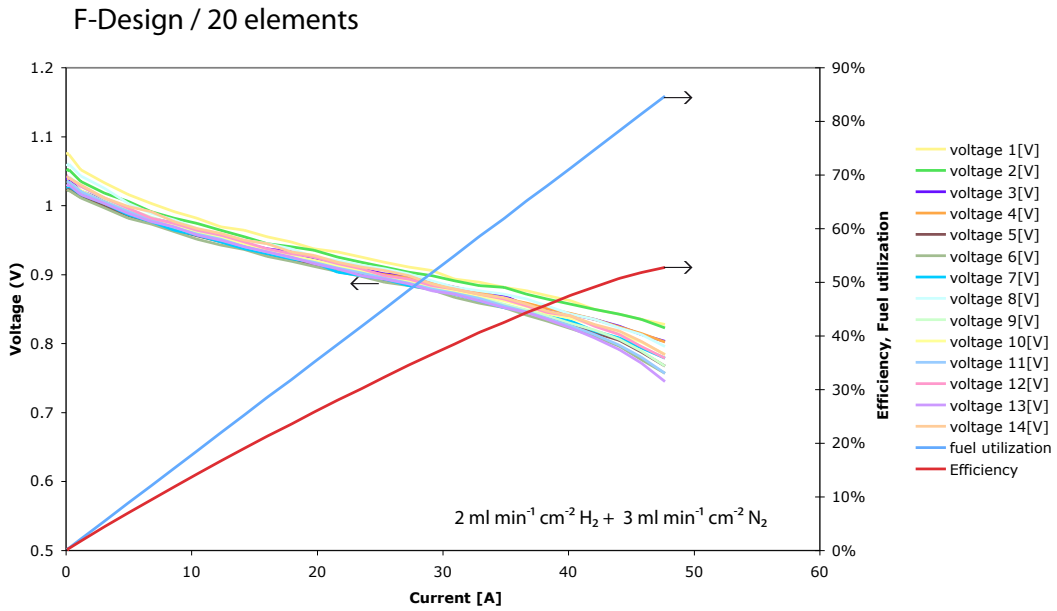

Figure 3.13: Detail of the i-V characterization of the *F-design* stack reaching maximum efficiency and fuel utilization. Operation under dilute fuel ($2\,\mathrm{ml\,min^{-1}\,cm^{-2}}$ hydrogen, $3\,\mathrm{ml\,min^{-1}\,cm^{-2}}$ nitrogen). Courtesy of N. Autissier, HTceramix S.A.

In addition, this stack offers the perspective to reach power ranges of a few kilowatts in the next months, with an integration in the CHP system developed in the frame of the Flame-SOFC project. Finally, it has to be noted that this stack fulfills completely the objectives of the FlameSOFC project, not only in terms of performance, but also in terms of system integration, with pressure drops within the specifications and limited thermal losses.

As the main output from the modeling and experimental work described in the following chapters, this design validates the developed modeling approach which includes degradation aspects, as well as the accuracy and applicability of the model for new design applications.

With the realization and successful operation of this stack, the main objective of this thesis is therefore attained.

Part I

Modeling tools for the study of SOFC performance and degradation.

Chapter 4

Modeling approach

4.1 Introduction

This chapter describes the models developed for investigations on degradation and for the development of SOFCs. It is based on first developments made by N.Autissier [35]. The core of the modeling tool consists of a CFD model completed by an electrochemical model. Implemented in the FLUENT^{TM} software environment, it consists of a series of additional routines implemented as *user-defined functions* (UDFs). These subroutines are used to control the electrochemistry, to set local properties dynamically, to describe degradation phenomena and to extract local information from the computation. The model is programmed to run on single processors and on parallel machines, exploiting the capabilities of the linux cluster *Pleiades* of the Institute of Mechanical Engineering at the Ecole Polytechnique Fédérale de Lausanne (EPFL).
It has to be specified that this model is different from the commercial SOFC package proposed by FLUENT.
Besides the core model, additional plug-ins have been added to describe non-ideal component properties and resulting degradation phenomena or risk of failure. Additional models complete this tool for investigations on interactions between stack and its environment, as well as for specific studies on degradation.
In a first part, the electrochemical model is presented, as well as the methodology used for its development from experimental data. The control of electrochemistry is presented for different repeat-element and stack configurations.
In a second part, two degradation plug-ins are presented. The first one concerns the description of parasitic diffusion through seal materials, the resulting parasitic combustion and the possible consequences for the integrity of the cell. The second plug-in concerns the generation and transport of pollutant species from different materials in a repeat-element, sub-model that couples thermodynamic and kinetic considerations for the generation of pollutants, with mass-transport phenomena.

Finally, the effect of stack design on reliability and performance is studied.

4.2 Nature of the studied flows

In SOFC systems, fluids are transported through different types of geometries (manifolds, distributors, gas-diffusion layers, surroundings of the stack), resulting in different flow properties.

Gas manifolds. The gas manifolds distribute gases at regular intervals to the repeat-elements (Fig. 3.3). For the 1 kW *S-design* stack, the air manifolds have an hydraulic diameter about 30 mm for an air flow comprised between[1] 200 and 300 $\mathrm{Nl\,min^{-1}}$. Typical velocities at the stack's inlet are in the order of magnitude of 20-30 m/s, which gives a Reynolds number of $Re = 4400 - 6500$, higher than the typical threshold value of $Re = 2400$ for transition to turbulent flows in pipes. The resulting pressure drops have an impact on the homogeneity of the gas distribution in the stack, and consequently on its performance. For such design studies, $(\kappa - \epsilon)$ turbulence models are implemented.

Flow in repeat-elements. In the gas distributors, which are located between the repeat-element's inlet/outlet and the gas-diffusion layers, pressure drops and flow distributions are principally determined by the distance between cell and interconnect (height usually about 1 mm). Typical Reynolds numbers are in the range of 30 to 100. In the *gas diffusion layers*, usual Reynolds numbers are in the range of $Re = 20$ for air. On fuel side, Reynolds numbers in the range of $Re = 1$ are common, approaching the situation of creeping flows. Consequently, flows can be considered as laminar inside of repeat-elements, allowing to neglect turbulence.

Flow around stacks and repeat-elements. When flows around the stack are consid-

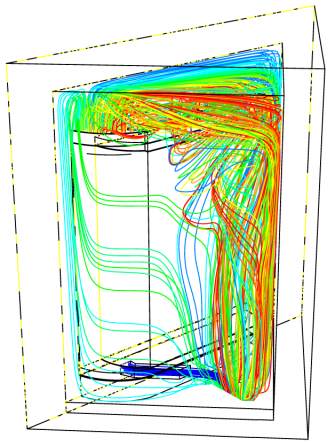

Figure 4.1: Simulation of flow around a *S-design* stack in a HoTbox^{TM} insulation.

[1]Normal liters (0°C and 1 atm).

ered, buoyancy effects and the resulting natural convection occur and are considered in the models, as they determine part of the heat transfer between stack and surroundings. This is particularly the case when post-combustion is modeled for the *R-design* or *S-design* stacks, where both buoyancy effects and turbulence are modeled as they determine the volume of the combustion.

Diffusion in porous media. A different type of flow occurs in the different porous media present in the fuel cell, in particular in electrodes and in seal materials which present a residual porosity. In those cases, diffusive mass transport competes with viscous flow, requiring specific mass-transport models.

High-temperature operating conditions. Due to operation at high temperatures, radiation represents a major part of heat transfer. This is in particular the case when the interaction between a stack and its insulation is modeled. In addition, when open combustion is modeled, radiative exchange between the hot gases and surrounding surfaces is taken into account.

Reactive flows Chemical reactions are modeled using kinetic models. This is the case for the internal steam reforming reaction (React. 2.3) and for combustion. The shift reaction (React. 2.5) is treated specifically to attain equilibrium.

Pollutant generation and transport Finally, the generation and transport of pollutant species is modeled in a specific way. The low partial pressure of usual pollutant species allows to neglect their impact on the mass-conservation, energy and momentum equations. The transport of pollutants is consequently determined by convection in the gas streams, and by diffusion. FLUENT^{TM} allows to model such additional transport mechanisms by the definition of *User-Defined Scalar (UDS)* functions.

4.3 Modeling approach

Due to the different types of flows described above and to the size of the cases, problems are treated separately when possible. The full stack case is not modeled in detailed manner, as it is extremely expensive in terms of computational time. This type of simulation would however bring information about the flow distribution and its stability, as well as about the homogeneity of temperatures over the height of the stack. Both parameters have a strong influence on the overall performance, due to the fact that the repeat-elements are organized in series, which implies that the less performing element dictates the maximum achievable performance of the stack. Consequently this type of simulations would be of interest. To investigate this class of problems, the stack is simplified to a full volume associated to heat sources that reproduce the heat generation occurring during operation. The resulting gas and temperature distributions are then evaluated to assess whether the manifolds' geometry, the construction of the high temperature insulation around the stack and the operating conditions (gas inlet temperatures) fulfill their role to homogenize the operating conditions.

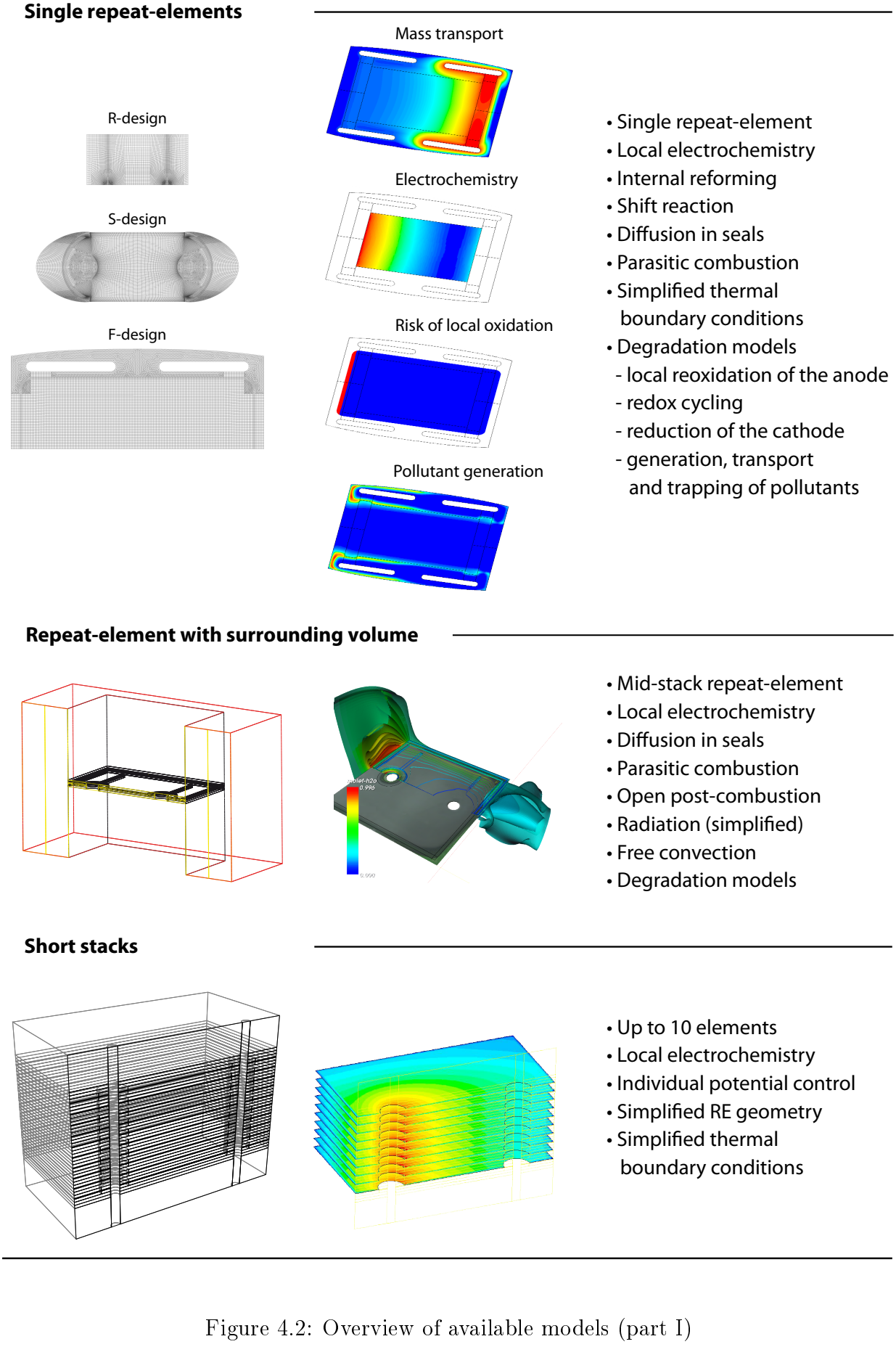

Figure 4.2: Overview of available models (part I)

Segmented repeat-elements

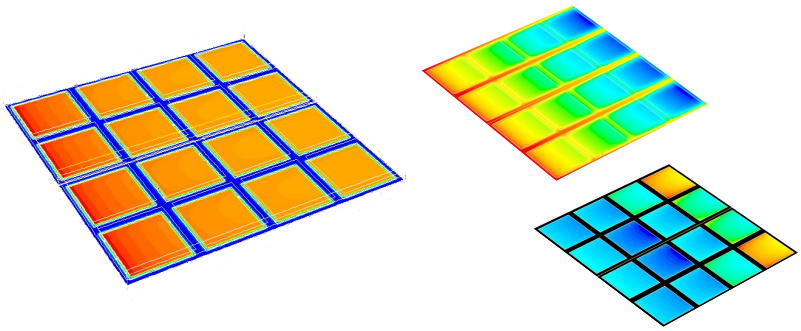

- Single repeat-element
- Local electrochemistry
- **Separate active areas**
- **Control mode:**
  - **constant collection potential**
  - **or losses in collection lines**

Tubular short stacks

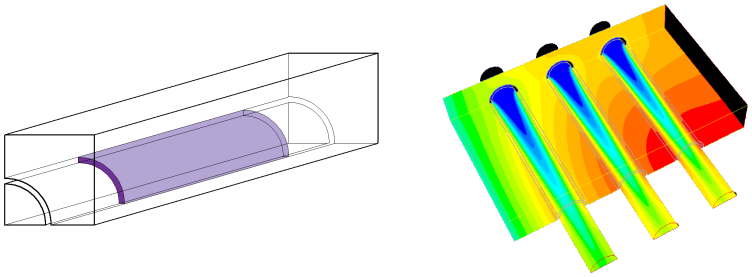

- Short stack model
- Local electrochemistry
- **Computation of electrical field (collection losses)**
- **Serial or parallel current collection**

HotBox™

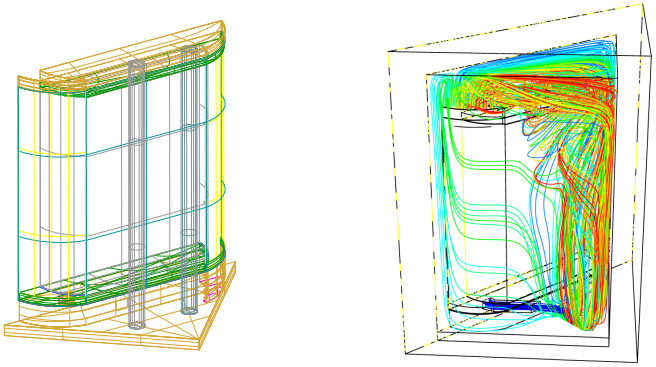

- Stack model (simplified)
  - single volume vith averaged properties
  - distributed heat source
  - imported electrochemistry
- Post-combustion
- Radiative exchange (complete)
- Free convection
- Turbulent flow

Gas manifolds

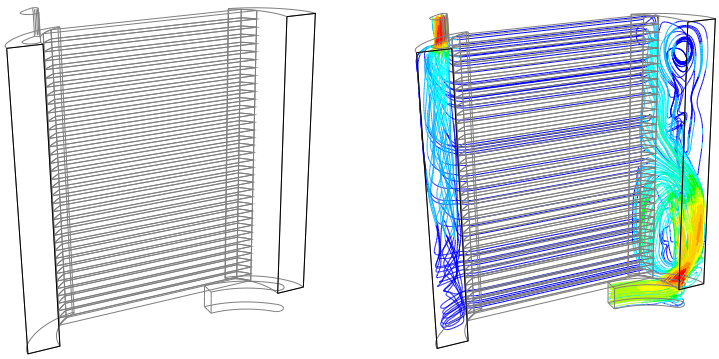

- Optimisation of flow distribution
- No electrochemistry
- Detailed manifold geometries
- Simplified stack geometry
- Turbulent flows

Figure 4.3: Overview of available models (part II)

Moreover, detailed studies on fuel and air manifolds are performed separately, to take into account turbulence and boundary layer effects. The effect of deviations in air or fuel supply resulting from pressure variations in the manifolds are investigated separately in a repeat-element model. Finally, this type of simulation is used to dimension the gas manifolds and serves as input for design iterations performed using single repeat-element models.
For studies about the electrochemical performance and degradation of a particular stack design, single repeat-elements are modeled, with adequate boundary conditions to model the situation of a single repeat-unit located in the middle of a stack, as shown in Fig. 4.4.

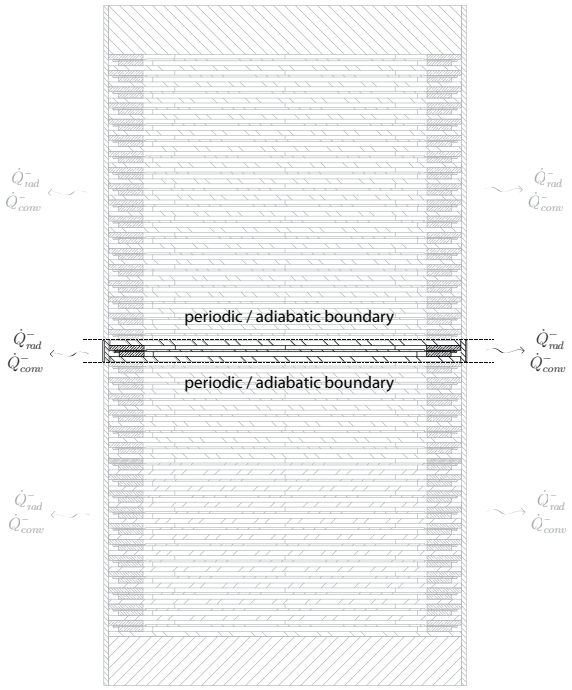

Figure 4.4: Simulation of a repeat-unit located in the middle of a stack.

Investigations on the effects of parasitic diffusion in seals is modeled by considering a single repeat-element and a surrounding volume of air.
Finally, to study thermal interactions between a stack and its surroundings, the complete stack is not modeled. In such cases, heat generation of the stack in the stack is modeled using zero-dimensional models that predict the heat generation and the fuel and air conversion at different points of operation.

4.4 Definition of the geometry and meshing

Depending on the studied case, a complete short stack or a single repeat-element is modeled. When symmetries are available, only half of the geometry is modeled, assuming symmetric flows (Fig. 4.5). For cases where the sole internal flow is considered, the surroundings of the repeat-element or stack are simplified by setting appropriate boundary conditions. In different studies presented hereafter, the gas volumes adjacent to the stack are modeled, in order to study the influence of the surroundings on the stack itself.

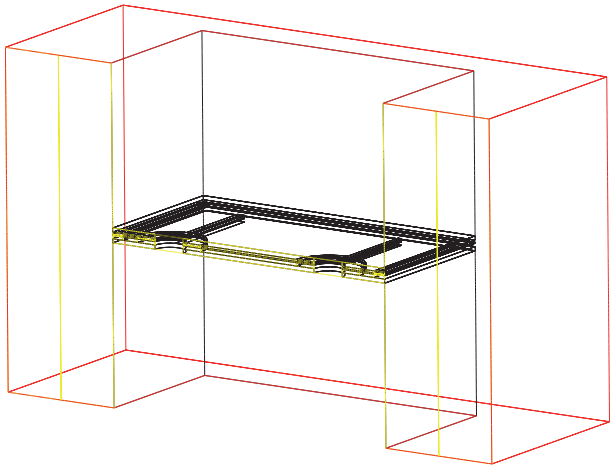

Figure 4.5: Volumes meshed to simulate a *R-design* repeat-unit in its environment.

Parallel computing and mesh partition Partition of meshes and distribution on several processors is a usual step in CFD modeling when considering large problems. In the specific case of SOFCs, exchange of information about local properties on either sides of the cell are required. Therefore, a mesh partitioning perpendicular to the cell's active area is required to facilitate exchange of information in parallel cases.The code is written to allow parallelization of the computation. In most cases however, the number of nodes is kept sufficiently low (<800'000) to be simulated on a single processor in affordable time (five to ten hours for one i-V characterization, depending on program size and number of used submodels).

3D and 2D models Despite the possibility to investigate fuel cells with a simplification to a two-dimensional problem (see Larrain et al. [8]) - which is highly beneficial in terms of computation time - the choice was made to investigate 3D-cases, in order to limit averaging of properties over the height of a repeat-element, as well as to guarantee the accurate simulation of flow distribution which is determined by boundary layer effects in the three dimensions

(see Fig. 3.3). Additional problems were studied in 2D configurations, in particular for studies of diffusive mass transport in damaged cells.

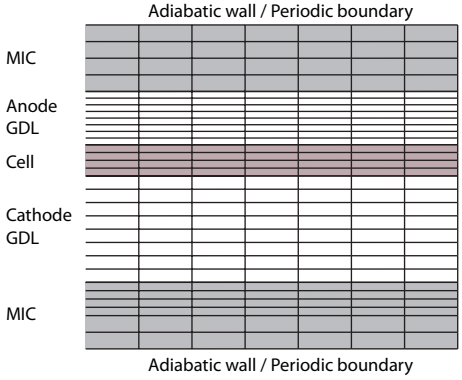

Figure 4.6: Side view of a repeat-element mesh.

Meshing In single repeat-element configuration, the cell, gas diffusion layers, gas distributors and seals are meshed as distinct volumes. The metallic interconnectors are also included as solid volumes in the mesh on both sides of the element, whereas only half of the thickness is considered in simulations focusing on stack conditions (4.6). In those cases, only the repeating geometry is considered, and appropriate thermal boundary conditions are set on the created surfaces adjacent to the stack (adiabatic or periodic). The volumes of the seals are either modeled as solids (where only heat transfer is considered), or as porous fluid volumes to account for residual porosity.
For planar stack designs, meshing is performed by extrusion of a 2D mesh in the direction normal to the plane of the elements, as shown in Fig. 4.6. An example of mesh for the *S-design* repeat-element is given in Fig. 4.7. The number of nodes in the normal direction is kept to a minimum to limit the total number of cells, whereas great care is taken to guarantee the accuracy of the computation. Figure 4.6 shows a typical discretization in the vertical direction. Due to the existence of a laminar, Poiseuille flow between MICs and cells in the gas distributors, this number of nodes associated to a second-order spatial discretization was found to be sufficient for an accurate modeling of pressure drops and heat and mass transfer in the boundary layer. Moreover, heat transfer in the reaction zone is mostly determined by conduction through the *gas diffusion layers* made of SOFConnex^{TM} .

Averaging methods in *gas diffusion layers* The modeling of the flow in the gas diffusion layers (GDLs) is performed by averaging the properties of HTceramix-SOFCpower proprietary material SOFConnex^{TM} , which is modeled as a porous medium with adapted thermal conductivity and permeability to the flow. Due to confidentiality reasons, the complete description of the GDLs cannot be given here, despite the fact that a large effort was set on the development of these layers for adequate gas distribution.

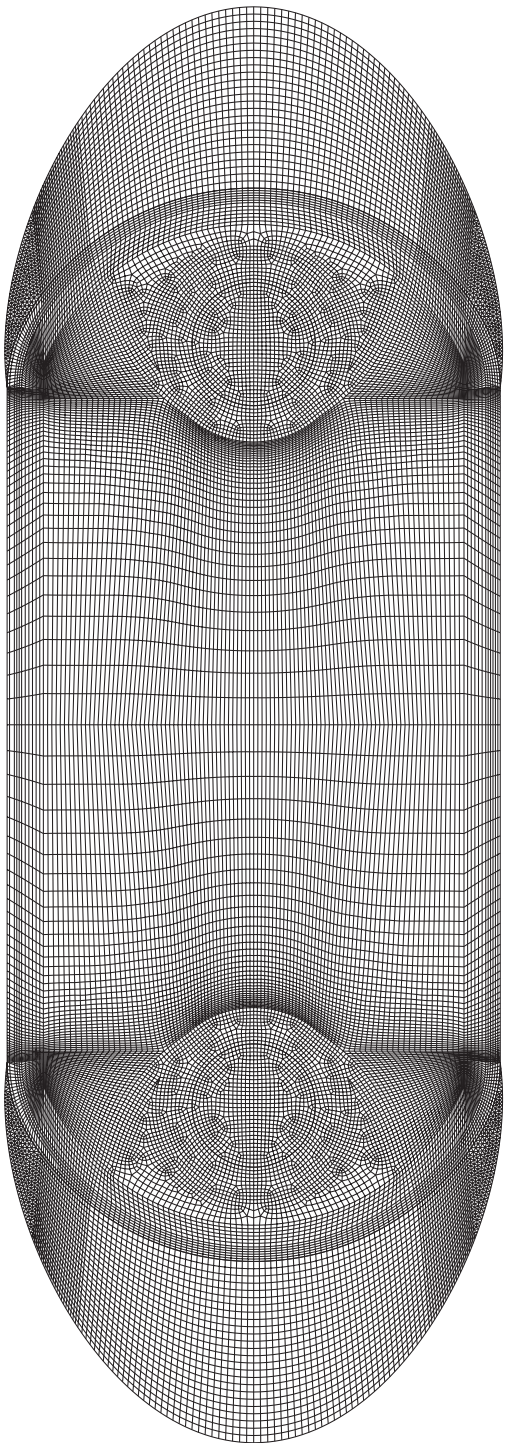

Figure 4.7: Top view of the mesh for a S-design repeat-element, including asymmetric air outlet

Chapter 5

The CFD model

5.1 Solver

The model is based on FLUENT's segregated solver. Second-order spatial discretization is used for all properties. For pressure-interpolation, the *PREssure STaggering Option (PRESTO!)* scheme is used, as it is specifically recommended for flows involving porous media.

5.2 Mass transport

5.2.1 Species transport and diffusion

Due to the presence of several gaseous species and the absence of a predominant one, the dilute approximation for Fickian diffusion is not valid and a multicomponent diffusion model is used. The diffusive mass fluxes $\overrightarrow{J}_k$ are computed using the Maxwell-Stefan diffusion model proposed in the solver.

$$\sum_{\substack{j=1 \\ j\neq i}}^{N} \frac{x_i x_j}{\mathcal{D}_{ij}} \left(\frac{\overrightarrow{J}_j}{\rho_j} - \frac{\overrightarrow{J}_i}{\rho_i}\right) = \nabla x_i - \frac{\nabla T}{T} \sum_{\substack{j=1 \\ j\neq i}}^{N} \frac{x_i x_j}{\mathcal{D}_{ij}} \left(\frac{D_{T,j}}{\rho_j} - \frac{D_{T,i}}{\rho_i}\right) \tag{5.1}$$

Present in the right term of the Maxwell-Stefan equation, thermal diffusion (or Soret-effect) driven by temperature gradients can be taken into account or disabled, simplifying the system

to:

$$\sum_{\substack{j=1 \\ j\neq i}}^{N} \frac{x_i x_j}{\mathcal{D}_{ij}} \left(\frac{\overrightarrow{J}_j}{\rho_j} - \frac{\overrightarrow{J}_i}{\rho_i}\right) = \nabla x_i \tag{5.2}$$

The Soret effect is taken into account only in the case of post-combustion and disabled in other cases, due to the low thermal gradients and to its negative effect on convergence.
The binary diffusion coefficients are computed from a modified Chapman-Enskog formula [89]

$$\mathcal{D}_{ij} = 0.0188 \frac{[T^3(\frac{1}{M_{w,i}} + \frac{1}{M_{w,j}})]^{1/2}}{p_{abs}\sigma_{ij}^2 \Omega_D} \tag{5.3}$$

where p_{abs} is the absolute pressure, and Ω_D is the diffusion collision integral, and σ_{ij} is an average of the Lennard-Jones parameters σ_k.

5.2.2 Mass transport in porous media

5.2.2.1 Diffusion

Diffusion transport in porous media is considered specifically for seal materials and for sub-models studying diffusive mass transport in electrodes. In the repeat-element model, diffusive mass transport in the electrodes is not modeled using FLUENT's mass conservation and momentum equations. In this case, diffusive mass transport is included in the electrochemical model and solved programmatically in the UDF.
Effective and precise models for diffusive transport in porous media, such as the 'dusty gas model' (DGM) [90], or the 'mean transport pore model' (MTPM) [91], are not directly implemented in the used versions of FLUENT (6.2.16-6.3.26) and would require a computationally-expensive implementation in UDFs [92][27]. Therefore, a Fickian multicomponent model is used instead, where the effective diffusion coefficients are corrected for the properties of the porous medium.
The correction of the diffusion coefficient depends on the Knudsen number [93] (eqn. 5.4) which relates the mean free path l (eqn. 5.5) of the gas molecules to the pore diameter of the porous medium.

$$Kn = \frac{l}{d_p} \tag{5.4}$$

$$l = \frac{k_b T}{\sqrt{2}\pi\sigma_{ii}^2 P} \tag{5.5}$$

The binary diffusion coefficients D_{i-j} are computed from the Fuller equation[1] (Eqn. (5.6)) [93] and the multicomponent diffusion coefficients computed from eqn. (5.7):

$$D_{ij} = \frac{1.43 \cdot 10^{-7}\, T^{1.75}}{p\sqrt{\frac{2}{M_i^{-1}+M_j^{-1}}}\left(V_{d,i}^{1/3}+V_{d,j}^{1/3}\right)^2} \tag{5.6}$$

with T: temperature (K); p: pressure (bar); M_k: molar mass (kg/kmol); V_i and V_j: Fuller et al. diffusion volumes [94].
The diffusion coefficient in the mixture $D_{i,m}$ is computed by Wilke's multicomponent Fickian :

$$D_{i,m} = \frac{1-x_i}{\sum_{\substack{j=1\\ j\neq i}}^{N}\frac{x_i}{D_{binary,i-j}}} \tag{5.7}$$

For low Knudsen numbers (Kn<1), interactions between gas molecules and pore walls are negligible and the effective diffusion coefficients are computed in the same way as in the absence of a porous medium, but with correction for porosity (ϵ) and tortuosity (τ) (Eqn. 5.8).

$$D_{i,eff}^{por,Kn<1} = \frac{\varepsilon}{\tau} D_{i,m} \tag{5.8}$$

For higher Knudsen numbers, the molecules collide mostly with the pore walls, and the additional Knudsen diffusion term (eqn. 5.9) is combined for each specie to the mixture diffusion coefficient ($D_{mixture,i}$) by the Bosanquet [90] formula (eqn. 5.10).

$$D_{Kn,i} = \frac{\overline{d_p}}{3}\sqrt{\frac{8\mathcal{R}T}{\pi M_i 10^{-3}}} \tag{5.9}$$

$$D_{eff,i}^{por,1<Kn<10} = \left(\frac{\varepsilon}{\tau}\right)\frac{D_{Kn,i}D_{i,m}}{D_{i,m}+D_{Kn,i}} \tag{5.10}$$

For large Knudsen numbers ($Kn > 10$), only Knudsen diffusion is considered.

For modeling studies involving diffusion in seals, the Maxwell-Stefan model (Eqn. (5.1)) is disabled and replaced by the multicomponent Fickian model, where the diffusion coefficients are given programmatically to the solver. In all fluid volumes with exception of the porous media, the mixture diffusion coefficients from Eq. 5.7are used. In the porous media, either the Knudsen-corrected diffusion coefficients (Eq. 5.10) or the non-corrected ones (Eqn. 5.8) are used, depending on the properties of the material.
To study the effect of porosity and tortuosity on the behavior of the fuel cell, their values

[1] It is used instead of the Chapman-Enskog formulation, for compatibility with the electrochemical model of A. Nakajo.

can be adapted programmatically to fit required values such as the open circuit voltages that are affected by diffusion in seals (see Chapter 8).
Finally, even if they are modeled as porous media, the GDLs present different properties from the porous materials considered here. Nevertheless, the diffusion coefficients are adapted to match the properties of the SOFConnex^{TM} , which cannot be described here.
A limitation in this approach concerns the description of diffusion in non-isotropic porous media, as for example in mica paper consisting of parallel mica foils. With the current solver options, it is not possible to define anisotropic diffusion coefficients.

5.2.2.2 Viscous flow

The momentum equation (Eqn. (5.11)) solved by FLUENT contains a momentum source term $\vec{F}$ that includes the viscous resistance from the porous medium.

$$\frac{\partial}{\partial t}(\rho\vec{v}) + \nabla\cdot(\rho\vec{v}\vec{v}) = -\nabla p + \nabla\cdot\bar{\bar{\tau}} + \rho\vec{g} + \vec{F} \tag{5.11}$$

$$\bar{\bar{\tau}} = \mu[(\nabla v) + (\nabla v)^T) - \frac{2}{3}\nabla\cdot\vec{v}I] \tag{5.12}$$

The viscous resistance is given by a Darcy source term :

$$\vec{F} = -\mu\overline{\overline{D}}\vec{v} \tag{5.13}$$

where $\overline{\overline{D}}$ is the permeability tensor. If the properties of the porous medium are isotropic, the permeability tensor is diagonal and its elements (Darcy coefficients) are equal:

$$D_{11} = D_{22} = D_{33} = \frac{1}{\alpha} \tag{5.14}$$

For porous media such as mica paper consisting of parallel mica-platelets, the viscous flow is assumed to occur principally along the platelets and to be limited in the normal direction. To model this highly non-isotropic behavior, the Darcy coefficient of the direction normal to the mica foils is set orders of magnitude higher than the in-plane ones.
In the case of the gas diffusion layers, the averaging methods lead to a dependance of the Darcy term to the orientation of the velocity vector. In this case, the permeability tensor is adapted programmatically to the orientation of the flow, requiring additional iterations to converge to a solution:

$$D_{11} = D_{22} = D_{33} = f(v_x, v_y, v_z) \tag{5.15}$$

To estimate the Darcy coefficients, a ring of porous material is pressed between two flanges and a pressure differential is imposed while measuring the resulting flow of gas, in similar manner to the method described by Simner and Bram in [2, 86]. In this configuration, the instationnary term, the convective and viscous terms can be neglected and the momentum equation is simplified to the Darcy expression:

$$\nabla p = -\frac{\mu}{\alpha}\vec{v} \tag{5.16}$$

By solving this equation for the tested seal geometry, the Darcy coefficients are estimated.

5.3 Heat transfer

5.3.1 Heat conduction

5.3.1.1 Anisotropic conduction

The materials used in repeat-elements are assumed to present isotropic heat conduction properties. However, anisotropic conduction (Eqn. (5.17)) is considered in two different cases. First, anisotropic conduction is used when an averaging of properties is performed to reduce several components to a single volume with simplified geometry. For example, if a stack is modeled as single volume with distributed heat source, in-plane thermal conduction is dominated by the conduction in the metallic interconnects, while it is reduced in the normal direction due to the presence of less-conductive gas layers. The resulting averaged properties can be computed for the principal axes and included in the solver (Eqn. (5.18)).

$$\overrightarrow{q} = \overline{\overline{K}} \nabla T \tag{5.17}$$

$$\overline{\overline{K}} = \begin{pmatrix} k_x & 0 & 0 \\ 0 & k_y & 0 \\ 0 & 0 & k_z \end{pmatrix} \tag{5.18}$$

The second case concerns parametric studies on the effect of thermal conductivity on temperature profiles and performance. A particular application is the study of the effect of interconnect thickness on temperature. Variations of component thicknesses would usually require a re-meshing of the concerned volumes or, if possible, in a deformation of the mesh. To simplify the procedure, anisotropic conduction can be applied. A doubling of the MIC thickness can in this case be modeled by a doubling of the in-plane heat transfer coefficients k_x, k_y, and a division by 2 in the normal direction. For a modified height $h^* = \alpha h$, the resulting anisotropic coefficients are:

$$\overline{\overline{K}} = \begin{pmatrix} \alpha\, k & 0 & 0 \\ 0 & \alpha\, k & 0 \\ 0 & 0 & \frac{1}{\alpha}\, k \end{pmatrix} \tag{5.19}$$

5.3.1.2 Porous media

In porous media, the effective thermal conductivity is modeled as the volume average of the fluid conductivity and the solid conductivity:

$$k_{eff} = \varepsilon k_{fluid} + (1 - \varepsilon) k_{solid} \tag{5.20}$$

where ε is the porosity and k_{fluid},k_{solid} are the respective thermal conductivities.
An anisotropic thermal conductivity of the solid can be modeled in the same way as pre-

sented above.

5.3.2 Radiation

Due to the high temperatures, radiation plays a major role in the heat transfer. As radiative heat exchange is computationally very expensive, different strategies are applied to model heat transfer within the repeat-elements and for heat exchange between stack and system.

5.3.2.1 Internal radiation

Yakabe et al. [95] performed detailed simulations of radiative heat transfer in a 2x1x100 mm straight gas supply channel. They found that a total temperature increase of 340 K along the channel was lowered by 40 K when solving the radiative exchange, however at the price of an important computational effort. The effect is therefore not negligible, but it is worth noting that the considered total temperature difference is 2 to 3 times higher than temperature differences considered in our case. Aguiar et al. [96] simplified the computation by considering radiation only between directly facing surface patches in the internal channels. In our case, radiative exchange between facing internal surfaces is simplified in the same way in the empty gas supply channels. This is however done only in the case of internal steam reforming where important temperature differences may exist between the different layers. To assess whether radiative exchange should be considered in the GDLs, the radiative and conductive heat transfers are compared. Considering two large parallel surfaces at different temperatures T_1 and T_2, the net radiative exchange flux is given by [97]:

$$\dot{Q}^{-}_{rad,1\,2} = \frac{\sigma\left(T_1^4 - T_2^4\right)}{\frac{1}{\epsilon_1} + \frac{1}{\epsilon_2} - 1} \tag{5.21}$$

A linearization of this expression is performed in the following way [97]:

$$\begin{aligned} \left(T_1^4 - T_2^4\right) &= \left(T_1^2 + T_2^2\right)\left(T_1 + T_2\right)\left(T_1 - T_2\right) && (5.22)\\ &\approx 4\overline{T}^3\ \left(T_1 - T_2\right) && (5.23) \end{aligned}$$

where T is the average temperature of the both surfaces. The radiative exchange is then simplified to:

$$\dot{Q}^{-}_{rad,1\,2} = h_{rad}\ \left(T_1 - T_2\right) \tag{5.24}$$

with

$$h_{rad} = \frac{4\sigma\overline{T}^3}{\frac{1}{\epsilon_1} + \frac{1}{\epsilon_2} - 1} \tag{5.25}$$

To compare the resulting heat exchange with the one obtained through a porous medium such as the GDL, an equivalent thermal conductivity is estimated:

$$\dot{Q}^{-}_{rad,1\,2} = h_{rad}\,\Delta T_{1\,2} \tag{5.26}$$

$$= h_{rad}\Delta z\frac{\Delta T_{1\,2}}{\Delta z} \tag{5.27}$$

$$\approx k^{*}_{rad}\frac{\partial T}{\partial z} \tag{5.28}$$

where Δz represents the distance between the parallel surfaces. For an average temperature of 1073 K, a usual material emissivity of $\varepsilon = 0.9$ and a distance of $\Delta z = 1\,mm$, the obtained equivalent thermal conductivity is $k^{*}_{rad} = 0.23\ Wm^{-1}K^{-1}$. This value is well below the thermal conductivity of the porous gas diffusion layers, as well as within the incertitude for the obtained coefficients. Consequently, radiative heat exchange is neglected in the concerned volumes.
Finally, the effect of radiation on internal heat transfer inside the porous electrodes themselves was investigated by several authors [98, 99]. The outcome of their simulations was that internal radiative heat transfer had a negligible effect on the temperature distribution and could therefore be neglected.

5.3.2.2 Radiation between stack and other components

Radiation between stack and insulation The complete radiative heat exchange between the stack, its insulation, and the gas volume comprised between both is only computed in studies focussing on the analysis of temperature distribution in a stacks and the interactions with system design options. In those cases, the electrochemistry is simplified to an important extent.

Simplified radiation exchange in post-combustion zones For studies focusing on the effect of parasitic combustion and post-combustion on the repeat-element's performance and reliability, a simplified radiative model is implemented in the combustion areas.
For gas mixtures, the radiation losses are given by eqn. (5.29)[100] where a is the Planck mean absorption coefficient for each specie. In our case, the absorption coefficient for steam is used as average absorption coefficient (Eqn. 5.30).

$$\dot{Q}^{-} = 4(\sum_{i} a_i p_i)\sigma(T^4 - T_s^4) \tag{5.29}$$

$$\dot{Q}^{-} = 4\overline{a}\sigma(T^4 - T_s^4) \tag{5.30}$$

5.3.3 Thermal boundary conditions

In the repeat-element model where the volume around the stack is not considered, simplified thermal boundary conditions are applied, as shown in Fig. 5.1. Two cases have to be distinguished: laboratory configuration (oven) and product configuration (insulation).

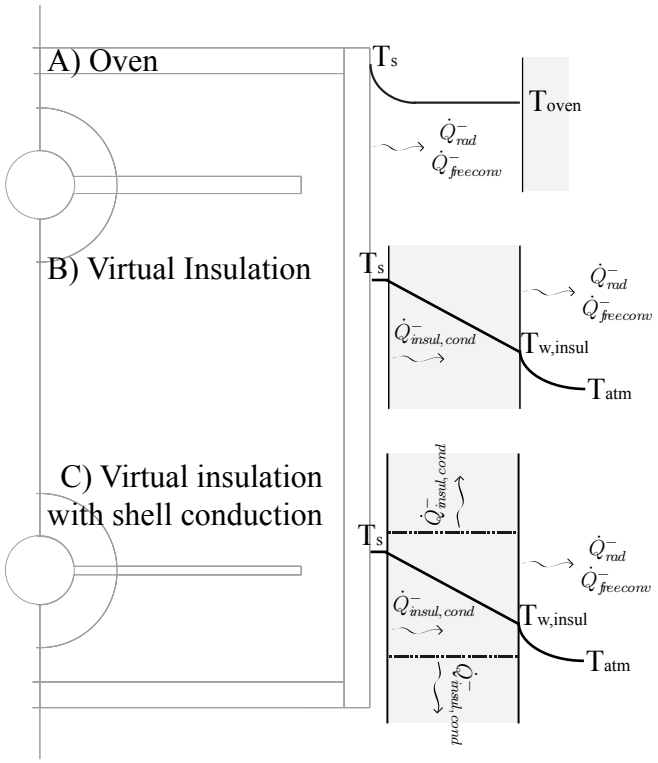

Figure 5.1: Thermal boundary conditions for repeat-elements.

Oven In laboratory conditions, stacks are tested in ovens whose temperatures are controlled to define the operating conditions. Distances of at least a few centimeters exist between the stack boundaries and the walls of the oven, and are assumed to have little influence on the surface temperature of the oven. The surfaces of the oven are therefore assumed to be isothermal and at fixed temperature. For the oven case, the applied thermal boundary conditions include both radiation and free convection in the heat exchange:

$$\dot{Q}^- = \dot{Q}^-_{rad} + \dot{Q}^-_{freeconv.} \quad (5.31)$$

$$\dot{Q}^-_{rad} = \epsilon_{rad}\sigma(T^4_{surf} - T^4_{oven}) \quad (5.32)$$

$$\dot{Q}^-_{freeconv.} = h_{freeconv.}(T_{surf} - T_{oven}) \quad (5.33)$$

where ϵ_{rad} is the emissivity assumed for the surface, T_{oven} is the temperature of the test environment and σ the Stefan-Boltzmann constant for radiation (in W.m^{-2}.K^{-4}).

The ratio of free convective heat transfer to radiative heat transfer can be estimated by calculating the Rayleigh number of the flow [97]:

$$Ra_L = Gr_L Pr = \frac{g\beta(T_s - T_\infty)L^3}{\nu\alpha} \tag{5.34}$$

where Gr_L is the Grashof number, Pr the Prandtl number, L the characteristic length of the heated surface, ν the kinematic viscosity and the thermal diffusivity $\alpha = \rho c_p k^{-1}$. The corresponding average Nusselt number for the resulting flow is calculated using the Churchill-Chu correlation [97] for vertical surfaces:

$$\overline{Nu_L} = \frac{\overline{h}L}{k} = 0.68 + \frac{0.670 Ra_L^{(1/4)}}{[1 + (0.492/Pr)^{(9/16)}]^{(4/9)}} \tag{5.35}$$

For typical temperature differences of 50 K around 1073 K, the heat transfer coefficient $\bar{h}$ is in the range of 6 to 10. With an emissivity of 0.8, the radiative heat transfer is of 4700 Wm^{-2}, while the convective heat transfer represents about 500 Wm^{-2}, representing 10% of the total heat transfer.

Insulation As product, the stacks are embedded in a high temperature insulation. Contrarily to other stack technologies, radiant cooling is not used in our case, in order to prevent strong thermal gradients on the repeat-element's sides. In such conditions, the operating temperature of the stack is defined by the gas inlet temperatures, the air excess factor (λ) and the heat released by the stack. The part of generated heat that is not removed from the system by the gas streams is transferred to the ambient through the insulation.
The insulation is placed at a short distance from the stack surface, which strongly reduces the heat transfer by free convection between stack and insulation. At nominal load, typical heat losses through the stack surfaces are in the range of 1 $\mathrm{kW}_{th}\mathrm{m}^{-2}$ for the *S-design* and *F-design* stacks. This represents an average temperature difference of 11 K between those surfaces when only radiative heat transfer is considered (Eqn. (5.33)), which is negligible when compared to the difference between the stack temperature and the ambient.
Two approaches are used to simulate this type of heat transfer. Either the volume of insulation is meshed for more accuracy, but without gap between stack and insulation, or a thin wall approach with shell conduction is used, as offered by the solver. In this case, the solver computes conductive heat transfer through a wall of given thickness, without requiring additional meshing. Radiation and free convection are computed on the outer surface of the insulation,

$$\dot{Q}^- = \dot{Q}^-_{insul,cond.} = \dot{Q}^-_{w,rad} + \dot{Q}^-_{w,freeconv.} \tag{5.36}$$

$$\dot{Q}^-_{insul,cond.} = k_{insul.}(T_s - T_{w,insul.}) \tag{5.37}$$

$$\dot{Q}^-_{w,rad} = \epsilon_{rad}\sigma(T_w^4 - T_{atm}^4) \tag{5.38}$$

$$\dot{Q}^-_{w,conv} = h_{freeconv.}(T_w^4 - T_{atm}^4) \tag{5.39}$$

$$\tag{5.40}$$

where the suffix w denotes the cold side of the insulation. In this simplified approach, it is possible to include conduction in directions parallel to the original surface. In this case, only one mesh cell is considered over the whole thickness of the created virtual volume, which is a strong simplification of real conditions. However, due to the low conductivity of used insulation materials ($k_{isol} \simeq 0.04 W m^{-2} K^{-1}$ for microporous insulation), this lateral conduction has in most cases a negligible effect on the temperature field inside the repeat-element, where in-plane thermal conductivity is orders of magnitude higher.

5.4 Chemical reactions

In laminar flows, chemical reactions are described by Arrhenius laws in laminar, finite-rate formulation. For the cases where non-premixed post-combustion is considered in a turbulent environment (HoTbox^{TM} , or repeat-element with surrounding volume, see Fig. 4.2), the Magnussen-Hjaertager eddy-dissipation model [89] is combined to the Arrhenius law. Using this formulation, the reaction rate is either limited by the kinetics of the reaction, or by the rate of turbulent mixing.

5.4.1 Steam methane reforming and water-gas-shift reactions

The methane steam-reforming reaction (React. 2.3) occurs at the surface of the nickel catalyst. The reaction rate (kmol m^{-2} s^{-1}) is given by Klein et al. [33]:

$$r_{SMR} = 63.6\ T^2\ exp\left(-\frac{27063}{T}\right)[CH_4][H_2O] - 3.7\ 10^{-14}\ T^4\ exp\left(-\frac{232.78}{T}\right)[CO][H_2]^3 \tag{5.41}$$

where [k] represents the concentrations of the gas specie k in kmol m^{-3}.
Due to the fact that the anode gas-diffusion layers are simplified to homogeneous porous volumes, a correction factor A^*_{SMR} is applied to this relation to take into account the ratio of catalyst surface exposed to the gas stream to the actual cell surface in the meshed volume. For confidentiality reasons, it is not possible to give the exact value of this factor.
The shift reaction React. 2.5 is assumed to be at equilibrium in the gas phase, a hypothesis which is usually made in SOFC modeling. In the solver, the forward r_f and backward r_b rate coefficients are chosen in appropriate manner to reach equilibrium:

$$K_{eq,shift} = \frac{k_f}{k_b} \tag{5.42}$$

where $K_{eq,shift}$ is the equilibrium constant of the water gas shift reaction.
Recent results by Haberman and Young [101] show that the hypothesis of equilibrium has to be revised, and the equilibrium formulation replaced by a kinetic model.

5.4.2 Combustion

The kinetic models for combustion reactions are taken from the reaction database of FLUENT™. The reaction rate for the combustion of hydrogen is given by:

$$H_2 + \frac{1}{2}O_2 \longrightarrow H_2O \tag{5.43}$$

$$r_{H_2} = 9.87 \cdot 10^8 \; exp(-\frac{3.1 \cdot 10^5}{\mathcal{R}T})[H_2][O_2]^{1/2} \tag{5.44}$$

with the reaction rate given in (kmol m^{-3} s^{-1}).
For carbon-monoxide, a combustion model involving a forward and backward reaction is proposed in the reaction database:

$$CO + \frac{1}{2}O_2 \longrightarrow CO_2 \tag{5.45}$$

$$r_{CO,f} = 2.239 \cdot 10^{12} \; exp(-\frac{1.7 \cdot 10^5}{\mathcal{R}T})[CO][O_2]^{1/4}[H_2O]^{-1} \tag{5.46}$$

$$CO_2 + \frac{1}{2}O_2 \longrightarrow CO + \frac{1}{2}O_2 \tag{5.47}$$

$$r_{CO,b} = 5 \cdot 10^8 \; exp(-\frac{1.7 \cdot 10^5}{\mathcal{R}T})[CO_2] \tag{5.48}$$

The dependance of the first reaction on the steam concentration results from the integration of the water-gas-shift reaction in the combustion model [89].
These simple kinetic combustion models, which do not involve intermediate species, might present slightly different results with more complete models. However, for both the parasitic combustion in porous seals as well as for the open post-combustion, non-premixed cases are studied, where the species transport properties are principally determinant for the location and extent of the reaction. Therefore, this simplified formulation is assumed to fulfill the principal objective, which is to determine the location and rate of combustion.

Chapter 6

Electrochemical model

6.1 Foreword

One of the principal objectives of this work is the optimization of the design of SOFC stacks, both in terms of performance and reliability. High performance is attained at high fuel utilizations (unless recirculation of fuel is used), where local properties strongly vary over the cell's active area. In lean fuel areas, the electrochemical reaction presents a strongly non-linear behavior due to the drop of local Nernst potential combined with an increase in diffusion overpotentials. These limiting areas have an important effect on the maximal achievable efficiency. Moreover, such areas are expected to present high risks of cell damage by reoxidation of the anode. Consequently, one major requirement for the electrochemical model is to provide an accurate description of the electrochemical reaction over the widest range of operating conditions.

The electrochemical model chosen for implementation in the developed CFD simulation tool is, as for usual CFD models, a compromise between calculation speed and level of detail. Accurate predictions are however guaranteed by the fact that the model was fitted on experimental data obtained on a wide range of operating conditions, therefore fulfilling the above-mentioned requirements. Therefore, even if the extent of individual losses attributed to different phenomena might differ somewhat from physical reality, the overall extent of losses corresponds to the fitted values.

Experimental data for the fitting procedure was obtained from P. Metzger et al. at DLR (German Aerospace Center, Stuttgart, Germany), who are gratefully acknowledged. *The segmented-cell experiment developed at DLR offered an access to conditions corresponding from zero to 82% fuel utilization, at different air excess factors, different fuel and oxidant dilutions, different temperatures, and current loads. The experiment is briefly described hereafter. Details about their measurement technique can be found in reference [9].*

The electrochemical model was developed and fitted by A. Nakajo from LENI, who is gratefully acknowledged. *The version implemented in FLUENT is the most simplified version of*

the model. A. Nakajo considerably improved the electrochemical model basing on the same dataset, resulting in a much more complete and precise description of the electrochemical reaction. A detailed description can be found in references [102, 103].

6.2 Choice of an electrochemical model

6.2.1 Equivalent circuit

The electrochemical model is based on a classical equivalent circuit approach, shown in Fig. 6.2. The cell is modeled as a solid volume, at the interface of which the resulting mass and energy sources are imposed (Fig. 6.1).

One specificity of the model is that it includes a small leakage current j_{loss} in the elec-

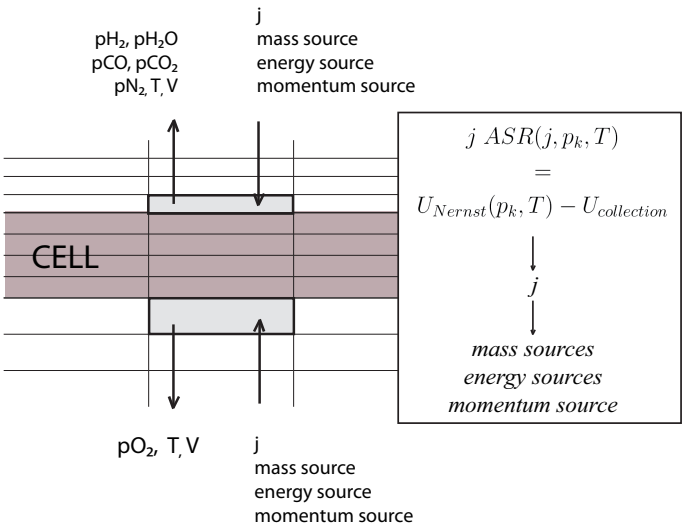

Figure 6.1: Control of the electrochemical reaction

trolyte. Proposed by Larrain [8] in 2005, it results from experimental observations on button cell experiments on HTceramix's anode-supported cells, where the open-circuit voltages were systematically lower than the expected theoretical Nernst potentials (1.03-1.07 V instead of the expected 1.1 V at 800°C, 97% H_2 + 3% H_2O). In the segmented experiment performed at DLR, the OCV was 1.03 V under similar condition, using an InDEC ASC2 cell with LSCF cathode.

This lowering of OCV could originate from leakage of the seals in the experiments, from pinholes in the electrolyte, or from a leakage current through the electrolyte. By parameter estimation on button-cell experiments, the latter was evaluated by Larrain et al. to represent an important contribution. The proposed explanation for the leakage current was a contamination of the electrolyte by nickel oxide or other pollutant species (Mn, Ti, Ni, Fe)

during sintering, resulting in an increased electronic conductivity.
With the development of a new generation of cells and improvements in measurement methods, the lowering of OCV was progressively reduced, approaching the theoretical values. Consequently, the importance of the leakage current on local electrochemistry has been considerably reduced.

The internal resistance R of the equivalent circuit includes the internal loses of the cell,

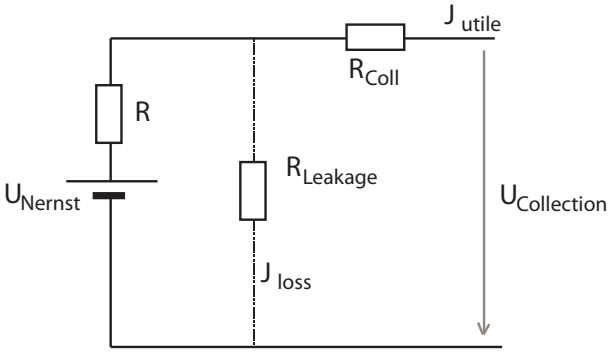

U_{Nernst}	Local Nernst potential
$U_{Collection}$	Local collection potential
R_{Coll}	Ohmic resistance of electrodes and interconnector
$R_{Leakage}$	Ohmic electronic resistance of the electrolyte
R	Cell's internal losses
J_{utile}	Output current
J_{loss}	Leakage current

Figure 6.2: Equivalent circuit

that is, the polarization losses in addition to the ionic resistance of the electrolyte. The polarization losses considered in the model are the diffusion of gases in the anode support and the charge transfer reactions on anode and cathode side.

$$R(j_{tot}, T, p_k) = R_{Ionic} + R_{Pol} \tag{6.1}$$

$$R_{Pol}(j_{tot}, T, p_k) = R^{an}_{diff} + R^{an}_{ct} + R^{cat}_{ct} \tag{6.2}$$

The collection resistance R_{Coll} includes the ohmic resistance occurring for the current collection, which includes the electrodes, the GDLs and MICs in the planar case.

$$R_{Coll} = R^{electrode}_{\Omega} + R^{GDL}_{\Omega} + R^{MIC}_{\Omega} \tag{6.3}$$

At open circuit, the useful (available) current j_{utile} is zero and the measured collection potential corresponds to the ratio $R_{Leakage}/(R_{Leakage} + R)$ of the Nernst potential.

The polarization resistance R depends on the local current density, gas compositions and temperature (Fig. 6.1). As it is the collection potential which is fixed by the control algorithm

(it is either constant on the cell's surface in the planar case or determined by the losses in the collection in the tubular case), the following implicit equation 6.4 is solved iteratively :

$$\underline{\underline{R}}(j_{utile}, j_{loss}, T, p_k) \begin{pmatrix} j_{utile} \\ j_{loss} \end{pmatrix} = \begin{pmatrix} U_{collection} \\ U_{Nernst} \end{pmatrix} \tag{6.4}$$

with

$$\underline{\underline{R}}(j_{utile}, j_{loss}, T, p_k) = \begin{pmatrix} -R_{Coll} & R_{Leakage} \\ R & R + R_{Leakage} \end{pmatrix} \tag{6.5}$$

and

$$j_{tot} = j_{utile} + j_{loss} \tag{6.6}$$

6.2.2 Loss terms

The electrochemical model is fitted on data obtained for an anode supported cell (InDEC ASC2). The cell consists of a 540 μm thick NiO/YSZ anode, a 7 μm thick 8YSZ electrolyte and a 7 μm thick yttria doped ceria (YDC) protection layer to avoid chemical interactions with the 28 μm thick LSCF cathode.

Ionic conductivity of the electrolyte The electrolyte layer consists of one dense YSZ layer, on which a porous YDC layer is sintered. The bulk conductivity of the both materials is given by:

$$\sigma_{ionic} = \sigma_0 \, exp\left(\frac{-E_a^{ionic}}{kT}\right) \tag{6.7}$$

with $E_a^{ionic,YSZ} = 0.79\ eV$ and $\sigma_0^{YSZ} = 1.6310\ S/cm$ for YSZ, and $E_a^{ionic,YDC} = 0.7\ eV$ and $\sigma_0^{YDC} = 218.68\ S/cm$ for YDC.
The resistance of the bulk YSZ layer is given by:

$$R_{ionic}^{YSZ} = \frac{h^{YSZ}}{\sigma_{ionic}^{YSZ}} \tag{6.8}$$

and the one of the porous YDC layer is given by:

$$R_{ionic}^{YDC} = \frac{1 - \varepsilon^{YDC}}{1 + \frac{\varepsilon^{YDC}}{2}} \cdot \frac{h^{YDC}}{\sigma_{ionic}^{YDC}} \tag{6.9}$$

where $\varepsilon = 0.2$ is the estimated porosity of the YDC layer. At the interface between the porous YDC and the YSZ, a constriction of the ionic current occurs, which results in a deviation between the effective total resistance of the double layer and the one estimated by simply adding the bulk resistances of the two layers, as shown by Fleig in [104]. Fleig proposes a correlation for the additional constriction term (R_{constr}):

$$R_{constr} = \frac{b}{\sigma_{ionic}^{YSZ}} \left(\frac{\frac{b}{d} - 1}{\frac{d}{b} + 1}\right) \tag{6.10}$$

where b represents the distance between YDC grains and d is the average particle diameter. The total ionic resistance is finally given by:

$$R_{Ionic} = R_{ionic}^{YSZ} + R_{constr} + R_{ionic}^{YDC} \tag{6.11}$$

Diffusion on anode side The diffusion overpotential η_{an}^{diff} is computed for the anode side only and neglected on the cathode side. To limit the computational cost, the diffusion mass transport in the anode support is not solved by a full discretization of the equations along the diffusion path. Moreover, as mentioned earlier, a multicomponent Fickian diffusion model is applied instead of a more complete diffusion model (such as the dusty-gas model or the mean-transport pore model).
This approach limits the accuracy of predictions for conditions that differ from the experimental dataset used to fit the model. In particular, this model has limited validity when considering fuel mixtures containing CO, CO_2 or CH_4 where the WGS and SMR reactions take place within the anode support. In such cases, it is considered that only hydrogen reacts at the electrolyte.

The binary diffusion coefficients are computed from the Fuller equation:

$$D_{i-j} = \frac{1.43 \cdot 10^{-7}\, T^{1.75}}{p\sqrt{\dfrac{2}{M_i^{-1} + M_j^{-1}}}\left(V_{d,i}^{1/3} + V_{d,j}^{1/3}\right)^2} \tag{6.12}$$

The mixture diffusion coefficients are evaluated by the Wilke equation, using the molar fraction of gases in the boundary layer:

$$D_{i,m} = \frac{1 - x_i}{\displaystyle\sum_{\substack{j=1 \\ j \neq i}}^{N} \frac{x_i}{D_{binary,i-j}}} \tag{6.13}$$

For each gaseous specie i, the Knudsen diffusion term is computed:

$$D_{Kn,i} = \frac{\overline{d_p}}{3}\sqrt{\frac{8\mathcal{R}10^3 T}{\pi M_i}} \tag{6.14}$$

The resulting effective diffusion coefficient is given by the Bosanquet formula:

$$D_{eff,i} = \left(\frac{\varepsilon}{\tau}\right)\frac{D_{Kn,i} D_{i,m}}{D_{i,m} + D_{Kn,i}} \tag{6.15}$$

The value of the porosity ε was obtained from quicksilver porosimetry measurements performed on a cell sample ($\varepsilon = 0.36$), while the tortuosity τ was estimated by the fitting

procedure.
The partial pressure of reactive species at the electrolyte is obtained by integrating the diffusion equation over the thickness of the anode l_{anode}, while considering constant diffusion coefficients. For the case of hydrogen and steam

$$\widetilde{J}_i = \frac{j}{2F} = D_{eff,i}\frac{\partial C_i}{\partial z} \tag{6.16}$$

$$p_{H_2,electroyte} = p_{H_2,GDL} - \frac{RT}{P_0}\frac{j}{2F}\frac{l_{anode}}{D_{eff,H_2}} \tag{6.17}$$

$$p_{H_2O,electroyte} = p_{H_2O,GDL} + \frac{RT}{P_0}\frac{j}{2F}\frac{l_{anode}}{D_{eff,H_2O}} \tag{6.18}$$

$$\tag{6.19}$$

with $P_0 = 101'325\,Pa$. The resulting diffusion overpotential and diffusion resistance are given by:

$$\eta^{an}_{diff} = \frac{RT}{2F} ln\left[\frac{p_{H_2,GDL}}{p_{H_2,electrolyte}}\frac{p_{H_2O,electrolyte}}{p_{H_2O,GDL}}\right] \tag{6.20}$$

$$R^{an}_{diff} = \frac{\eta^{an}_{diff}}{j} \tag{6.21}$$

Charge transfer on anode side On the anode side, the charge-transfer reaction is described by a general Butler-Volmer relation, according to the relation from Bessler [20].

$$j = j^{an}_0 \left[exp\left(\beta^{an}_a \frac{nF}{RT}\eta^{an}_{ct}\right) - exp\left(-\beta^{an}_c \frac{nF}{RT}\eta^{an}_{ct}\right)\right] \tag{6.22}$$

The temperature and gas composition dependance of the exchange current density is considered:

$$j^{an}_0 = k^{an}_0\, T \cdot x^{r_{H_2}}_{H_2,elec} \cdot x^{r_{H_2O}}_{H_2O,elec}\, exp\left(-\frac{E^{an}_{a,ct}}{RT}\right) \tag{6.23}$$

The gas compositions $x_{H_2,elec}$ and $x_{H_2O,elec}$ at the electrolyte are computed from the diffusion model.
To calculate the resulting overpotential η^{an}_{ct}, the generalized form of equation 6.22 has to be solved numerically, which is computationally expensive. Therefore, the usual simplification of the equation is performed by setting the symmetry coefficients β^{an}_a and β^{an}_c to 0.5.

$$\eta^{an}_{ct} = \frac{RT}{F} asinh\left(\frac{j}{2j^{an}_0}\right) \tag{6.24}$$

Values for the above-listed parameters are available in literature. They can vary in more or less large ranges, which reflects different morphological properties, compositions and experimental conditions. Therefore, fitting of the parameters is required to reproduce the behavior of a particular cell. In this case, the reaction orders r_{H_2} and r_{H_2O}, the activation energy $E^{an}_{a,ct}$ and k^{an}_0 were fitted.

Charge transfer on cathode side On the cathode side, a model for mixed ionic electronic conductor (MIEC) is applied. The reaction is modeled to occur only in the vicinity of the electrolyte.

$$j = j_0^{cat} \left[exp\left(\beta_a^{cat} \frac{F}{RT} \eta_{ct}^{cat}\right) - exp\left(-\beta_c^{cat} \frac{F}{RT} \eta_{ct}^{cat}\right)\right] \tag{6.25}$$

The temperature and gas composition dependance of the exchange current density is considered:

$$j_0^{cat} = k_0^{cat}\, T \cdot x_{O_2,GDL}^{r_{O_2}}\, exp\left(-\frac{E_{a,ct}^{cat}}{RT}\right) \tag{6.26}$$

where the oxygen fraction is evaluated in the boundary layer, hence neglecting diffusive mass transport in the cathode.

6.3 Fitting procedure

The measurement setup developed by Metzger at DLR gives access to local electrochemistry on an anode-supported or electrolyte-supported cell of 74 cm^2 active area. For anode-supported cells, the air electrode and contacting interconnect are segmented into 16 electrically insulated areas, organized as 4 rows of four segments disposed along the flow (see Fig. 6.3). The polarization control of the segmented repeat-element is performed through an external active load to which the 16 segments are connected through a collection bus bar (see Fig. 6.4). Local temperatures, potentials and currents are measured on each separate segment while the operating conditions are varied. Due to the finite conduction of the collection lines, potential losses occur between the segments and the collection bus bar. Therefore, the local collection potentials $U_1, ..U_{16}$ vary depending on local current densities and line resistances. Additional details on the measurement technique can be found in references [9, 105].

To extract the electrochemical performance of the cell, successive i-V characterizations

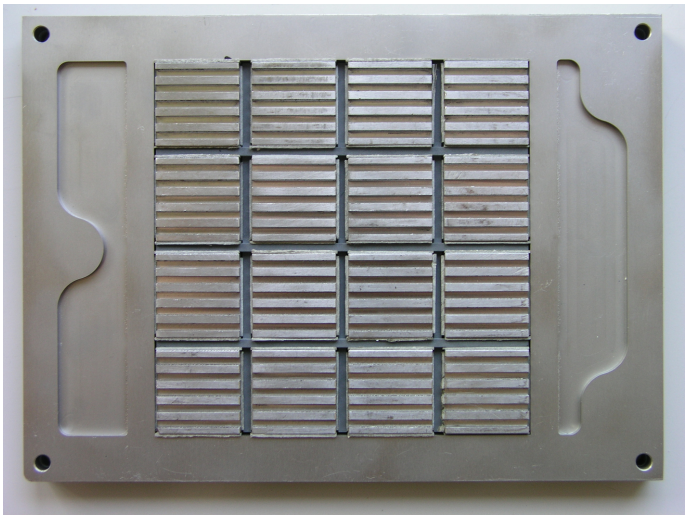

Figure 6.3: Setup used for cell characterizations at DLR. Source: P. Metzger, DLR

were performed, while recording local properties. Local Nernst potentials were estimated by resolving a mass flow balance along each line of segments, using the recorded currents to determine each segment's inlet and outlet gas compositions. The fuel inlet composition was successively modified from 100% H_2 to significant dilutions of 2%H_2 -98%N_2 , with a constant addition of 3%H_2O . Measurements were performed with air as oxidant, and additionally with composition reaching from 5% to 100% O_2 diluted in nitrogen. Temperatures were varied between 650°C and 800°C. For each operating point, an i-V characterization was performed until a minimum potential of 0.6 V was attained.
The complete dataset consists of 25'000 distinct measurement points, on which a parameter estimation was performed using the capabilities of the equation solver gPROMS.

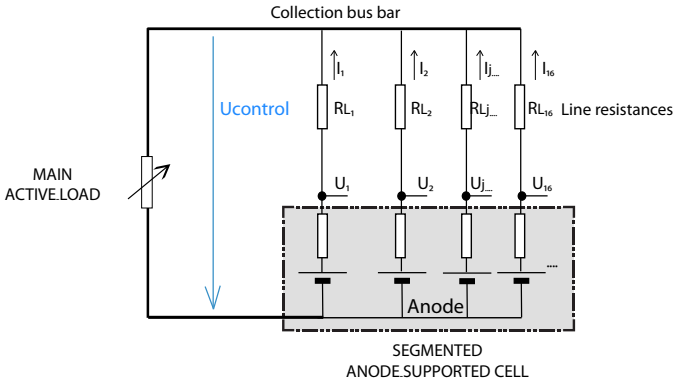

Figure 6.4: Control of the polarization for the segmented experiment at DLR.

6.4 Result

The quality of the fit is shown in Fig. 6.5, showing a good agreement between experimental and fitted data over the whole range of tested operating conditions. The estimated parameter values and confidence intervals for the electrochemical model are given in table 6.1.

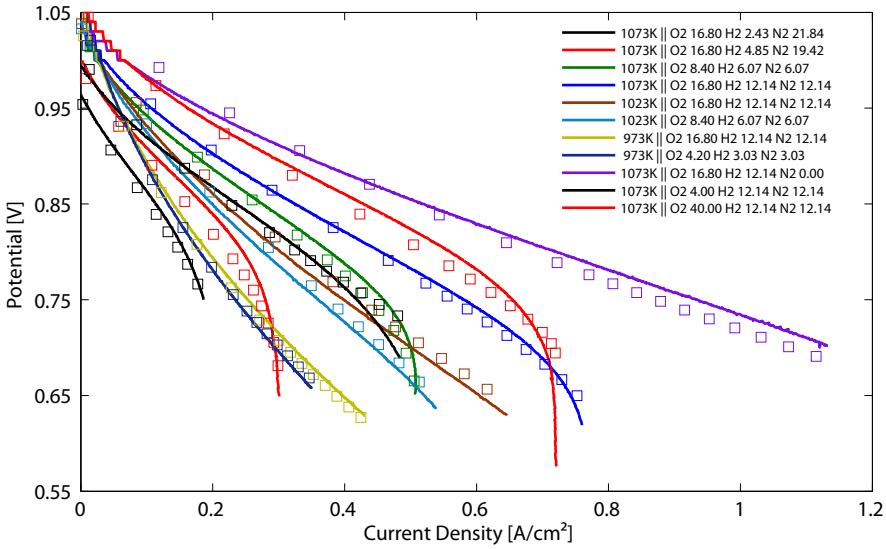

Figure 6.5: Experimental and fitted data.

The confidence intervals for the obtained values are in the range of 10% of the optimal estimate for the activation energies, which is a fairly acceptable result. The activation en-

Parameter	Optimal Estimate	90%	95%	99%
$E_{a,ct}^{an}$ (kJ/mol)	99	11.4	13.6	18.0
k_0^{an} $(Am^{-2}K^{-1})$	$1.980{\cdot}10^6$	$0.519{\cdot}10^6$	$0.620{\cdot}10^6$	$0.815{\cdot}10^6$
r_{H_2}	0.236	0.034	0.041	0.054
r_{H_2O}	0.280	0.033	0.039	0.052
τ^{an}	12.4	0.50	0.60	0.79
$E_{a,ct}^{cat}$ (kJ/mol)	172	11.6	13.9	18.3
k_0^{cat} $(Am^{-2}K^{-1})$	$1.822{\cdot}10^9$	$0.489{\cdot}10^9$	$0.590{\cdot}10^9$	$0.776{\cdot}10^9$

Table 6.1: Fitted parameters of the electrochemical model.

ergy for the charge transfer reaction on the anode side $E_{a,ct}^{an} = 99\,kJ/mol$ is in the range of values found in literature. For instance, Zhu and Kee use a slightly higher value of $E_{a,ct}^{an} = 120\,kJ/mol$ in their model [1].
On the cathode side, the activation energy $E_{a,ct}^{cat} = 172\,kJ/mol$ is slightly higher than the ones reported by Beckel et al. ($1.55eV = 149kJ/mol$) [106] or by Dusastre and Kilner [107]($1.40..1.54eV = 135..148kJ/mol$).

The fitted reaction orders $r_{H_2} = 0.236$ and $r_{H_2O} = 0.280$ present values close to 1/4 found in different studies. Confidence intervals are about 15% of the optimal value. In literature, considerable disagreement is found for the values of these parameters. From experimental studies, values comprised between -0.5..0.5 for H_2 and 0..1 for H_2O are reported [20, 108, 109]. Theoretical studies about rate-limiting elementary reaction steps come to different conclusions depending on their hypotheses. Bessler uses a reaction order of 1/4 for H_2 and 3/4 for H_2O in one of his models [20]. Using a different formulation for the exchange current density i_0, Zhu et al. report a reaction order of 3/4 for H_2O [27]. It cannot be excluded that the difference between the fitted and reported values results from an error on the estimated steam and hydrogen partial pressures at the electrolyte due to limitations in the used diffusion model.

Finally, the estimated ohmic resistance of the electrolyte $R_{leakage} = 45\,\Omega\ cm^2$ allows to estimate leakage currents in the order of 20 $\mathrm{mA\,cm^{-2}}$ at a cell potential of 0.8V.

6.5 Parameters of the electrochemical model

The complete set of parameters for the electrochemical model is summarized in the following table:

Parameter	Symbol	Value	Unit
Anode			
Charge transfer			
Activation Energy	$E_{a,ct}^{an}$	99	kJ/mol
Kinetic constant	k_0^{an}	$1.98{\cdot}10^6$	$\mathrm{AK^{-1}m^{-2}}$
Reaction order H_2	r_{H_2}	0.236	
Reaction order H_2O	r_{H_2O}	0.280	
Symmetry coefficients	$\beta_a^{an}, \beta_c^{an}$	1	
Reference temperature	T_{ref}	873	K
Diffusion			
Porosity	ε^{an}	0.309	
Tortuosity	τ^{an}	12.4	
Pore Diameter	d_p^{an}	0.349	μm
Anode thickness	h_{an}	540	μm
Cathode			
Charge transfer			
Activation Energy	$E_{a,ct}^{cat}$	172	kJ/mol
Kinetic constant	k_0^{cat}	$1.822{\cdot}10^9$	$\mathrm{AK^{-1}m^{-2}}$
Reaction order O_2	r_{O_2}	3/8	
Symmetry coefficients	$\beta_a^{cat}, \beta_c^{cat}$	1	
Reference temperature	T_{ref}	873	K
Electrolyte			
YSZ thickness	h_{YSZ}	7	μm
YDC thickness	h_{YDC}	7	μm
YDC porosity	ε_{YDC}	0.2	μm
YDC particle diameter	b	2	μm
YDC particle diameter	b	0.4	μm
Current collection			
Collection resistance	R_{Coll}	60	$\mathrm{m\Omega\,cm^2}$
Leakage Current			
Electrolyte's ohmic resistance	$R_{Leakage}$	45.1	$\mathrm{\Omega cm^2}$

Table 6.2: Parameters of the electrochemical model

6.6 Control of the electrochemical model

Different control modes for the electrochemical model are implemented in the CFD model, which are briefly exposed in the following paragraphs. The corresponding cases are visible in the figures 4.2 and 4.3 (pp. 70-71).

Planar repeat-element For planar repeat-elements, it is assumed that potential variations in the interconnects are negligible. In this case, it is assumed that the collection potential equals the controlling cell potential ($U_{Coll} = U_{cell}$). In potentiostatic mode, U_{cell} is fixed. In galvanostatic mode, the cell potential is regulated U_{cell} iteratively through a PID-like controller to reach the target current. The use of the PID controller enhances considerably the convergence of the model.

Stack configuration In stack configuration, an individual control of the cell potentials is performed through the PID controller to reach a common target current.

Planar, segmented repeat-element with ideal current collection In segmented experiments with ideal current collection, that is, without line resistances in the current collection lines (see Fig. 6.4), the collection potentials U_{Coll} are constant on the individual segments. In the model, the control of polarization is made in the same manner as for a single planar repeat-element, with equal potentials on all segments. In galvanostatic mode, the individual currents are added to control the potential through the PID controller.

Planar, segmented repeat-element with losses in current collection lines To reproduce the DLR experiment, the line resistances measured by P.Metzger were introduced in the model. The PID controller regulates the control potential $U_{control}$ (see Fig. 6.4) and the individual collection potentials are calculated as a function of the segment's output currents and line resistances. In such cases, convergence to a solution becomes slow.

Cathode-supported tubular cells In the frame of the development of tubular SOFC stacks, complements for the CFD model have been made to couple the electrochemical model with a simulation of the electric field in electrodes and current collection. This is done by using the generic $User - Defined - Scalars$ module of FLUENT™.
The following generic equation is solved for any scalar variable ϕ_k of interest:

$$\frac{\partial \rho \phi_k}{\partial t} + \frac{\partial}{\partial x_i}\left(\rho v_i \phi_k - \Gamma_k \frac{\partial \phi_k}{\partial x_i}\right) = S_{\phi_k} \tag{6.27}$$

where Γ_k and S_{ϕ_k} are respectively a diffusion coefficient and additional source term. This equation contains a convective term that can be canceled. In its stationary form, and without source term it then reduces to the Laplace equation:

$$\frac{\partial}{\partial x_i}\left(-\Gamma_k \frac{\partial \phi_k}{\partial x_i}\right) = 0 \tag{6.28}$$

with summation over the indices i. By defining ϕ_k as the electrical potential ϕ and Γ_k as the electronic conductivity σ, this equation can be used to compute the current flux $\overrightarrow{J}$ in the current collection and in the electrodes with:

$$\overrightarrow{J} = -\sigma \overrightarrow{\nabla} \phi \tag{6.29}$$

The computed potential difference between the considered reaction point of the electrode and the cell's current collector is then locally introduced in the equivalent circuit.

6.7 Conclusion

In this chapter, the CFD model is presented. It offers several different options enabling to model repeat-elements, short stacks, segmented elements and tubular cells in different configurations. The core of this CFD model is represented by an electrochemical model fitted on experimental data over a wide range of operating conditions. This represents a major requirement for a model aiming to predict performance, and in particular performance limitations in fuel cells.
The fact that the electrochemical model is fitted on experimental data offers in addition an important confidence on the reliability of the results. Therefore, significant deviations between experiments and modeling outputs can be used to detect problems in the tested prototypes. This feature opens up therefore possibilities for model-assisted diagnostics. Moreover, this electrochemical model allows to design new prototypes with a certain confidence in the obtained results. As demonstrated throughout the following chapters, an excellent match could be obtained between experiments and simulation in newly developed prototypes. Finally, the use of a segmented experiment to fit the electrochemical model shows at this stage already the interest of this type of instrumentation for the development of reaction laws, as it provides large amounts of experimental data over wide ranges of operating parameters, which is required for fitting procedures.
The model presented in this chapter contains numerous features that will not be illustrated in the following chapters, as the focus is set on the resolution of reliability and degradation issues. In particular, simulations of the interactions between the stack and its insulation are not presented. These studies concluded on the large importance of radiative exchange in such enclosures, affecting to an important extent the thermal distribution in the height of stacks.
Results involving internal steam methane reforming and/or syngas are also not presented, whereas results of interest are obtained by simulation. Investigations made on the *R-design*

stack operated on steam methane reforming (including partial internal reforming) showed as expected strong endothermal cooling of the fuel inlet region. Due to the lack of verification of the modeling outputs with experiments, and also due to the fact that these results are out of the main focus of this writing, they were not included in this work.

Part II

Effect of stack design on performance and reliability

Foreword

In the following chapters, modeling and experimental topics are presented simultaneously in the context of the investigations on performance, degradation and failure for SOFCs, without strict separation of purely general methodological aspects and their application. This is done on purpose, as methodological problems in the simulation and experimental work arose from specific needs in the stack design phase or from the need of specific explanations requiring modeling support. Therefore, each of the following chapter leads to modeling specific conclusions, as well as to conclusions specific for the understanding of SOFCs.

One might regret the lack of generalization of the simulation results on standard stack geometries. However, the experience made in the present work shows that it is often the detail of a stack design, of an operating point or of specific testing conditions that leads to a particular performance limitation, failure or degradation. Moreover, due to the high level of interaction between phenomena in SOFCs, intuitive predictions based on generalized results are not rarely contradicted by detailed modeling or experimental work.

In a first part, the link between stack design and performance limitations is analyzed. Starting from the simulation of the first generation *R-design* stack and from the identification of its limitations, a first re-design iteration is described. This chapter demonstrates the central importance of an homogeneous internal fuel distribution on the maximal performance of the stack, as well as the role played by at first sight insignificant geometrical details on the final reliability and performance.

In a second chapter, a modeling-supported diagnostic of the principal failure mode for the *R-design* and *S-design* stacks is performed. The introduction of non-ideal component behavior in the model, specifically for the sealing materials, leads to completely different simulation results which enables not only a much better match with experimental observations, but also bring a complete explanation of the observed failures of repeat-elements. Local redox-cycling of the cell's anode support is identified as main failure source, caused by the stack construction, the choice of materials, and by the effect of polarization which influences local redox properties.

The subsequent application of corrective actions, as well as the design of the less sensitive *F-design* stack is made possible by using the consequently completed CFD model. More important, an experimental validation of the approach is brought by the absence of redox patterns on cells after operation.

Chapter 7

Stack design and performance

7.1 Introduction

This chapter presents the investigations on performance-limiting stack design options, and the subsequent design of improved stack geometries based on modeling work. Investigations on SOFC stack design and performance have been proposed earlier by numerous authors, with one class of studies dealing with general flow configurations (co-flow, counter-flow, cross-flow, etc.) [110][111], and the other analyzing specific stack designs [112].
More recently, Larrain [8] focussed on the optimization of stack designs by using evolutionary optimization algorithms generating successive generations of flow configurations and operating conditions, tested in a dedicated repeat-element model and evaluated by the optimizer. The stack developments presented hereafter were made in close collaboration, using his tools for the dimensioning of the stacks, and the herein developed tools for the detailed design of internal flows.
Based on investigations on the first-generation *R-design* stack, it is shown that performance limitations are strongly linked to the detailed distribution of gases in the repeat-element, requiring a sufficient level of geometric detail, as well as an electrochemical model able to predict such limitations. To provide evidence of the effect of the stack's geometry on performance, a generic repeat-element with ideal flow distribution is studied and compared to the designed prototypes.
It is shown that the herein developed *S-design* and *F-design* stacks, for which a special care was given to avoid design-related limitations, are foreseen to achieve higher efficiencies and larger operation ranges than the reference design (*R-design*). More important, this prediction is validated by experimental results which are presented at the end of this chapter.

7.2 Performance of a generic repeat-element with ideal gas distribution

7.2.1 Model and boundary conditions

The performance of a generic repeat-element is studied to provide comparison with the real stack designs. It consists of a rectangular cell of 50cm^2 active area, whose *aspect ratio* (ratio of length over width) is similar to the one of the *S-design* and *F-design* stacks (1.5). The aspect ratio was identified by Larrain et al. to have a significant impact on the stack's performance [8, 36] and represented therefore one of the design parameters for the developed prototypes.
Fuel and air are supplied in co-flow arrangement over the full width of the element, providing an ideal distribution of gases over the surface. The co-flow configuration is chosen as it is the one used in the *S-design* and *F-design* stacks, basing on the results of Larrain who determined it as ideal compromise between low thermal gradients and performance in a bi-objective optimization.
Metallic interconnects of 1 mm thickness are modeled, as well as the thermal conduction in the gas-diffusion layers, in order to provide similar internal heat transfer properties than the ones occurring in real stacks. The air and fuel are supplied at a temperature of 973 K. Adiabatic conditions are considered for the outer surfaces of the MICs to model mid-stack conditions. In addition, the lateral sides of the repeat-unit possess periodic boundary conditions. Heat transfer to an enclosure is therefore neglected. In addition, these boundary conditions enable to avoid any boundary limit effects in the flows, that would reduce the convective mass transfer near the boundaries. Furthermore, these boundary conditions allow to limit temperature gradients in the direction perpendicular to the flow direction, which else would affect the rate of the electrochemical reaction and create concentration gradients in the transverse direction, which is further avoided by the homogenous flow distribution.
Therefore, the model reduces to a 2D-problem, even if it had to be computed in 3D due to the intrinsic 3D features of the written model [1].
To assess the effects of stack design on performance, the different designs are analyzed for increasing power outputs, that is, at different fuel flow rates and fuel utilizations. The fuel composition is kept constant at 97% H_2 + 3%H_2O , in order to avoid the intrinsic limitations from the cell itself under lean fuel mixtures. The air excess factor λ is fixed at a constant value of 6. This high value is representative of standard operation conditions when using hydrogen as fuel, in order to limit temperature differences in stacks by providing sufficient cooling. In a real system, this value is modulated depending on the operating point, with values above $\lambda = 8$ to limit temperature differences below 100 K at high fuel utilizations. The air and fuel temperatures are fixed at 700°C, which is representative of conditions for LSCF cathodes. For these simulations, the effect of the leakage current through the electrolyte is neglected.

[1] The computation can therefore be performed for a smaller area but same length, the latter fully determining the spatial distribution of the electrochemical reaction.

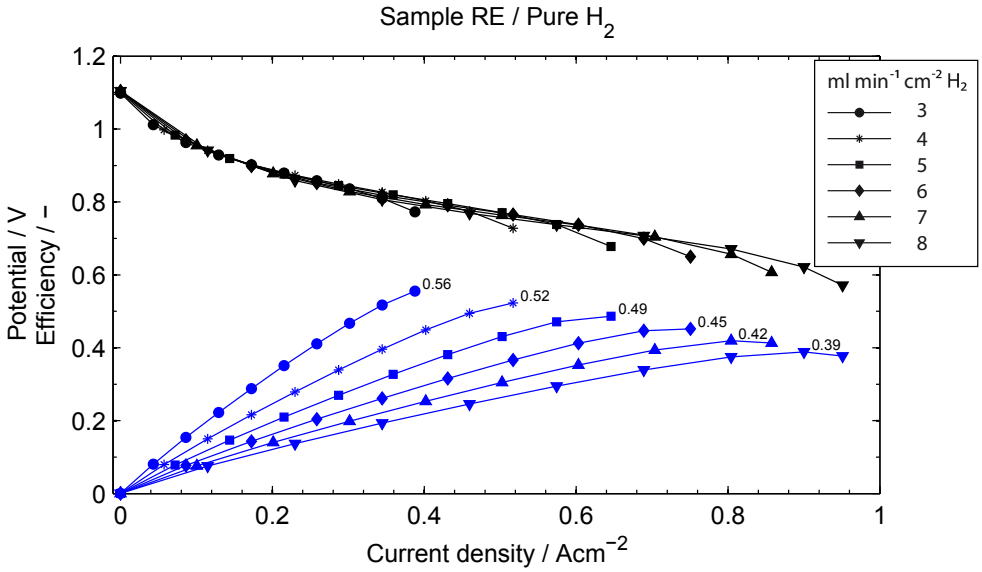

Figure 7.1: Series of i-V characterizations simulated for a generic repeat-element (co-flow) at various fuel flow rates ($\lambda = 6$). Black: potential. Blue: Efficiency.

7.2.2 Performance map

Figure 7.1 shows a series of i-V characterizations simulated under increasing fuel flow rates from 3 to 8 $\mathrm{ml\,min^{-1}\,cm^{-2}}$ H_2 (humidified)[2]. The maximum average current density varies between 0.4 and 1 $\mathrm{A\,cm^{-2}}$. The highest efficiency is obtained at the lowest fuel flow rate, reaching 56% of electrical efficiency. Efficiencies are always expressed as function of the *Lower Heating Value* (LHV). At the usual fuel flow rates in our laboratory, that is, at a fuel flow rate of 6 $\mathrm{ml\,min^{-1}\,cm^{-2}}$ H_2 , the maximum efficiency decreases to $\varepsilon = 45\%$. At the highest fuel flow rate, the efficiency drops to 39%.

The same series of simulations, represented as function of the fuel utilization, shows that the maximal efficiency is attained for the low flow rates at the maximal fuel utilization of 90%. Beyond this limit, the convergence of the model becomes more difficult, due to intrinsic limitations of the cell which are described hereafter. For the larger fuel flow rates, the highest efficiency is attained between 80% and 90% of fuel utilization. This shows that a SOFC stack should enable to reach this operating point to attain best efficiencies. In addition, this figure shows the decrease of performance with increasing average current densities, originating from higher electrochemical and ohmic losses.

A complete map of performance of the generic repeat-element is shown in Fig.7.3, including

[2]Gas flow rates are always given for the normal conditions (SI system), that is 0°C and 1 atm.

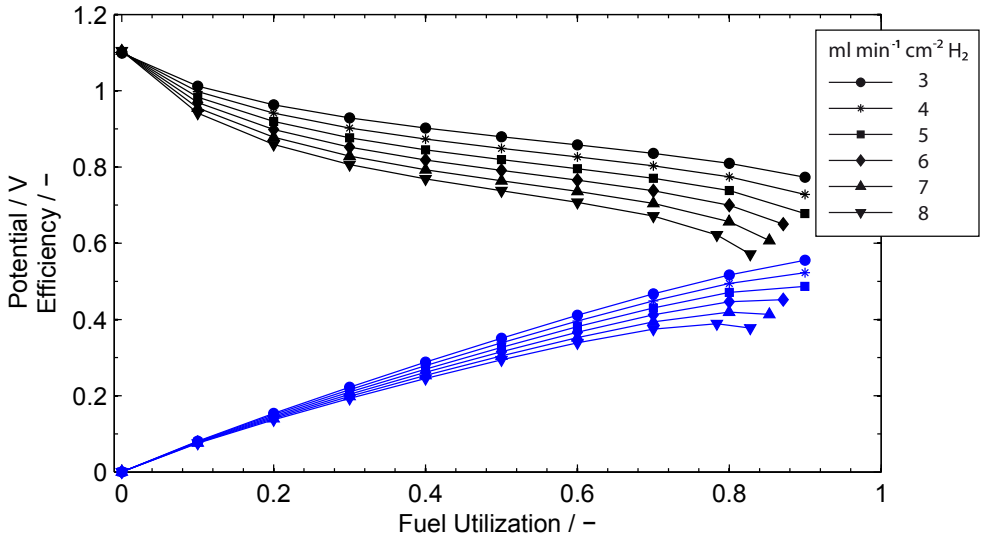

Figure 7.2: Simulated characterization of the generic repeat-element as function of the fuel utilization. Black: potential. Blue: Efficiency.

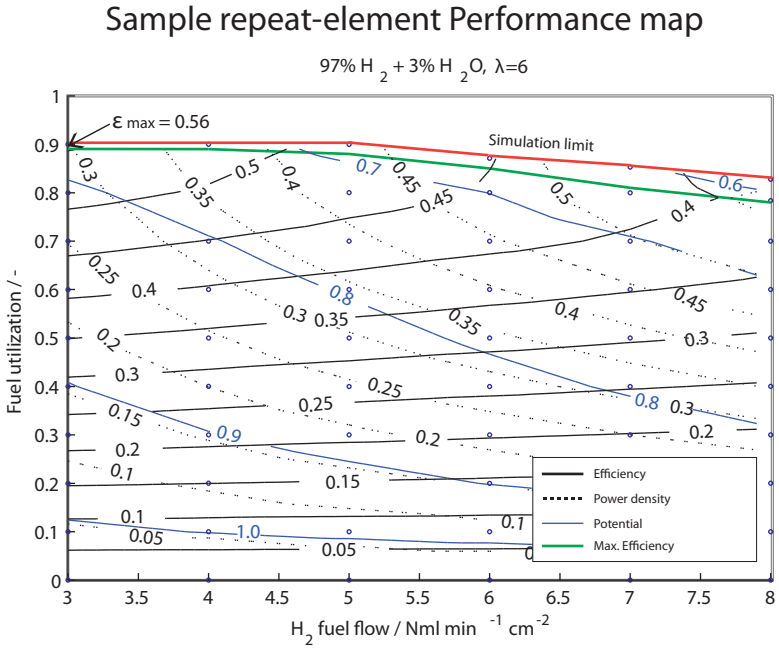

Figure 7.3: Simulated performance map of the generic repeat-element operated with humidified hydrogen ($\lambda = 6,\ T_{in} = 973K$).

the efficiency, power density and cell potential at different operating points. The green curve represents the optimal operating points in terms of efficiency. The red curve represents the simulation limit, where a decreasing potential doesn't provide any increase in current density any more.
At the minimal flux, the best efficiency of 56% is attained for a power density of 0.3 $\mathrm{W\,cm^{-2}}$, at a potential slightly below 0.8V. At the nominal fuel flow rate, a power density of 0.48 $\mathrm{W\,cm^{-2}}$ can be expected, increasing to 0.55 $\mathrm{W\,cm^{-2}}$ at the highest flow rate.
These simulations show that, for this fuel composition and these operating conditions, the type of cell for which an electrochemical model was established is able to provide efficiencies over 50% LHV at low fuel fluxes and reduced air inlet temperature, as well as a power modulation from 0,3 to 0,55 $\mathrm{W\,cm^{-2}}$.

7.2.3 Local electrochemistry

The detail of local electrochemistry is shown in Fig. 7.4 for a fuel utilization of 80% achieved at a nominal fuel flow rate of 6 $\mathrm{ml\,min^{-1}\,cm^{-2}}$ H_2 ($\lambda = 6$). On the cell, the temperature increases from 995K at the inlet to 1130K, resulting in a total difference of 135K which exceeds the targeted 100K difference [3]. This shows that the air excess factor of 6 is not sufficient to limit the fixed maximal temperature difference at high fuel utilizations. At the inlet, the cell's temperature is 22K higher than the inlet temperature of the gases, due to internal heat transfer.

While the gas composition on anode side varies to a large extent along the flow, the oxygen partial pressure presents only low variations due to the large air excess factor.
The Nernst potential decreases along the flow, from 1.1 V at the inlet to 0.86 V at the outlet. The resulting current density presents a maximum slightly after the half of the length of the element, with a maximal current density of 0.79 $\mathrm{A\,cm^{-2}}$. At the inlet and outlet, the current density is close to 0.5$\mathrm{A\,cm^{-2}}$. This spatial distribution originates from a combination of high overpotential and an area specific resistance close to its minimum at this location. Higher total ASRs are attained at the inlet (0.73 $\Omega\,\mathrm{cm^2}$) and outlet (0.31$\Omega\,\mathrm{cm^2}$). As the reactivity of the cathode is strongly thermally activated, the cathode ASR predominates at the inlet due to the low air temperature. At the outlet, it is the diffusion resistance on anode side which represents the major contribution to the losses due to a low hydrogen partial pressure (and high steam partial pressure). Finally, the ionic resistance represents only a minor part of the losses, with a slight decrease along the flow due to increasing temperatures.

As shown by the important losses at the inlet on cathode side, an increase in air inlet temperature would increase the overall efficiency of the repeat-element by decreasing the

[3] This temperature difference was chosen arbitrarily in design studies to limit excessive outlet temperatures to limit degradation (for ex. oxidation of materials) and risk of failure (temperature gradients), the minimum temperature being determined by the cathode's performance.

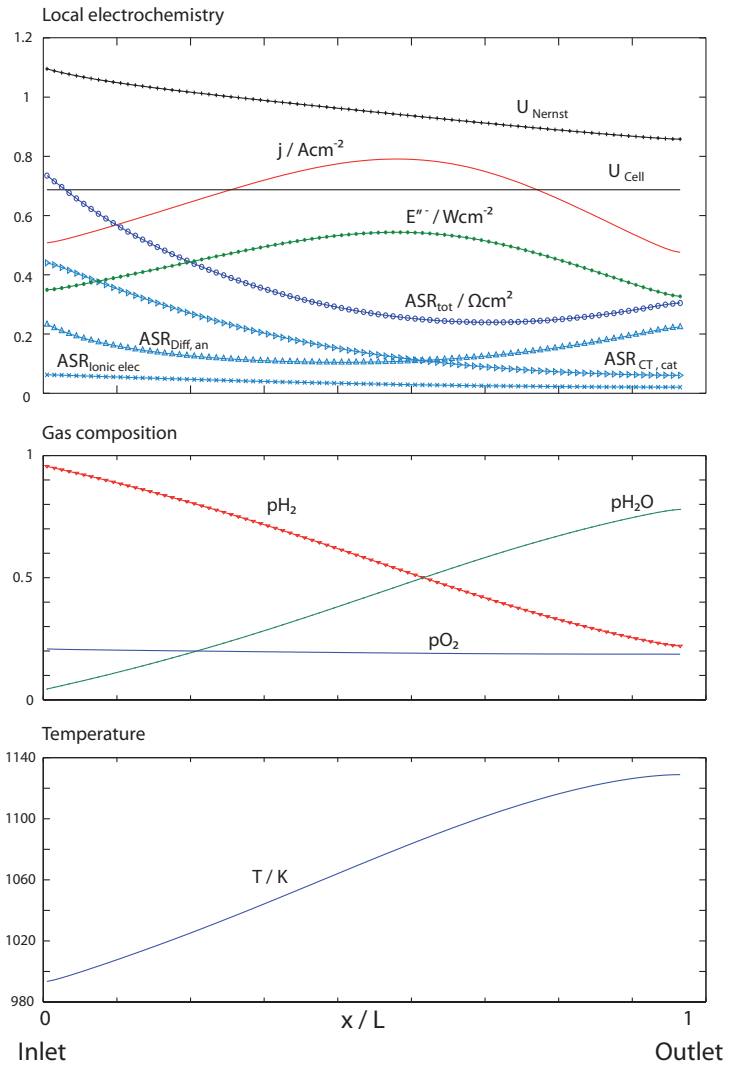

Figure 7.4: Local properties and local electrochemistry in the generic co-flow repeat-element, at a fuel utilization of 80%. (6 ml min^{-1} cm^{-2} H_2 , humidified, $\lambda = 6$

cathode overpotential, however at the price of a higher outlet temperature or of an increased air flow rate.

7.2.3.1 Nature of the operation limit

It is of interest to study the process leading to the operation limit of the repeat-element at high fuel utilization, as it is representative of the performance limiting phenomena in real stack designs. The transition from a high fuel utilization (80%) to the point where a limitation occurs is depicted in Fig. 7.5. The situation corresponds to the nominal fuel flow

rate of 6 $\mathrm{ml\,min^{-1}\,cm^{-2}}$ H_2 ($\lambda = 6$). For this fuel flow rate, an operation limit is expected at a fuel utilization close to 90%, as shown in Fig. 7.3.

From a fuel utilization of 80% to 87%, the point of maximal current density shifts towards

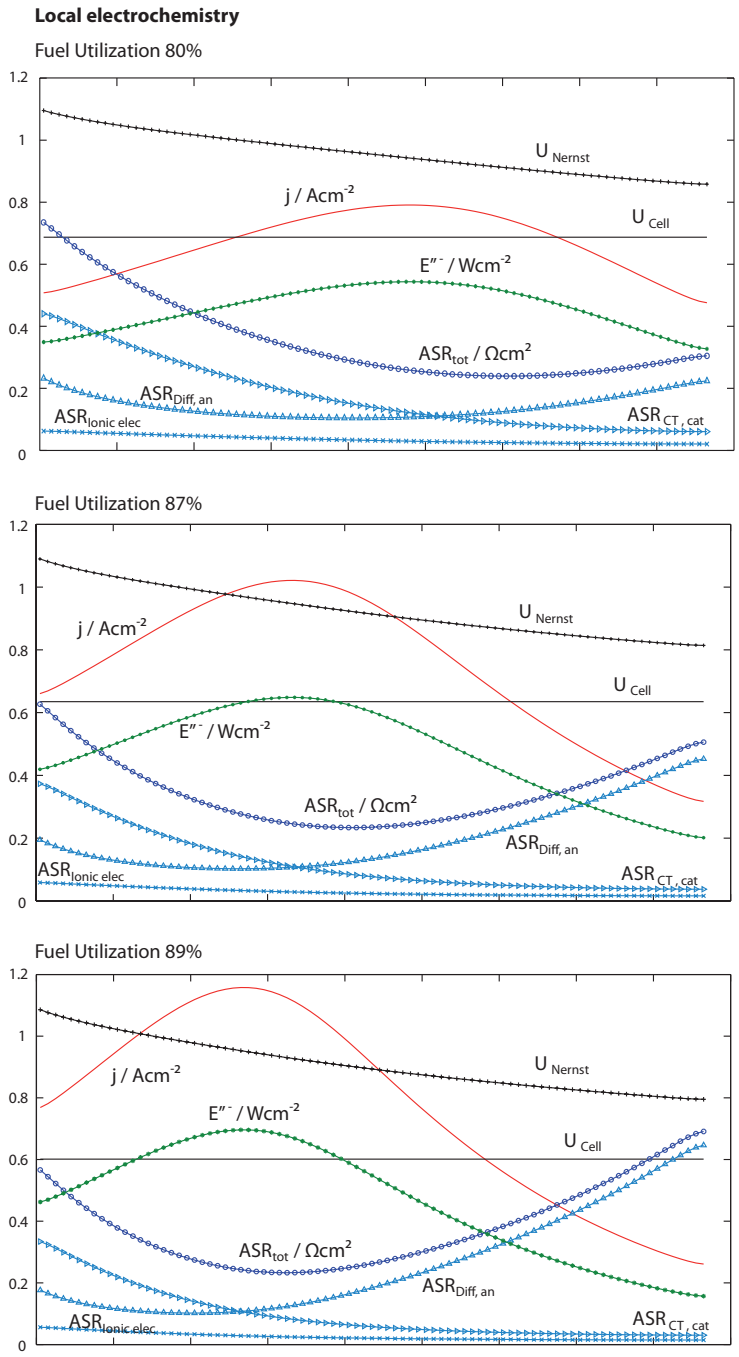

Figure 7.5: Evolution on local electrochemistry at increasing fuel utilizations approaching the limitation. (6 $\mathrm{ml\,min^{-1}\,cm^{-2}}$ H_2 , humidified, $\lambda = 6$

the inlet, with increasing maximal current densities (from 0.79 to 1.02A cm^{-2}). The cause of this shift is an increase of the anode diffusion ASR in the outlet region. At the outlet, the diffusion ASR varies from 0.22 to 0.45 $\Omega\,cm^2$. On the cathode side, the ASR remains relatively constant.
From 87% to 89% fuel utilization, the diffusion ASR increases again in important manner at the outlet, reaching 0.65 $\Omega\,cm^2$. In parallel, the current density profile changes in important manner, with a maximal current density reaching 1.16 A cm^{-2}.
At the operation limit, the current density tends to zero at the repeat-element's outlet, while the electrochemical reaction is ensured by the less depleted areas. Consequently, in the vicinity of the operation limit of the cell, an important balancing effect takes place between depleted and fuel-rich areas.

7.2.4 Dilute fuel mixtures

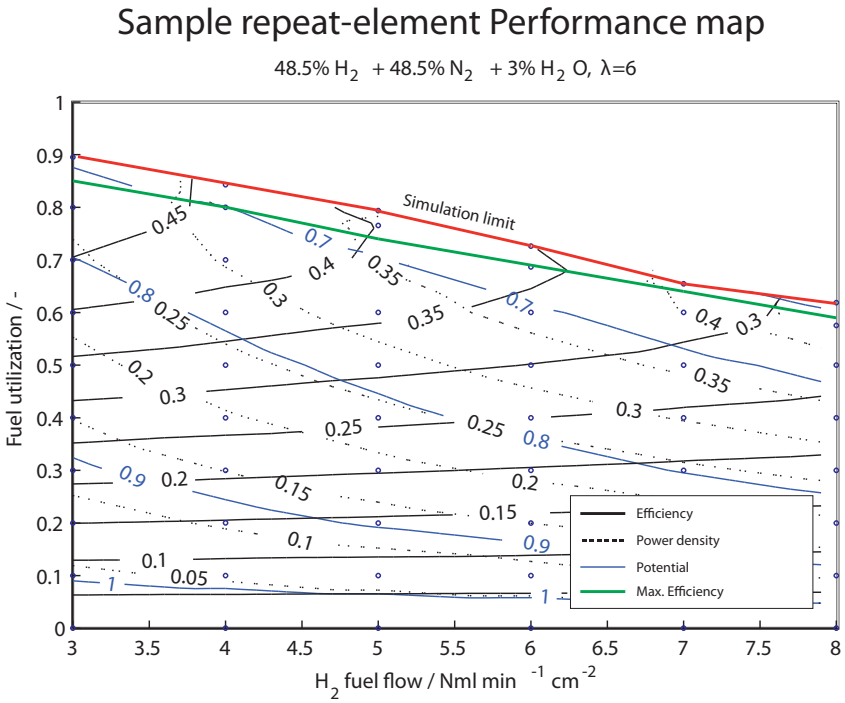

Figure 7.6: Simulated performance map of the generic repeat-element operated with dilute fuel.

If a dilute fuel mixture is used instead of pure hydrogen (humidified) for the generic repeat-element, the performance changes in an important manner, as shown in Fig. 7.6. For a 50%H_2 -50%N_2 mixture (humidified), the maximal achievable efficiency is 48% for a hydrogen flow rate of 3 ml $min^{-1}\,cm^{-2}$. This operating point is the only one where a fuel utilization of 90% is achievable. For increasing hydrogen flow rates, the highest fuel utilization diminishes, reaching only 63% at 8 ml $min^{-1}\,cm^{-2}$ H_2 . At the nominal flow rate, the maximal

efficiency is 35% LHV for a power density of 0.35 $W\,cm^{-2}$. Finally, at the maximal flux, efficiencies below 30% are expected. This result shows that a dilution of fuel on anode side has a significant impact on the performance, originating from the intrinsic properties of the cell.

7.3 Performance limitations of a R-design repeat-element

The performance and its limitations of the *R-design* repeat element were previously analyzed by Larrain [8] and Autissier [35], the first by using a repeat-element model written for the gPROMS equation solver, and the second using the first version of the present CFD model. The first simulation tool is based on a finite-difference discretization of space on a regular grid, hence permitting only a less accurate description of the repeat-element's geometry, a disadvantage that is shadowed out by the fast computation of simulations, hence allowing multi-criteria optimizations of the general flow distribution. The published studies concluded that an inadequate fuel distribution of fuel in the repeat-element explained the performance limitations of this particular stack design. The present study, benefitting from a more accurate electrochemical model and more detailed geometrical descriptions, points out additional limiting aspects. In addition, significant differences in the flow fields and in the resulting spatial distribution of electrochemistry are found when comparing the herein presented results with the ones obtained on simplified geometries (see references [8][35]).

7.3.1 Flow distribution and temperature fields

The *R-design* repeat-element is made of square cells of 50 cm^2 active area fed by internal gas manifolds of 10 mm diameter. Details of its construction can be found in section 3.4. The air GDL is 0.9 mm thick, while it is 0.5 mm on anode side. The thickness of the metallic interconnect is 1 mm. In the gas diffusion layers, a small channel is present on either side of the gas supply holes to distribute the gases to the repeat-element's sides (see Fig. 7.7).
For this study, and as it is usually done in CFD models, the seals are modeled as fully gas-tight solids. In fact, if the seal material presents a residual porosity, additional limitations of performance and reliability issues are found to occur, as demonstrated in the following chapters.
The resulting simulated flowfield is visible in Fig. 7.7, for a repeat-element operated with 6 $ml\,min^{-1}\,cm^{-2}$ H_2 at λ=6. The maximal velocities on the air side are one order of magnitude higher than the ones on the anode side. From the gas manifolds, the gases are distributed sideways through distribution channels. Behind the gas channels, the gas velocity is considerably reduced, reaching almost stagnant flow in the corners. Despite this situation, the cathode was screen-printed over the whole surface of the cell to maximize the active area (see Fig. 7.7), making poorly fed areas available for the electrochemical reaction.

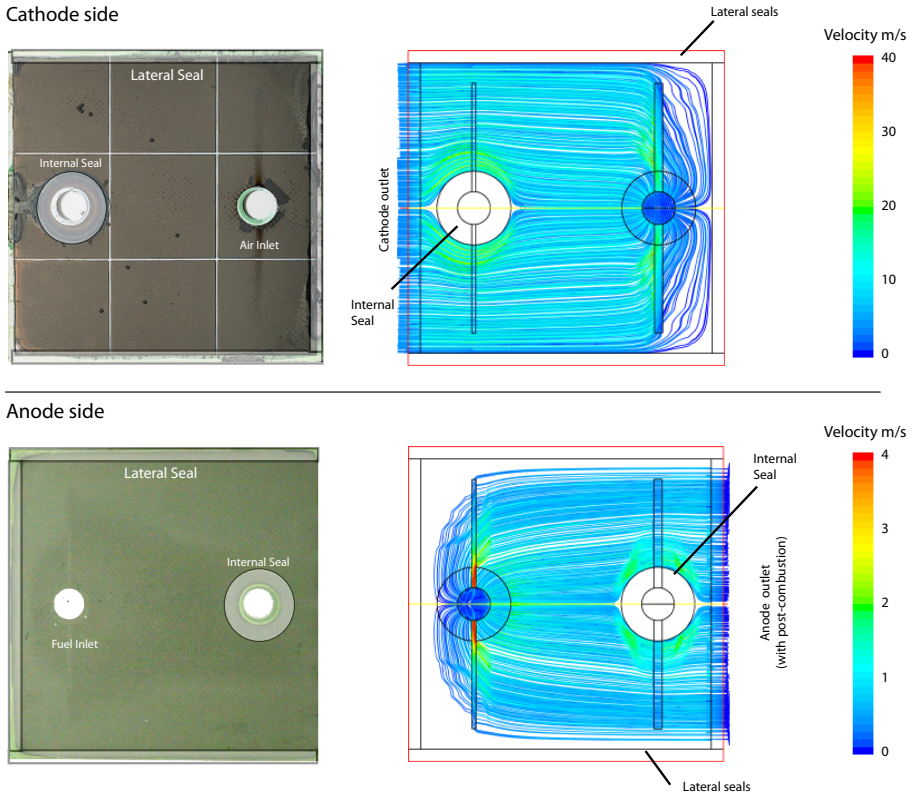

Figure 7.7: *R-design* cell with overprinted position of the seals, and simulated flowfield. 6 $ml\,min^{-1}\,cm^{-2}$ H_2 , λ=6

Concerning the thermal boundary conditions, the repeat-element is considered in an oven configuration operated at 750°C (see section 5.3.3), while no heat-exchange is allowed with adjacent repeat-elements to reproduce mid-stack conditions. The gas volume surrounding the stack is modeled, including a post-combustion zone in the vicinity of the repeat-element's outlet (Fig. 7.8). Free convection and buoyancy effects are considered in the surrounding volume, as visible in the upward direction of the post-combustion flame. For an operation at 60% fuel utilization, strong temperature elevations are predicted at the stack's outlet. In the post-combustion zone, temperatures over 1200K are attained in the gas phase, which increase at lower fuel utilizations.
The impact of the post-combustion zone on the internal temperature distribution is shown in the bottom part of figure 7.8. Despite an air inlet temperature of 973K, the minimum temperature on the active area is 1060K, due to an important heat transfer from the post-combustion zone (right-side of the element). An experimental validation of this situation is given by D. Larrain in [8]. Finally, it has to be noted that the elevated temperatures in the post-combustion area increase with an increasing number of repeat-elements due to proportionally lower heat exchange with the oven. Experiments with large stacks (max. 29 elements) showed important damages of these areas after operation.

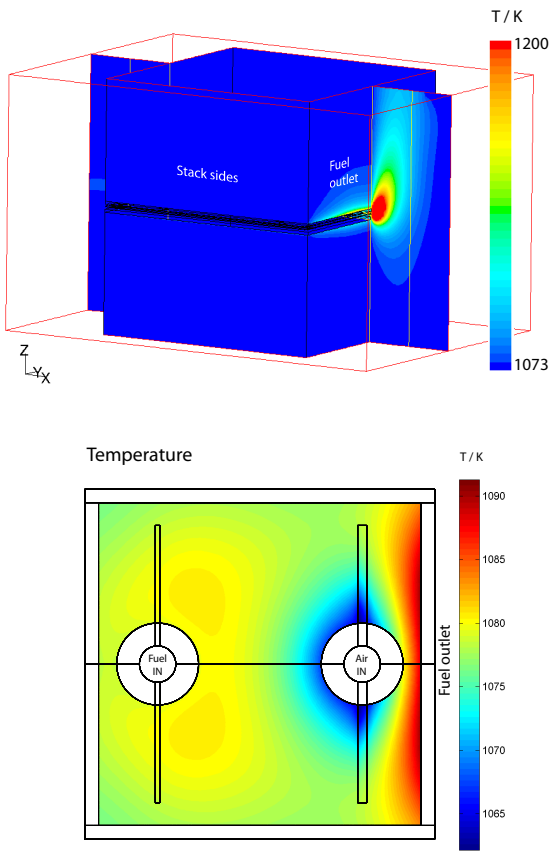

Figure 7.8: Bottom: Simulated temperature field in a *R-design* repeat-element with open post-combustion. Top: external temperature on stack walls and symmetry plane. 6 $\mathrm{ml\,min^{-1}\,cm^{-2}}$ H_2 , λ=6

7.3.2 Local properties and performance limitations

7.3.2.1 Performance map

To assess the intrinsic performance limitations of the *R-design* stack, a characterization is performed for the same conditions as the generic repeat-element (constant lambda $\lambda = 6$, gas inlet temperatures 973K, increasing fuel flow rates). The resulting i-V characterization is shown in Fig. 7.9, presented as function of the fuel utilization, and the corresponding performance map of the *R-design* stack can be found in figure 7.10.

Important differences can be observed between the obtained characteristic and the one of the generic repeat-element (see Fig. 7.2).

Similarly to the generic repeat-element, the maximum reachable fuel utilization decreases with increasing fuel flow rates, but the maximal achievable fuel utilizations are lower for fuel flow rates above 4 $\mathrm{ml\,min^{-1}\,cm^{-2}}$ H_2 . For the largest fuel flow rate, the maximum fuel

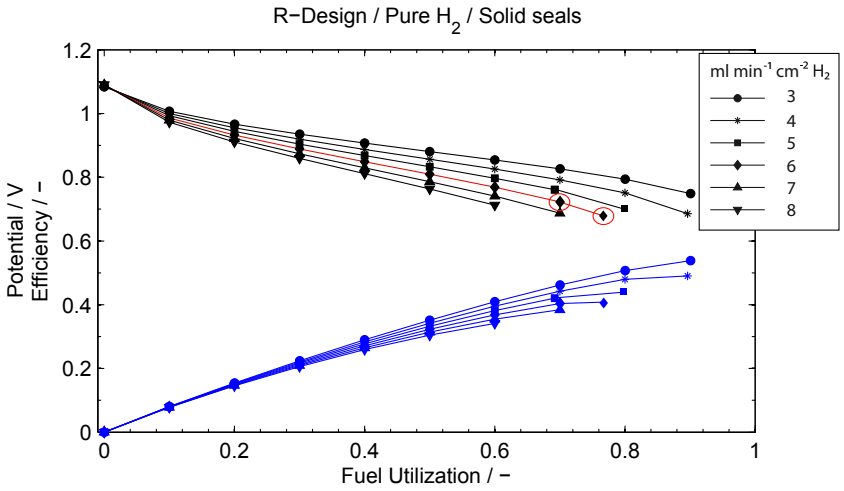

Figure 7.9: I-V characterization of the *R-design* stack ($\lambda = 6$, 97% H_2 + 3% H_2O).

utilization drops to 60%, while the generic repeat-element is limited at 80% FU.
At the lowest hydrogen flow rate, an efficiency of 54% is achievable, which is close to the 56% obtained with the generic repeat-element. At a nominal flow rate of $6\,\mathrm{ml\,min^{-1}\,cm^{-2}}$ H_2 , the maximal efficiencies are 41% for the *R-design* element and 45% for the generic repeat-element. Finally, more significant differences appear at higher fluxes, with respectively 31% and 39%.
These comparisons of performance based on the efficiency however suffer from a bias resulting from differences in the temperature fields. The higher temperatures in the R-Design stack, resulting from heat exchange with the oven (whose temperature is 50K higher than the entering air) and from heat transfer from the post-combustion area, result in lower losses in particular on the cathode side whose reactivity is strongly activated thermally.
Nevertheless, limitations induced by the design are attested by two facts. First, the maximum achievable fuel utilization is lower than in the generic repeat-element. And second, the line of maximum performance (green line in Fig. 7.10) coincides with the maximum feasible fuel utilization. This indicates that a potential would exist for higher efficiencies if no internal limitations would occur.

7.3.2.2 Local properties and limitations

To investigate the nature of the internal limitations, the local properties and resulting local electrochemistry are detailed. Figure 7.11 depicts the case obtained at 60% of fuel utilization for the nominal fuel flow rate, an operating point that immediately precedes the maximal feasible fuel utilization (the computation is made by steps of 10% FU). The local gas partial pressures are represented over the active area, as well as the local electrochemistry: Nernst

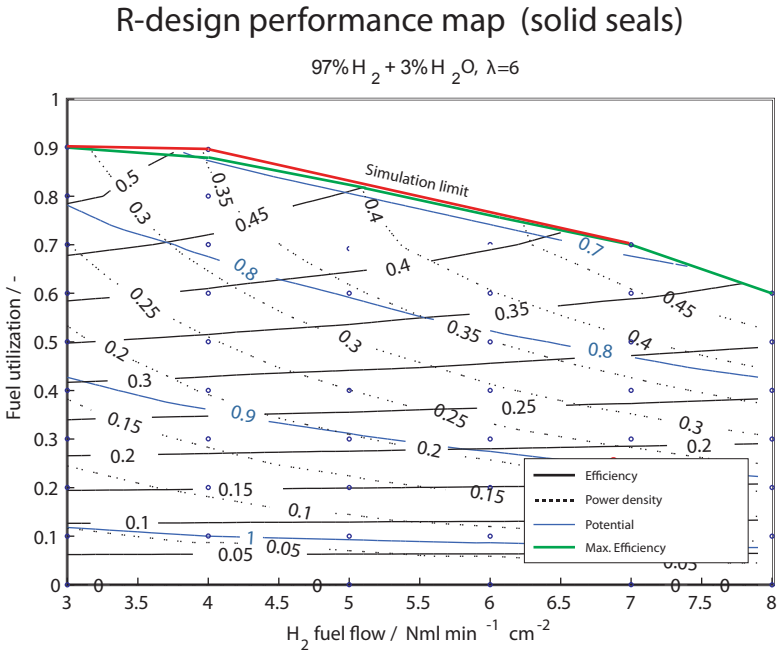

Figure 7.10: Deviations of performance between cells in a 6-element experiment.

potential, local overpotential, ASR, and resulting current and power densities. The corresponding local temperatures can be found in figure 7.8.

Gas distribution on the anode side On the anode side, the spatial distribution of gaseous species indicates a non-ideal distribution of fuel over the active area. First, despite a fuel utilization of 60%, the hydrogen mole fraction reaches a minimum of 5% in the corners behind the gas distribution channels, resulting from the previously described stagnation of gases at this location. Secondly, the profile of gas concentrations at the repeat-element's outlet are non-homogeneous. Steam mole fractions comprised between 52% and 88% can be found along the outlet's surface. In fact, as diffusion losses in the anode increase in important manner at high steam contents, it would be preferable to maintain -over the entire active area- the maximum steam partial pressure to values close to the ones dictated by the fuel utilization.
The poor distribution of fuel on the surface results on the one hand from the low efficiency of the lateral gas feeding channels which were under-dimensioned to distribute the fuel homogeneously, and on the other hand from the fact that part of the active area is located behind the distributor where convective mass transport is low. In addition the path length between fuel inlet and outlet differs along the different stream lines. This explains the important steam partial pressures along the repeat-element's sides in the vicinity of the outlet, as the path covered by the fuel is longer than for instance the one passing along the symmetry axis of the element.

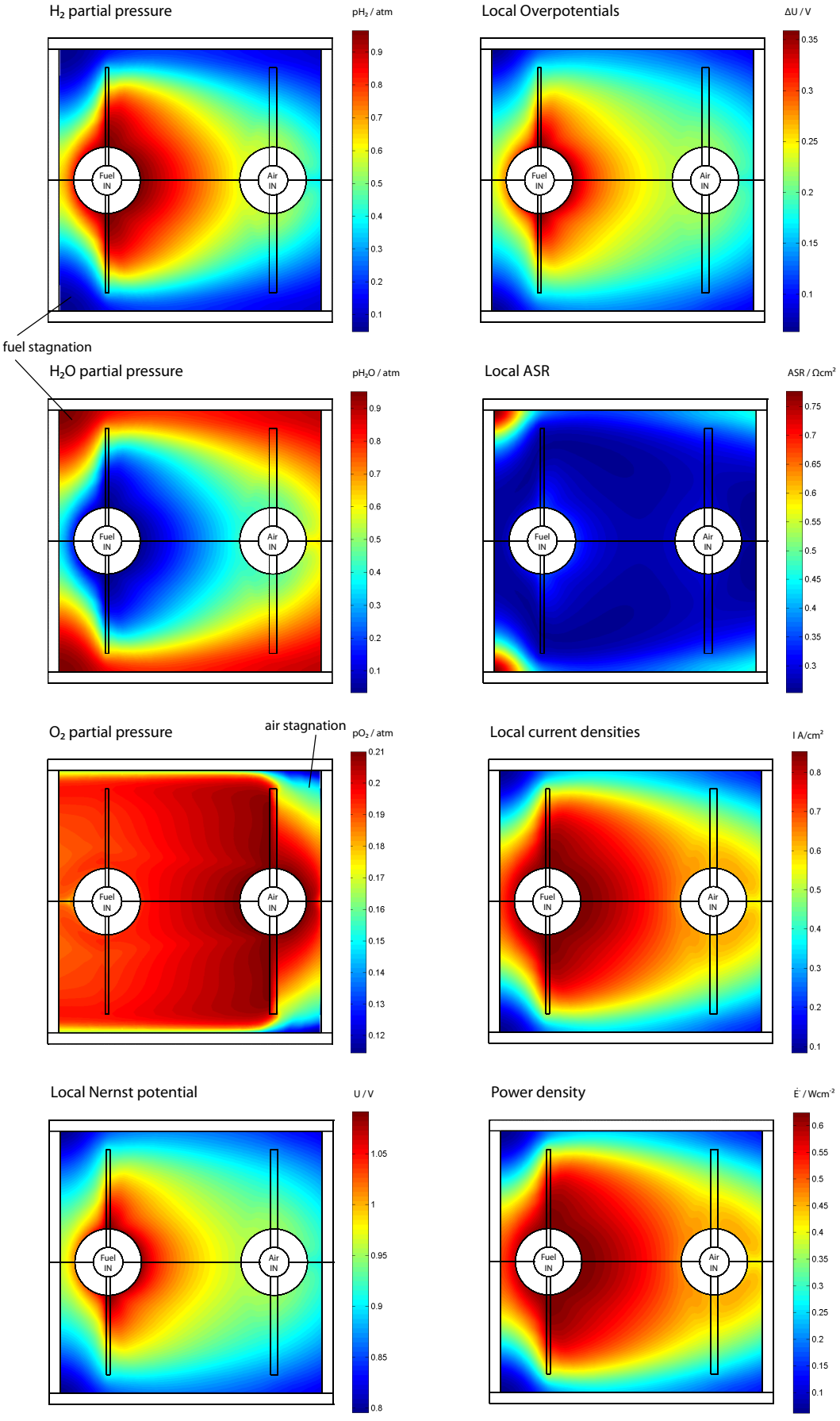

Figure 7.11: Simulated spatial distribution of local properties at 60% fuel utilization. (6 $\mathrm{ml\,min^{-1}\,cm^{-2}}$ H_2 , λ=6)

Gas distribution on the cathode side On the cathode side, the lateral air distribution ensures a sufficient supply with oxygen, but only downstream of the distribution line. In the corners, oxygen partial pressures of 0.12 atm are found, despite an air excess factor of 6.

More generally, the apparent depletion of reacting species in the regions where low convective flow occurs -despite a convective flow stream located a dozen of millimeters away- indicates that diffusive mass transport in the gases does not contribute significantly enough to compensate any inhomogeneity of the gas distribution.

Local electrochemistry The resulting distribution of the electrochemical reaction over the active area can be found on the right hand side of Fig. 7.11. The local Nernst potential decreases from 1.1 V at the inlet to a minimum of 0.8 V in the corners behind the fuel distribution line, due to the presence at this location of the minimum hydrogen partial pressure. The resulting local overpotential is of 0.06 V at this location, while maximal values of 0.36 V can be found in the vicinity of the fuel inlet [4].

The computed spatial distribution of ASR and resulting current densities show that a maximal reactivity is attained in direct vicinity of the fuel inlet, contrarily to the case of the generic repeat-element which is operated in a co-flow arrangement (see Fig. 7.4). The largest ASR are found in the corners behind the fuel distribution line, with values exceeding 0.75 $\Omega\,\mathrm{cm}^2$. More important, a strongly non-homogeneous distribution of current densities can be found across the flow in the vicinity of the repeat-element's outlet.

The detailed distribution of losses over the active area can be found in Fig. 7.12. The contribution of the cathode to the total ASR is strongly correlated with the temperature profiles, found in Fig. 7.8. The maximum cathode ASR is 0.16 $\Omega\,\mathrm{cm}^2$, found in the vicinity of the air inlet. On the other hand, the anode diffusion ASR represents the major contribution to the total ASR, with limiting areas found in the corners and along the sides of the repeat-element, where high steam partial pressures are found.

The spatial distribution of the resulting power dissipation differs strongly from the anode to the cathode side, as shown on the right side of Fig. 7.12. While the losses on cathode side present a spatial distribution close to the one of the current density, with a highest power dissipation of 0.11 $\mathrm{W\,cm}^{-2}$, the dissipated power on anode side concentrates in the vicinity of the fuel inlet. In the corners, where the anode diffusion ASR is high, the power dissipation is low due to low current densities. The highest power dissipation can be found on anode side, attaining 0.17 $\mathrm{W\,cm}^{-2}$.

[4] This observation can be of interest for post-experiment analyses in degradation studies, as large overpotentials are known to possibly accelerate the degradation of performance [45]. Simulation can in this case help to determine the affected areas.

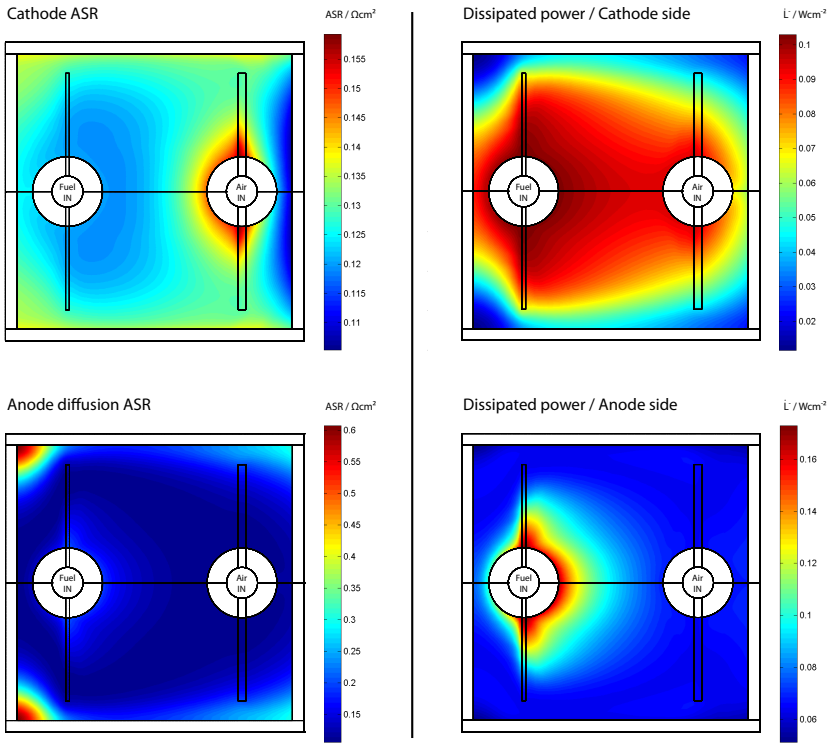

Figure 7.12: Detail of anode-related and cathode-related ASR and associated dissipated power. (60% FU, 6 $\mathrm{ml\,min^{-1}\,cm^{-2}}$ H_2 , λ=6)

Detail of the operation limit As shown in the performance map of the *R-design* stack, an operation limit is found above 70% of fuel utilization at the nominal fuel flow rate. The evolution of local electrochemistry between 60% and 70% fuel utilization is shown in Figure 7.13, giving insight in the limiting process.
From 60% to 70% fuel utilization, the minimal hydrogen mole fraction reduces from 5% to virtually zero in the corners and along the sides in the vicinity of the outlet, which could lead to severe degradation issues of the anode due to local reoxidation. The comparison of total and anode diffusion ASR allows, as expected, to identify the anode contribution as predominant. While at 60% fuel utilization the diffusion losses present values above $0.35\Omega\,\mathrm{cm^2}$ in the corners only, the situation changes dramatically at 70% FU where high diffusion ASRs are also found along the sides. Both situations are represented with the same color scale for comparison, whereas the maximum diffusion ASR at 70% FU largely exceeds the maximal value of $0.6\ \Omega\,\mathrm{cm^2}$ of the color scale.
More important, the model predicts diffusion limiting areas in the corners and along the sides (overprinted with semi-transparent white color), that is, areas where the electrochemical reaction has to be disabled due to an hydrogen partial pressures tending to zero at the electrolyte [5].

[5]This type of limitation can cause important convergence issues in the model, requiring appropriate under-relaxation to converge to a solution

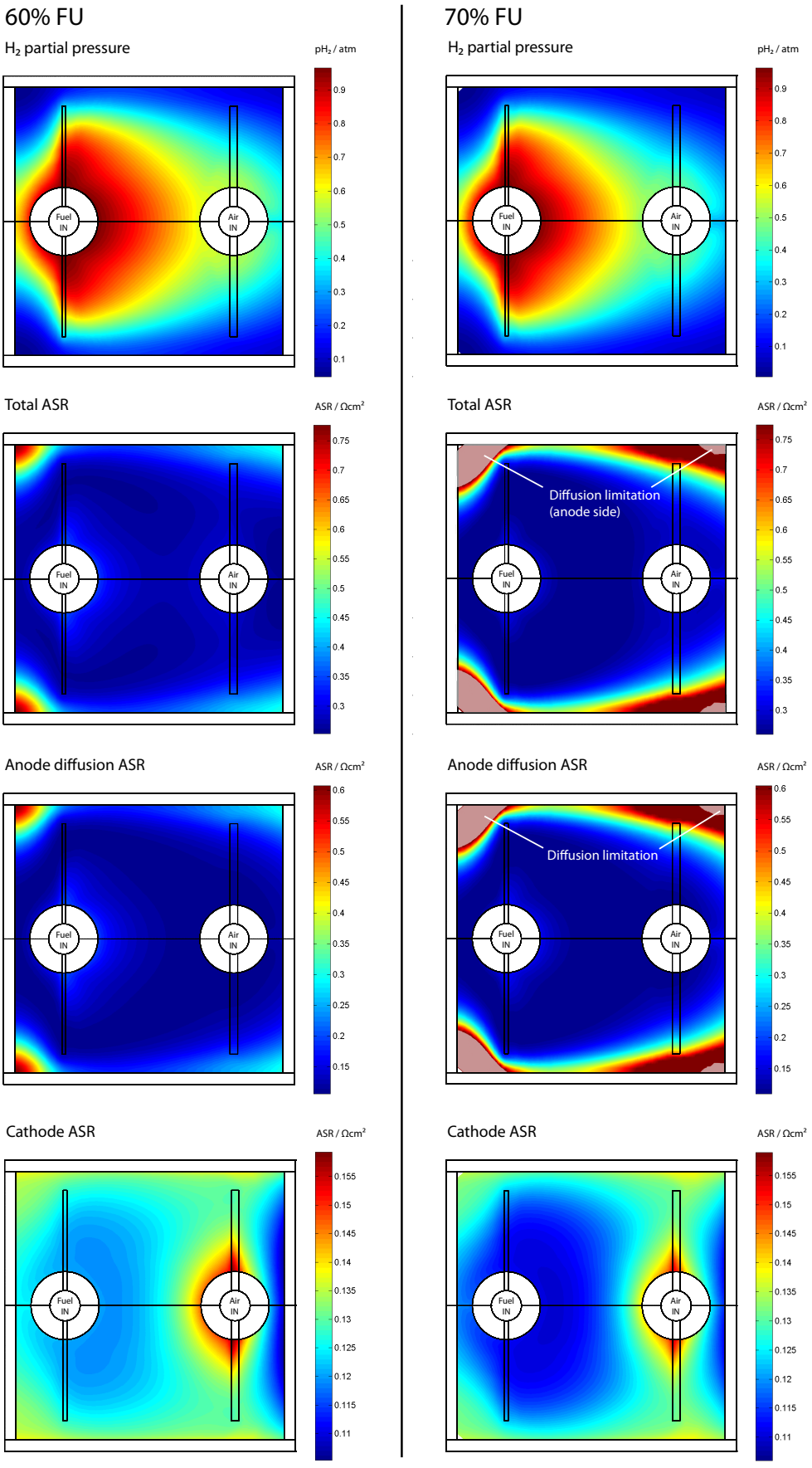

Figure 7.13: Apparition of limitations under increasing polarization from 60% to 70% FU. (6 $\mathrm{ml\,min^{-1}\,cm^{-2}}$ H_2 , λ=6)

As shown in Fig. 7.10, it is at 70% fuel utilization that the maximum efficiency can be reached, for this fuel flow rate and composition. However, this operating point has to be avoided due to the important risk of reoxidation of the anode support caused by the local depletion of reducing species.
Therefore, it has to be concluded that poor distribution of gases lead not only to lower performances due to increased losses, but also to a restriction of the operating domain due to a risk of damage for the components.

7.3.3 Summary

Simulations made on the *R-design* prototype show that the design of the stack plays an important role in the achievable performance. In particular, the operation domain is limited by the apparition of local limiting areas in the fuel cell, which not only modify the distribution of the reaction and the losses over the active area, but also lead to severe degradation and failure.
The cause of limitations is found in a non-ideal distribution of gases, where on the one hand stagnation of gases, and on the other one different flow path lengths lead to fuel depleted areas. Moreover, the model shows that only convective mass transport can ensure an adequate distribution of gases, the diffusion fluxes being not important enough to provide a sufficient distribution of reactive species.
The comparison with a generic repeat-element, despite its limitations in terms of equivalent temperature distributions, offers therefore valuable information about the achievable performance when gas distribution issues are avoided.
From a modeling point of view, the results show the interest of an electrochemical model able to predict diffusion limitations in the anode support, as these determine to a large extent the operation domain of a specific stack design.

7.4 Development of optimized designs

7.4.1 Introduction

Despite the modeled capability of the *R-design* prototype to reach efficiencies over 50% LHV at low power densities, the stack suffered from additional limitations such as the absence of fuel recovery for system integration, and, more important, from severe degradation issues and failures related to the open post-combustion and, as shown later, to construction issues inducing severe degradation of the cells. In addition, up to 100 tests on repeat-elements and short-stacks were performed without achieving the predicted efficiencies. The best ever attained electrical efficiency was 39%.

These limitations led to the development of a new prototype of equivalent active area, started in 2004. This stack was developed in a joint effort, combining the herein presented tools in addition to the modeling tools developed by Larrain and Autissier. The resulting *S-design* stack was developed with a specific focus on adequate fuel distribution and system integration in a HoTbox^{TM} , a high temperature enclosure including the stack and its thermal insulation, a C-POX reformer, a post-combustor and a high-temperature heat exchanger.
In a second iteration, the *F-design* stack was designed to reach 2.5 kW_{el} range, based on an analysis of the limitations of the *S-design* stack, however less in terms of performance than in terms of reliability.

7.4.2 The S-design stack

The *S-design* stack is based on oblong cells of 50 cm^2 active area, including two holes for fuel supply and recovery. Details of its construction can be found in paragraph 3.4 p.55. Air and fuel are supplied in parallel direction (co-flow arrangement), resulting as mentioned above from a compromise between performance and reduced temperature gradients (see Larrain in [8]). The resulting arrangement of the flows in the repeat-element is described in Fig. 7.14.

The designed geometry is a compromise between improved gas distributions, as promoted from modeling work, and design constraints originating from production issues or from geometric constraints resulting from the integration in the HoTbox^{TM} . An in-line arrangement of the gas manifolds was chosen, with internal manifolds for the fuel requiring holes in the cells. Air is provided to the stack by external manifolds.

On the fuel side, non-active distribution and collection areas were placed around the fuel manifolds to ensure proper lateral distribution of the fuel, and this without consumption

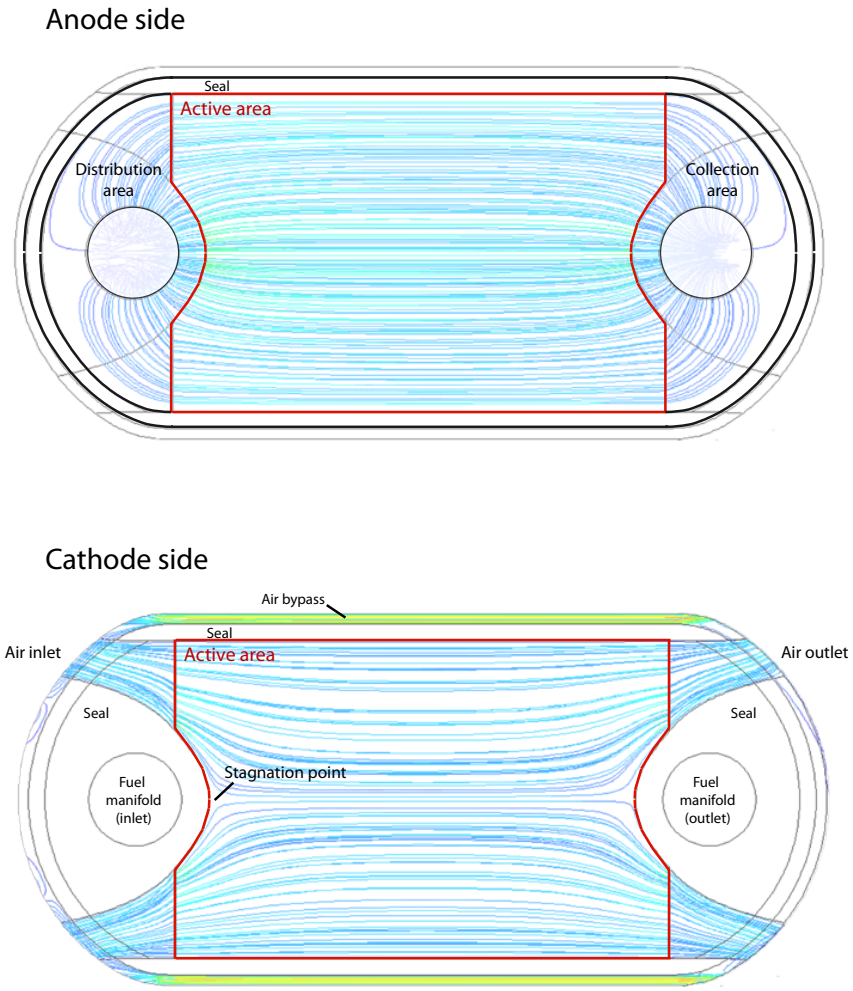

Figure 7.14: Flow distribution in a *S-design* repeat-element.

of species to avoid limitations caused by different flow path lengths. A rounded shape was chosen for the repeat-element, avoiding any 'corner' where stagnation of gases could occur. Due to geometric constraints, the fuel manifolds could not be placed far enough from each other to obtain a completely rectangular active area, whose actual shape is depicted by a red line on figure 7.14. As a consequence, the active area is shorter on the symmetry axis of the repeat-element.

Additional compromises were made in terms of gas distribution, raising from the alignment of fuel manifolds along the symmetry axis and their placement close to the active area. In particular, a difficulty appeared to provide air by convection downstream of the inlet fuel manifold, leading locally to lower air supply.

7.4.2.1 Predicted performance map

The performance map obtained for the same conditions as for the *R-design* stack is shown in Fig. 7.15. Contrarily to the *R-design* stack, the operation limit is comprised between 80% and 90% of fuel utilization over the complete operation domain, approaching the situation of the generic repeat-element operated in the same configuration. More important, the points of highest efficiency (green line) are attained at fuel utilizations that are lower than the operation limit, contrarily to the case of the *R-design* prototype.

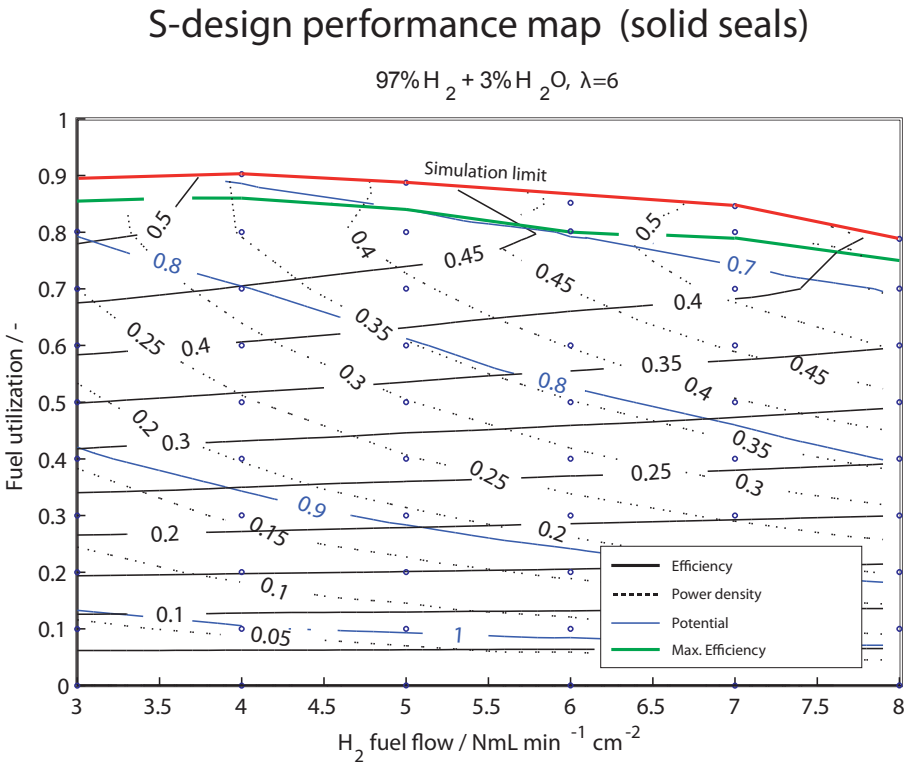

Figure 7.15: Simulated performance map of the *S-design* stack.

At the lowest fuel flow rate, a maximum efficiency of 53% is expected for a maximum fuel utilization of 89%, which is slightly lower than the 56% of efficiency attained with the generic repeat-element (see Fig. 7.3). For fuel flow rates larger than $3\,\mathrm{ml\,min^{-1}\,cm^{-2}}$ H_2 (humidified), the performance becomes similar to the one of the generic repeat-element. At the nominal fuel flow rate, a maximum efficiency of 44% is reached at 80% of fuel utilization, slightly lower than the 45% of efficiency of the generic repeat-element under the same conditions. Finally, at the maximal fuel flow rate, a maximum efficiency of 38% is achieved at a maximum power density of $0.55\,\mathrm{W\,cm^{-2}}$, similarly to the generic element.

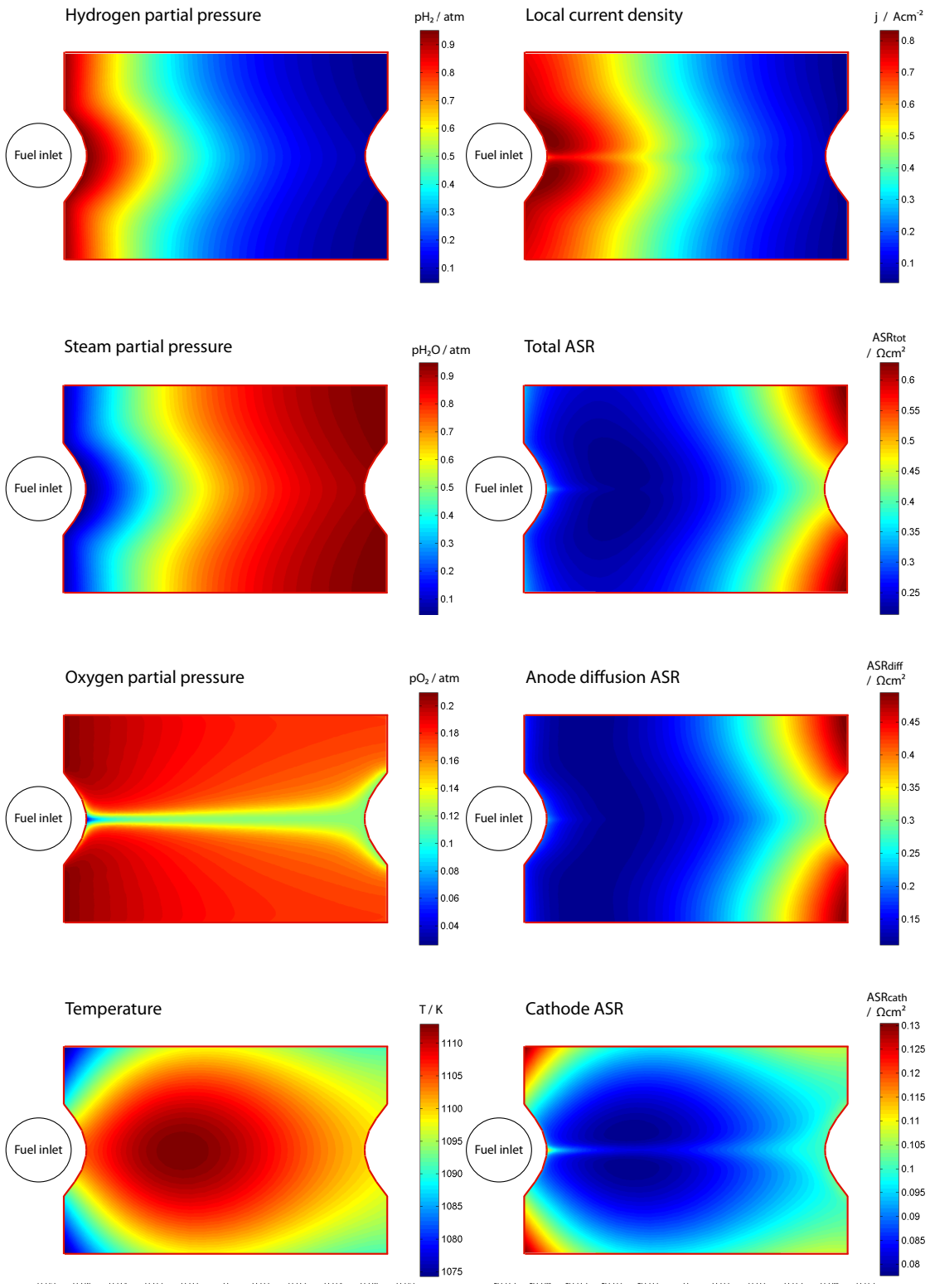

Figure 7.16: Local properties in a *S-design* prototype operated with a reduced fuel flow rate at 88% fuel utilization (3 $\mathrm{ml\,min^{-1}\,cm^{-2}}$ H_2 humidified, $\lambda = 6$).

7.4.2.2 Internal limitations

The local properties leading to the operation limit at the lowest fuel flow rate are depicted in figure 7.16. The considered fuel utilization is 88%, which just precedes the operation limit.

Distribution of gases Contrarily to the *R-design* case, the gaseous species on the anode side are distributed homogeneously over the entire width of the active area. Moreover, the fuel compositions along the entry region of the active area is almost constant, showing that the non-active inlet distribution area (see Fig. 7.14) fulfills its requirements.

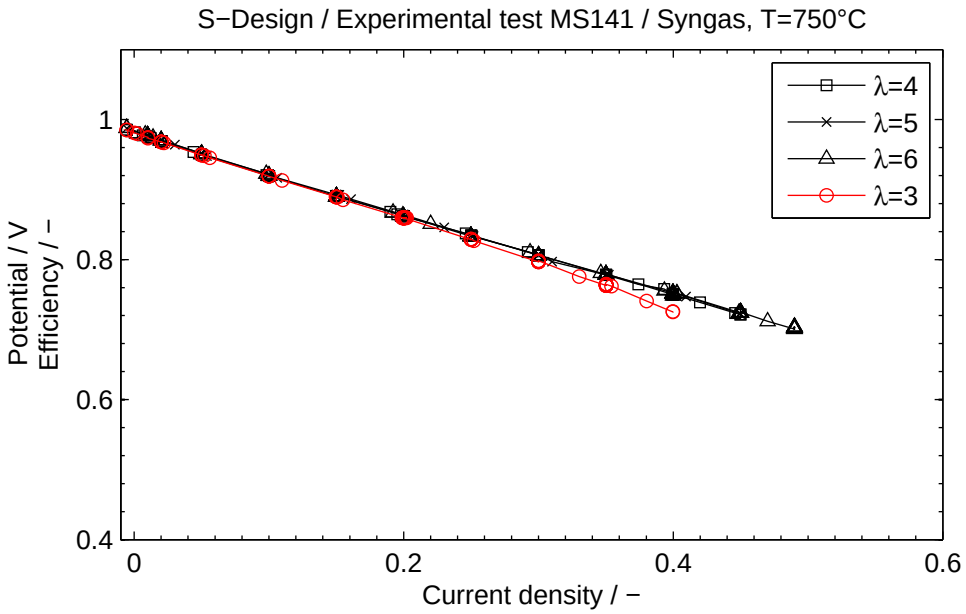

Figure 7.17: Effect of the air flow rate on the performance of a *S-design* repeat-element (Test MS141).

The contrary is true on the cathode side, as indicated by the spatial distribution of oxygen over the active area. The low convective mass transport of air behind the inlet's fuel manifold (see Fig. 7.14) leads to a depletion of oxygen at this place, a situation that is worsened by the high reactivity of this region due to high overpotentials and moderate ASRs. The result is the presence of local oxygen partial pressures as low as 0.05 atm. As attested by the local cathode ASR and local current densities, the relative impact on the performance is limited. However, in a degradation study, Hagen et al. showed that certain cathode types (LSM-YSZ in this case) experience more pronounced degradation under low oxygen partial pressures

than under air or oxygen [68]. For this reason, oxygen depleted areas should preferably be avoided.

More important, the oxygen depleted region expands downstream of the air stagnation point, which again demonstrates the low contribution of diffusion to the mass transfer in the repeat-element. Again, this situation points out the negative effect of inadequate gas distribution on performance or possible degradation.

The reality of this air distribution problem was confirmed experimentally in a single-repeat element test operated with syngas as fuel. An anode-supported cell was used, on which a LSM-YSZ cathode was screen-printed. Successive I-V characterizations were performed under constant conditions, and at increasing air excess factors. The resulting characterization is shown in Fig. 7.17. For air excess factors comprised between $\lambda = 4$ and $\lambda = 6$, no difference was observed among the different curves. The contrary was true at a lambda of 3, where a net decrease in performance was observed above a current density of $0.2\mathrm{A\,cm^{-2}}$.

Operation limit At 88% fuel utilization, the contribution of the anode diffusion ASR to the total ASR is again predominant. The largest ASR are attained sideways on the outlet surface of the active area. They result from slightly higher partial pressures of steam along the sides of the repeat-element where the active area is longer. This result shows again that a homogeneous length of the reaction zone represents the best option to reach high efficiencies.

7.4.3 The F-design stack

The development of the *F-design* stack was started in 2006 in the frame of the FP6 European Project *FlameSOFC*, with the goal to develop a 2.5 kW_{el} CHP system based on a SOFC stack coupled to a T-POX[6] reformer. Based on the experience on the *S-design* prototype, a new stack concept was developed in the frame of this thesis. The main priorities in the development of this stack were:

- to improve the gas flow field of the *S-design* stack by avoiding any stagnation of air and by imposing an active area of constant length
- to increase the active area by a factor of 4 to limit the number of cells required to achieve a power output of 2.5 kW_{el}
- and, more important, to solve an important source of failure inherent to the stack construction for the *R-design* and *S-design* prototypes (see next chapter).

The constraints were a nominal electrical power output of 2.5 kW_{el}, an operation under lean fuel mixtures due to the use of a T-POX reformer, a maximum of 500 W of thermal losses through the insulation of the stack, maximal pressure drops on air and cathode side limited to 20 mbar, and finally the ability to modulate the power output down to 1/3 of the nominal power. Due to the low thermal losses through the insulation, the entire cooling of the stack had to be performed by the cathode air stream, which required a maximal air excess factor of 8 to limit internal temperature differences.
Additional constraints were a targeted lifetime of 30'000 hours and limited costs. The first objective remains challenging for any planar SOFC stack, requiring deep knowledge of degradation processes and their link to the stack design, a task which is addressed later in this work. The targeted lifetimes, the cost targets and the constraints in terms of thermal losses lead to the design of highly integrated components coupling several functions: current collection, mechanical loading and gas supply to the stack. A view of the stack in its insulation is shown in Fig. 3.11.

7.4.3.1 Gas distribution

The internal gas distribution in the *F-design* prototype is shown in Fig. 7.18. The fuel enters the repeat-element from manifolds disposed along the sides of the stack. Similarly to the *S-design* stack, non-active distribution and collection areas are placed at the entry and outlet of the active area (depicted by a red line). The distribution areas are dimensioned to limit inhomogeneities in the flow distribution. A seal of large width is disposed on the sides

[6]Thermal Partial OXidation reformer.

of the element, limiting any leakage of fuel when compressive seal materials are used which present a residual porosity. On the cathode side, the air enters and leaves the stack from the sides, supplied and collected by external external manifolds.
The rectangular active area presents a surface of 200cm^2 , with an aspect ratio of 1.5. The gas diffusion layers are made of SOFConnex^{TM} , ensuring contact and gas distribution between the cell and the interconnects.

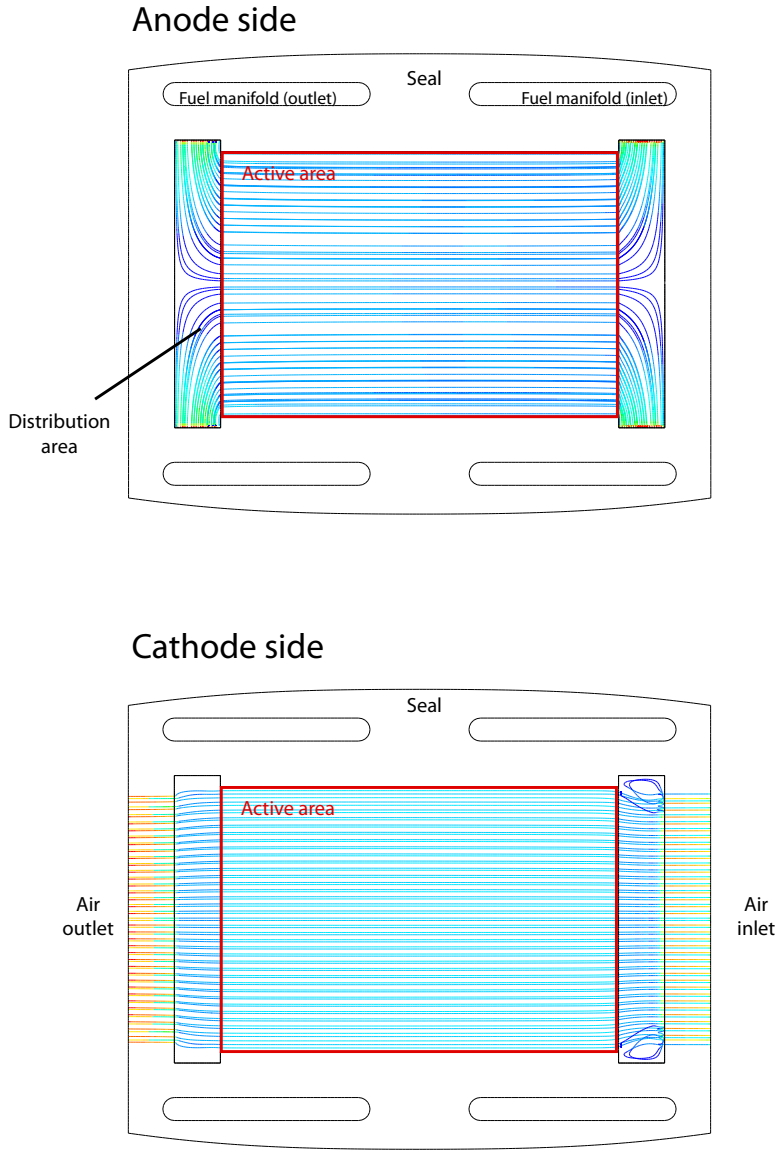

Figure 7.18: Gas distribution in a *F-design* repeat-element.

7.4.3.2 Performance

The homogeneity of the gas distribution over the active area is attested by the gas composition and current density profiles obtained on the active area, as shown in Fig. 7.19. For a fuel utilization of 90% attained at a nominal fuel flow rate of 6 $\mathrm{ml\,min^{-1}\,cm^{-2}}$ H_2

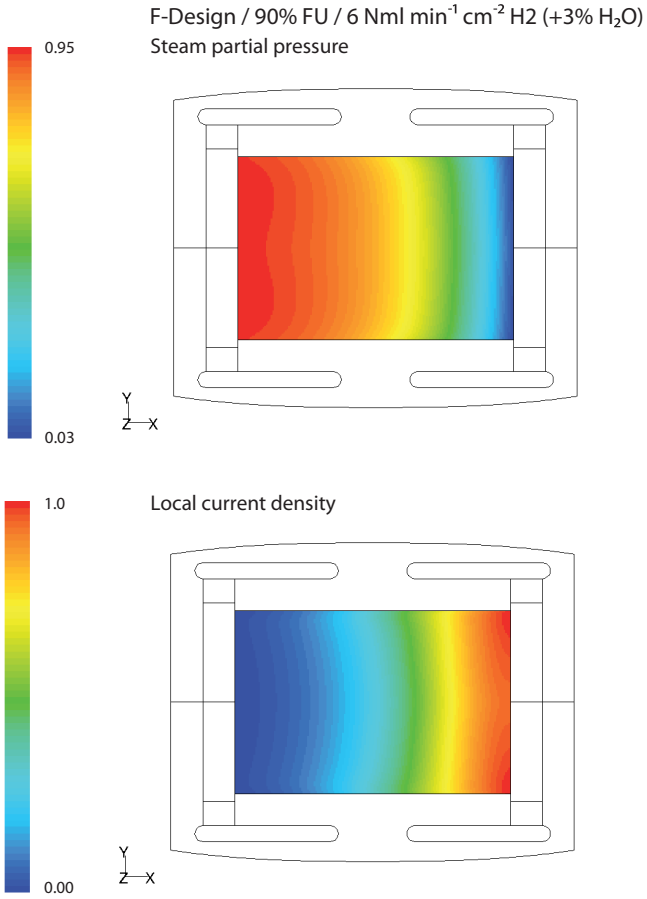

Figure 7.19: Gas composition profiles and current density profiles in a *F-design* repeat-element operated at 90% FU.

(humidified), the resulting profile of steam partial pressure is almost homogeneous over the entire width of the element. With an inlet steam partial pressure of 0.03 atm and a maximal steam partial pressure of 0.95 atm along the outlet of the active area, the extent of the flow deviation is minimal. The resulting current density profile follows the same trend, with a maximal current density of $1.0\,\mathrm{A\,cm^{-2}}$ found on the lateral sides of the active area's inlet. On the cathode side, the homogeneity of the gas stream is obvious due to the construction of the element.
These results show that the *F-design* prototype approaches the situation of the generic repeat-element with homogeneous gas distribution.
The resulting performance map is shown in Fig. 7.20. Over the complete operation do-

main, the performance is very close to the one of the generic repeat-element. The operation limit is comprised between 83% and 90% of fuel utilization, with highest values below 6 $\mathrm{ml\,min^{-1}\,cm^{-2}}$ H_2 and a decrease to 83% FU at 8 $\mathrm{ml\,min^{-1}\,cm^{-2}}$ H_2 . At the lowest fuel flow rate, a maximum electrical efficiency of 55% is attained, nearly equal to the one of the generic element (56%). At the highest fuel flow rate, the respective efficiencies are 40% and 39%.

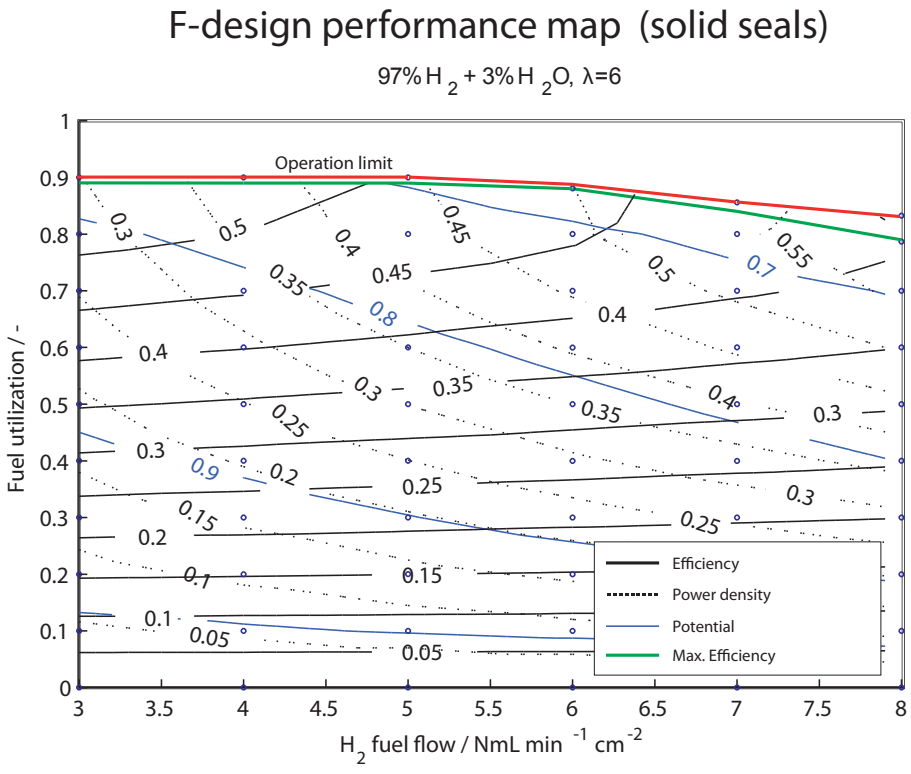

Figure 7.20: Performance map of the *F-design* stack operated under pure (humidified) hydrogen. ($\lambda = 6,\ T_{in} = 973K$)

Therefore, it is shown that the *F-design* approaches the situation of an ideal gas distribution, where the properties of the cell and the operating conditions become the limiting factor in terms of performance.

7.5 Limitations introduced by stacking and production tolerances

As shown in the previous paragraphs, the highest efficiencies are attained at fuel utilizations close to the point where the cell becomes limiting due to diffusion losses on anode side.

In real stacks however, deviations of the distributed fuel occur, resulting on the one hand from production tolerances determining the pressure losses through an element, and on the other hand from pressure drops in the fuel manifolds which may induce significant differences across the height of a stack.
These differences in supplied fuel lead to effective fuel utilizations that differ from the nominal one with, as consequence, the apparition of limitations in the less fueled elements. As shown on the i-V characterizations of the *R-design* stack however (Fig. 7.9), the limitation is not necessarily accompanied by an evident drop of cell potential which could be monitored. This type of situation can therefore represent an important risk of cell damage without direct evidence of its cause.
This situation has been mentioned by different authors and will therefore not be detailed here. However, it is worth mentioning that one key of the successful operation of large stacks was first the implementation of large fuel manifolds in the *S-design* and *F-design* stacks, and second the introduction of strict quality control procedures to verify the nominal flow rates of the repeat-elements under constant pressure drops [113].

7.6 Experimental validation

As mentioned above, the *R-design* stack was limited to efficiencies below 40% in repeat-element configurations, with even lower values attained in stacks due to the presence of limiting elements [114]. In addition, difficulties appeared when attempting to reach fuel utlizations above 60%, with frequent failures of cells under such conditions.
The experimental results that best illustrate the capability of the designed stacks to reach high efficiencies as well as high power outputs were obtained recently (2008-2009), after several years of developments on the production and assembly. Moreover, it was not possible to obtain a strict correspondence of the model and of the experimental conditions, due to repeated changes in electrode compositions, cell suppliers, assembly procedures and testing conditions. Finally, one core issue had to be solved concerning the sealing of the stacks, which has a significant impact on performance, as shown in the next chapter.

7.6.1 Performance of the *S-design* prototype

7.6.1.1 High efficiencies

To investigate the maximal efficiency of a *S-design* stack, series of i-V characterizations were performed on a 6-element stack in SOFCpower's facilities. The cells were anode-supported cells of 0.5 mm thickness, made of a classical Ni-YSZ cermet. The electrolyte was made of 5 μm thick YSZ. On cathode side, a LSCF cathode with LSCF current collection layer was screen-printed on top of a YDC barrier layer. This configuration is close to the one of the

cell used for the determination of the electrochemical model.
The stack was mounted in a high-temperature oven, pressed between two metallic flanges ensuring a mechanical load of 0.6 $kgcm^{-2}$. The stack was reduced at 800°C and polarized under a constant fuel mixture of 97% H_2 + 3% H_2O . The air excess factor was fixed at $\lambda = 4.2$. The stack was characterized for an oven temperature of 750°C and 800°C , with respective air inlet temperatures of 720 and 775 °C.

The result of a characterization at 750°C under increasing fuel flow rate is shown in figure 7.21, together with simulation results obtained for the same conditions. The simulation results are represented in red, with empty markers.
At a fuel flow rate of 3 $ml\,min^{-1}\,cm^{-2}$ H_2 , the best efficiency was 51%, obtained at a fuel

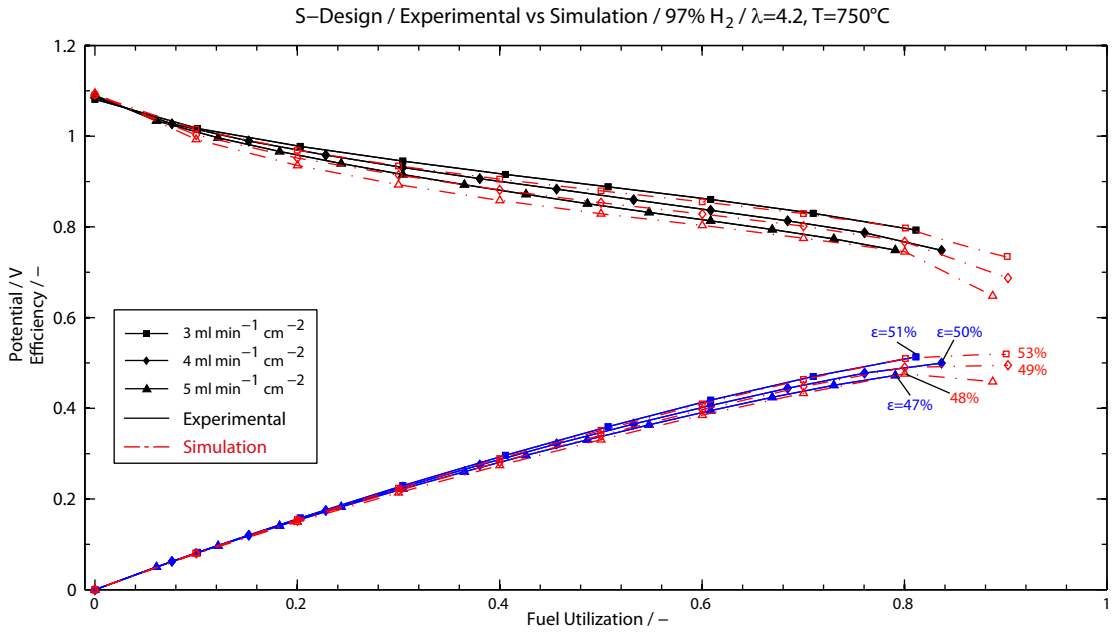

Figure 7.21: Comparison of experimental and simulation results (red lines, empty markers) for a *S-design* short stack (6 elements). $\lambda = 4.2$, $T_{gas,in} = 973K$, $T_{oven} = 1023K$

utilization of 81%. The corresponding simulated value is an efficiency of 53% attained at 88% FU. For increasing fuel flow rates (4 and 5 $ml\,min^{-1}\,cm^{-2}$ H_2) the maximal efficiency diminishes to 50% and 47% of efficiency (respectively 49% and 48% in the simulation). The highest fuel utilization attained experimentally is 84%.
These values are obtained for the complete 6-element stack. Therefore, it represents an average value over the cells, avoiding biases due to differences in effective fuel flow rates among elements. The differences among the cells during the characterization at 4 $ml\,min^{-1}\,cm^{-2}$ H_2 are shown in Fig. 7.22.

Below a fuel utilization of 60%, the difference in potential among the cells is limited to

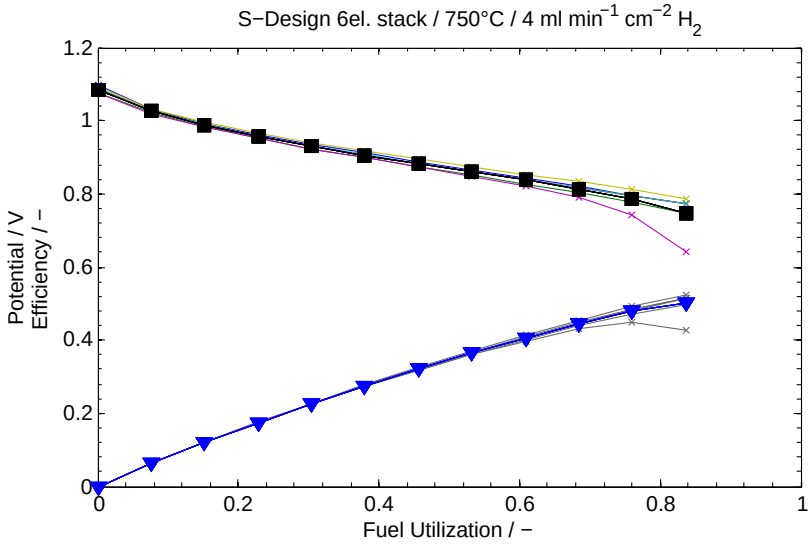

Figure 7.22: Construction details of a SOFC stack.

values below 40 mV. At open circuit, the cells present close OCVs, which attest of an adequate gas tightness of the seals. Above 60% of fuel utilization however, one cell presents a limiting behavior and a rapidly decreasing potential as the fuel utilization increases. At the maximal fuel utilization of 84%, the difference in potential exceeds 100 mV with the other cells. This type of behavior is typical of a deviation in the effective fuel flow provided to the elements, whereas no definitive conclusion can be made due to the absence of experimental verification means.

The results obtained on this 6-element stack show that the *S-design* prototype is capable to reach the range of high fuel utilizations necessary to achieve high efficiencies, which in this case are attained. A remarkable agreement is found between simulation and experiment. However, some care has to be taken in terms of validation of the performance prediction, as differences exist between the reference cell of the model and the used ones. Nevertheless, this result shows that the performance limitation occurring in the *R-design* was overcome in the new design, hence validating the analysis and the chosen corrections.

7.6.2 Performance of the *F-design* prototype

A validation of the performance of the *F-design* prototype was obtained on a 20-element stack operated at HTceramix's testing facilities. The stack was operated using anode-supported cells (Ni-YSZ cermet), with YSZ electrolyte, YDC barrier layer and LSCF cathode and cathode current collection layers. The stack was characterized with a dilute fuel mixture consisting of 40% of hydrogen and 60% of nitrogen (dry), in order to simulate a fuel mixture from a T-POX reformer. The air flow was varied depending on the operating point to limit internal temperatures, while keeping an air inlet temperature of 973K.
The stack was successively characterized at 4 and 6 $\mathrm{ml\,min^{-1}\,cm^{-2}}$ H_2 . The result is shown in Fig. 7.23, together with simulation results for the lowest fuel flow rate.
The average potential of the cells is depicted by a black line, using error bars to indicate the extent of deviations among the 20 cells of the stack.
At a hydrogen flow rate of 4 $\mathrm{ml\,min^{-1}\,cm^{-2}}$ H_2 , a maximum power output of P=1460 $W_{el}$was attained at a fuel utilization of 80%, reaching an efficiency of 49.7% and a power density of 0.36 $\mathrm{A\,cm^{-2}}$. The average cell potential was 0.775 V with a deviation of $\pm$0.030, indicating a correct homogeneity of the fuel distribution among the elements. At this operating point, the air excess factor was set to a value of $\lambda = 4.6$ to ensure cooling. More important, the stack was autothermal at this operating point, compensating the thermal losses of the insulation.
Due to the importance of the test for the qualification in the *FlameSOFC* project, it was not attempted to increase any further the fuel utilization. However, the capability to reach high fuel utilizations and efficiencies in a 20-element stack configuration attests of the performance capabilities of the designed stack. It has to be added that the efficiency of 49.7% was attained with a dilute fuel mixture, which adds to the interest of the prototype for operations with reformed C-fuels.
An interesting deviation is observed between the simulation results (obtained for a lambda of 4.6 corresponding to the highest power output) and the experimental ones, with lower efficiencies predicted by the model. The obtained difference can result from different error sources, which cannot be determined with certitude. On the one hand, it is possible that the internal temperature differed, with larger temperatures inside the stack explaining the higher performance. As the discrepancy between simulated and measured potentials increases with increasing current, a possible difference could originate from different ohmic losses.

At the higher hydrogen flow rate, a maximal power output of 1840 W was attained (0.46 $\mathrm{W\,cm^{-2}}$) for a total current of 119 A (0.59 $\mathrm{A\,cm^{-2}}$). This corresponds to a fuel utilization of 70% and an efficiency of 42.7%. This operating point was attained with an air excess factor of 5. The polarization could not be increased any more as the maximal air flow rate was attained on the system side, not allowing sufficient cooling any more. The small difference between the cell potentials at this operating point (0.771V$\pm$0.020) shows however that larger fuel utilizations could have been achieved at this fuel flow rate also. This additional result demonstrates consequently the power modulation capability of the stack. Finally, the stack was operated at a low fuel flow rate of 2 $\mathrm{ml\,min^{-1}\,cm^{-2}}$ H_2 (diluted with 60% nitrogen).

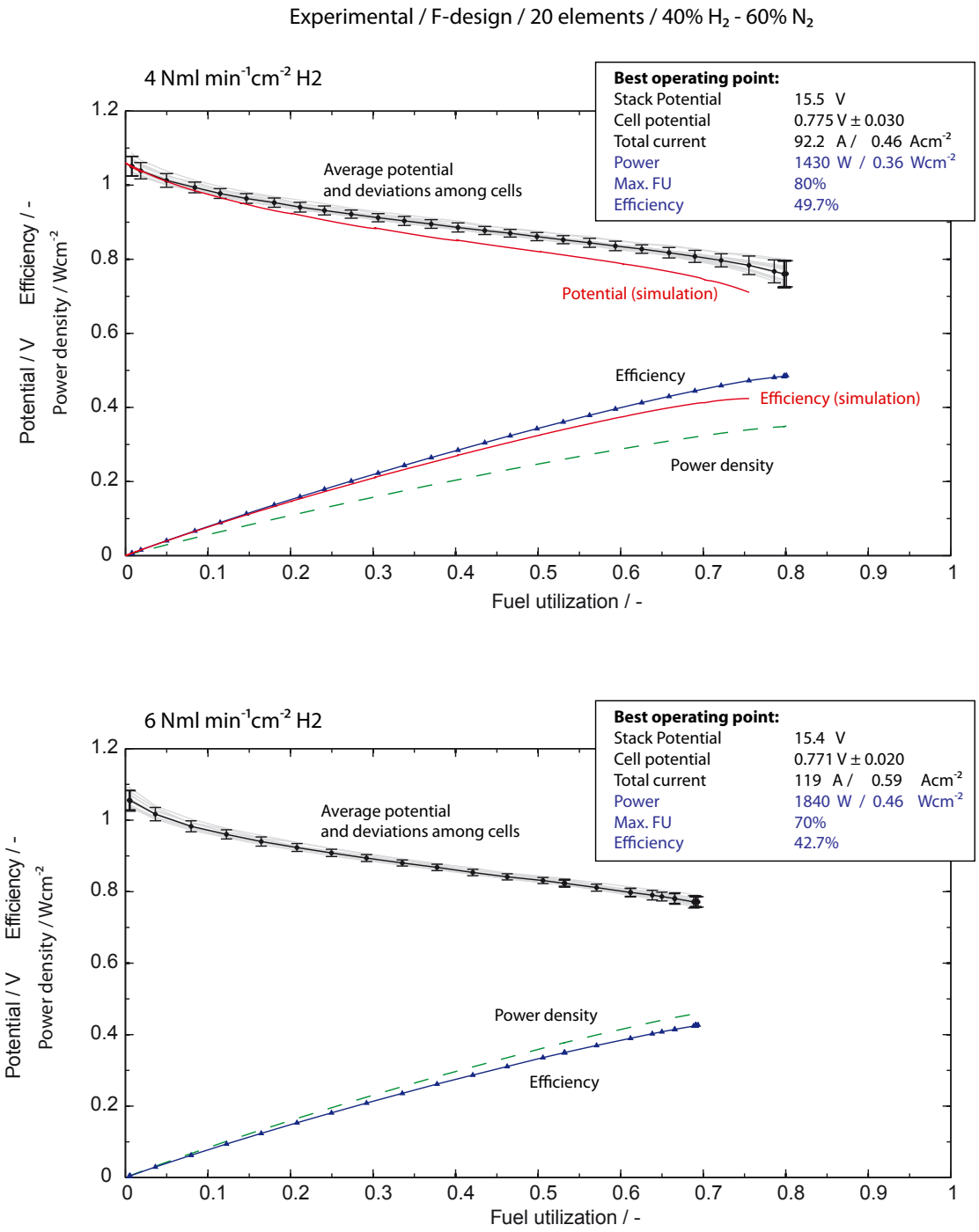

Figure 7.23: Best performance attained with a *F-design* stack and comparison with simulation results.

Under these operating conditions, it reached a power output of 780 W and an efficiency of 53% at 85% of fuel utilization. These results are shown in paragraph 3.6.

7.7 Conclusion

Throughout this chapter, the effect of the stack design on the final performance was investigated. The importance of an homogeneous fuel and air distribution on the final performance and reliability was pointed out as determinant factor. Limitations of performance were found to be principally induced by fuel depleted areas in the fuel cell, leading to diffusion limitations in the anode support and to redistribution of the electrochemical reaction towards fuel-rich regions. Therefore, on the modeling side, the performed analyses show the importance of the accuracy of the electrochemical model, in particular of an accurate modeling of the diffusive properties on anode side to predict limitations and risk of damage by oxidation.

Nevertheless, even if the predicted power and efficiency outputs depend on the fitted electrochemical model and can therefore be contradicted by experimental results, the comparative approach presented here allows to maintain the generality of the assessment of the stack's performance limitations. Further investigations could however complement this analysis, in particular for the case of partial internal steam reforming, where internal heat transfer or local catalytic properties of the materials are expected to influence the resulting performance.

Based on a comparison with a generic repeat-element providing ideal gas distribution, two stacks were designed in the frame of this work. In collaboration with HTceramix-SOFCpower, they were realized and could finally be tested. In the models and in experiments, both prototypes show an important improvement from the reference design *R-design* .

The performance maps of the *S-design* stack, as well as the obtained experimental results show that, despite strong constraints in the design phase, it was possible to largely improve the performance, approaching on the anode side the situation of an ideal fuel distribution. These results were obtained not only in the model, but much more with a real prototype whose internal gas distribution was designed with the herein developed CFD model. As expected, a weakness in the air distribution remained in the *S-design* prototype, leading to possible performance limitations at low air excess factors. A fact that was confirmed experimentally.

Experimental results made on stacks and short-stacks enabled to validate the predicted increase in performance of the designed stacks. The *S-design* stack permitted to successively attain a 500 W and 1 kW milestone in a 36, resp. 72-element configuration. Moreover, tests performed on short stacks enabled to attain efficiencies of 50% and more at fuel utilizations exceeding 80%.

The larger *F-design* stack was tested experimentally up to 1.84 kW in a 20-element configu-

ration, while being operated with a dilute fuel mixture. More important, an efficiency of 50% was attained at a fuel utilization of 80% and with an appreciable power output of 1.43kW$_{el}$. Finally, a maximal efficiency of 53% was attained at 780W, attaining a fuel utilization of 85%. These results were attained using dilute hydrogen as fuel. In other words, an operation on reformed natural gas would allow to reach efficiencies above 60%.

These experimental results validate therefore the analyses of performance limitations and the undertaken optimization steps.

However, these satisfying experimental results are the conclusion of long developments, not only to master the production, assembly and quality of the stacks, but also to understand the discrepancies between predicted and obtained performance in addition to the numerous failures observed in experiments. The undertaken investigations on the fundamental aspects limiting the reliability of the stacks and their implications on stack design are presented in the following chapter.

Chapter 8

Stack design, reliability and degradation

8.1 Introduction

As shown in the previous chapter, an adequate performance of SOFC stacks can be ensured by the choice of dedicate design options. However, besides performance, *reliability* and *durability* are the core issues for the development of SOFCs. This chapter focuses on this second aspect, investigating concrete reliability issues on the developed stacks. In this case, it is shown again, that design options and choice of materials play a central role in the reliability of SOFCs.

Based on a specific case, the possibility of model-based diagnostics is illustrated, giving insight in the coupled phenomena leading to failure. More central, it is shown that one necessary requirement for model-based diagnostics is the avoidance of the (in modeling usual) idealization of components, geometries or material properties which don't match experimental reality. Moreover, this approach tries to avoid another trend which consists in including in the models sufficient additional adjustable parameters in order to reproduce experimental observations. This last point requires therefore that the reality of the established diagnostics is tested for consistency against experimental observations.

Based on an attempt to explain low open circuit voltages in *R-design* prototypes, the hypothesis of non-ideal properties of the used sealing materials was made. In particular, it was investigated whether diffusion across seals, which is else neglected in seal testing, could induce sufficient mass fluxes to influence the open-circuit voltage.
In fact, the introduction of diffusive mass transport across seals not only allowed to explain the drop of open-circuit voltage, but surprisingly also described the presence, in the seals, of moving redox-limits exposing the cell to local redox-cycling upon changes in the operating

point. This additional, model-based diagnostic is in excellent agreement with experimental observations, offering new interpretations of post-experiment analyses, as well as an explanation for typical failures of the tested stacks.
Even more important, it is shown that, both for the *R-design* and *S-design* stacks, the combination of design options and chosen materials would inevitably lead to severe damage or failure of the cells upon repeated load- and thermal-cycling. This represents an unacceptable situation in terms of reliability and lifetime.

The validity of this diagnostic was finally completely confirmed by the successful application of corrective actions for the *S-design* stack, which unfortunately cannot be presented here. But more important, the *F-design* prototype, which was developed with the specific focus to avoid local redox-cycling issues and which was therefore designed with the therein complemented CFD model, proved to fulfill the objectives by presenting fully reduced cells after operation. This result demonstrates therefore that the model is not only capable of reproducing existing situations, but offers a predictive capability independently of a specific stack design. Finally, it shows the interest of model-based diagnostics for SOFCs.

8.2 Context

Repeated failures In the development phase of the R-design stack, an important number of experiments ended prematurely after a few hundreds of hours of operation due to breakage of one or several cells. A typical case of failure for a *R-design* short stack is shown in Fig. 8.1. First, important damages of the cells were frequently found near the gas feeding holes, along the fuel outlet where post-combustion takes places, but also all along the lateral sides of the cells, with propagation of cracks inside of the repeat-elements.
In addition, chromium-rich residues (see Fig. 8.1, top left) were found not only in the post-combustion area, but also in the middle of the air outlet (top right) where no obvious origin for these deposits was identified.

Post-experiment examinations of stack and cells were systematically performed to understand causes of failure, ending up in numerous, but sometimes contradictory hypotheses (thermal stresses, component quality, assembly...). No fully conclusive explanation could be given, in particular due to the difficulty to perform in-situ diagnostics during operation. In fact, breakage of cells was certainly a conjunction of several factors, such as quality issues in the component's production, defects in assemblies or inadequate operating conditions, but also, as shown here, resulting from an inherent weakness of the stack design exposing the components to inadequate operating conditions.

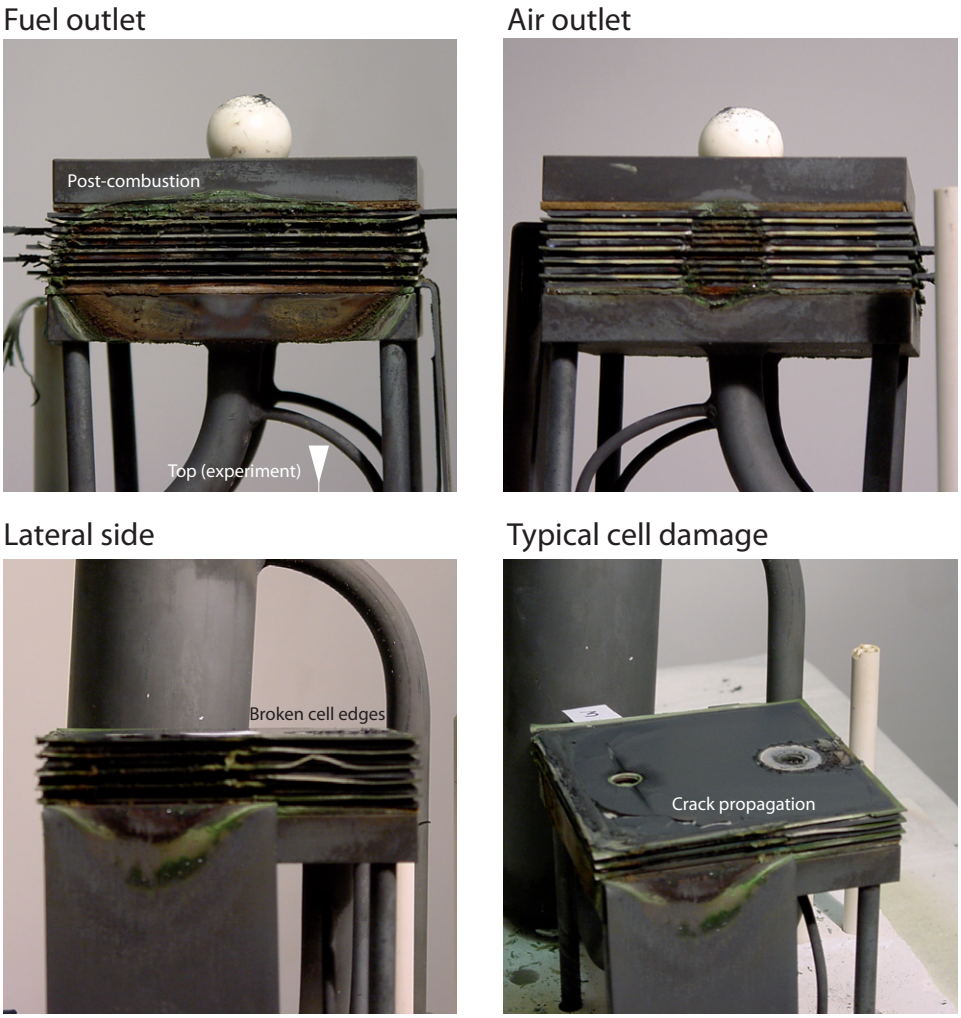

Figure 8.1: Typical damage observed on *R-design* stacks.

Low performances Besides reliability issues, experimental results obtained on stacks presented relatively low performances, showing important disagreement with the ones obtained on button cells. The low performance was not uniquely related to an important apparent ASR determining the loss of potential by current increment, but much more by the inability to reach high fuel utilizations, and this, well below the maximal feasible fuel utilizations presented in the previous chapter. In fact, the maximum fuel utilization was dictated by a monitoring of the potential transients during i-V characterizations. The maximal fuel utilization was defined by the moment where one cell started to present a decreasing potential under constant current, indicating a limitation. Attempts to overcome this limit were often followed by a failure of the stack.
Besides limited operation ranges, recurrently low open circuit potentials were recorded, with

values ranging between 940mV in the worst cases to 1020mV, well below the theoretical value of 1.099V expected at 800°C for a 97%H_2 -3%H_2O fuel mixture.

The lack of direct information from experiments lead to different possible interpretations of the results and hypotheses for their causes. One hypothesis for the low OCVs was the presence of a leakage current through the electrolyte, as described in the presentation of the electrochemical model (see paragraph 6.2.1). By fitting the ohmic resistance of the electrolyte, Larrain et al. were able to reproduce the experimental OCV's in a *R-design* repeat-element model [8], opening a field of application for modeling-based diagnostics. From the segmented experiment used to establish the electrochemical model however, the ohmic resistance of the electrolyte could be quantified later on, resulting in open circuit voltages that were systematically higher (1.03-1.07V) than the ones observed on the stacks, hence calling for additional explanations.

The sealing question One of the unknowns in this context was the behavior of the mica-based compressive seal gaskets used in the repeat-elements. In some tests, obvious leakage of the seals had been observed, resulting from a mismatch in the assembly. However, in most cases, no clear leakage was observed in the broken repeat-elements, leading to the conclusion of an absence of influence of the seals on the observed failures.
However, the presence of an internal leak remained a tempting hypothesis to explain to some extent the low OCVs (by generation of steam due to combustion) as well as part of the loss of performance.

8.3 Diffusion in compressive seals

As shown in paragraph 3.3, different sealing alternatives have been developed to ensure gas tightness in SOFCs, an overview of which is given by Fergus in [59]. Among them, compressive seal gaskets based on mica papers were proposed as a promising alternative to glass-ceramic sealants. Simner et al. [2] proposed to use muscovite and phlogopite micas. The sealing behavior of such materials was successively enhanced by Chou et al. [84, 115] using composite arrangements with mica and glass. Other composite options were studied by Bram et al. [86] using a combination of mica paper and metal.
The ability of materials to serve as compressive seals for SOFC is often studied by tests where a differential pressure is applied to a gasket and where the leakage flow is measured [2, 86]. These tests are mainly run using air or inert gases. They allow to compute the Darcy coefficient of the porous medium, hence to compute the pressure-driven transport of gas.

For the mica paper gaskets used in the hereafter detailed investigations on the *R-design* stack, Darcy coefficients in the range of $1/\alpha = 3 \cdot 10^{12}$ $[1/m^2]$ were determined by the experimental method described in literature [2, 86]. For pressure differences of 10mbar across the internal seals of the *R-design* stack (10mm inner diameter, 18mm o.d., 0.8mm height),

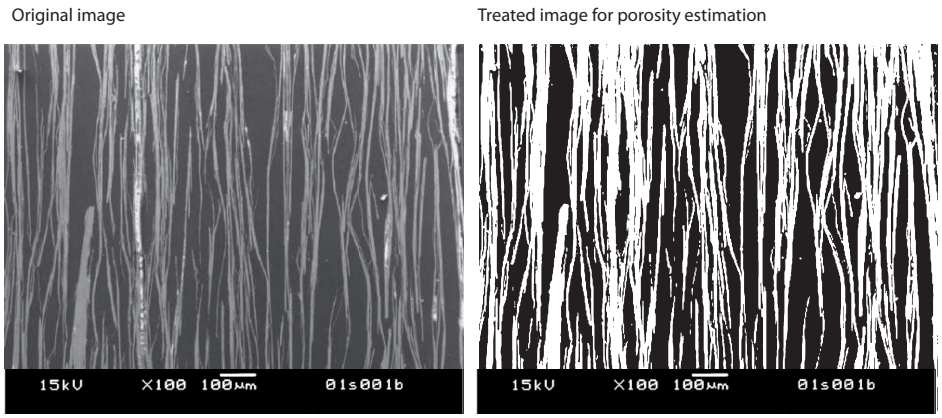

Figure 8.2: Microstructure of un-pressed muscovite mica-paper after heat treatment, reproduced from Simner et al. [2]. Corresponding image treatment for the estimation of porosity.

the corresponding air leak rates were comprised between 0.5 to 2Nml min^{-1}. This order of magnitude is consistent with measurements performed for instance by Le et al. [116] who measured air leak rates in the range of 1Nml min^{-1} for pressure differences of 100mbar across gaskets of 40mm outer diameter, 20mm inner diameter and 0.5mm thickness.
Due to the arrangement of flows and manifolds in the *R-design* stack, and in the case of sole pressure-driven mass transport across the seals, only an air to fuel leakage could have had a significant impact on the measured OCVs by burning part of the fuel internally. On the other hand, the fuel lost through the seal would only result in a loss of fuel towards the surrounding of the stacks and to the air manifold, resulting only in a lowering of the maximum achievable fuel utilization.
From the above-mentioned pressure-driven leakages of air measured through the seal gaskets, only up to 0.21Nml min^{-1} $(= 2/(0.21 * 2))$ of hydrogen were therefore expected to be burnt by this type of parasitic leakage. Compared to the 200-400Nml min^{-1} of hydrogen injected in the repeat-elements, this contribution to a lowering of the open circuit voltage was considered as negligible.
Moreover, although promising results were obtained by different researchers with such seal materials in terms of gas tightness (pressure driven), similar problems were reported by different authors. Among others, low OCVs were reported by Chou et al. [84], or even difficulties to reduce the anode supports in dilute fuel mixtures (Bram et al. [86]).

From these observations, it appeared that one additional transport phenomenon, which is frequently neglected when evaluating seal materials, could explain these observations: ***diffusive mass transport across the seals***. Confronted with the same inconsistencies, Chou et al. from PNNL[1] , independently from us, came to the same conclusion [84].

[1]Pacific Northwest National Laboratory

Due to the difficulty to perform in-situ experimental diagnostics, it was chosen to evaluate this hypothesis by modeling. As less dedicated literature was found describing specific aspects of diffusive transport in such materials, standard models for diffusion in porous media were implemented in the CFD model.

8.4 Model

8.4.1 Geometry and boundary conditions

The *R-design* repeat-element is modeled including the solid parts (interconnectors and cell) and the seals, which are considered as porous media. A surrounding air volume is modeled in which post-combustion occurs, in the same configuration as the case presented in the previous chapter (see Fig. 7.8). Similarly to the case of experiments on the *R-design* prototypes, the stack is placed in an oven operated at a controlled temperature of 780°C.
Due to the stack construction of the *R-design* prototype, shown in Fig. 3.3 pp. 56, seals and cells are exposed to free-convecting air in the external volume. In the model however, the bent edges of the cells are not modeled to simplify the meshing and avoid convergence problems, hence limiting the cell to the footprint of the seals and resulting in a flat stack side.
As the cathode was screen-printed on the complete surface of the cell for historical reasons, as shown in Fig. 7.7, the active area is extended under the lateral and internal seals, where gases have to be transported through the seal material. Even if these areas are expected to deliver negligible power, they are included in the model to reproduce the experimental reality with accuracy.

8.4.2 Mass-transport in the seals

To model mass transport in the seals, the relations described in paragraph 5.2.2 pp. 78 are applied.

8.4.2.1 Darcy coefficients

The Darcy coefficients of the mica paper were estimated by experiments performed on seal rings of $\phi 10mm$ i.d. - $\phi 18mm$ o.d. - $0.80mm$ thick on which a mechanical load of $0.4 \mathrm{kg/cm^2}$ was applied. Tests were made at operating temperature ($800°C$) with air, nitrogen or hydrogen. Depending on the type of mica paper used, values varied between 0.9 and $20 \cdot 10^{12}$

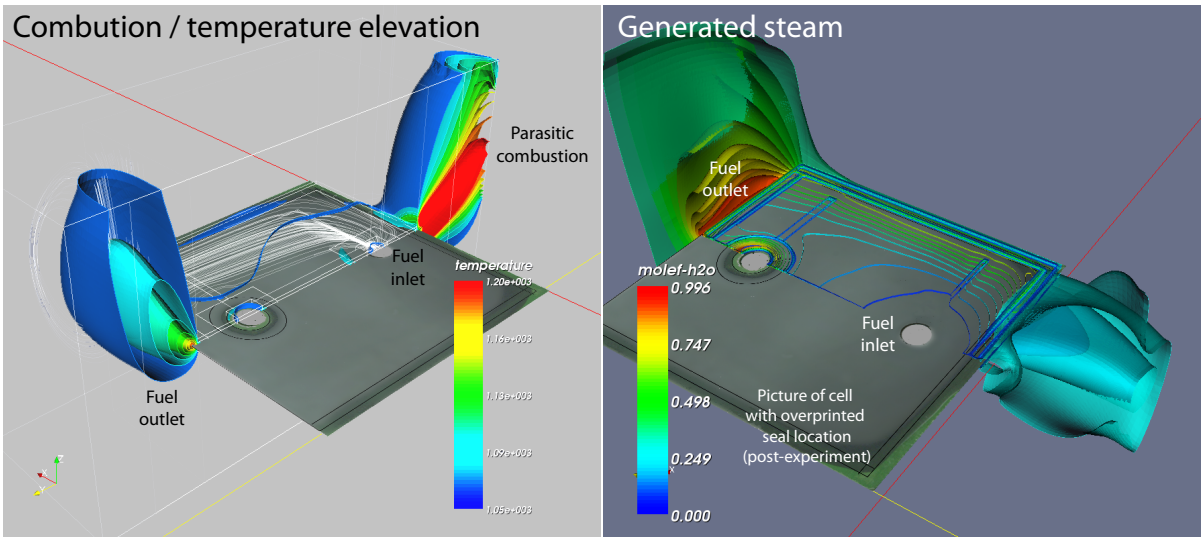

Figure 8.3: Simulation of *R-design* stack, including its surrounding volume. Example of simulated post-combustion and parasitic combustion, and associated generation of steam.

[$1/m^2$], with an average Darcy coefficient of:

$$\frac{1}{\alpha} = 3.17 \cdot 10^{12} [\frac{1}{m^2}] \tag{8.1}$$

As shown above, the mass fluxes transported by viscous flow were estimated to present a negligible amount with respect to the total injected gases. Therefore, the important differences among the measured coefficients is assumed to have a minor impact on the final result.

8.4.2.2 Diffusive transport

Diffusion in seals is modeled using the multi-component Fickian diffusion model (Eqn. 5.7) described in paragraph 5.2.2. One example of microstructure of mica paper is shown in Fig. 8.2, taken from Simner et al. [2]. This microstructure corresponds to unpressed mica paper analyzed after one thermal cycle at 800°C.
Simner shows that the open pathways between the mica-foils depend on the mechanical loading of the mica samples, as well as on the pre-compression before thermal cycling. In the case of the *R-design* stack, the mechanical loading corresponds to 0.04MPa, well below usual loads for such seal materials. Therefore, it is expected that the order of magnitude of the seal's porosity is of the same order than the one that can be estimated from the cross-sections shown by Simner et al. By image processing (see Fig. 8.2, the porosity of Simner's samples was estimated at $\varepsilon = 59\% \pm 3\%$. However, this value is only indicative, and the effective seal porosity is estimated from a fit of the measured OCV, as shown hereafter.

An additional question appears when considering the need for a correction of the effective diffusion coefficients by a Knudsen diffusion term (Eqn. 5.9). The latter has been established for cylindrical pores, not planar pathways such as in the case of mica paper [93]. Therefore, the validity of its formulation for the planar pathways has to be investigated, which is beyond the scope of this work. As consequence, the usual formulation is applied.
For hydrogen at a temperature of 800°C, and considering a characteristic pore size of 10μm from the SEM images (see Fig. 8.2), a Knudsen number of Kn=0.04 is estimated (Eqn. 5.4). This low Knudsen number indicates that the correction of the diffusion term is *a priori* negligible, which is further proved below.
Finally, from the SEM images of mica paper, it can easily be seen that the tortuosity of the material is close to $\tau = 1$.

8.4.3 Combustion and flame radiation

As parasitic leakage of fuel and post-combustion are considered, the kinetic reaction models presented in section 5.4.2 are implemented in the whole computation volume.
The resulting radiative heat transfer is only considered in its simplified form (see section 5.3.2.2) to limit computational time. Moreover, it is computed only in the post-combustion area of the stack, but not in the interior of the stack, where parasitic combustion takes place principally in the seal materials themselves.

8.4.4 Electrode damage indicators

As observed in experiments, internal leakages in stacks can either lead to an oxidation of the anode-supported cells, or to a deterioration of the cathode layer. In order to provide a concrete evaluation of the risk of electrode damage for a repeat-element, we propose here the definition of specific indicators.

8.4.4.1 Risk of reoxidation

The post-experiment analyses made on the *R-design* stacks show oxidized zones on the cells in most cases. Moreover, the simulations presented in the previous chapter show that this design presents zones where the circulation of gases is low, inducing stagnation of gases and possible depletion of reductive species under polarization. In these zones, mass transfer is mostly ensured by diffusion. If, in addition to these effects the porosity of seals is considered, an additional consumption of hydrogen is expected due to internal parasitic combustion, leading to possible oxidation of the anode.
To define an indicator for the risk of re-oxidation of the anode, the equilibrium partial pressure of oxygen found in the gas phase is compared to the equilibrium oxygen partial

pressure existing over nickel. In the fuel, the local oxygen partial pressure can be computed from thermodynamic data (Eqn. 8.4).

$$H_2 + \frac{1}{2}O_2 \leftrightarrow H_2O \tag{8.2}$$

$$K_{eq,O_2} = e^{(-\frac{\Delta G}{\mathcal{R}T})} \tag{8.3}$$

$$p_{O_2,eq} = (\frac{1}{K_{eq,O_2}}\frac{p_{H_2O}}{p_{H_2}})^2 \tag{8.4}$$

Fitting thermodynamic data obtained from *HSC 4* software[2], the equilibrium constant can be estimated as:

$$K_{eq,O_2}(T) = 1.47358 \cdot 10^{-3} exp\left(\frac{2.9675 \cdot 10^4}{T}\right) \tag{8.5}$$

Similarly, the equilibrium partial pressure of oxygen over nickel is determined by:

$$Ni + \frac{1}{2}O_2 \leftrightarrow NiO \tag{8.6}$$

$$K_{eq,Ni} = e^{(-\frac{\Delta G_{Ni,O}}{\mathcal{R}T})} \tag{8.7}$$

$$p^*_{O_2,eq} = (\frac{1}{K_{eq,Ni}})^2 \tag{8.8}$$

The equilibrium constant is obtained in the same manner, yielding :

$$K_{eq,Ni}(T) = 3.0225 \cdot 10^{-5} exp\left(\frac{2.8361 \cdot 10^4}{T}\right) \tag{8.9}$$

Combining eqn. (8.8) and (8.4), we can define an indicator for the risk of anode re-oxidation (eqn.8.10).

$$\zeta_{O_2} = \frac{p_{O_2,eq}}{p^*_{O_2,eq}} \tag{8.10}$$

Re-oxidation of the anode support will hence occur if $\zeta_{O_2} \geq 1$. Due to low oxygen partial pressures in the vicinity of the redox-limits described hereafter, relatively slow oxidation kinetics [64] can be expected. Therefore, this indicator doesn't indicate immediate damage of the electrode. However, as this work focuses on the long-term use of the cells, the resulting risk of local electrode damage and resulting failure is considered as significant.

8.4.4.2 Damage of the cathode layer by exposure to reducing atmospheres

Due to leakage of fuel through the seals, another risk of electrode damage is represented by a local reduction of the cathode layer by a reducing atmosphere. The stability of standard $(La, Sr)MnO_3$ cathodes and $(La, Sr)CoO_3$ current collection layers was estimated from data

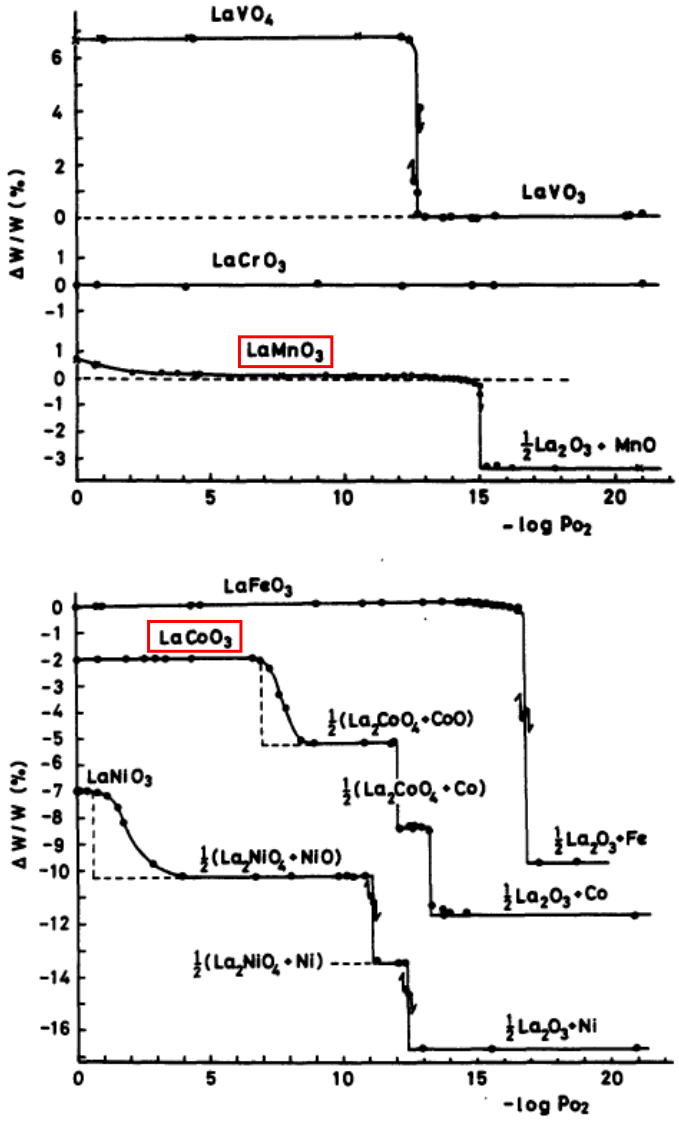

Figure 8.4: Stability of perovskites under different pO_2 at 1000°C. Reproduced from Nakamura et al. [3]

on undoped $LaMnO_3$ and $LaCoO_3$ established by Nakamura et al. [3] for reducing atmospheres at 1000°C (see Fig. 8.4).

As shown in Fig. 8.4, a stable region is found for $LaMnO_3$ in oxygen partial pressures above 10^{-15} atm , while $LaCoO_3$ experiences several successive transformations starting at a pO_2 inferior to 10^{-7} atm. For strontium-doped perovskites, it is expected that the stability limit occurs at higher oxygen partial pressures, as shown for instance by Yokokawa et al. for

[2]Outokumpu Research, Finland

$(La, Sr)CoO_3$ [117].

Due to the lack of available data for the exact stoichiometry of the used components, a threshold value was determined beyond which it is expected that $(La, Sr)MnO_3$ cathodes are irremediably damaged, defined as a minimum oxygen partial pressure of pO_2=10^{-15} atm[3]. A cathode damage indicator is consequently defined similarly to the case of nickel reoxidation, considering the local equilibrium oxygen partial pressures given by Eqn. (8.4):

$$\zeta_{cat,reduct} = \frac{p_{O_2,eq}}{10^{-15}} \tag{8.11}$$

This criterion is a very simplified representation of the real thermodynamic properties of Sr-doped perovskites, simplification which could affect the accuracy of the simulation. However, as shown hereafter, the transition from an oxidizing to reducing atmosphere occurs through a thin parasitic combustion front, on either side of which the partial pressures of oxygen are either much lower[4] or higher than this threshold value. Therefore, the position of this limit is rather defined by the transport properties of gases than by the thermodynamic properties of the material.

[3]This value is given for 1000°C. The same value is used for the presented cases, due to the lack of data at lower temperatures.

[4]In fact, for a hydrogen-steam mixture, a hydrogen partial pressure of 0.02 atm is sufficient to achieve the threshold pO_2 for reducing conditions.

8.5 Validation of the diffusion hypothesis, validation of the model

The validation procedure has two objectives: first, to validate the model, and second, to validate the hypothesis of diffusive mass transport in the seals. Therefore, the validation procedures consist in a verification of the consistency of the simulation outputs based on experimental observations.

8.5.1 Effect of the seal porosity on the OCV

To study the effect of diffusion in seals, a reference experiment (MS95) is reproduced. The test was performed during 3000 hours on a 5-element R-design stack operated at constant current (0.46 $A\,cm^{-2}$). This experiment is chosen due to the use of anode-supported cells of the same type than the ones used to fit the electrochemical model, as well as for its long-term operation.
The reference experiment was made under the following conditions: $8ml\,min^{-1}\,cm^{-2}$ H_2 + 3%H_2O, λ=1.6, 800°C, 3000 hours operation. The Darcy coefficient of the seals is set to the average measured value of $3.17 \cdot 10^{12} m^{-2}$, while the porosity of the seals is varied to study the effects of diffusion.

Figure 8.5 depicts the local gas fractions in a *R-design* repeat-element at open circuit, obtained for the hereafter fitted seal porosity of 29%. On the anode side, the hydrogen mole fraction presents important variations over the surface of the cell, despite the absence of electrochemical consumptions of species apart from the residual leakage current through the electrolyte. In the interior of the element, the hydrogen mole fraction drops to values below 0.3 atm along the lateral seals, with even lower values in the corners behind the fuel distribution line. In parallel, steam partial pressures comprised between 40% and 70% are found at the same location, resulting from parasitic combustion with oxygen. Moreover,a dozen of millimeter wide zones with steam partial pressures of about 50% are found along the fuel flow on the sides. One notable exception is found in direct vicinity of the fuel inlet, where hydrogen crosses the entire width of the seal towards the exterior.
Underneath the internal seal gasket on the anode side, the hydrogen partial pressures steadily decrease until reaching the air manifold. The opposite trend occurs for steam, resulting in high partial pressures at this location.
On the cathode side, a depletion of oxygen is found in the corners behind the distribution lines, reaching values inferior to 0.05 atm. A similar depletion is found, as well, along the lateral seals, despite a larger convective mass transport and a lambda of 1.6. In addition, an important oxygen-depleted area is found underneath the internal seal (fuel manifold), where the oxygen partial pressure drops to zero. In fact, hydrogen from the fuel manifold diffuses through the seal, reaching the cathode GDL volume. Moreover, an oxygen-depleted area is found downstream of this seal gasket, ranging into the exterior volume of the stack. This area indicates the presence of parasitic combustion with hydrogen, which is sufficient

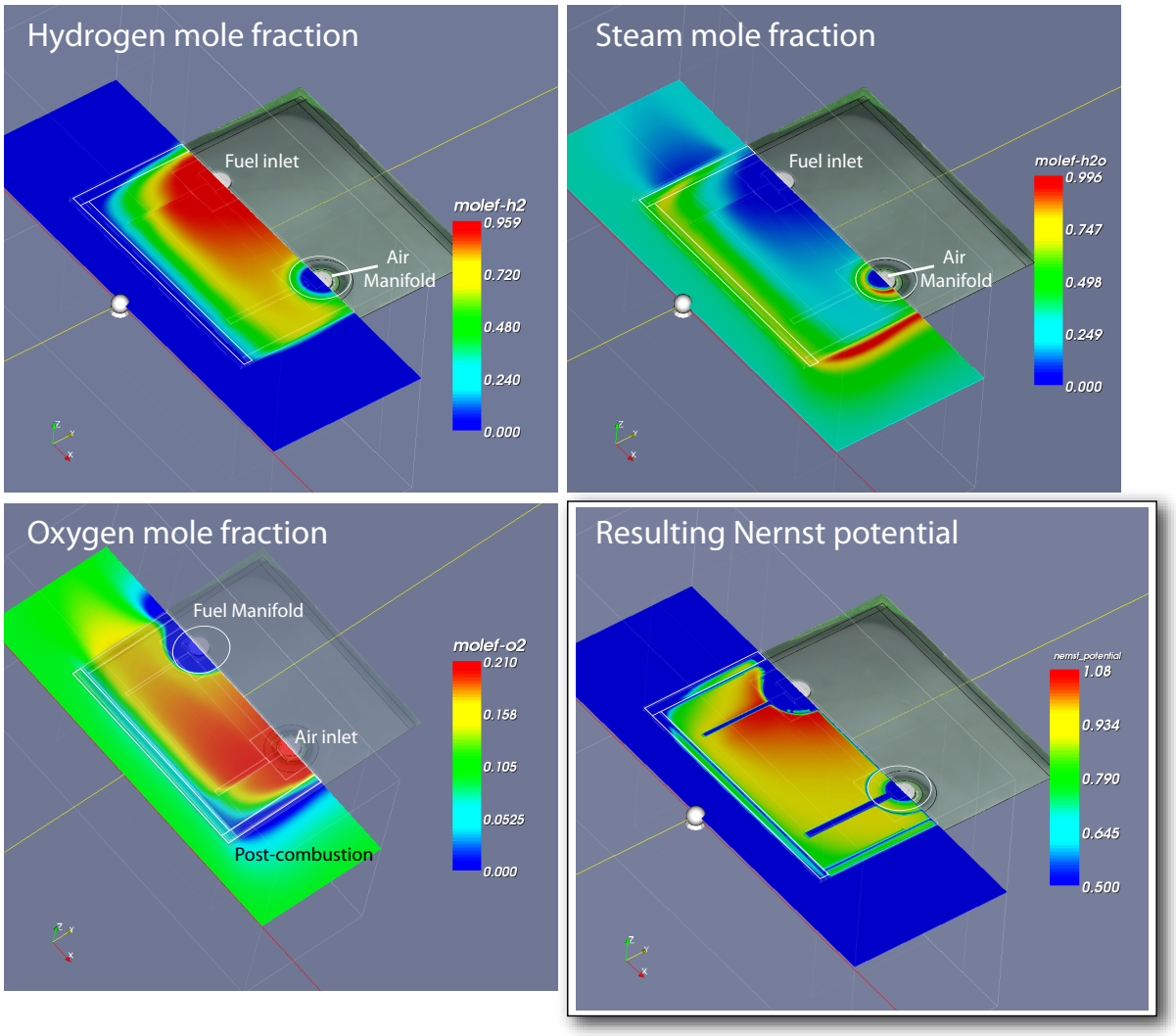

Figure 8.5: Simulated local gas fractions at OCV, and corresponding local Nernst potential.

to lower the oxygen partial pressure to virtually zero.
Finally, both on the fields of steam and oxygen partial pressures, the post-combustion volume is easily visible, resulting in an oxygen-depleted area in contact with the lateral seal on the cathode side, in the vicinity of the air inlet.

With important local differences in gas compositions, a pronounced effect is visible on the spatial distribution of Nernst potential. First, at the fuel inlet, the Nernst potential reaches 1.08V instead of the theoretical value of 1.10V, essentially due to the fitted leakage current through the electrolyte. In areas away from the seals, Nernst potentials in the range of 0.95 to 1.08V are found. Along the seals, the Nernst potential drops to values comprised between 0.73 and 0.85V. Despite the depletion of hydrogen in these areas, Nernst potentials

of the same order are attained underneath of the seals, with two notable exceptions. First, in the corners behind the fuel distribution line, local values drop below 0.5V with, as shown hereafter, areas where oxidizing conditions exist. Second, the Nernst potential drops to zero at the location of the seal gasket of the fuel manifold. In this case, it is not the lack of reacting species on anode side which lowers the Nernst potential, but the lack of oxygen on the cathode side.

The consequence of this situation is a lowering of the repeat-element's potential at OCV. As the electrical potential in the MIC can be assumed as constant, areas with Nernst potentials above the cell potential deliver a positive residual current, while the areas with lower Nernst potential present a negative current, hence working in electrolysis mode. Due to the operation at OCV, the integral of local current densities is zero. To enable the simulation of this situation, reverse currents are consequently allowed in the model.

As shown in this paragraph, the combination of diffusion across the seals and presence of an air electrode in these areas results in an important difference between the expected and attained OCVs. Therefore it is shown that, theoretically, diffusion in seals might be the missing explanation for the observed low OCVs.

8.5.2 Fitting the OCV

As shown in the following paragraph, variations of the seal porosity affect the obtained OCVs. Therefore, from one experimental OCV, it is possible to estimate the effective diffusive parameters for the used seal materials. In the reference test, the average OCV was 1.001 V with deviations of ± 15 mV, well below the theoretical value of 1.1V.
To enable the comparison of the modeling output with post-experiment analyses performed on a specific repeat-element, the OCV of an intact cell (at disassembly) is considered for the fitting procedure, with a value of 1.006V ± 1 mV.

As shown in Fig. 8.7, it is possible to vary the simulated OCV in a wide range by adjusting the porosity parameters, from 1.035V to values below one volt. The result is presented as function of the effective diffusion coefficient for hydrogen in the seals, independently of the considered diffusion regime (Knudsen correction or not). Therefore, the effective diffusion coefficients for each specie are alternatively given by eqn. (5.8) or eqn. (5.10), where a pore size of 10μm is considered for the Knudsen diffusion term. The pore size of 10μm corresponds to typical spacings between mica foils, as observed in Fig. 8.2[5].

[5]In fact, due to the non-cylindrical shape of pores in mica paper, a larger equivalent pore diameter should probably be used instead.

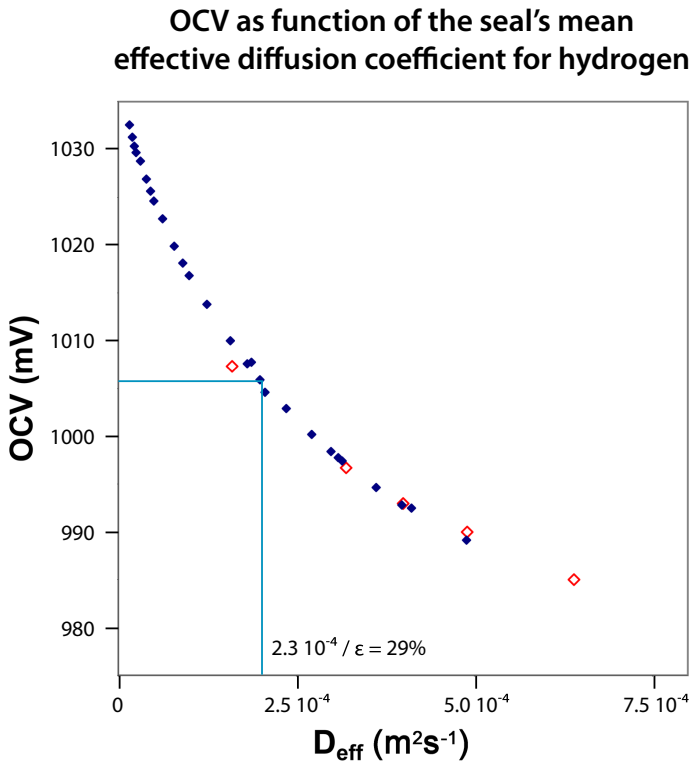

Figure 8.6: Simulated OCVs with varying porosity parameters. • With Knudsen correction ◇ Without Knudsen correction.

As shown in Fig. 8.7, it is possible to fit the experimental OCV of 1.006V with an effective mean diffusion coefficient of $D_{eff,H_2} = 2.3{\cdot}10^{-4}\ m^2 s^{-1}$ for hydrogen. Therefore, the existence of a solution for the targeted OCV is proven.
If we consider that diffusion in mica paper occurs without important contribution of the 'Knudsen diffusion regime' (eqn.5.8), the fitted seal porosity is 28.8%, considering a tortuosity equal to unity.
If we consider instead a diffusion regime requiring correction of the diffusion coefficients by a Knudsen diffusion term, we find using eqn. (5.10) a set of solutions for the pore diameter d_p and the porosity ε shown in Fig. 8.7. It shows that the estimated resulting porosity strongly increases for pore diameters below 10 μm. For a diameter of 10 μm, the porosity is 31.3%, and for 20 μm, it is 29.8%. For high pore diameters, it asymptotically tends to the computed value of 28.8%.

The SEM images of mica paper shown in Fig. 8.2 indicate typical gap sizes over 10 micron [2], which means that the effective porosity is close to the asymptotic value. From this result, it can therefore be assumed that diffusion in the mica seal gaskets is less influenced by interactions between gas molecules and pore walls (Knudsen diffusion regime), hence allowing the use of simplified multicomponent diffusion models for porous media presenting large pores.

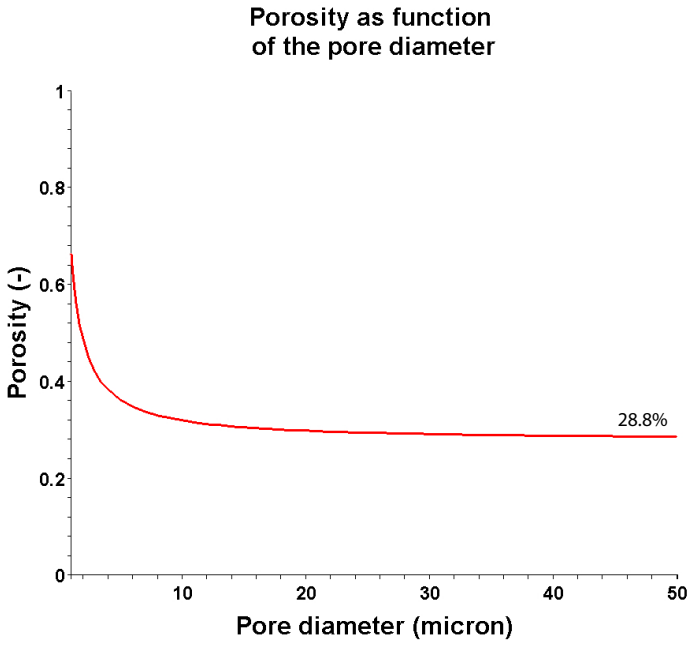

Figure 8.7: Set of porosity parameters for an effective diffusion coefficient $D_{eff} = 4.90 \cdot 10^{-4}$ $m^2 s^{-1}$ for hydrogen.

In fact, the fitted asymptotic porosity of 28.8% is of the similar order as the $59\% \pm 3\%$ porosity of mica paper estimated by a statistical processing of SEM images [6]. Difference between the fitted and estimated porosities are assumed to originate from differences in the raw materials or from differences in the applied mechanical load.[7]

A final indication of the consistency of the fitted solution is given by the ability of the model to reproduce the changes in the measured OCVs upon variations of the fuel flow rates, as reported in Table (8.1). For a fuel flow rate varied between 250 and 400 Nml min^{-1} H_2 , the measured OCV changes from 989 to 1006 mV on the considered cell, while the simulated one is shifted from 984mV to the fitted value of 1006mV.

These simulations show therefore that it is possible to find a set of diffusive properties enabling to reproduce the low OCV of a repeat-element over a certain range of operating conditions. As shown by Fig. 8.6, if the diffusive transport in the seals was a negligible phenomenon, the model would not be able to fit low OCVs in the range of 1.006 V, hence

[6] That is, in this case, not in the range of a few percent.

[7] The error on the fitted value of 61% found in our published article [118] results from a mistake in one equation of the model.

Fuel (mln/min)	$\mathrm{OCV}_{Simulation}$	$\mathrm{OCV}_{Experiment}(mV)$
400	1006	1006 ± 1
300	995	992 ± 1
250	989	984 ± 1

Table 8.1: Simulated ocv with variation of the flux of hydrogen. comparison with reference experiment.

requiring other explanations. These results support therefore the hypothesis of an important contribution of diffusive transport in the seal materials. However, a complete validation of this hypothesis and of the model can only be established by further investigations on the consequences of diffusion through the seals on the repeat-element.

8.5.3 Associated effects on degradation and performance, and experimental validation

As shown in the following paragraphs, in addition to explain the low OCVs, the simulations predict parasitic combustion, redox-cycles during polarization and local reduction of the cathode in excellent agreement with experimental observations, effects that were not expected when making the hypothesis of parasitic diffusion in the seal materials.
In the following figures, simulation outputs are superimposed on pictures of real cells illustrating the observed phenomena.

8.5.3.1 Parasitic combustion

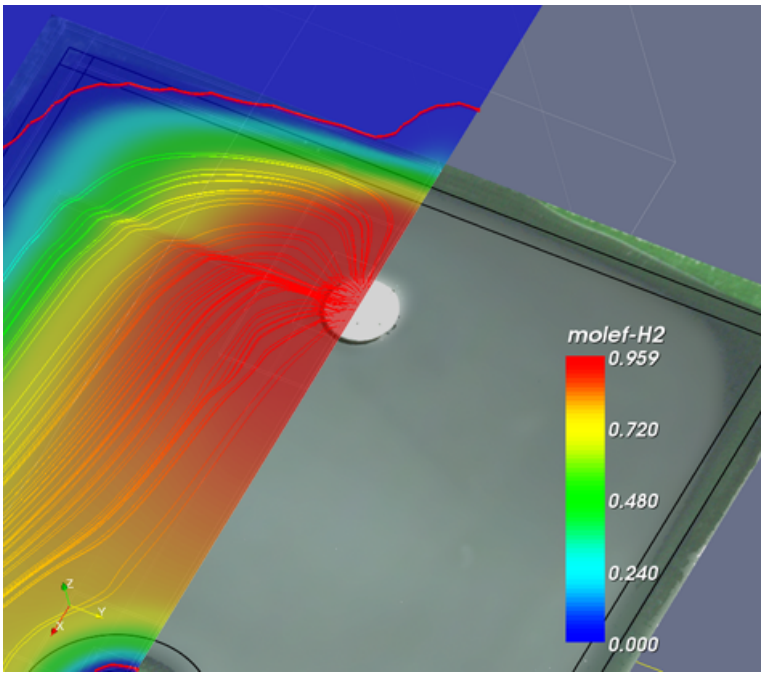

Figure 8.8: Diffusion through the seal next to the fuel inlet hole. Simulated hydrogen fraction and cell after operation. The red line is the redox limit.

Figure 8.8 depicts a detail of the simulated hydrogen profiles shown in Fig. 8.5 - in particular of the fuel inlet region - together with the picture of an operated cell. The position of the seals on the cell is recalled by black lines. The red line indicates the location of the separation between reducing and oxidizing atmospheres, resulting from local combustion of the reactive species. This line is called *redox-limit* in the following paragraphs.
As attested by its position, part of the parasitic combustion occurs in the repeat-element itself (in particular in the corners behind the fuel distribution line), but also outside of the repeat-element. As indicated by the high hydrogen partial pressures found throughout the

seal in vicinity of the fuel inlet, an important diffusive fuel leakage is predicted to occur at this location.
Looking at the cell, a typical 'redox pattern' is visible, with the presence of reduced areas (grey metallic nickel) and oxidized ones (green nickel oxide). The limit between oxidized and reduced areas matches well the position of the simulated redox-limit, as confirmed hereafter. In addition, the fact that fuel diffuses outside of the repeat-element in the vicinity of the fuel inlet is confirmed by the reduced state of the cell at this location.
To confirm the existence of the parasitic combustion front and to evaluate its effects on the temperature field, the local temperature elevation resulting from the introduction of hydrogen on the anode side was measured experimentally. A set of shielded K-type thermocouples (Omega Newport) were disposed all along the lateral seal in a dummy-test configuration, where the cell was replaced by a metallic sheet of same geometry. Presented in Fig.8.9, the comparison of the measured and simulated temperature increments presents a reasonable agreement. The position of the measurement points is shown on the top figure. Point 1 corresponds to the parasitic leakage in the vicinity of the fuel inlet. Points 2 and 3 were placed on the lateral seals, and point 4 was placed in the post-combustion region. The corresponding transient of the temperature elevation is detailed, attesting of a sharp rise of temperature at the introduction of the fuel. The fluctuations of temperature in the post-combustion area (point 4) are due to variations of the fuel fluxes, with a rapid response on the measured temperature.
Along the lateral seals (point 2 and 3), the measured and simulated temperature increases are in the range of 20 to 30K. In the post-combustion region (point 4), temperature elevations over 100K are measured and simulated. In this case, the discrepancy between the measured (100K) and simulated values (150K) can be ascribed to the sensitivity of the measurement to its location in the reaction volume. Finally, in the vicinity of the fuel inlet, the temperature elevation is higher, comprised between 50K (measure) and 90K (simulation). This attests of the larger leakage of fuel at this location. In fact, this temperature is due to the combined effect of the diffusive flux through the seal on anode side (see Fig. 8.8), and through the internal seal on the cathode side (see Fig.8.5 and 8.15).
Figure (8.10) shows the simulated location of this flame and the resulting local high temperature (above 1150K). The superimposed picture of the short stack 'MS 95' after 3000 hours operation shows the traces of oxidation products, resulting from the exposure to high temperatures (and probably also to steam) of the interconnectors and of the stack's top-flange.

Summary *The simulation, confirmed by experimental measurements, predicts a modification of the temperature field resulting from parasitic combustion at different locations in the fuel cell. Parasitic combustion occurs either in the seals or, if the flux is sufficiently important like near the fuel inlet, outside of the element. The importance of the parasitic combustion is further revealed by the presence of combustion traces at the center of the air outlet, whose origin could therefore be explained.*

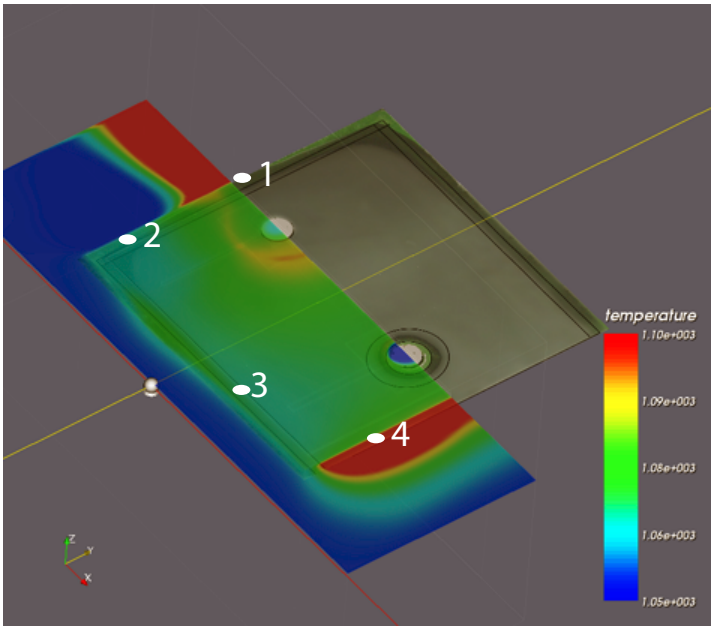

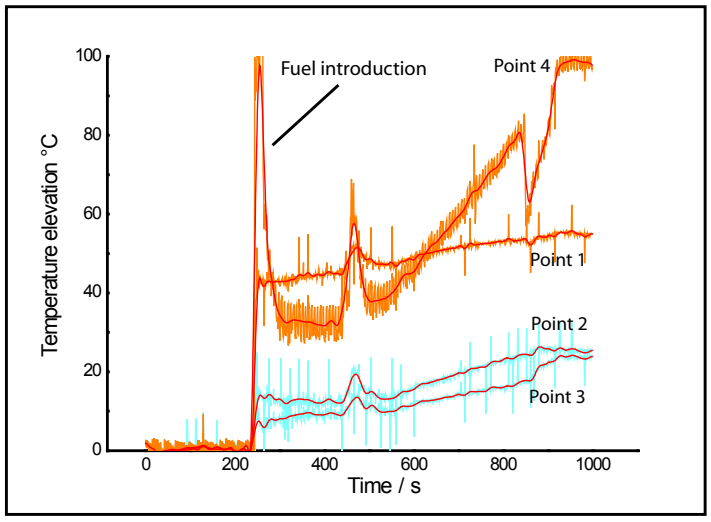

	Location	$\Delta T_{Measure}(K)$	$\Delta T_{Simulation}(K)$
1	Seal near anode inlet	$+53\pm2$	$+90$
2	Lateral seal	$+25\pm2$	$+29$
3	Lateral seal	$+22\pm2$	$+28$
4	Anode outlet	$+100\ \pm2$	$>+150$

Figure 8.9: Local temperature elevation on lateral seals. comparison of measured value and simulation output.

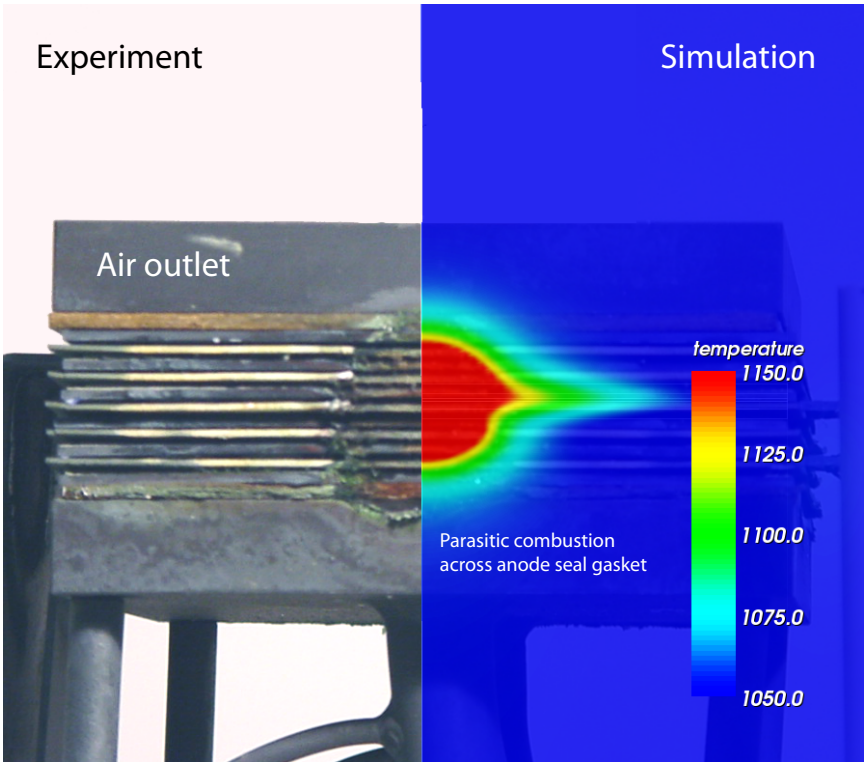

Figure 8.10: Damaged air outlet on short stack 'ms 95' after operation (left). Simulation of the local overheating due to a parasitic flame, for one repeat element (right).

8.5.3.2 Redox-cycling of the anode support under polarization

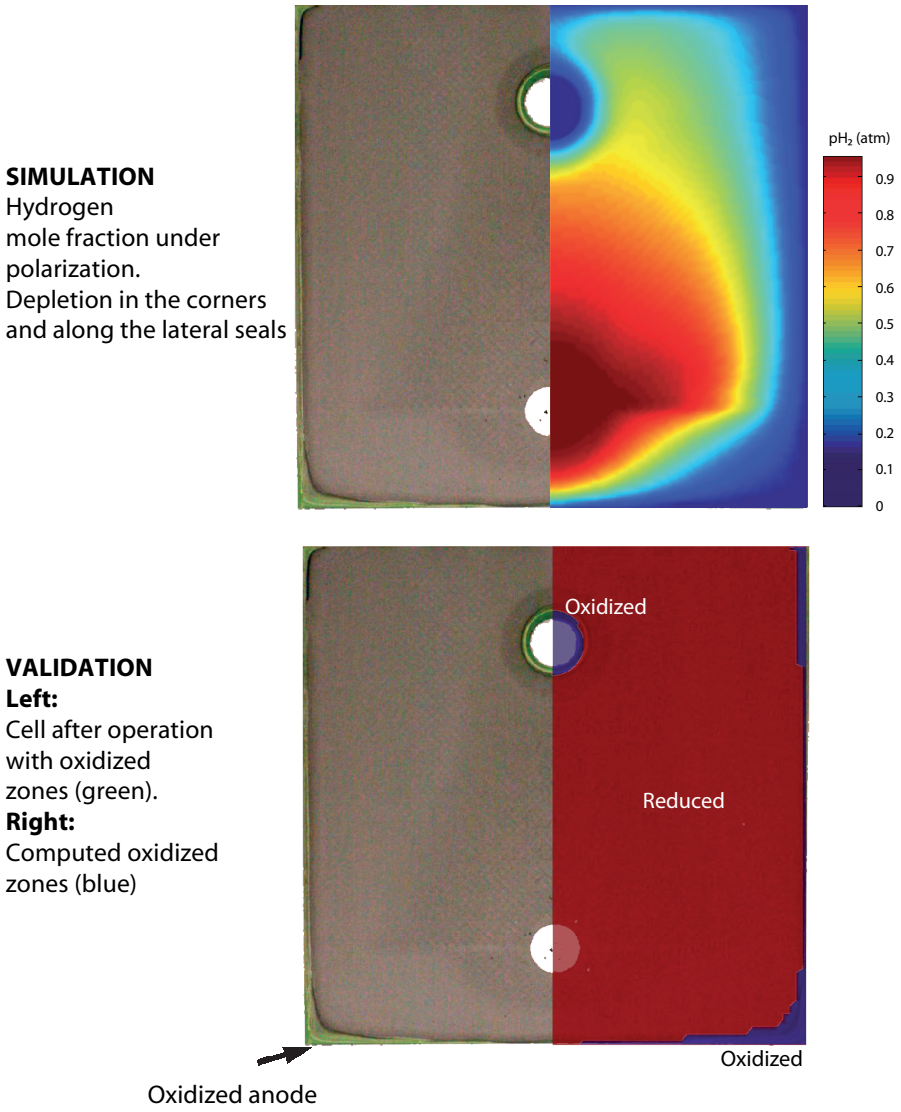

Figure 8.11: Oxidation of the anode support due to the combined effect of seal porosity and fuel depletion. (40 %FU, 800°C, 8 ml min^{-1} cm^{-2} H_2 + 3% H_2O).

Figure (8.11) shows a simulation output obtained at a fuel utilization of 40% compared to a used cell, depicting the spatial distribution of hydrogen over the active area (including the active areas under the seals) and the predicted oxidized areas. At this fuel utilization, the minimal hydrogen partial pressure in the corners near the fuel inlet attains zero. This situation is similar to the simulated hydrogen partial pressures obtained at 70% fuel utilization with solid seals, shown in the previous chapter. Therefore, the porosity of the seals is expected to induce additional performance limitations.

On the bottom part of Fig. 8.11, the computed electrode damage indicators predict a reoxidation of the anode in the corners, but also along the sides of the element and, even more critical, around the air supply hole of the cell.

At the locations where no redox-front is observed along the cell's sides, the hydrogen partial pressure is high enough to move the combustion front outside of the element. This is particularly the case near the fuel inlet, as shown earlier.
The comparison with the used cell shows an excellent agreement of the predicted oxidized (green) and reduced (grey) areas. On the operated cell, oxidized regions are found principally in the corners near the fuel inlet, but also along the sides at the fuel outlet, and around the air supply hole. Not only the position of the affected areas is correctly predicted by the model, but also their surface and shape. This indicates the capability of the model to predict the position of redox-limits with accuracy.
A more critical issue is predicted by the simulation. Depending on the polarization point,

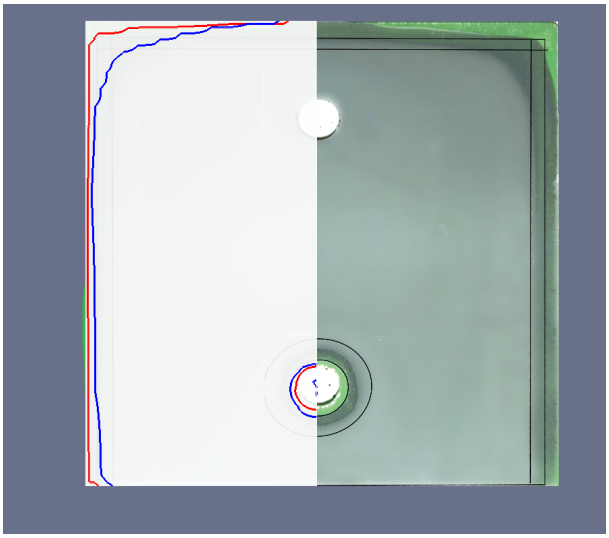

Figure 8.12: Redox-front on the anode predicted by simulation, at OCV (red) and at 50% FU (blue). Comparison with the reference cell of test 'MS 95' (right).

the internal field of reactive species changes, as already shown for the case of solid seals. If the polarization is increased, the partial pressures of hydrogen decrease generally in the element, and more specifically along the seals. The diffusive flux of hydrogen consequently decreases, allowing the combustion front to move towards the interior of the element. Figure (8.12) shows the oxidation front computed from Eqn.(8.10) under an increasing polarization from OCV to 30A (0.6 A/cm^2), showing important displacement of the redox limit.

The successive IV-curves between OCV and high fuel utilization will lead in the affected areas

to the equivalent of local redox-cycles. Due to the poor ability of anode-supported cells to withstand repeated redox-cycles, it is expected that repeated load cycles will unavoidably lead to rupture [64].
Experimental evidence of this prediction is given by the observation of non-broken cells after operation, shown in Fig. 8.13. The different shadings reveal the successive redox-cycles (Fig. 8.13 A), with resulting micro-cracks parallel to the seal. The evidence of local combustion is indicated from the sintered Ni-microstructure (fig. 8.13 B).

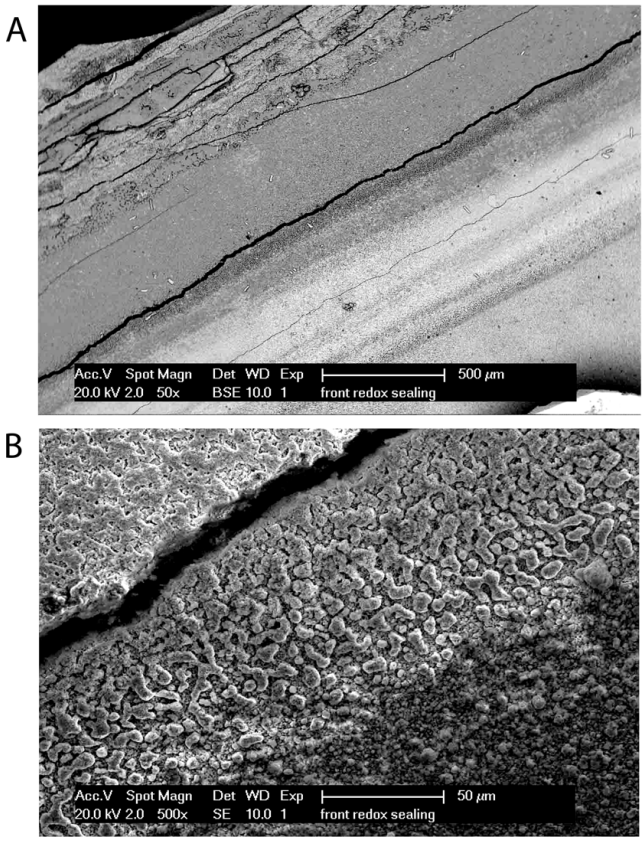

Figure 8.13: (A)Cracks due to redox cycles under the lateral seals. (B) Sintered ni-microstructure due to high-temperature combustion of hydrogen under the seal.

A final confirmation of the presence of local redox-cycling is brought by the large number of experiments where broken cells present fractures starting from oxidized areas, along the cell's edges or from the air supply hole where a similar redox-cycling feature is predicted. A typical example of a damaged cell is shown in Fig. 8.14.

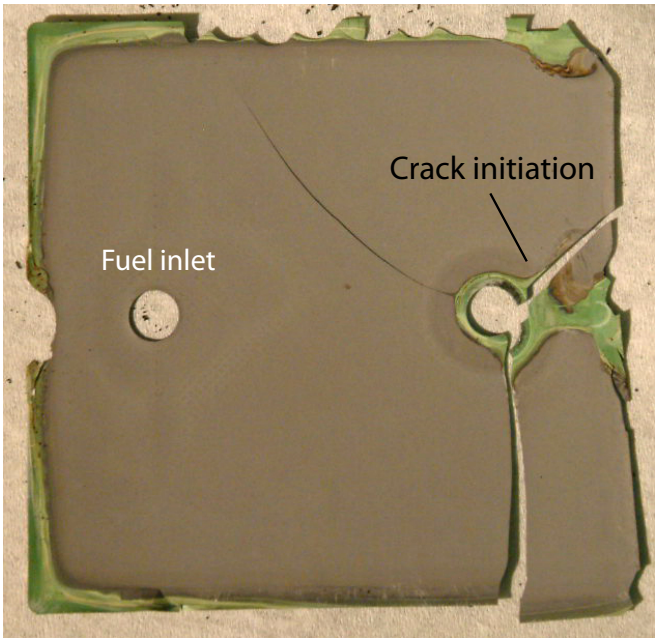

Figure 8.14: Example of typical redox-patterns and resulting cell damage.

8.5.3.3 Local reduction of the cathode

Besides damages on anode side, the computed cathode damage indicator (Eqn. (8.11)) indicates the existence of areas where the cathode is exposed to reducing conditions. Figure 8.15 shows the simulated local oxygen fractions obtained at the same fuel utilization of 50%. A strong depletion of oxygen is not only found downstream of the internal seal (fuel manifold), but also along the lateral seal near the air entry. Similarly to the case of solid seals, shown in the previous chapter, oxygen-depleted areas are found in the corners behind the distribution lines, resulting however in the case of porous seals in lower oxygen partial pressures reaching virtually zero. This situation is caused by the presence along this side of the fuel outlet, where reducing species and combustion products are present at the stack's surface, leading to a depletion of oxygen (see Fig. 8.5).
Traces of damage are easily visible on the cathode's surface of the used cell, with again a good match of the predicted damaged areas.

SIMULATION
Oxygen mole fraction
under polarization
on cathode side:
depleted areas
in the corners
and under the seals

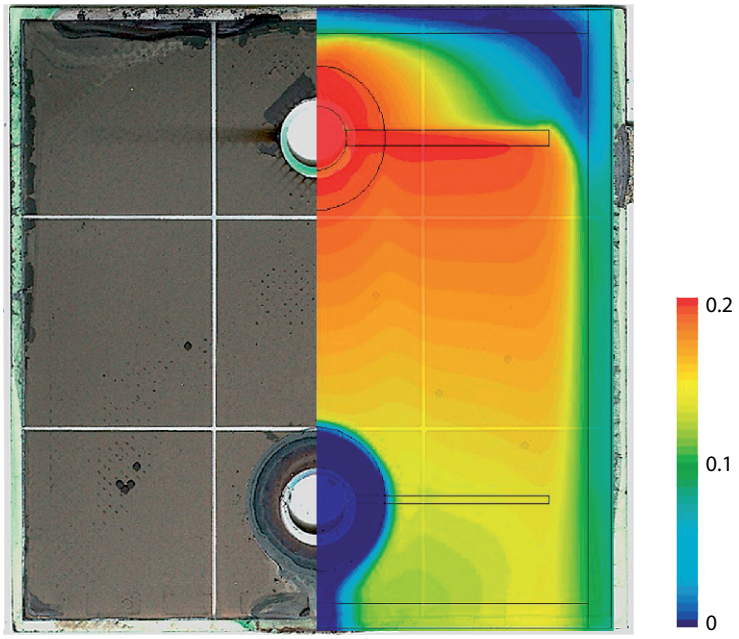

VALIDATION
Left:
Damaged cell
after operation
Right:
Field of log (pO_2).
Zones where
$pO_2 < 10^{-15}$ (blue)
match degraded areas

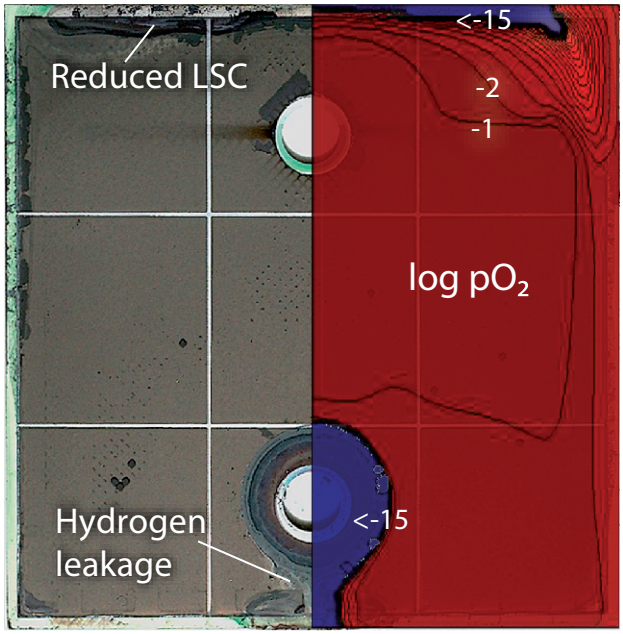

Figure 8.15: Reduction of the cathode current collection layer (LSC) due to the combined effect of seal porosity and air depletion. (40 %FU, 800°C, 8 ml min^{-1} cm^{-2} H_2 + 3% H_2O).

8.5.3.4 Local gas composition and parasitic diffusion of inert species

A final validation of the hypothesis of important diffusive transport in the seals was obtained in the frame of one diploma thesis [8] by locally-resolved measurements of the gas composition on the anode side of a *R-design* repeat-element. A total of 16 capillaries were introduced in the anode gas diffusion layer and connected to a mass spectrometer (MKS mini-lab, Spektra(TM) Products) through a manual 16-port valve (Valco). The test setup is shown in Fig. 8.16, placed in a high temperature oven. The repeat-element was fed with a humidified mixture of 250Nml/min H_2 with addition of 50Nml/min argon as tracer gas.

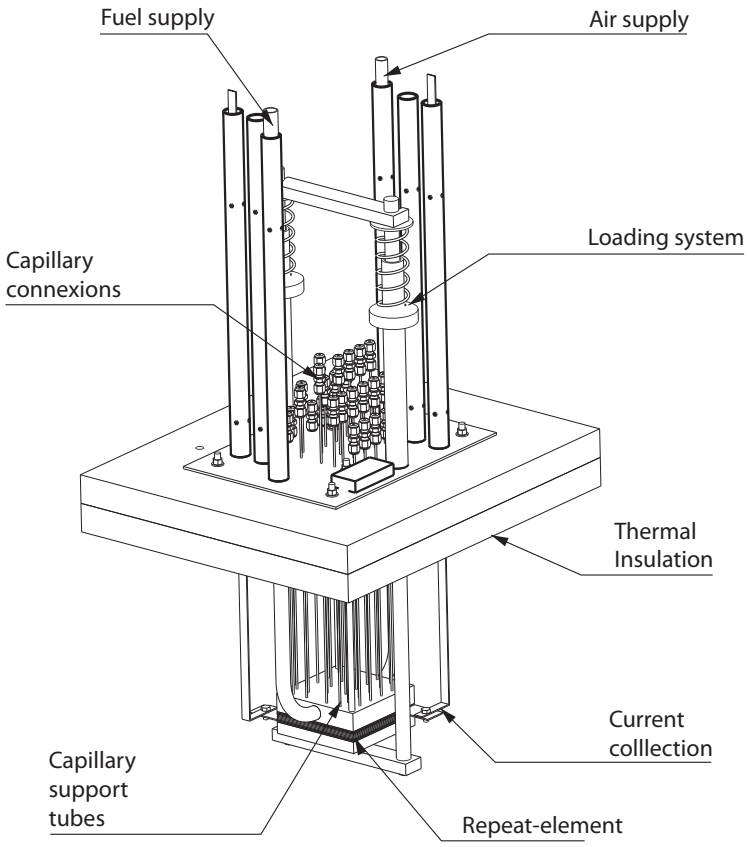

Figure 8.16: Test setup for the measurement of local gas composition.

After calibration of the mass spectrometer (MS), local gas compositions were measured under varying operating conditions. The result obtained for a fuel utilization of 50% is depicted

[8] Luong, M.T., *Résolution spatiale des réactifs gazeux dans une pile à combustible de type SOFC*, Master thesis, 2005

in Fig. 8.17, showing for hydrogen a measured spatial distribution which matches the simulated one (see Fig. 8.11), even if the latter was obtained for a slightly lower fuel utilization of 40%.
The location of the gas sampling points is shown by empty circles. This experiment was set up to investigate local electrochemical reaction rates in a repeat-element, both when using hydrogen or syngas as fuel, and not to investigate its at this time not clarified limitations. Therefore, the accent had not been set on poorly fed regions, which explains why no gas sampling port had been placed in the corners or the element, both at inlet and outlet. This missing information is indicated in the figure where extrapolation of measurements occurs.

At 50% fuel utilization, the inhomogeneous lateral distribution of fuel reported in the previous chapter is visible, particularly along the seals where partial pressures of hydrogen are found around 0.1-0.2atm. At this location, the measured steam partial pressures are in the range of 0.8-0.9 atm, whereas important uncertainties exist due to fluctuations in the calibration and in the measurements (only for steam).
Behind the fuel distribution line, the measured hydrogen partial pressure drops below 0.15 atm, while the estimated steam partial pressure is 0.3 atm, with a total inferior to unity.
In fact, the complement is found in the presence of nitrogen which was measured in im-

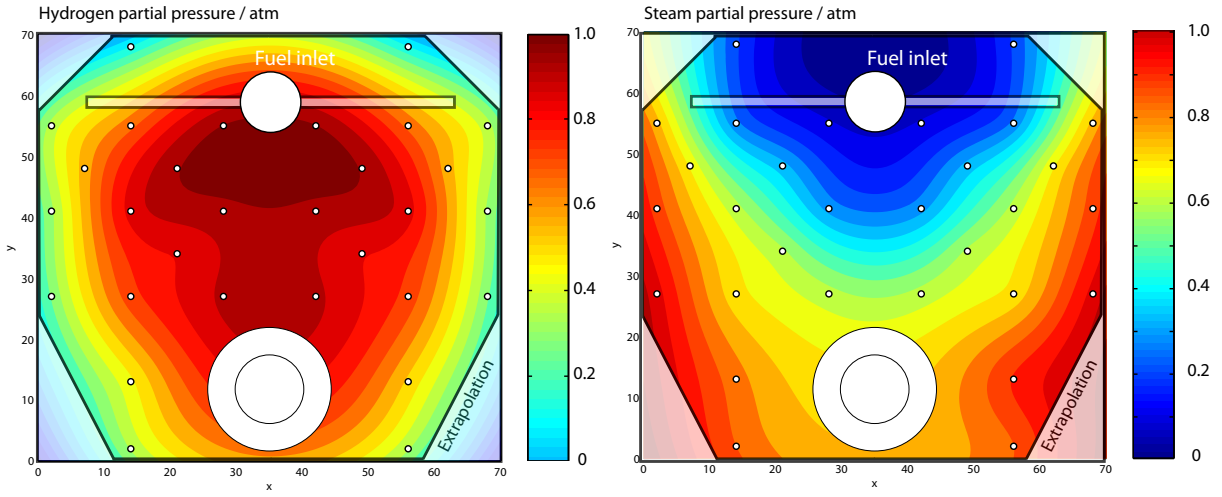

Figure 8.17: Measured local gas fractions at fuel utilization of 50%.

portant amounts in the anode GDL, despite its absence in the injected fuel mixture. The amounts of nitrogen measured at OCV are shown in Fig. 8.18, together with simulation results obtained for the same conditions and for the seal porosity fitted above. The comparison is given at OCV, as steam partial pressures are minimal and the consecutive error induced by the calibration problems for steam are minimized.

This experimental result shows that nitrogen is present in important amounts in the fuel

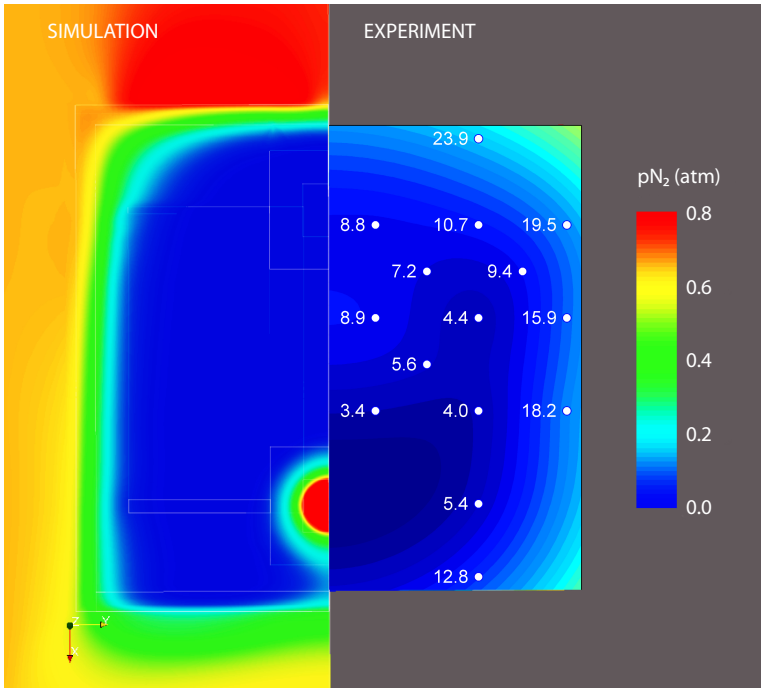

Figure 8.18: Simulated and measured local fraction of nitrogen in the anode GDL.

GDL, especially behind the fuel distribution line where it reaches a partial pressure of 0.24 atm. Along the lateral seals, nitrogen partial pressures comprised between 0.16 and 0.2 atm are found. On the simulation side, nitrogen partial pressures in the range of 0.2 to 0.4 atm are found along the lateral seals, reaching highest values of 0.7 atm in the corners behind the fuel distribution line.

Proof of diffusive mass transport across compressive seal materials. *T*he presence of nitrogen measured experimentally at these locations is an important indicator of diffusive mass transport across the seals. For an operation with dilute hydrogen, pressure drops across the stack were in the range of 10 to 20mbar, which corresponds to an overpressure of the anode GDL with respect to the oven due to the open post-combustion. Consequently, if diffusive mass transport didn't occur in the seals, only transport towards the oven would occur along the lateral seals, in contradiction with the observed presence of nitrogen at these locations.

Consequently, this final result completely demonstrates the importance of diffusive transport in compressive seal materials for the resulting behavior of the fuel cell and for a complete assessment of their applicability.

8.5.4 Summary of validation

Besides its effect on the resulting OCVs, the diffusion in the seal materials induces numerous possible degradation and failure issues, which are not only predicted by the model but also observed experimentally. Therefore, the hypothesis of an important contribution of diffusion to the real seal behavior is assumed to be fully validated.

From a qualitative point of view, the model reproduces the problems observed in experiments well:

- Low OCV
- Parasitic combustion
- Redox-cycles induced by polarization
- Degradation of the cathode near the internal seal
- Presence of nitrogen on anode side

A quantitative comparison could be obtained with good agreement on the following points:

- For the simulated OCV, the porosity parameters that fit the OCV ($\varepsilon = 28.8\%$) are of the same order as the estimated porosity of mica paper ($\varepsilon = 59\%$)
- The fitted porosity is valid for different fuel flow rates
- The overheating resulting from combustion on the lateral seals is well reproduced
- The measured nitrogen fractions on the anode side are well reproduced by the model

Therefore, the model is considered as validated and applicable for degradation studies, because it represents and explains in consistent manner degradation and failure phenomena observed in experiments, presenting at the same time a good agreement with the performed quantitative analyses.

8.6 Conclusion

As shown in this chapter, the use of compressive seal materials presenting a residual porosity, as well as the way the *R-design* stack is constructed, is identified by modeling and by experimental work as one major source of failure. The reason for this is the existence of local redox-limits in the vicinity of seals, which leads to repeated redox-cycling of the cells under varying operating conditions. In addition, similar damage of the cathode layer is found to occur by exposure to reducing conditions. This type of damage leads however uniquely to losses of performance, and less to reliability issues.

To obtain this explanation, the hypothesis of diffusive mass transport in seals was made. By including it in the model, several degradation patterns observed in experiments were reproduced with accuracy, giving an insight in the coupling of design aspects, choice of materials and operating conditions leading finally to a strong risk of failure. Moreover, by introducing these non-ideal properties of the used materials, a reconciliation of the experimental observations and of the modeling work could be obtained, in particular also on performance.

Finally, these developments allowed to clarify the reason for the low OCVs observed in experiments, therefore allowing to conclude the investigations on this topic.

In the next chapter, the consequences of this result on the operation range of the *R-design* stack is presented, and possible solutions are presented to solve this issue.

Chapter 9

Operation guidelines and design of reliable stacks

9.1 Introduction

In this chapter, the consequences of the reliability issues identified in the previous chapter are analyzed. First, it is shown that with the seal material used originally, it is not possible to find any operation range which might prevent failure. Second, it is investigated whether improved seal materials would solve the problem. It is shown that, even with better seal properties, the *R-design* stack remains heavily affected by the redox-cycling issue.
More important, modeling made on the *S-design* stack shows that this design is also sensitive to this problem.
Finally, it is demonstrated that design solutions are possible to prevent this issue, showing excellent results obtained with the consequently designed *F-design* stack.

9.2 Critical operation phases

In the validation procedure, the CFD model has shown its ability to predict numerous degradation effects related to the use of porous seals in a specific stacking configuration. It can now be used for design, for the investigation of different sealing materials, and for the definition of operation guidelines. To define operation guidelines, the critical operation phases for the stack are described.

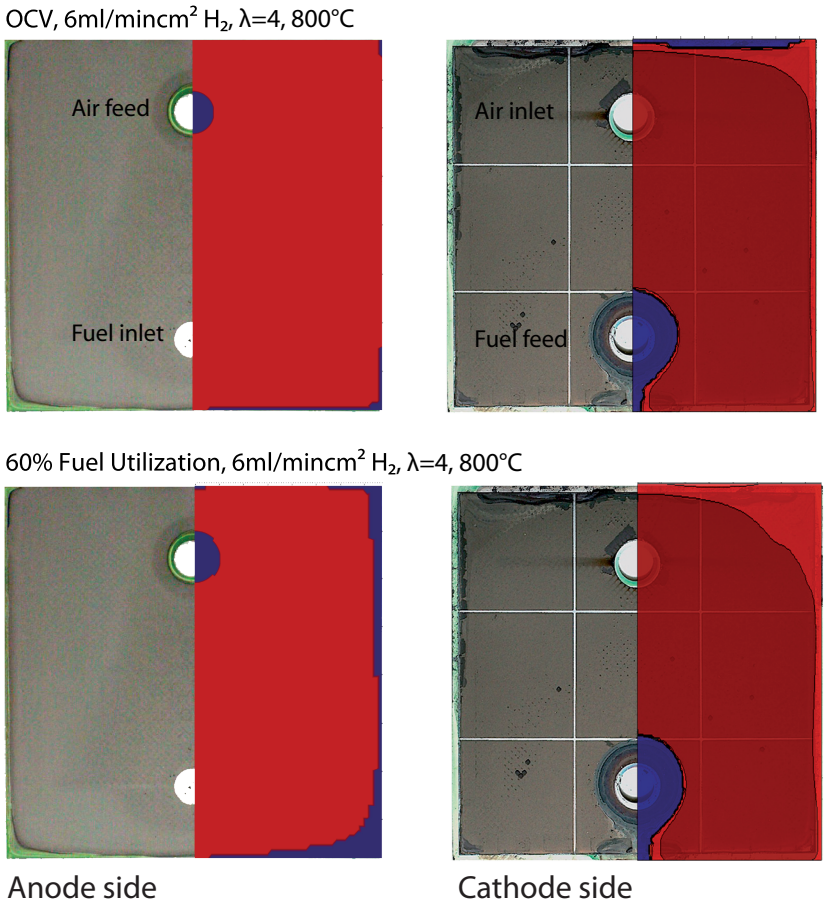

Figure 9.1: Predicted damage of the electrodes at different operating points (right). Picture of typical cell damage after operation (left). OCV, 60% FU.

9.2.1 Load cycling

As described in the previous paragraphs, load cycling results in local redox-cycling of the anode in defined areas, in addition to a degradation of the cathode by reduction. Additional aspects are treated in the following paragraphs.

OCV Figure 9.1 depicts the predicted degraded areas both on the anode and cathode sides for different operating points. At OCV, for a nominal fuel flow rate of 6 $\mathrm{ml\,min^{-1}\,cm^{-2}}$ H_2 and a lambda of $\lambda = 4$, the corners near the fuel inlet are already oxidized. In addition, the hole for air feed presents a ring of oxidation under the seal. On the cathode side, an important area is reduced along the post-combustion side, as well as the totality of the cathode located under the fuel manifold's seal gasket. In addition, a band of cathode is exposed to reducing species downstream of it, as attested by visible traces on the depicted cell.

High fuel-utilization At a (for the *R-design*) high fuel utilization of 60% (see previous chapter), important areas of the anode are oxidized in the corners. More important, this oxidized area does not only affect the part of the cell pressed between the seals, but also the internal volume of the gas-diffusion layers. The risk of internal leakage is therefore increased in the presence of propagating micro-cracks in the anode support. Similarly, the totality of the cell's edges is oxidized, with exception of the fuel outlet. Around the air supply hole, the oxidized ring expands towards the interior of the repeat-element. Finally, a singular oxidized spot is found in the center of the outlet region, not far from the oxidized region of the air supply hole.
On the cathode side, the reducing region decreases with increasing fuel utilization, due to a diminution of the hydrogen partial pressure in the post-combustion flame, allowing the reduction front to move outwards. The situation around the fuel manifold remains unchanged, as it is principally dictated by the composition of entering fuel.

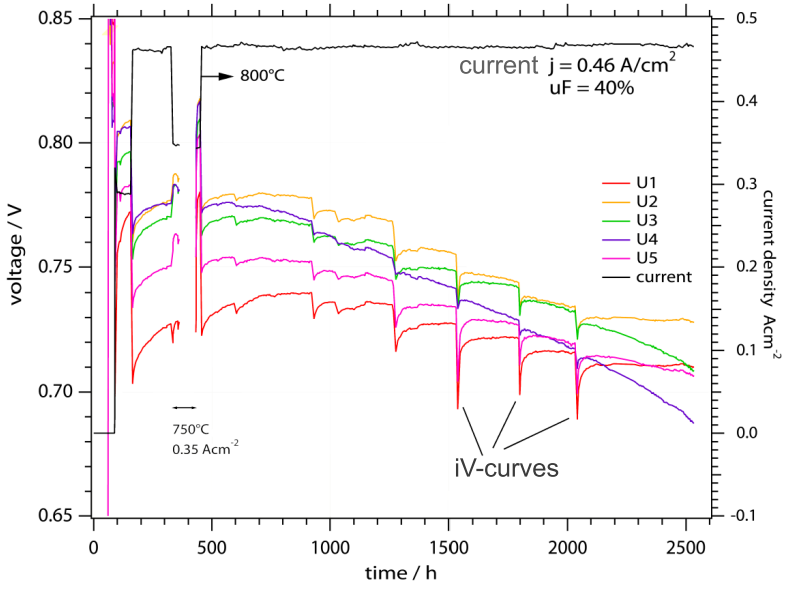

Figure 9.2: Reference test ms95: stepwise degradation of performance with load-cycling during long-term testing (800°C, 0.4 NL/min H_2 + 3% H_2O).

Load cycling Lowering of OCV with time and degrading performances are systematically observed on long-term tests. One part of the degradation can be explained by the degradation of materials, which however is expected to occur in continuous manner. Instead, a step-wise degradation was observed in several experiments each time when performing i-V characterizations (corresponding to successive load-cycling), as shown in fig. 9.2.
This figure shows the behavior of the reference short stack MS95 during its long-term test at

constant current (40% FU, 23A). During the i-V characterizations, the current was increased, exceeding the stationary polarization current. As result, a drop of OCV and potential was observed on all cells after each load cycle.

The corresponding simulated performance and oxidation of the anode support are shown in

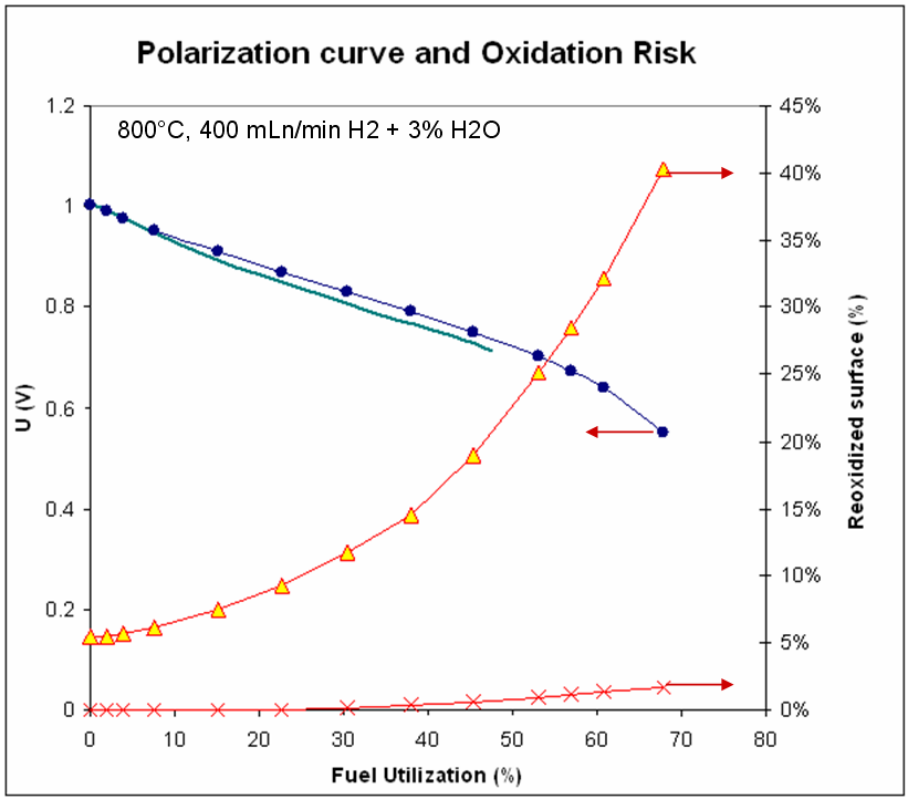

Figure 9.3: Test MS95: measured (−) and predicted electrochemical performance (•), predicted oxidized area in the reacting zone (×) and under the seals (△)

Fig. 9.3. The IV-curve is starting at the fitted OCV of 1.006V. At a fuel utilization of 60%, an inflexion is observed and the potential starts to drop, indicating the presence of internal limitations. The percentage of the cell area located under the seals that is re-oxidized (△) is increasing up to 40.3%, with one part (5%) already oxidized at OCV, as shown above. For the active cell area (×), the re-oxidation process starts at 30.4% FU and reaches 1.69% at 67.9% FU.

These predicted redox-cycles can here explain the observed drop of potential if the redox-cycle is accompanied by an irreversible degradation of the cells. This topic is addressed hereafter.

As the redox-cycling is present in the full range of fuel utilization, it is difficult to establish operation guidelines that could prevent or reduce degradation. For the *R-design* stack, an operation above 30.4% FU should have been avoided in order to prevent the reacting zone from being re-oxidized, this operation limit, indeed, being unrealistic in terms of efficiency.

9.2.1.1 Maps of performance and operation risk

To investigate the risk associated with a specific operating point, maps of operating risk were established, similarly to the ones describing the performance of the stack. These maps summarize the risk to oxidize the anode support, with separation of the inactive anode areas from the active one, and the risk to degrade the cathode by reduction. The resulting map for the fitted case (28% seal porosity) is shown in Fig. 9.4.

First, when compared to the case of solid seals (see paragraph 7.3.2.1), the performance of

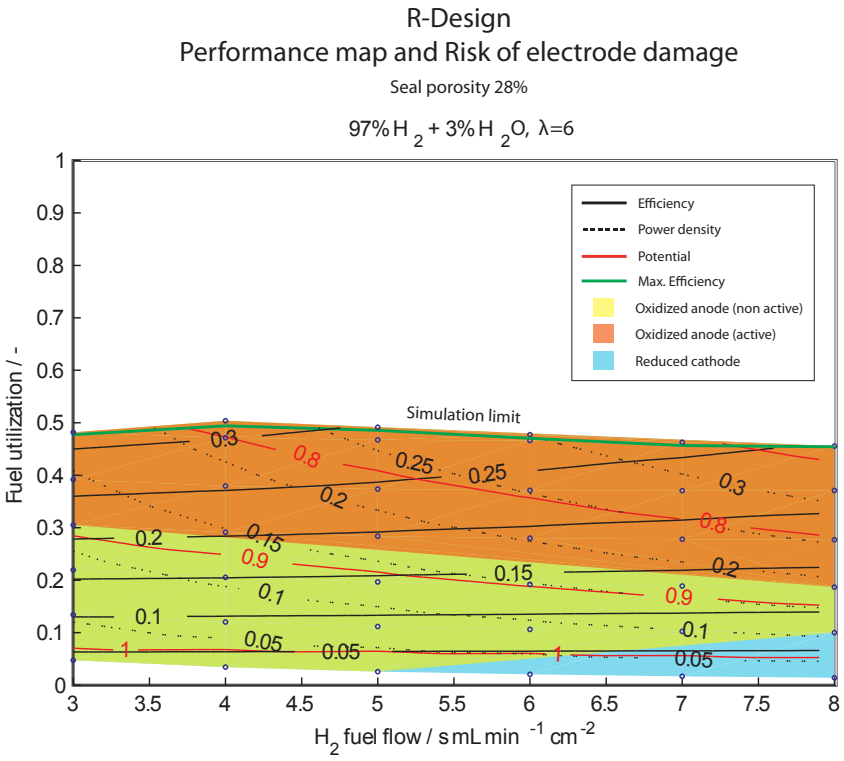

Figure 9.4: Performance map of the *R-design* prototype with associated risk of electrode damage ($\varepsilon = 28\%$).

the *R-design* prototype is completely modified by the introduction of the seal porosity, even for an operation under humidified hydrogen. First, the best efficiency is attained at fuel utilizations lower than 50%, corresponding to the simulation limit chosen for the computation of such maps. Beyond this limit, diffusion-limiting areas are found in the repeat-element. To discriminate between diffusion-limited areas (where hydrogen starvation at the electrolyte occurs due to the electrochemical reaction) and oxidized areas (due to the presence of oxidizing gases), the electrochemical reaction is disabled in any region of the cell where oxidizing conditions are found for the anode support. The simulated maximum efficiencies are 31%, attained at low fuel flow rates (3-4 $\mathrm{ml\,min^{-1}\,cm^{-2}}$). In fact, a maximal efficiency of 39% was obtained with *R-design* stacks, which is higher than than the predicted value, but much less than the 54% in the case of solid seals.

For the case of the experiment MS95, an efficiency of 25% was attained for the best cell at a fuel utilization of 40%. The fuel flow rate was 8 $\mathrm{ml\,min^{-1}\,cm^{-2}}$ H_2 (humidified). The corresponding simulated efficiency at this operating point is 24%, as shown in the performance map. This indicates that the performance of the repeat-element can be estimated correctly even when parasitic diffusion is taken into account.
The resulting operation risk is indicated by colored areas. The yellow area indicates the points where the anode support is being re-oxidized, but only for the surfaces apart from the principal active area (that is, for the *R-design* stack, the active areas under the seals). A threshold value of 5% of the surface is set as minimum, explaining the absence of the indicator at OCV.
The blue area corresponds to operating points where the cathode is partly reduced. Finally, the red area corresponds to the case of an oxidation of the main active area (the active area for the other stack designs).
For the three colors, transparency is used to indicate cumulative damage of different type. In this case however, the important overlapping of critical operating conditions complicates the interpretation of the map.
For instance, the damage of the cathode by reduction occurs over the complete operation range, similarly to the oxidation of the non-active anode zones. On the other hand, the oxidation of the principal active area occurs at a threshold fuel utilization which varies depending on the fuel flow rates. At the lowest fuel flow rate, the threshold value is found at a fuel utilization of 30%, while it occurs at about 20% for the highest flow rate corresponding to the test MS95. This difference results from slight differences in the flow fields.
From this map, it is evident that there is no operating point where reasonable fuel utilizations can be attained without damaging the cell, and this for the whole range of fuel flow rates. Therefore, the combination of this stack concept and the use of mica paper as seals leads to a strong limitation of the reliability of the stack, together with a limitation of its performance. As shown hereafter, the situation changes when using seal materials presenting lower porosities.

9.2.1.2 Operation risk with improved seal materials

As shown in the previous paragraph, both the performance and reliability of the *R-design* stack are strongly affected by the use of mica paper as seal materials. Therefore, the use of improved seal materials was considered as a possible solution, while maintaining the use of compressive seal materials for production issues. By using the model, the expected modification of the map of performance and risk was assessed. The resulting maps are shown in Fig. 9.5, where different seal porosities (5% and 10%) are considered, both for pure and 50%-dilute hydrogen.

First, a considerable improvement in the maximum achievable fuel utilization is obtained in all cases, with diffusion limitations occurring in the range of 70% FU at low fuel flow rates for pure hydrogen (humidified). Due to the lower porosity, this value is shifted to 75% FU for a seal porosity of 5%. At high fuel flow rates, the maximum achievable fuel utilization is found around 60% for both porosities. Similarly, the consequence on the maximum

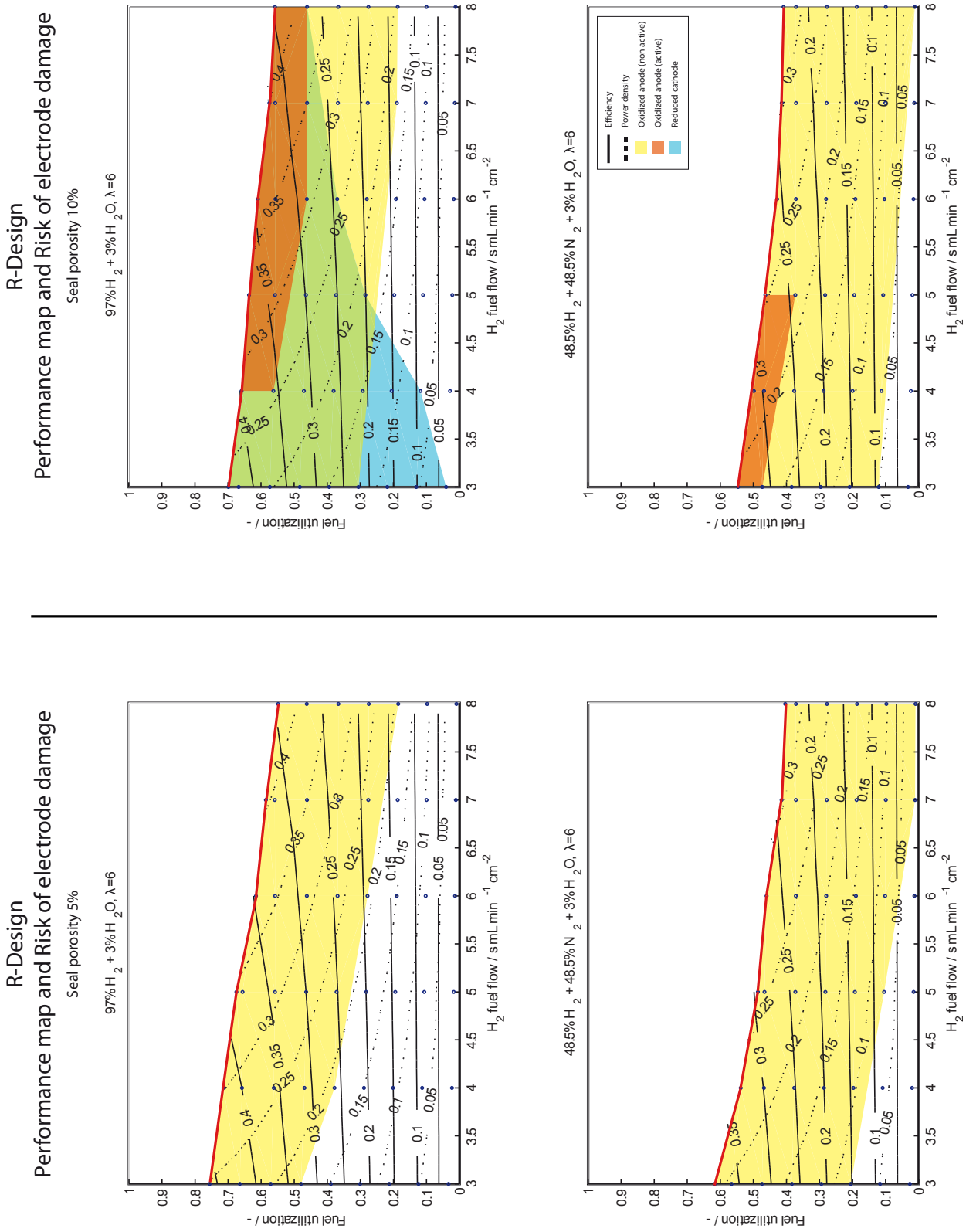

Figure 9.5: Performance map of a *R-design* stack with associated risk of damage of the electrodes.

achievable efficiencies is important. At the lowest porosity, maximal efficiency of 45.5% is achievable, whereas it is slightly lower (43%) for a porosity of 10%. At the highest fuel flow rates, which correspond to the reference test MS95, the maximal efficiency remains below 30% in any case.
When operating the repeat-element with dilute fuel mixtures, the maximum achievable fuel utilizations and efficiencies are further reduced, achieving with the best seal highest fuel utilizations of 60% and 37% of efficiency at the lowest flux .

The improvement of the porosity of the seal not only affects the performances, but also the associated operation risk. The most important effect is found for the risk of a reoxidation of the principal active area, indicated by a dark-orange color. For the seal with highest porosity, an oxidation of the main active area appears at fuel utilizations larger than 50 to 60% when operated with pure hydrogen, with a notable exception at low fuel flow rates. The explanation for this is the difference in the generated steam amounts, which, for large fuel flow rates, accumulate in more important amounts in stagnating areas.
For dilute mixtures, the operation limit occurs before or simultaneously with the oxidation of the main active area for fuel flow rates larger than 5 $\mathrm{ml\,min^{-1}\,cm^{-2}}$ H_2 , explaining the absence of red area above this threshold flow rate. At low fuel flow rates, a risk of damage occurs starting at fuel utilizations comprised between 40% and 50% FU.
The other risk of damage, which only occurs with the higher seal porosity, is the reduction of part of the cathode. This risk is only present for pure hydrogen (humidified). In fact, the dilution with nitrogen reduces the diffusive leakage through the fuel manifold towards the cathode GDL.
To conclude, and as attested by the established maps, an improvement of the seal's porosity principally improves the protection of the stack against the reoxidation of the anode in the active area, as well as against the reduction of the cathode. However, in all cases, parts of the anode outside of the active area are being oxidized upon increases in the applied current. This result shows therefore that an improvement in the properties of the seal is not sufficient to solve the redox-cycling problem for *R-design* stacks.

9.2.2 Thermal cycling

Another highly critical operating point is represented by the operation with lean fuel mixtures (10% H_2 - 90% N_2) during thermal cycling, as shown in Fig. 9.6. In this case, the predicted redox limit on anode side is located far inside the repeat-element. As the cell shown on the left hand side of the picture was not cooled down with this dilution, this pattern is not visible. It is however visible in Fig. 8.12 or in Fig. 9.7, indicated by a dark-green / dark-grey area.

The attribution of dark-green / dark-grey areas to a (partial) oxidation during thermal

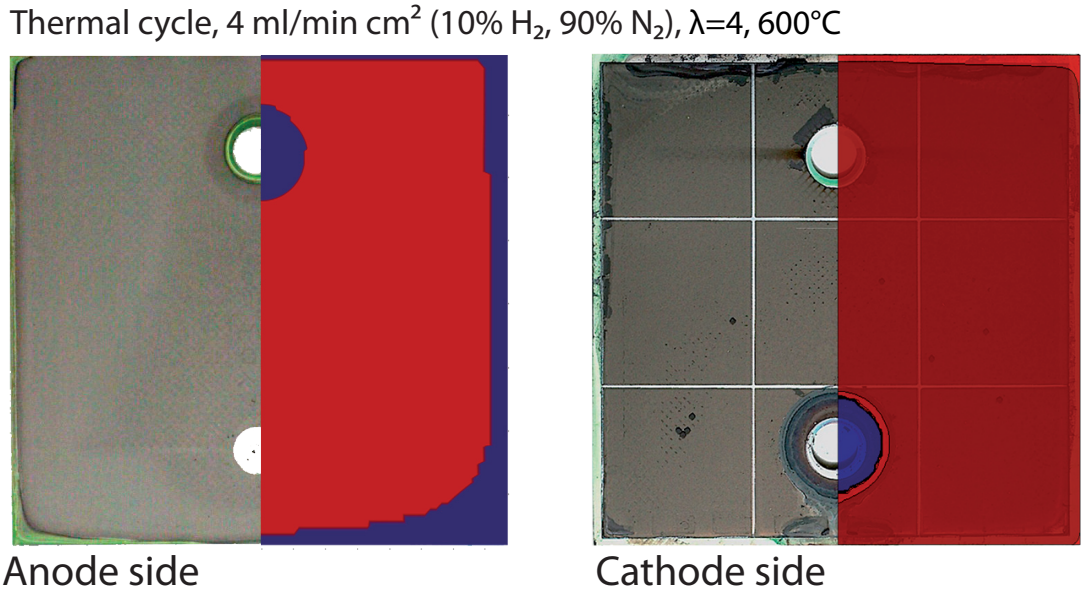

Figure 9.6: Damage of the electrodes during thermal cycling under dilute fuel.

cycling was possible thanks to an analysis of NiO samples oxidized at defined temperatures. The color of NiO samples oxidized at different re-oxidation temperatures is shown in figure 9.7 [1]. The samples were obtained by the reduction of NiO powder at 800°C, followed by a re-oxidation at a controlled temperature.

The samples oxidized at low temperature present the already mentioned dark colors, resulting from the presence of black nickel oxide Ni_2O_3 formed preferentially at low temperatures. This analysis technique based on the color of the obtained oxides can in this case contribute to the interpretation of post-experiment analyses.

An extreme example of reoxidation during cool-down is shown in Fig. 9.8, showing a cell after disassembly and the corresponding simulation. This cell was operated in the frame of the SOFC600 European Project. After a reduction at 800°C, the repeat-element was operated at 600°C. Before cooling down, the fuel composition was set to a strongly dilute mixture of 2% H_2 - 98% N_2 . On this cell, the presence of nickel re-oxidized at low temperature is visible, resulting in an almost black color of the oxides. An excellent match of the oxidized areas is

[1] Samples prepared by A. Faes, who is gratefully acknowledged.

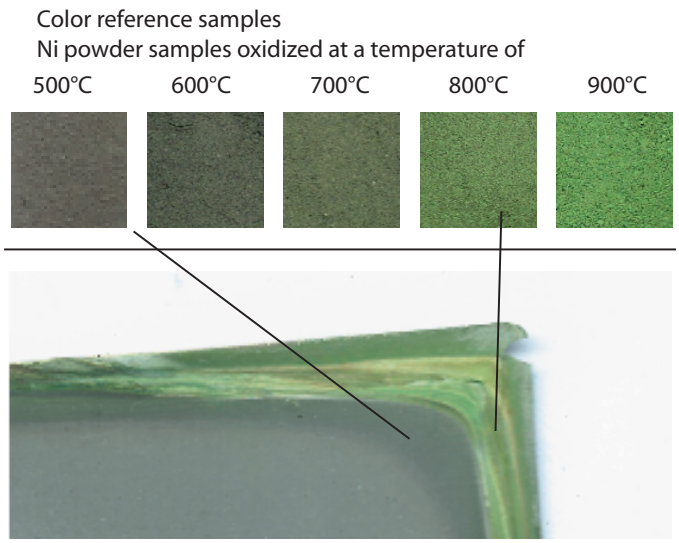

Figure 9.7: Color of re-oxidized nickel as function of the oxidation temperature. Corresponding identification of the local re-oxidation temperature on a cell sample after operation.

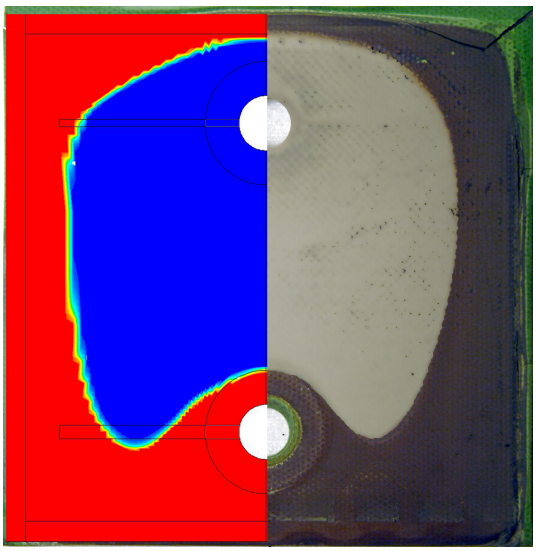

Figure 9.8: Low-temperature re-oxidation of a *R-design* repeat-element by lean fuel mixture during cool-down. Corresponding simulation of the redox-limit (red: oxidized, blue: reduced)

found between simulation and experiment for this case again. This demonstrates finally that *R-design* prototypes cannot be implemented in systems where such lean fuel mixtures are mandatory during cool-down and startup, as it represents an unacceptable risk of damage for the cells.

9.3 Cumulative effect of successive critical operating points

As shown throughout this chapter, local redox-cycling issues are inherently linked to the design of the seal system of the *R-design* prototype, together with the utilization of compressive seal materials showing residual porosity. As consequence, a series of possible corrective actions on the design side were considered. Besides a complete redesign or the stack, one possibility was to limit the areas exposed to redox-cycling. However, as attested by the loss of performance upon load-cycling observed for the MS95 experiment (see Fig. 9.2), a risk of propagation of the damaged areas was assumed to possibly exist, resulting from successive critical operating points. To verify this hypothesis, the redox-cycling ability of the cells was studied in more detail, in collaboration with A. Faes (CIME, EPFL).
To investigate the effects of local redox-cycling on cells, samples were reduced and oxidized several times and at various temperatures. A. Faes observed that, even if the anode-support of the samples remained macroscopically intact, micro-cracks were systematically observed through the electrolyte, as shown in Fig. 9.11. Moreover, it was found that the width of such cracks increases with the number of redox-cycles [4], in addition to an increase in the porosity of the anode support. Based on these results, Faes was able to establish a relation

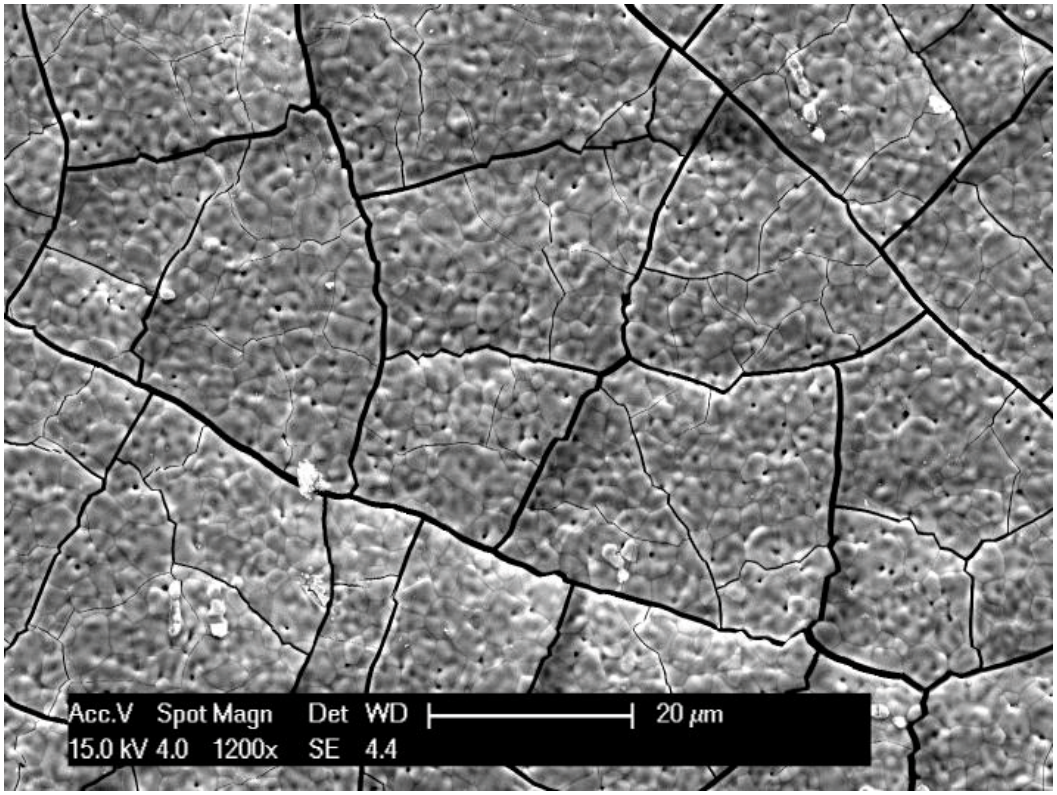

Figure 9.9: Fractured electrolyte surface after one redox-cycle at 800°C. *Courtesy of A. Faes, CIME LENI, EPFL*

between the number of local redox-cycles and the resulting anode strain, evaluated either by measuring the width of cracks in the electrolyte or the resulting porosity variations. The result is shown in Fig. 9.10. In addition, Faes proposes a fit of the data by a relation of the

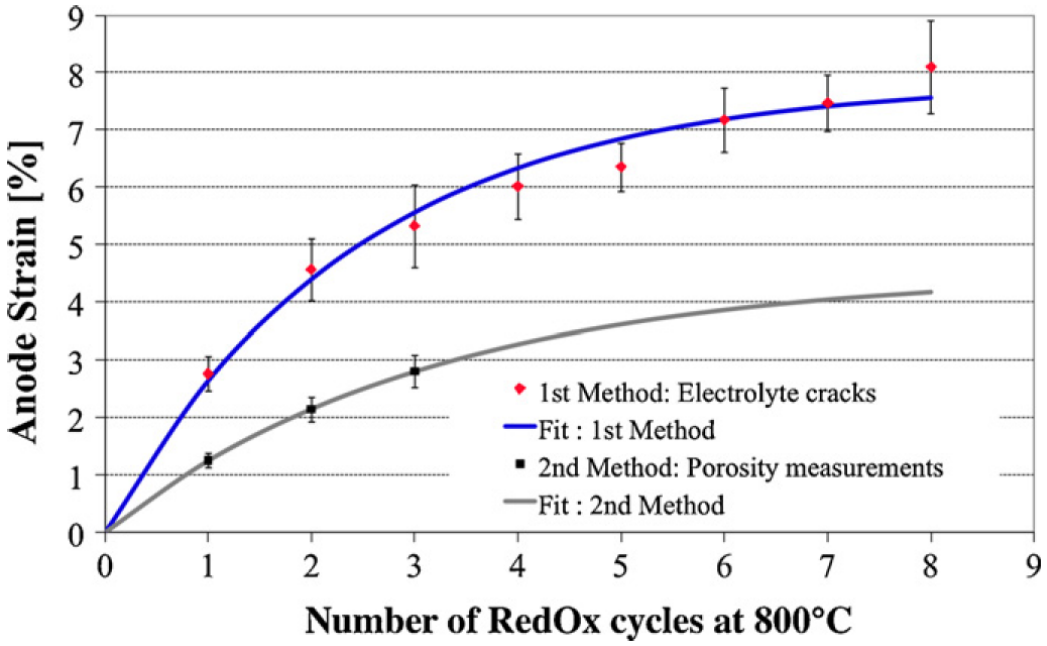

Figure 9.10: Top: Cross-section of an anode support at the edge of a cell where redox-cycling occurred (R-design stack). *Reproduced from Faes et al. [4]*

type:

$$\varepsilon_{anode} = \varepsilon_{max}\left[1 - exp(-\frac{N}{\mathcal{N}_0})\right] \tag{9.1}$$

where ε_{max} represents the maximal strain, N the number of redox-cycles at 800°Cand $\mathcal{N}_0$ is a characteristic number of redox cycles. Depending on the evaluation method, the maximal strain ε_{max} was estimated between 4.5% and 7.9%, while the characteristic number $\mathcal{N}_0$ was evaluated between 3.0 and 2.5 [4].

In parallel, post-experiment analyses were performed on cell edges that had been damaged during stack operation. Figure 9.11 shows a cross-section of a damaged anode-support situated under a lateral seal of a *R-design* stack, where redox-cycling occurred. Large cracks are present throughout the anode support. The presence of micro-cracks in the electrolyte is confirmed, propagating through the cathode layers.
Moreover, a porous microstructure is visible in a layered arrangement, resulting from parasitic combustion in the anode support itself, as shown below. Faes et al. estimated the local porosity at the points marked in Fig. 9.11 by image processing. Based on the above-mentioned relation, he was able to evaluate the number of local redox cycles experienced by the cell, details of which can be found in reference [4].
This figure attests of the important damage of the cells exposed to redox-cycling.

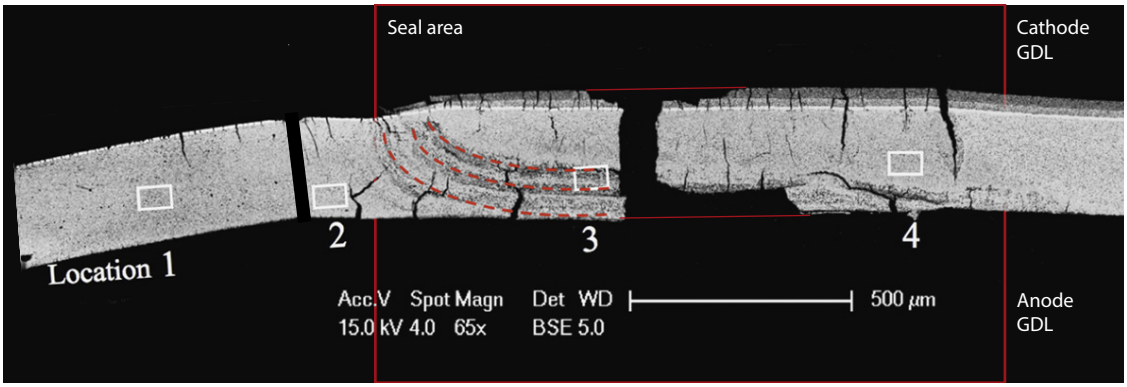

Figure 9.11: Top: Cross-section of an anode support at the edge of a cell where redox-cycling occurred (R-design stack). *Reproduced from Faes et al. [4]*

9.3.1 Modeling of the effect of a fractured electrolyte

In order to understand the effect of micro-cracks in the electrolyte on the local electrochemical behavior, a model was developed that allows to study the diffusion of oxidant and fuel through the electrodes and the electrolyte resulting in parasitic combustion. The model was established in 2-dimensions, but respecting the ratio of crack area over total area of the electrolyte observed experimentally.
As the anode support is exposed to varying fuel compositions, which is particularly true near the seals and under varying fuel utilizations, the effect of fuel composition was studied. An example is given for a hydrogen-steam mixture on fuel side (Fig. 9.12), with cracks of 2 microns width in the electrolyte. The model shows the zone where the anode support should be exposed to oxidizing atmosphere at various hydrogen partial pressures (Fig. 9.12, top). Below 20% H_2 , the anode support is oxidized under the electrolyte, which should disable the electrochemical reaction. Combustion of hydrogen and oxygen occurs in the anode support, which corresponds to the porous layers observed in Figure 9.11. Above 20% H_2, the model predicts that the combustion front reaches the electrolyte, passing on the cathode side and starting to reduce the cathode layers. At 80% H_2, the cathode layer is completely exposed to a reducing atmosphere, with additional degradation due to parasitic combustion.
Even if the values may vary depending on the properties of the porous electrodes and on the density of cracks, the model allows to illustrate the process occurring in such areas. From the model, it can be concluded that, once the electrolyte is cracked and for most of the fuel compositions, either the anode is being re-oxidized under the electrolyte, or the cathode is exposed to a reducing atmosphere. In both cases, the electrochemical reaction will be highly affected.
As it is not possible to solve this micro-model over the whole cell area in a repeat-unit model, a simplified model is established. As it is known from experiments that cracking of the electrolyte occurs at the first redox-cycle, the electrochemical reaction is therefore simply disabled after the first local redox-cycle. In addition, a leakage flux is applied in form of leakage current, which is proportional to the above-mentioned function that links the anode

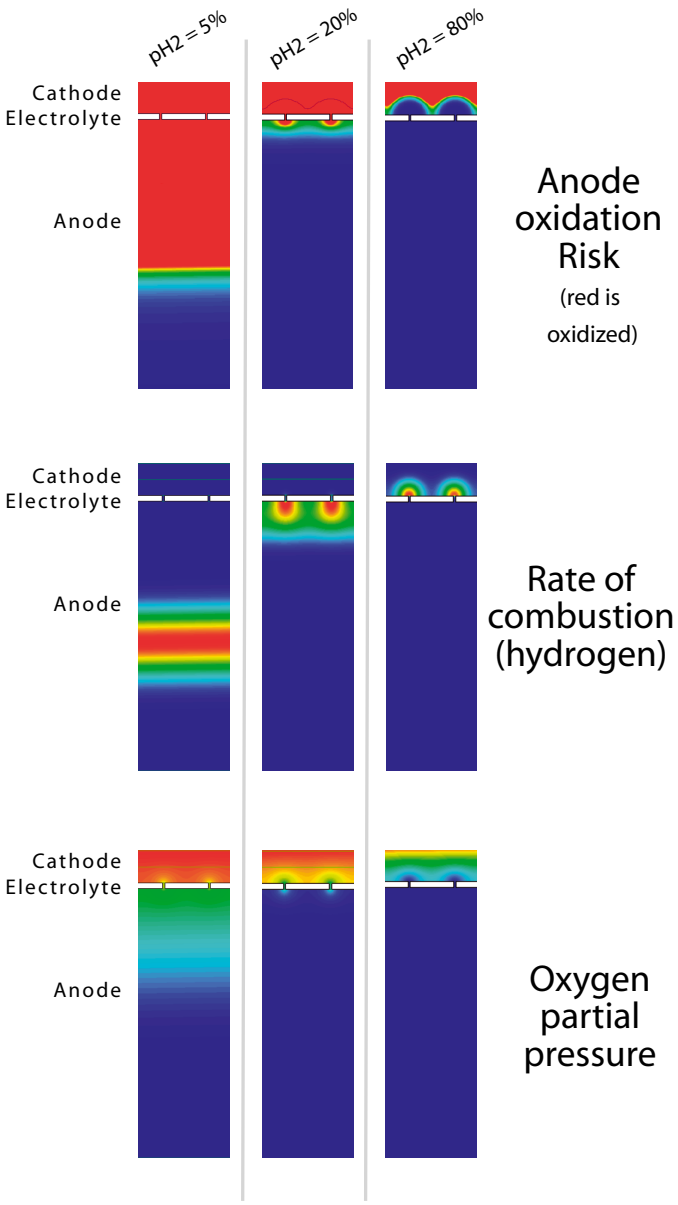

Figure 9.12: Simulation of parasitic diffusion and combustion across a cell with cracked electrolyte, as function of the fuel composition. Anode is oxidized under the electrolyte at low hydrogen content. Cathode layer is reduced at large hydrogen partial pressures.

strain, and hence the crack width, to the number of local redox-cycles registered by the model:

$$j_{loss,crack} = j_{max} \cdot pH_2 \cdot \left[1 - exp(-\frac{N}{\mathcal{N}_0})\right] \tag{9.2}$$

where j_{max} $[Am^{-2}atm^{-1}]$ is a constant corresponding to an equivalent leakage flux for pure hydrogen and an infinite number of cycles, pH_2 $[atm]$ is the local hydrogen partial pressure, and N and $\mathcal{N}_0$ are respectively the number of redox cycles and the corresponding character-

istic number for the electrode.
In this relation, a dependance of the hydrogen partial pressure is introduced, as it determines the rate of combustion in the anode support. This relation is of course a very simplified approach of the reality. However, it has to be pointed out that it is a qualitative behavior which is searched for in this case, a quantitative one being impossible to attain due to strong differences among damages of electrodes.

9.3.2 Propagation of damaged areas

With an increasing anode porosity and crack density with each local redox cycle, a cumulative effect appears, which has an incidence both on cathode and anode side. As an example, a series of 4 successive load cycles is modeled, first up to 40% fuel utilization, and then three times to 60% fuel utilization. In Figure 9.13, the affected areas are indicated by color changes depending on the number of local re-oxidations (anode) or reductions (cathode). Interestingly, it shows that the degraded areas increase with the number of cycles, with the presence of certain zones which particularly cumulate the damaging cycles.
In addition, not only the damage on the anode side is increased, but also the one on cathode side, where the resulting leaks across the cell result in a permanent reduction of the cathode. This increase in damaged areas can explain the successive drops in performance reported in Figure 9.2, as well as the presence of highly damaged cells at these locations after operation. In addition, it can partly explain the observed losses in performance accompanying thermal cycles with this design, due to the large oxidizing areas on anode side under diluted fuel mixtures.

9.3.3 Consequences for the stack design

With this assessment on the cumulative damage resulting from inappropriate operating points, it is clearly shown that the *R-design* prototype is not only exposed to damaging conditions for its components, but much more that the resulting damage will inevitably propagate upon changes in the operating points.
This gives a final evidence for the need of a complete redesign of the stacks to prevent this major source of failures.

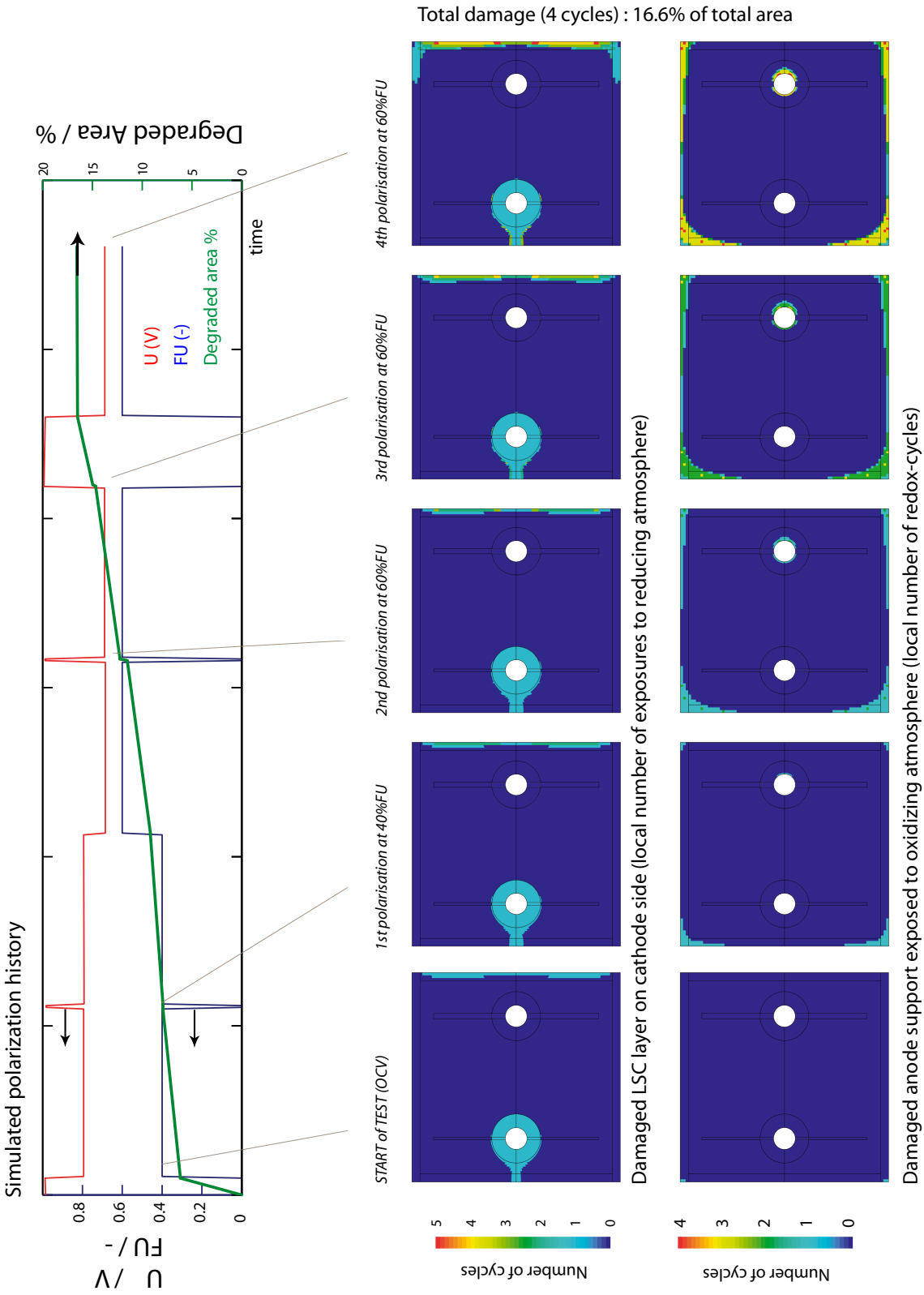

Figure 9.13: Example of cumulative degradation effect obtained during a series of load cycles.

9.4 Generalization of the result to the *S-design* stack

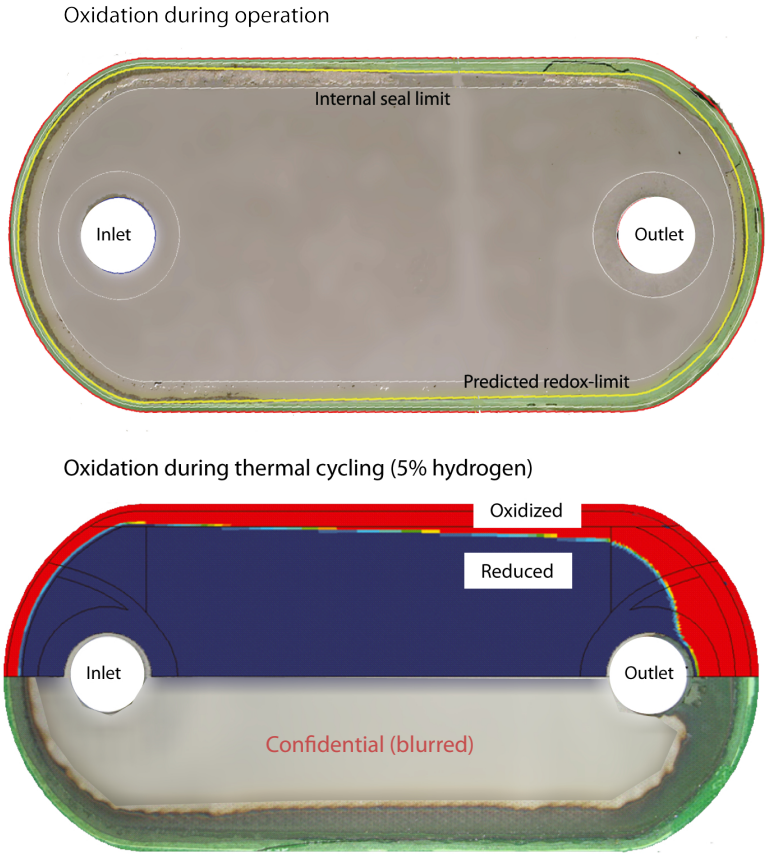

Figure 9.14: Typical re-oxidation patterns observed on *S-design* cells after operation. Top: re-oxidation during operation. Bottom: during thermal cycling with use of highly diluted fuel.

As mentioned in the previous paragraphs, the *S-design* stack suffers from issues similar to the *R-design* prototype, as its sealing arrangement is analogous (compare Fig. 3.4 and Fig. 3.3). In particular, the seals on anode side are again placed in a dual atmosphere, resulting in moving redox-limits upon load changes.
Fig. 9.14 attests of this situation, both for a partial reoxidation of the cell during operation (top) and an important risk of reoxidation during thermal-cycling (bottom).
On top, a cell is depicted which was operated at a maximum fuel utilization of 70%, under a 50% dilute hydrogen-nitrogen mixture. The simulated redox-limit for a fuel utilization of 70% is indicated by a yellow line. An excellent match is obtained between simulation and experiment, showing that the redox-pattern observed on the cells corresponds to the worst operating conditions in terms of redox issues, that is in this case, a high fuel utilization. As the stack was cooled down without additional dilution of the gases, no associated re-oxidation pattern is visible (dark grey/green areas).

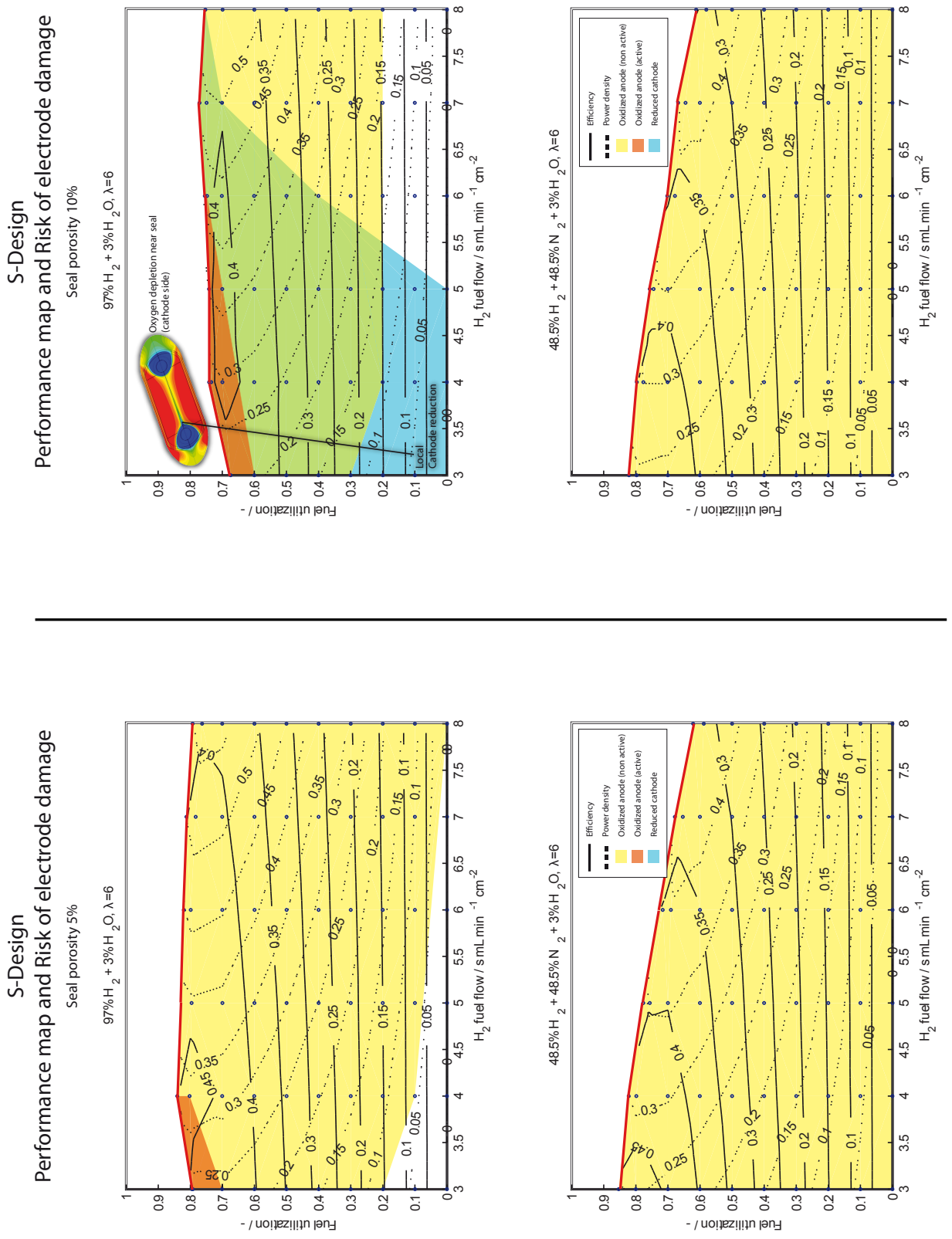

Figure 9.15: Performance map of *S-design* stack with associated risk of damage of the electrodes.

The contrary is true for another experiment, shown on the bottom of Fig. 9.14. This repeat-element comes from a 36-element stack operated in a HoTbox^{TM} , where a strongly diluted fuel (5% H_2 , 95% N_2) was injected during cool-down. The CFD model was used to determine the cause of the observed re-oxidation pattern, using the gas flow rates and dilutions used during this critical operation phase. Again, a good match is obtained between simulation and experiment, giving an explanation for the observed degradation.

As a synthesis of the risk of damage, a complete *map of performance and risk* of the *S-design* stack is shown in Fig. 9.15 for different seal materials presenting porosities between 5% and 10%.
First, a noticeable effect of the seal porosity on the maximal achievable performance is found, both for pure and dilute fuels. Using a 10% porous seal, a maximal efficiency of 41% can be attained with pure hydrogen, at fuel flow rates comprised between 4 and 6 $\mathrm{ml\,min^{-1}\,cm^{-2}}$ H_2 . In this case, the maximum fuel utilization is attained between 70% and 80% of fuel utilization. These values are well below the ones attained with solid seals.

For the lower porosity, the maximal efficiency attains 46%, while the maximal fuel utilizations are shifted above 80%. This case is therefore closer to the ideal situation of fully gas tight seals.
A similar impact on performance is found for dilute fuels, where the maximal efficiencies are respectively 44% and 46%, presenting in addition more similar maps of performance and risk.

Concerning the risk of electrode damage, the maps indicate that in all cases an oxidation of the non-active anode areas is present, with at least 5% of the surface oxidized above 30% of fuel utilization for all cases. A more critical issue is predicted to occur at low fuel flow rates and high fuel utilizations, with a partial reoxidation of the anode in the active area. The corresponding situation is depicted in Fig. 9.16 for a fuel utilization of 75% at a fuel flow rate of 4 $\mathrm{ml\,min^{-1}\,cm^{-2}}$ H_2 . Along the lateral seal, the hydrogen mole fraction is lowered and the steam partial pressure increased due to the parasitic combustion in the seals. Moreover, the nitrogen mole fraction increases up to 30% along the flow in vicinity of the seals, resulting in a higher dilution of the fuel at this location. The situation is even worse in the outlet collection area, where the hydrogen mole fraction reduces to zero, as attested by the presence of oxygen in the anode GDL. Even if this region is not electrochemically active, the resulting oxidation of the cell represents an unacceptable risk. The same occurs at the end of the active area where an oxidation of the cell is predicted locally by the presence of oxygen.

To explain the more important risk observed at low fuel fluxes, the parasitic combustion of hydrogen is determined by its diffusion in the seal, and therefore by its partial pressure along the seal's surface. The consequence is a larger amount of hydrogen burnt in the seals for the pure hydrogen case, contrarily to the case of dilute fuel. This gives an explanation for the larger impact of the seal's porosity on the pure fuel case, both in terms of performance and

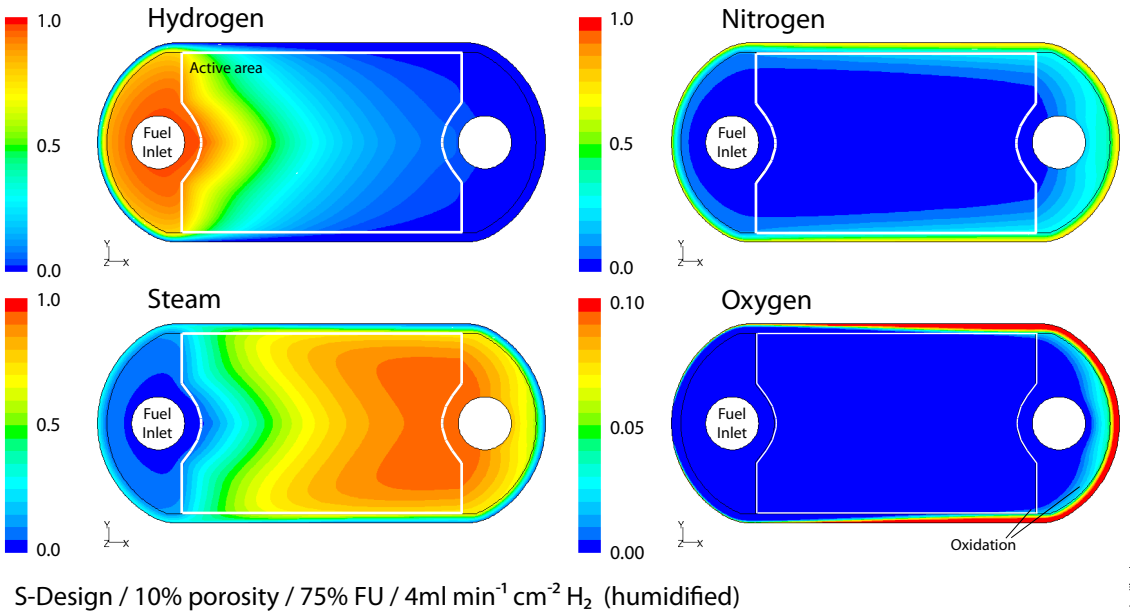

Figure 9.16: Local gas fractions in a *S-design* repeat-element at a fuel utilization of 75% (Seal porosity 10%, 4 ml $\mathrm{min}^{-1}\,\mathrm{cm}^{-2}$ H_2).

reliability.
Moreover, the amount of burnt fuel does not change significantly with the flow rate (similar gas compositions at equivalent fuel utilizations), resulting in a proportionally higher ratio of burnt fuel for low fuel flow rates. This explains why the reoxidation of the active area occurs at low fuel flow rates only.

Finally, a deterioration of the cathode is predicted for pure hydrogen (humidified), and this only for the largest seal porosity. This results from the depletion of oxygen downstream of the inlet's fuel manifold, which was already observed for the case of solid seals. With the additional effect of leakage through the fuel manifold, the local oxygen partial pressure along the seal is further lowered (see Fig. 9.17) and accompanied by the generation of steam on the cathode side. This situation is therefore not satisfying due to the possible damage caused to the cathode, but also due to the internal generation of steam which may for instance promote the generation of pollutant species such as $CrO_2(OH)_2$.

These results show therefore that, despite an improved fuel flow field and high performances with ideal seals, the achievable performance and reliability of the *S-design* stack is strongly affected by the quality of the implemented seal materials. This situation required therefore corrections of the stack design, which were successfully implemented by HTceramix-SOFCpower.

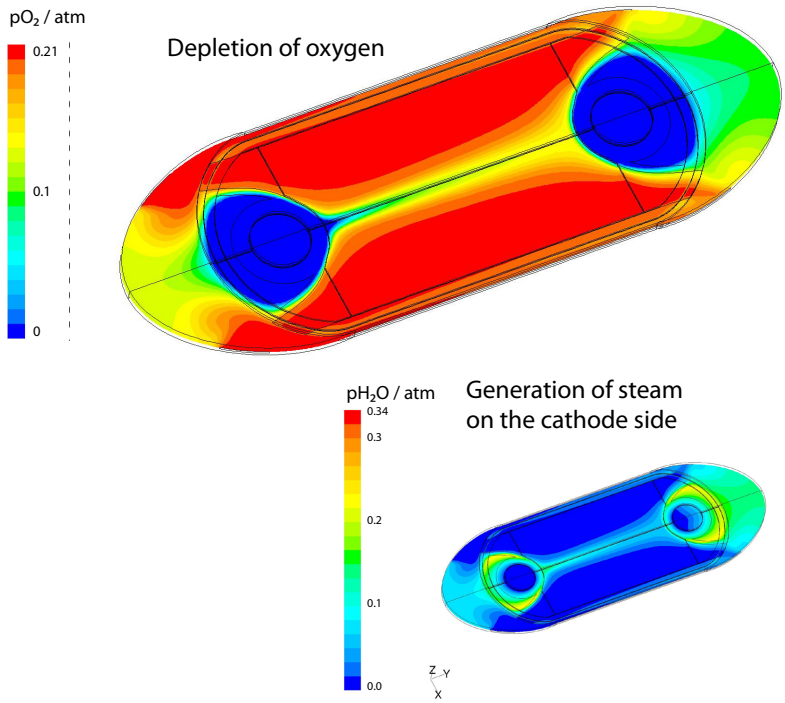

Figure 9.17: Performance map of *S-design* stack with associated risk of damage of the electrodes.

This analysis concludes the investigations on performance limitations and reliability issues caused by the inappropriate combination of porous seal materials and specific design options. In the following section, it is shown that a complete redesign of the stack enables to avoid these limitations.

9.5 Design of reliable stacks

As shown throughout this chapter, the implementation in the *R-design* stack of compressive seals presenting a residual porosity is a principal cause of failure. As presented in the risk and performance maps, lower porosities of the chosen seal material might help to reduce the losses of performance as well as the inherent risk of electrode damages, however without solving the problem. And finally, a trend to a propagation of the damaged areas was demonstrated, leading to unavoidable damages on the long term.
To solve these issues, a complete redesign of the stacking concept was started in the frame of the development of the *F-design* stack. As one of the production constraints remained the use of compressive seal materials, the conclusions and the tools developed in this chapter were intensively used to iteratively optimize a new concept from the beginning. These optimization steps were performed without intermediate experimental investigations, based only on the expected predictive capabilities of the model.
In parallel, an effort was set on the production side to use less compressible, but also less porous seal materials. A solution was found for the implementation of a compressive, mica-based material[2] presenting a residual porosity estimated between 3% to 10%.
By implementing the properties of this new (confidential) material in the model, a solution was found to prevent the cell from being re-oxidized during load or thermal cycling. Moreover, to avoid the possible reduction of the cathode such as in the case of the *S-design* stack, a specific arrangement of seals, manifolds and flows was elaborated to prevent starvation of air and leakage of reducing species.

9.5.1 Maps of performance and reliability

The validity of the developed concept is illustrated by the *maps of performance and risk* shown in Fig. 9.18.
First, when the maps are compared for the different seal porosities, only minor differences in terms of performance are observed, contrarily to the *R-design* and *S-design* stacks. This results from a specific arrangement of seals and gas streams limiting the extent of diffusive leakage through the seals, as well as from the decrease of the ratio between seal length and active area. Moreover, the predicted performances are extremely close to the ones predicted for the case of solid seals, enabling to attain efficiencies of 53% at low fuel flow rate. This shows that the residual porosity of the seal materials presents a much lower impact on the expected performance, which enables the use of this type of seals in high-performance SOFCs. This last point was obtained among others by the implementation of adequate seal widths where diffusive leakage could have induced unacceptably high losses.

[2]For confidentiality reasons, it is not possible to reveal its exact properties.

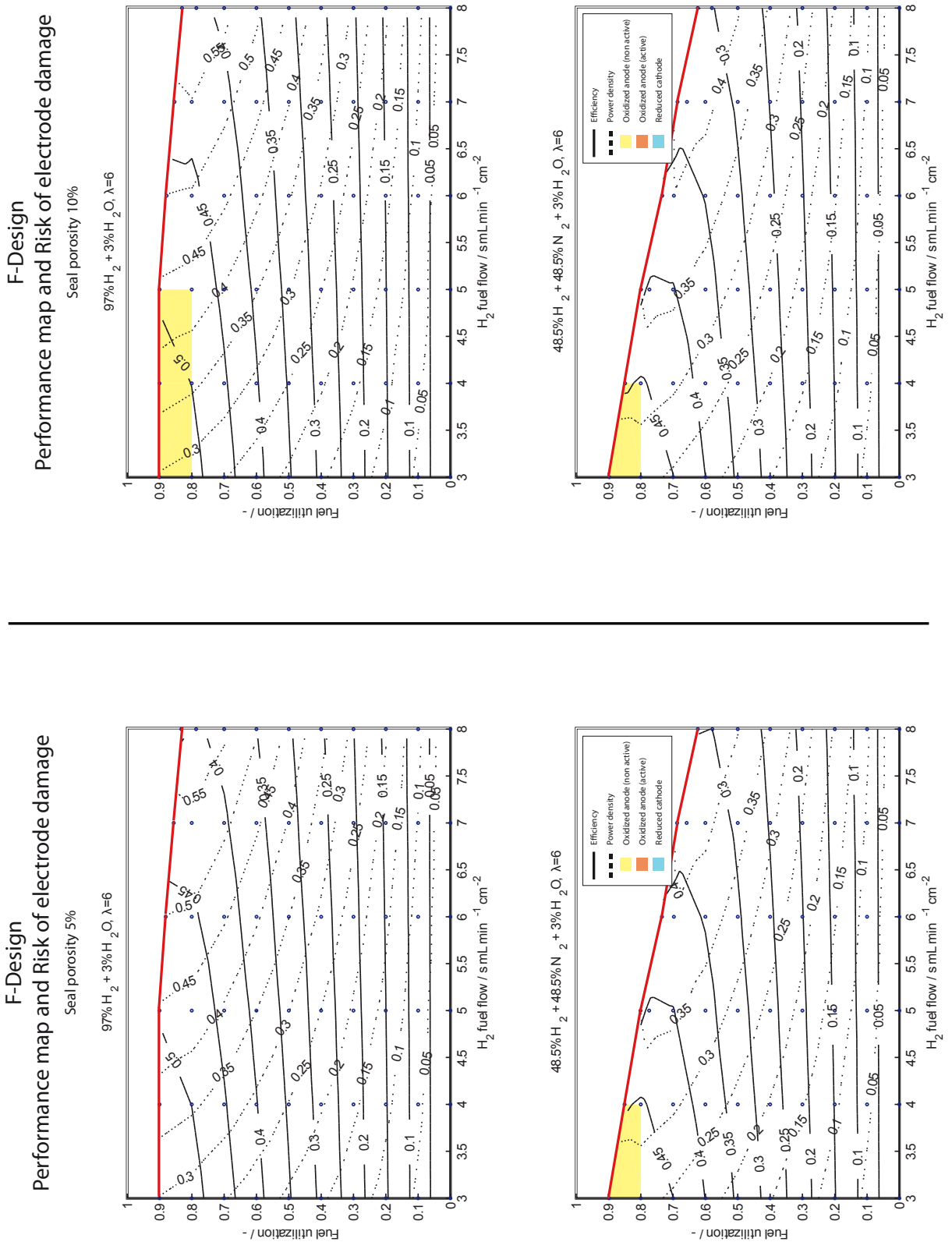

Figure 9.18: Performance map of *F-design* stack with associated risk of damage of the electrodes.

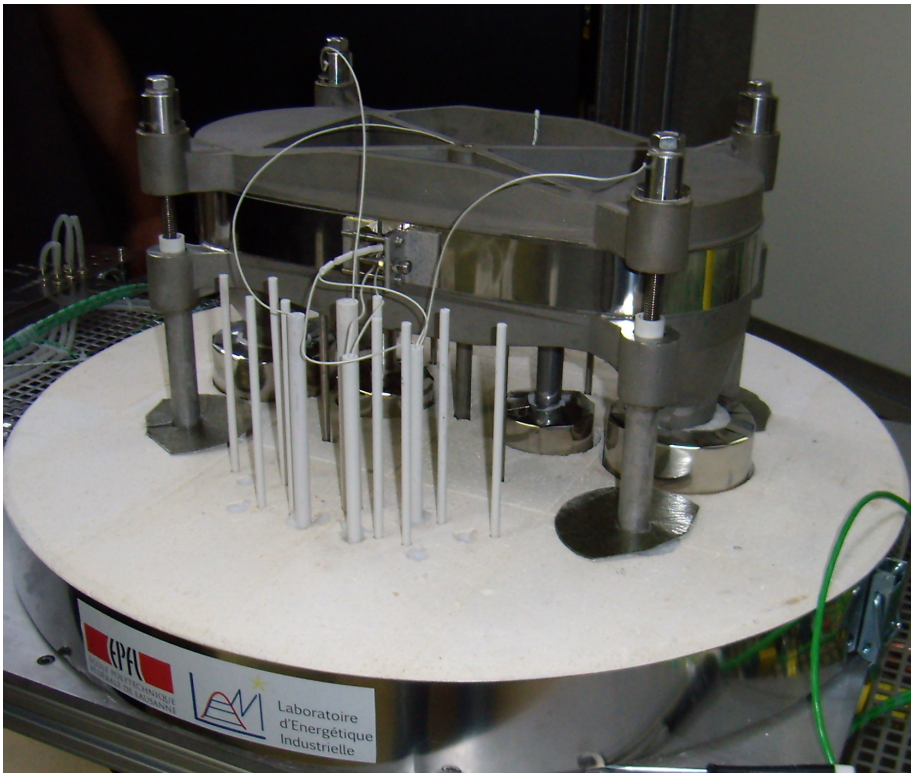

Figure 9.19: *F-design* repeat-element test assembled between the designed multi-function stack end-plates, on the diagnostic test station.

Concerning the risk of damage for the electrodes, only a limited oxidation of the anode support is predicted at low fuel flow rates and at fuel utilizations over 80%, affecting only on the non-active parts of the anode. As this risk might be sufficient to induce cracks propagating into the element, the necessary corrective actions were undertaken.

The comparison of the obtained maps with the ones of the *R-design* and *S-design* gives a clear picture of the attained improvements, first in terms of performance, but much more in terms of reliability. This validates therefore a modeling-based design approach including the necessary reliability indicators.

9.5.2 Experimental validation

The solution found to solve these issues remains confidential, as it represents an important advantage in terms of stack construction. Despite the few aspects developed in the following paragraphs, it represents a major part, in terms of time and developments, of the work done during this thesis. Not only a generic repeat-element concept was established from modeling work, but a detailed design of all parts was done, including the stack and its sub-components,

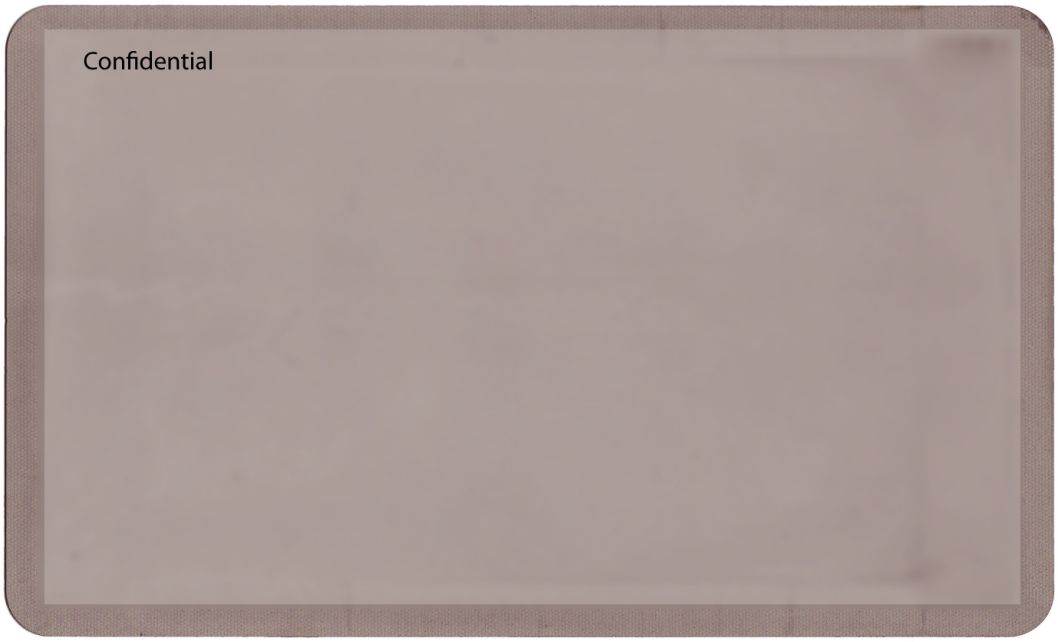

Figure 9.20: Fully reduced cell after operation in a *F-design* stack.

the gas manifolds, the current collection, the mechanical loading system, as well as part of the testing setup and of the high-temperature insulation. Moreover, an important time was spent on the choice of materials (in particular the heat-resistant alloys) in order to ensure thermomechanical stability on one side, and limited generation of pollutant species (chromium for instance) on the other side. An important effort was also set on the prototyping methods enabling to produce in small series the required components, as well as on the definition of the quality control procedures needed to ensure a correct distribution of fuel in the stack. Finally, and most important, a diagnostic testing station, including its instrumentation, was developed to perform in-situ measurements in the created stack.

With this done, the designed prototype remained not only a virtual design study, but was realized and tested experimentally, as shown in Fig. 9.19. The experimental results shown in the previous chapter attest of the capability of the design to reach high efficiencies, approaching the situation of an ideal repeat-unit. But even more satisfying, the experimental results show that the correction of the redox-cycling issue was indeed successful, as expected from the modeling work.

Figure 9.20 shows the intact anode side of a cell after operation in a *F-design* stack. This repeat-element was operated with 50%-diluted hydrogen at a fuel flow rate of 6 $\mathrm{ml\,min^{-1}\,cm^{-2}\,H_2}$

, achieving as predicted in the performance map (see Fig. 9.18) a maximum fuel utilization of 67% without any damage to the cell.

This result was obtained several times. More important, the 20-element stack presented in the previous chapter was operated at a steady fuel utilization of 80% without apparent damage, attaining a peak fuel utilization of 85% at a low fuel flow rate. This stack had however not been disassembled at the time of writing, hence not allowing a definitive verification.

These results show that, contrarily to the previous designs, the therein developed stack can be operated reliably at high efficiencies. This results validates therefore completely the starting hypothesis of diffusive leakage in seal materials, the modeling-based diagnostics made on previous prototypes, as well as the universality of the developed model which is not only capable to reproduce existing situations by adequate fits, but much more to correctly predict the behavior of new concepts.

9.6 Conclusion

Throughout this chapter, the interest of model-based diagnostics has been demonstrated on a concrete example affecting the reliability of SOFC stacks. These developments have allowed to identify the diffusion in the applied sealing materials as a key issue for the reliability and performance of the prototypes, as well as the detrimental design options leading to unavoidable damage of the components.

This situation affects not only the first-generation *R-design* stack, but also the *S-design* stack which was built in similar manner. Despite its proved enhanced performance in the case of ideal seal properties, the *S-design* stack is expected to attain more limited performance in the case of non-ideal seal properties, showing that not only a more ideal flow distribution is mandatory to achieve the expected high efficiencies. Much more, it is by a dedicated integration in the design phase of the limitations of the key components that an adequate performance can be attained, as demonstrated in the case of the *F-design* case.

The therein completed CFD model is not only capable to establish diagnostics on observed phenomena, but its ability to correctly predict the behavior of different designs and materials enables the development of concrete and applicable solutions. With this support, corrective actions were undertaken for the *S-design* prototype, allowing finally to achieve high performances and more reliable operation, as attested by the high efficiencies attained experimentally (see previous chapter).

Much more, the integrated design of the *F-design* prototype has allowed not only to improve the flow distribution, approaching the performance of an ideal repeat-unit, but to solve at the same time the most critical reliability issue. This predicted result was finally confirmed by the high efficiencies attained by the prototype in a 20-element configuration, as well as by the absence of redox-issues in the stacks.

With the resolution of local redox-cycling issue, a major source of failure was identified and solved to a large extent. However, other sources of failure exist. Besides issues in assembly and component quality, thermomechanical constraints can play a significant role in potential failures of the stacks. This is demonstrated by modeling work made by A. Nakajo on the *F-design* prototype, which can be found in references [103][102]. His work shows that additional perspectives for model-based diagnostics and for new developments exist.

After having addressed the question of performance limitations and one aspect of the reliability issues, the next step addresses the investigation of degradation mechanisms affecting the long-term performance of SOFCs. This is the subject of the following chapters.

Part III

Locally-resolved study of degradation in a SOFC prototype

Chapter 10

In-situ measurements of local performance and degradation in a SOFC

10.1 Introduction

Besides performance and reliability, the core issue for SOFCs remains the long term degradation of performance. After having addressed the two first aspects by modeling , prototyping and experimentation, the degradation issue is investigated by advanced experimental methods. Unlike for usual degradation studies, the focus is, here, not set on the degradation of individual components or complete stacks, but rather on the coupling of phenomena inside a stack which lead to degradation.
In a paper published in 2007, Yokokawa et al. underline the difference between the degradation observed on individual cells and on stacks, pointing out the possible interactions at the stack and system level which impact on the degradation behavior [119].
To contribute to this question, the challenge was set to measure degradation in-situ in a real SOFC stack, with the underlying idea to extract from local information a more complete understanding of the processes occurring in the fuel cell. This was done by setting up the tools necessary to measure and analyze the local degradation inside a *F-design* repeat-element.

This experiment could successfully be performed, giving insight in the internal degradation sequence, showing indeed very different degradation behavior than the one expected from individual cells.

It appears that this experiment is the first of this type to have been performed in a Solid Oxide Fuel Cell.

10.2 Approach

As shown in Chapter 2, degradation of materials and components involves numerous physico-chemical processes. Moreover, it is often the combined action of several elementary processes which leads to particular types of degradation. Degradation processes are often investigated at the scale of separate components (electrodes, electrolyte, cell, metallic interconnects, seal materials) or else in repeat-element and stack configuration. The first approach allows to separate contributions from various sources, and the second represents a coupling of the various internal degradation sources at the stack level, in addition to possible ones coming from system components. The disadvantage of the first approach is the study of isolated processes only, without the coupling at stack level that may induce additional degradation sources. The drawback of the second approach is that the extent of degradation can only be measured as an average response over a repeat-element or stack, providing only few details about the degradation processes.
In addition, the difficulty to understand and predict the overall degradation of a SOFC repeat-element is aggravated by the fact that the local gas composition, the local temperature and local current density vary along the flow path, all parameters having an influence on degradation. It is therefore expected that these local operating conditions imply different local degradation mechanisms and degradation rates.
Furthermore, some degradation sources such as pollutant species are transported by convection and diffusion, and therefore locally depend on upstream conditions and components. This implies that the stack design, the choice of materials and the system components can have a significant influence on degradation.
To enable a detailed study on repeat-element degradation, locally-resolved measurements represent a major advantage, as the information of interest becomes available in direct manner. Unlike for PEMFC and DMFC, locally-resolved measurements are rarely performed in SOFCs, due to the difficult access at high temperatures. Experiments performed at DLR [9] (German Aerospace Center, Stuttgart, D) and in our laboratory [16] showed the interest of this method to study local electrochemistry and to establish electrochemical models. Degradation was however not studied in those configurations.

To study the performance and degradation of the *F-design* stack, a dedicated diagnostic test station, which allows to monitor an instrumented repeat-element, was realized. Allowing up to 20 local measurements on small segments in addition to a main segment, the station offers a high spatial resolution, as well as flexibility for the placement of measurement points. Active control of each individual segment enables an operation at constant cell potential on all segments.

The experiment presented and analyzed here, allowed to follow local degradation over 1900 hours. Cumulating an experimental dataset of 36'000 hours (19 segments x 1900 hours), it offers a huge amount of electrochemical data, that is being analyzed and linked to post-experiment analyses.

10.3 Experimental

The diagnostic test station (shown in Fig. 10.1) consists of a setup similar to the ones used for repeat-element and stack testing on which a specially instrumented repeat-element is mounted. This test station can receive different stack and repeat-element concepts for dedicated experiments. It is equipped with computer-controlled mass-flow controllers (Red-Y, Vögtlin Instruments, CH) allowing to vary the composition of fuel mixtures, not only with hydrogen and nitrogen, but also with carbon-monoxide or methane. The fuel is humidified before injection into the repeat-element or stack.

On the cathode side, air from a compressed air line is used. After the experiment presented

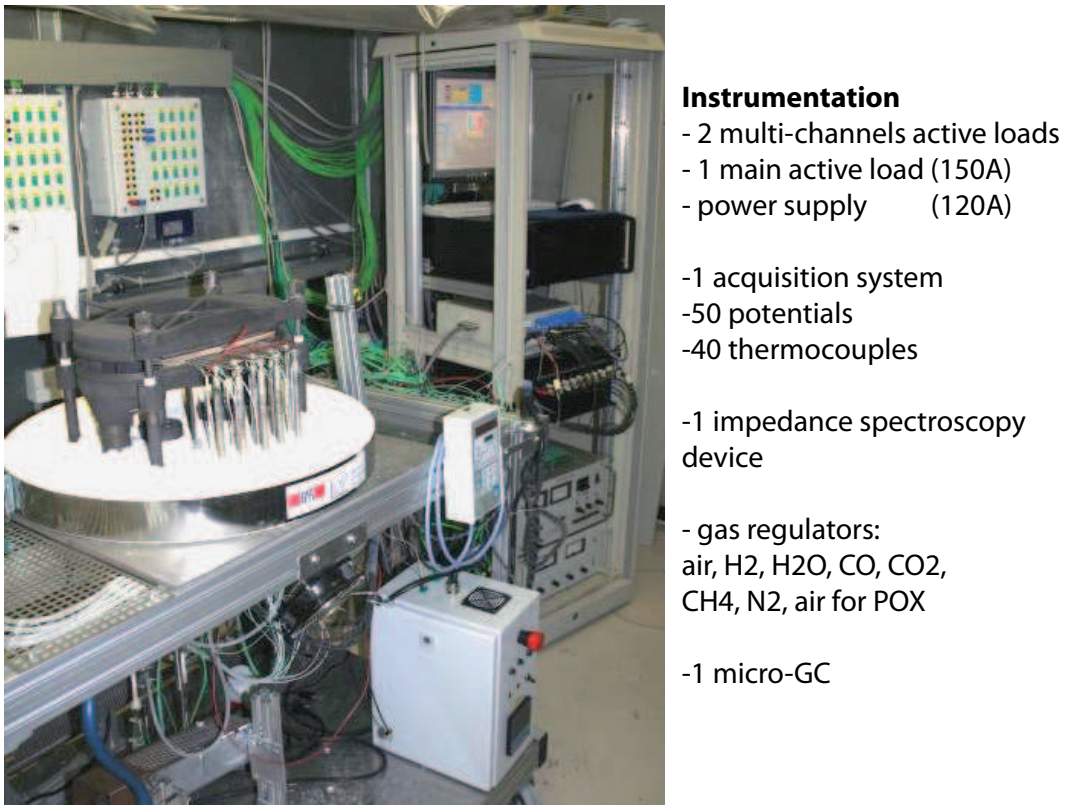

Figure 10.1: The diagnostic test station developed for in-situ measurements.

hereafter, a possibility was added to dilute the air with nitrogen, in order to study the effects of the oxygen partial pressure on the electrochemical response of the cathodes.

On the air side, a shielded electrical air heater is used to preheat the air to the desired temperature (Watlow, US).

The stack is connected to an active load and power supply able to work with currents up to 120 A. In addition, multi-channel active loads are used for the local measurements, as described hereafter.

Due to its large active area (200 cm^2), the *F-design* stack design is well suited for local investigations. A dedicated test setup was designed, with major contributions from A. Nakajo (PHD student) and P. Oberholzer, diploma student, who are gratefully acknowledged for their work.
The investigated prototype is placed on a specific test setup (see Fig. 10.1) and inserted in a high-temperature oven (Rhode, DE). A close view of the test setup is shown in Fig. 10.2, with the instrumented repeat-element assembled between multi-functional end-plates. On the lateral sides of the element, a series of current collection bars are visible, as well as thermocouple wires and potential probes, which are used for the local measurements.

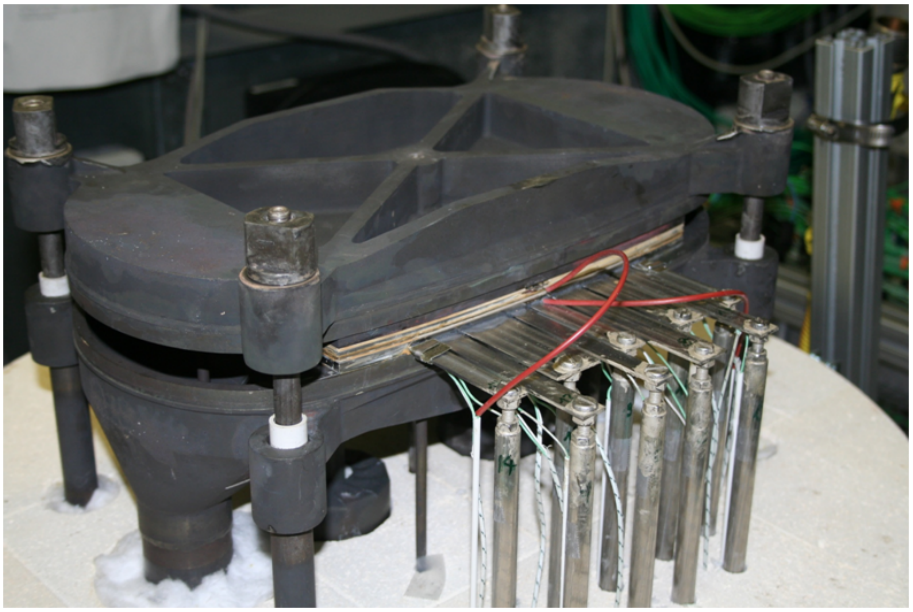

Figure 10.2: Close-view of the test setup with assembled segmented repeat-element.

The control of the diagnostic station and of the data acquisition are ensured through a data acquisition unit (Hewlett Packard, US) controlled by routines written in the LabView programming environment . Besides the values recorded in the instrumented repeat-element, the system parameters are monitored, such as pressure drops in the stack or the inlet and outlet temperatures of the gases.

Based on the herein obtained results, an extension of the diagnostic test station is planned for the future, with in particular the implementation of gas-sampling ports to measure local gas compositions, as well as the implementation of a steam reformer to investigate the performance of a stack under reformed C-fuels. A view of these complementary tools is shown in Fig. 10.3.

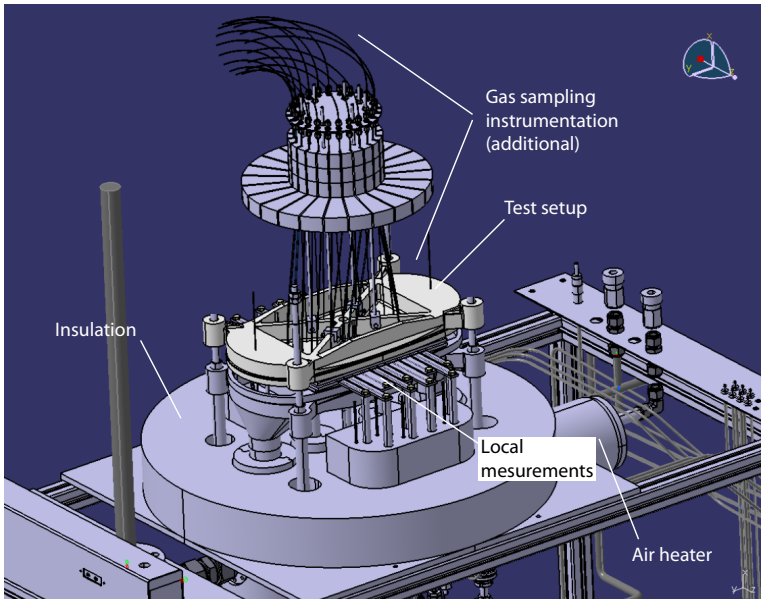

Figure 10.3: Extension of the test station for local gas analyses.

10.3.1 Principle

The local characterization is performed by separating the active area of the cell in electrically independent areas called segments (see Fig. 10.4 and 10.5), in a similar manner as presented by Ravussin et al. [16] and Metzger et al [9]. The polarization of each single segment is controlled externally for electrochemical characterization. The local Nernst potential is measured by disabling the polarization at the required location. In addition, the electrochemical reaction and its degradation are studied in more detail by using an electrochemical impedance spectroscopy (EIS) device (Zahner-Elektrik, Germany, IM6), which can be connected to individual segments. Finally, each segment is equipped with a K-type thermocouple to monitor the local temperature.

10.3.2 Segmentation

A total number of 18 segments of 1.7 cm^2 active area each were distributed on the surface, in addition to a large main segment of 133 cm^2. The segments were organized as one 6-segment row along the flow, and three 5-segment columns perpendicular to the flow path (see Fig. 10.4). The inlet and outlet segment columns are used to verify the gas composition, fuel distribution and mass balance. The segment row parallel to the flow (horizontal) is used to get a profile of temperature, current density or Nernst potential along the flow path.

To simplify the lecture of the following paragraphs, the distribution of the segments on the

active area is recalled on the bookmark in postcard format found on this page. Additionally, important results are summarized on the back of this card to clarify the links established throughout the analysis of the results.

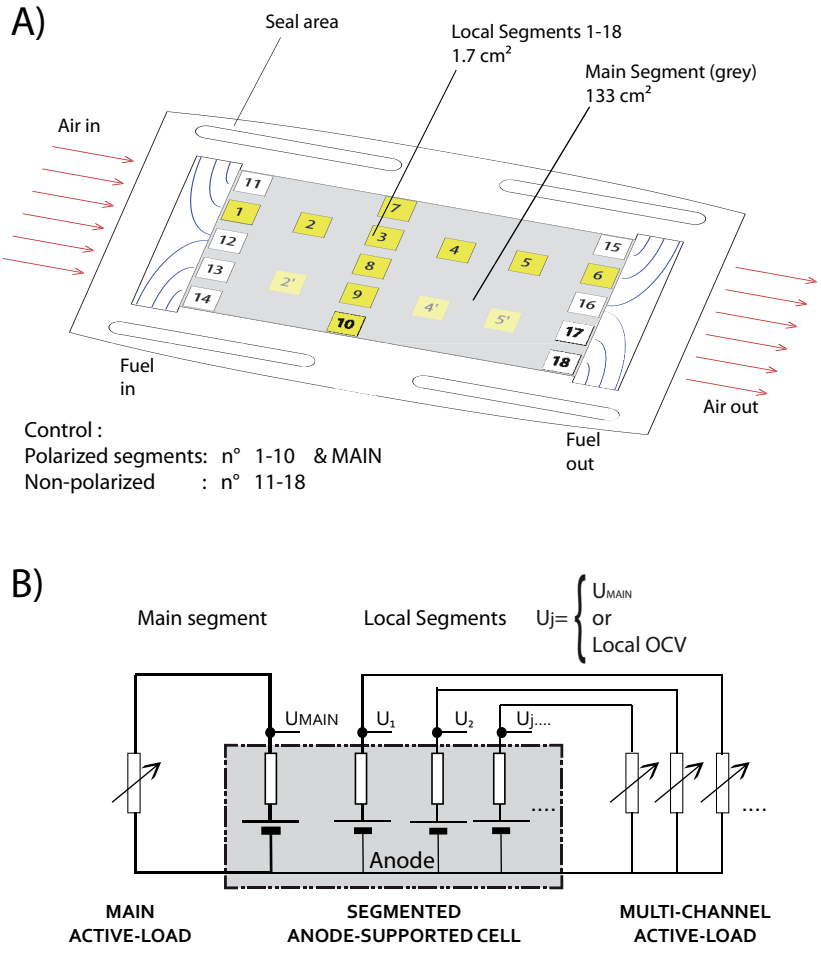

Figure 10.4: Distribution of the segments on the active area and connection to the active loads.

For the present experiment, an anode-supported cell provided by HTceramix-SOFCpower was used, on which a segmented $(La, Sr)MnO_3$ / Yttrium-stabilized-zirconia (LSM/YSZ) composite cathode and segmented $(La, Sr)CoO_3$ (LSC) current-collection layer were screen-printed. Metallic interconnects (MICs) were used, made of F18TNb alloy. The segmentation was performed by laser cutting and milling the cathode-side MIC, through which the current collection lines of the segments, the potential probes and thermocouples, are extracted on the sides of the repeat-element (Fig. 10.5). The segments are joined to the main MIC with insulating ceramic paste. Finally the segmented GDL layers made of SOFConnex^{TM} are put in contact. Sealing is performed in the same manner as for a standard repeat-element.

Apart from the thicker cathode MIC, the segmented repeat-element has the same geometry as standard repeat-elements and could therefore be mounted at the end-side of a larger stack. In the present test, it was mounted as single repeat-element on the flanges used for standard tests.

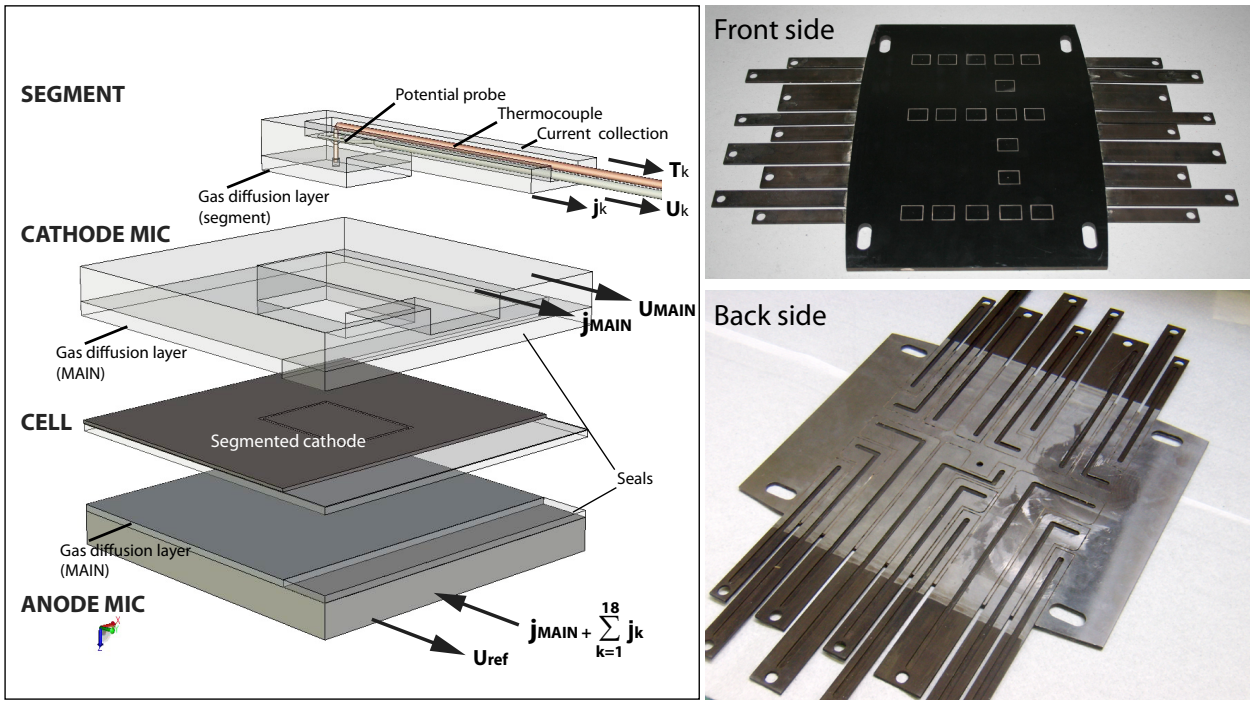

Figure 10.5: Segmentation of the cathode MIC and instrumentation.

10.3.3 Control and Instrumentation

The main segment is connected to a 150A computer-controlled active-load (main active load). The 18 small segments are connected to two different multi-channel active loads built in house. The most recent multi-channel active load was designed in the frame of this thesis to provide specific functions for this experiment.

The particularity of these active loads is that they allow to set the cell potential of all segments to a common value (the one of the main segment), i.e. to create an equipotential in the cathode MIC similarly to the situation in a repeat-element. This active polarization control of each segment allows to avoid the limitations encountered by Ravussin and Metzger [9, 16] in similar experiments, where the cell potentials of all segments differed due to voltage losses in the current collection lines. This was found to affect the resulting local current densities (see section 6.3) and could therefore modify the local degradation behavior.

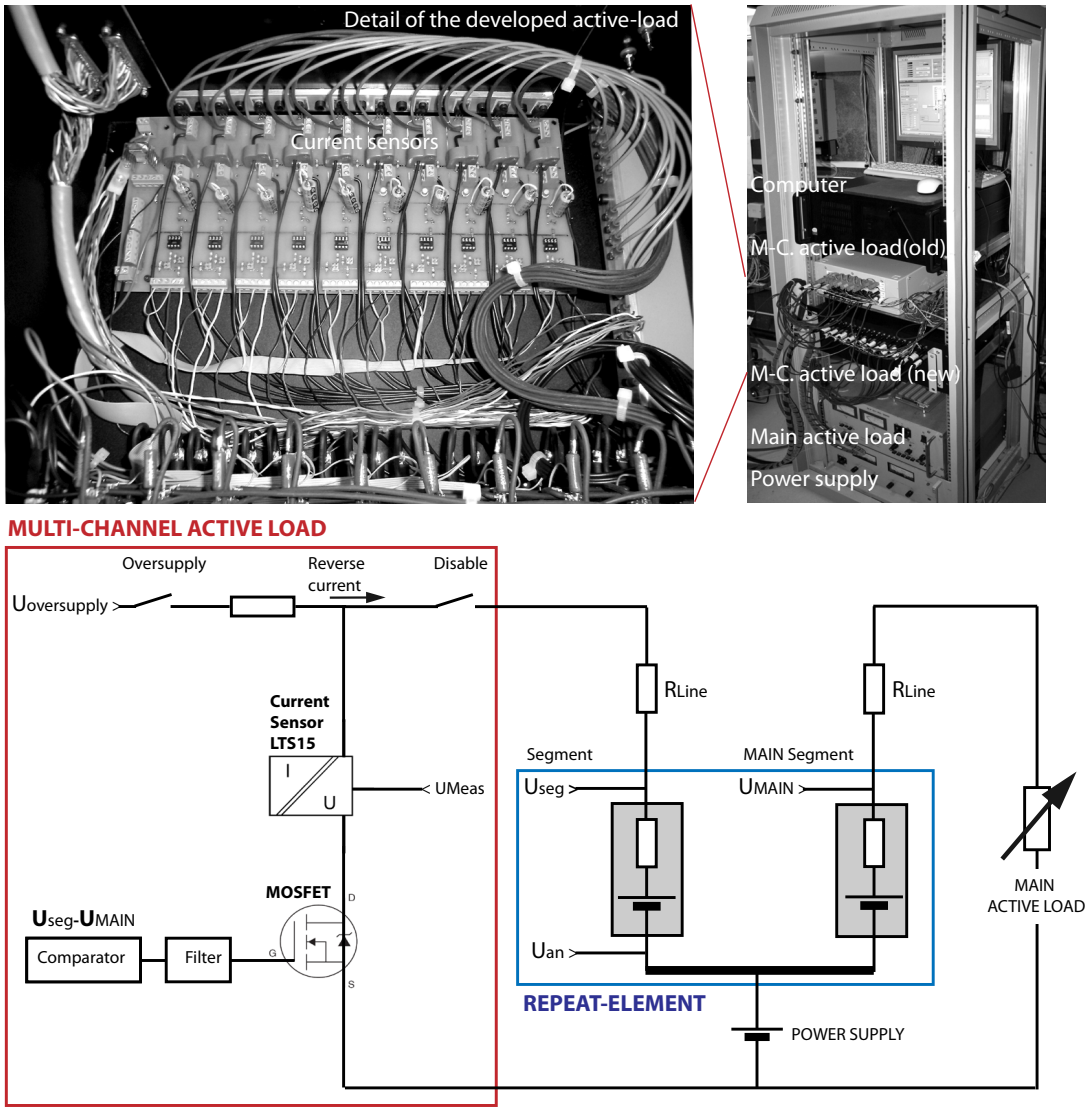

Figure 10.6: Operation principle of the developed multi-channel active-load and connection to the segmented element.

In this experiment, each segment is equipped with a current collection bar and a potential probe for individual polarization control (Fig. 10.5). The working principle of the developed multi-channel active-load is depicted in Fig. 10.6. The current of each segment is measured by loss-free closed-loop Hall sensors (LEM LTS15). Individual current control is made in potentiostatic mode through a MOSFET transistor, by comparing each segment's potential to the one of the main segment. To compensate voltage losses in the wiring, a common power supply connected to the anode of the repeat-element increases the segment's potentials with respect to ground. With this instrumentation, the potential biases between small segments and main segment were lower than 4mV, with residual perturbations of less than 2mV amplitude.

Moreover, to enable operation at a constant potential over the full range of operating conditions, a current 'oversupply' function is implemented that allows to increase the potential of an individual segment if required by applying a reverse current. This feature is implemented to study the local behavior at OCV or in the case of limitations, which however were not found in the tested *F-design* prototype.

On the herein developed active load, the polarization of each segment can be stopped individually to measure the local open circuit voltage (OCV) as a measurement of the local Nernst potential and hence indirectly of the local gas composition. This is used to verify the integrity of the seals, to investigate the quality of the fuel distribution over the active area, and to measure the local cell overpotentials.
In addition, this active load (second version) which controls the segments n°1 to 10, was especially designed to filter signal perturbations, in order to avoid any instable interaction between the segments and with the main and second multi-channel active loads. The first version multi-channel active load, controlling segments 11-18, not equipped with this filtering, became unstable in the first seconds of operation and was then disabled. For this reason, the segments 11 to 18 remained unpolarized during the whole test, giving the possibility to study the effect of polarization on local degradation, by comparison with segments 1-10.

10.4 Characterization

With the access to local properties and electrochemistry on 18 points on the active area, the measurement setup gives a unique possibility to validate the design of the fuel cell, as well as to control its correct assembly. The verification and validation procedure was performed by first studying the reduction procedure, followed by a characterization of the repeat-element which is accompanied by a comparison with modeling results.

10.4.1 Reduction procedure

The repeat-element was heated up to 800°C and reduced. Local measurements allowed to follow the reduction sequence, showing that more than 2 hours were necessary to completely stabilize the potentials.
During the reduction procedure, the multi-channel active loads were disabled to allow variations of potential between the different areas of the fuel cell. First, the system was flushed with pure nitrogen, followed by the introduction of hydrogen whose partial pressure was progressively increased. As depicted on Fig. 10.7, the local potentials were already non-zero under pure nitrogen, as usually observed in repeat-element and stack tests. From previous experiments, it was known that this potential gives a good indication of the gas tightness of the seals, as it is directly related to the oxygen partial pressure on the anode side. With about 0.1V attained homogeneously on all segments, and this independently of the vicinity of the segments to the seals, the good gas tightness of the seals could be verified. In addition, this potential was higher than the ones recorded in previous experiments, hence confirming this conclusion.
At the introduction of hydrogen, a sharp rise of potential occurred, followed by a plateau around 0.76V and finally a slow increase to the final OCV found around 1.1V. During the whole reduction procedure, the two segments located in the vicinity of the fuel inlets (n° 11 and 14) preceded the ones located downstream of them, the former showing higher potentials.
The spatial distribution of the local Nernst potentials, measured by the 18 segments during the reduction sequence, can be found in Fig. 10.8. On these maps, the potential of the main segment is not represented, but only the one of the individual measurement points.
During this first rise of potential, up to the plateau of 0.76V, the other segments, as well as the main segments, presented close potentials. The plateau of potential is related to the reduction of nickel oxide to nickel. The local Nernst potential is dictated by the oxygen partial pressure on either side of the electrolyte, and therefore by the resulting local partial pressure of oxygen on anode side. The latter depends on the equilibrium between nickel and nickel oxide during the reduction sequence. From equations (8.9) and (8.8), an oxygen partial pressure of $pO_{2,eq} = 1.205 \cdot 10^{-14}$ is found for a temperature of 1073K. The corresponding local Nernst potential is:

$$U_N = \frac{\mathcal{R}T}{4F} ln \left(\frac{pO_2^{cath}}{pO_2^{an}} \right) = \frac{\mathcal{R}T}{4F} ln \left(\frac{0.21}{1.205 \cdot 10^{-14}} \right) = 0.705\ V \tag{10.1}$$

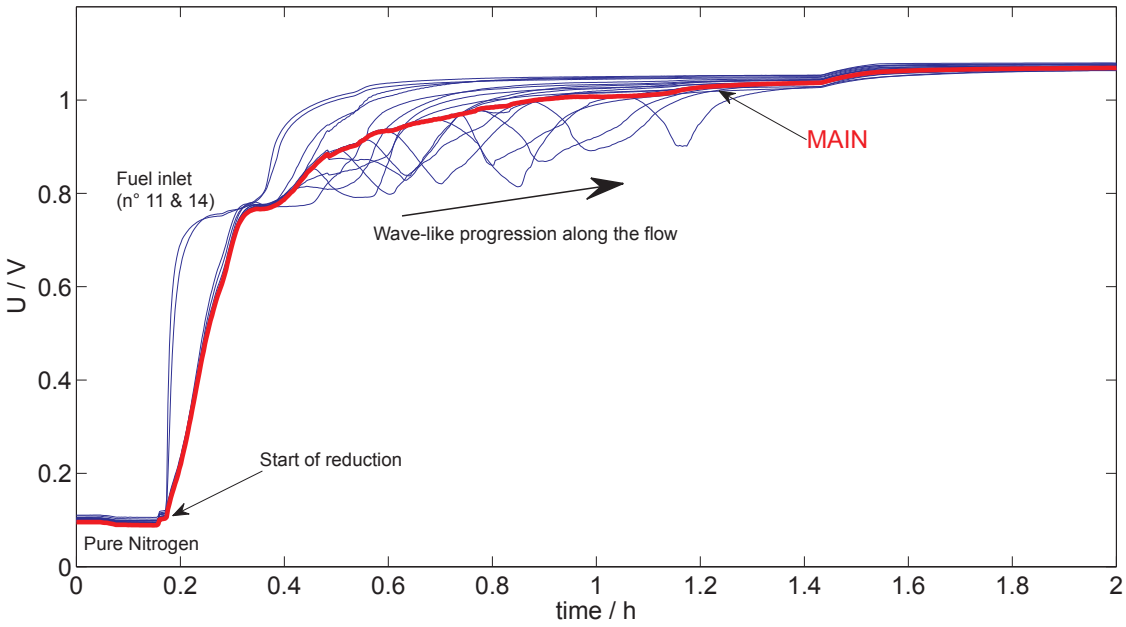

Figure 10.7: Evolution of the local potentials during the reduction procedure.

The potential of the observed plateau (0.76V) is slightly higher than the computed one, which can result from an internal drop of temperature, caused by the endothermal reduction reaction, or from the large excess of fuel impeding the reaction from reaching equilibrium.

After the period at stable potential, a second potential increase starts, initiated by the two segments located near the fuel inlet. From this point on, the potentials of the other segments detach from the one of the main segment, first accompanied by a drop of potential below the one of the main segment, and then overtaking it. This transient follows a wave-like progression, affecting first the inlet region and then progressing towards the outlet. This behavior is particularly evident on the maps represented in Fig. 10.8.
After 1.4 hours of reduction, the fuel flow rate and dilutions were set to the nominal operating point for the whole duration of the test, with a 3% humidified mixture of 6 $\mathrm{ml\,min^{-1}\,cm^{-2}}$ H_2 - 6 $\mathrm{ml\,min^{-1}\,cm^{-2}}$ N_2 (air excess factor was 7). After two hours of reduction, the local OCVs obtained finally were between 1079mV at inlet and 1069mV at the outlet, with a main segment at 1075 mV. OCVs near the seals were as high as elsewhere, indicating proper sealing of the repeat-element and hence confirming the gas-tightness observed under pure nitrogen. With the analysis of this procedure, not only the gas tightness of the seals was verified, and therefore the quality of the assembly, but one of the design objectives for this prototype could be validated, which was to limit diffusive leakage through the seals. As shown in the previous chapters for both the *R-design* and *S-design* stacks, an effect of an important diffusion would else have been visible on the local Nernst potentials.

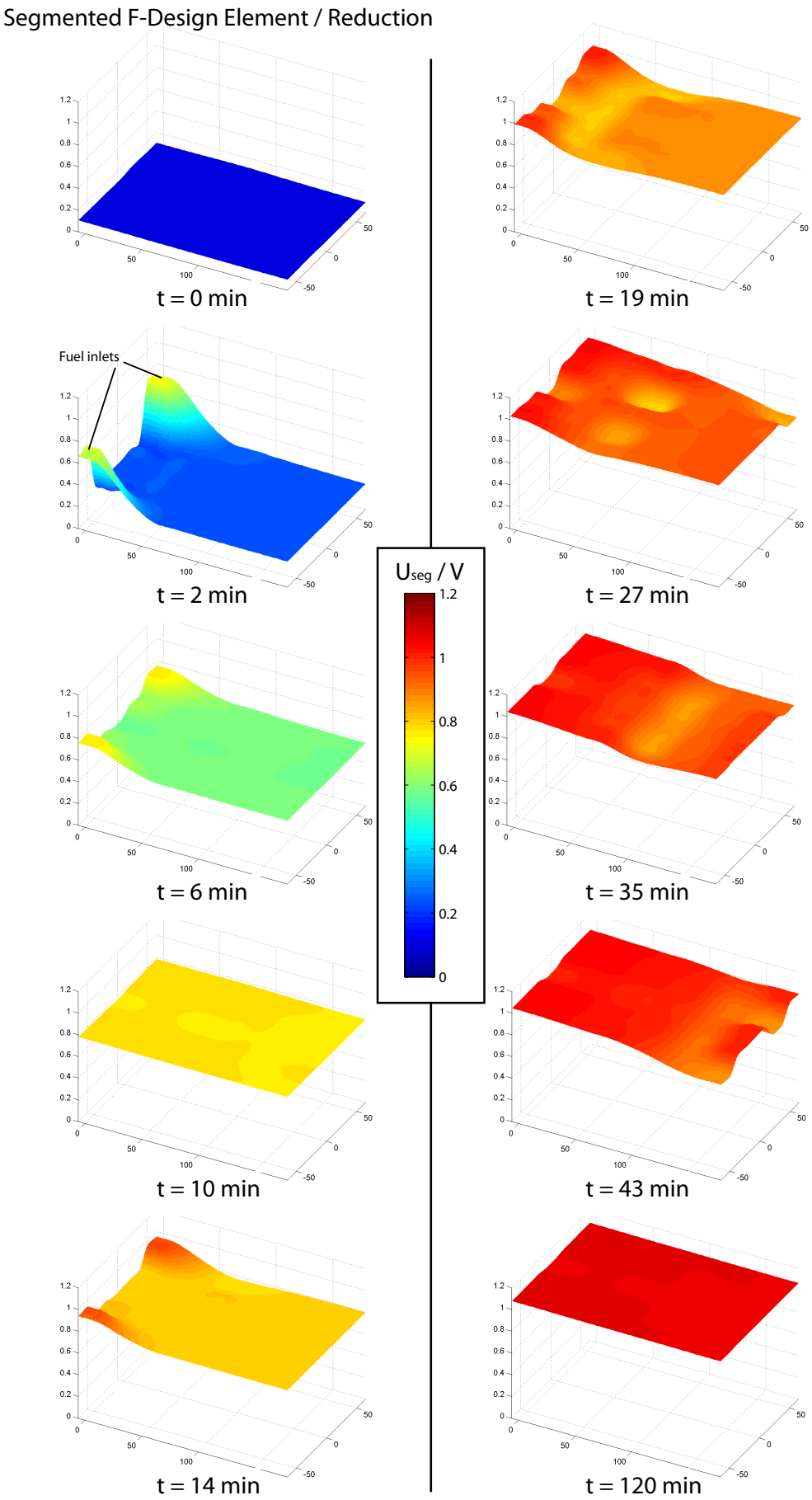

Figure 10.8: Spatial evolution of potentials during the reduction sequence.

10.4.2 Local electrochemical performance

In order to validate both the design and the modeling prediction, the local electrochemical performance was investigated by performing i-V characterizations and measuring the local current density on each segment, while keeping the cell potential constant on all segments. Figure 10.9 shows the typical iV-characteristic of the segments along the flow path, obtained

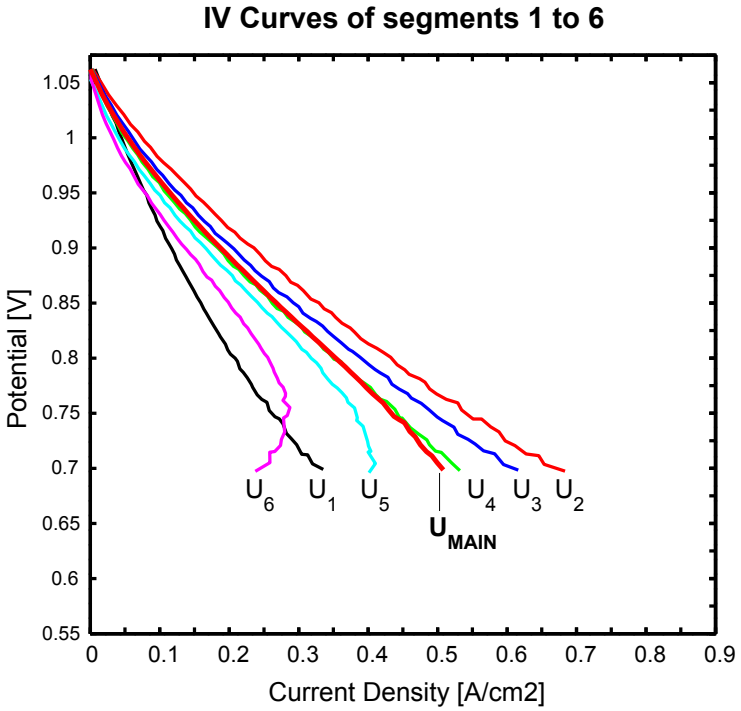

Figure 10.9: Local current densities and potentials recorded during an i-V characterization on the segments 1-6 disposed along the flow.

after 63 hours of operation under constant fuel and air fluxes. The best performance is obtained on segment 2. Segment 6, situated at the fuel outlet, shows a typical drop in current density below 0.75 V cell potential, resulting from the local drop in Nernst potential due to increasing fuel utilization, and due to additional diffusion losses in the anode. The local output power density varies from 0.2 to 0.45 W/cm^2. As shown further below by impedance spectroscopy, the unexpectedly low performance of segment 1 can be explained by a large polarization resistance, while its ohmic losses remain similar to those of the other segments, hence excluding a contacting problem.

10.4.2.1 Current density profiles

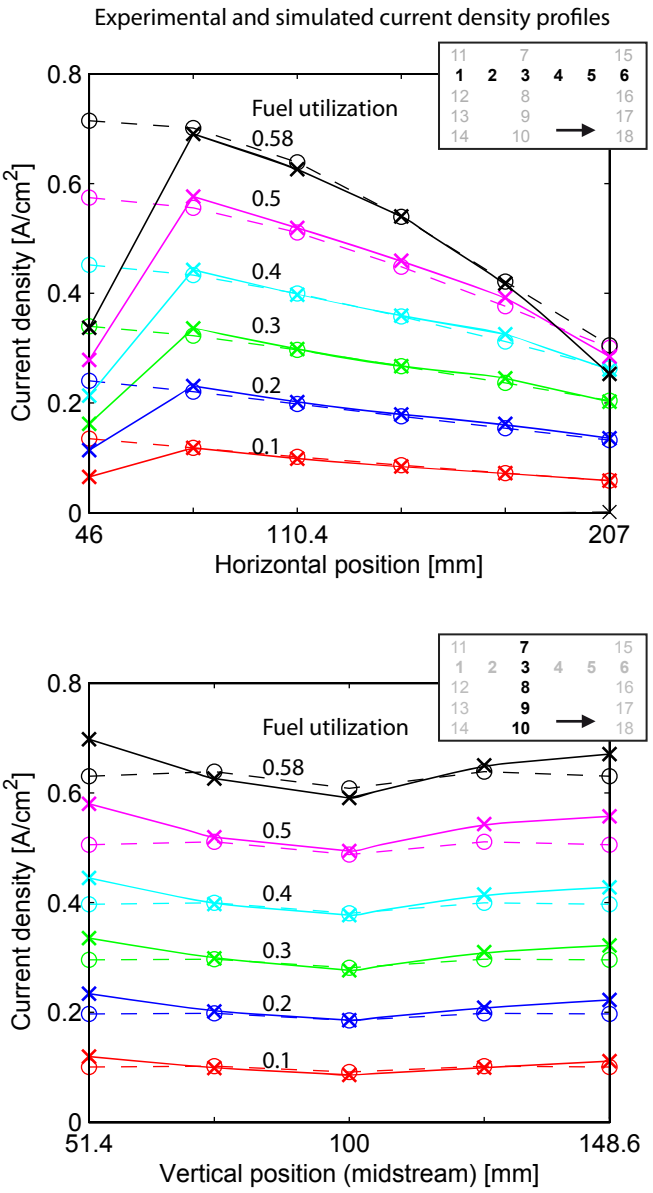

Figure 10.10: Current density profiles recorded at different fuel utilizations along (n. 1-6) and across the flow (n. 3, 7-10). Comparison with modeling outputs.

To investigate the local electrochemical behavior in the repeat-element, the current density profiles recorded during the test are compared with modeling results at different fuel utilizations. It has to be pointed out at this point that the cathode used in the test (LSM/YSZ) and the one described by the model (LSCF) differ. Therefore, it is more the qualitative behavior which is investigated, even if a good quantitative agreement is found. To model the repeat-element, the thermal boundary conditions are set to an oven configuration, where

the MIC's top and bottom surface can exchange heat with the oven through the stack's end-plates. In addition, it has to be emphasized that the electrochemical model was fitted on data obtained on a cell after a short time of operation, i.e. before important degradation occurred.
For these reasons, some discrepancies are observed between model and experiment. As illustration, the current density profiles recorded after 63 hours are shown in Fig. 10.10, along with modeling results for the same fuel utilization. An important discrepancy is essentially observed on segment 1 which presents an unexpectedly low performance. Experimentally, the low current density on segment 1 induces a compensation on the other segments to maintain the same total current, explaining the slightly higher experimental values on the remaining segments.
One possible explanation for the poor performance of segment 1 could have been a much colder temperature at the air inlet, resulting in high cathode overpotentials. However, the temperature profiles shown hereafter reject this hypothesis. A bad contact on segment 1 could also be excluded from impedance spectroscopy results, indicating another cause for low performance.
Looking at the transverse direction (Fig. 10.10, bottom) on the second column of segments (3 and 7-10), it can be seen that the current density is up to 16% higher on the sides of the repeat-element than at the center, indicating a slight mismatch in fuel distribution. The observed current density is higher than the simulation output, as already observed in Fig. 10.10 (top) for the same location along the flow path.
Despite the mismatch on segment 1, an overall good agreement is found between model and experiment, showing that the highest current densities in this configuration are expected in the vicinity of the air inlet. This differs therefore from the stack configuration where the highest current densities are located further downstream due to increasing temperatures along the flow, as attested by the current-density profiles shown in paragraph 7.2.3 for the general repeat-element.

10.4.3 Temperature profiles

For the same operating conditions as the presented current density profiles, the temperature profiles were recorded and compared to simulation outputs (Fig. 10.11). Discrepancies are observed, resulting from simplifications in the modeled geometry (simplified end-plates and segmented MIC geometry). In addition, the signal for temperature was lost on segment 6, explaining the lack of data. With an oven temperature of 1073K and an air inlet temperature between 1058 and 1063 K (left), the highest observed temperature is 1085K on segment 4. The small temperature difference between inlet and outlet is explained by the large lambda of 7 and by a large heat transfer between the endplates and the oven. This represents a major difference with a stack configuration.

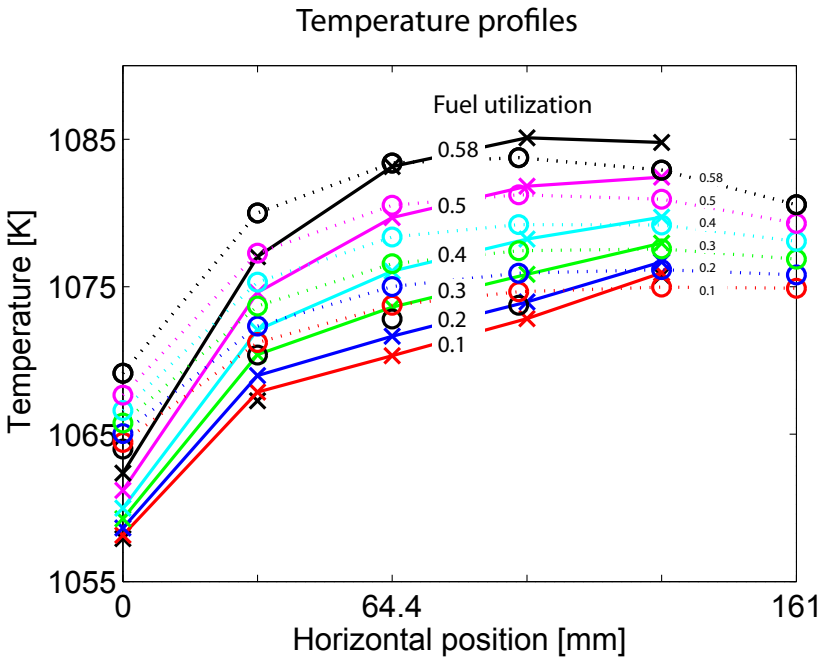

Figure 10.11: Temperature profiles recorded along the flow at different fuel utilizations. Comparison with modeling results.

10.4.4 Discussion

The locally-resolved characterization of the repeat-element reveals information which is hardly accessible in other experimental configurations. In particular, local limitations can be identified. An example is given in the i-V-characterization (Fig. 10.9), where an important limitation is observed below 0.75V on segment 6 located at the outlet. This limitation could lead to damages of the cell if the polarization was further increased. In this case, the average response of the element (main segment) presents only a minor inflexion.
The same observation is made for segment 1 located at the inlet. The simulation results, else in correct accordance with the experimental data, present an important discrepancy at this location, indicating an important degradation of this area. In this case again, this phenomenon cannot be detected from other measurements, because the global response of the repeat-element remains similar to other experiments performed on other stack designs with this type of cells. These observations illustrate the large differences in local properties in an operating SOFC.
Moreover, the characterizations presented in the previous paragraphs give detailed insight in the quality of the design and of its assembly. From the behavior during the reduction procedure and from the attained local Nernst potentials, it is verified that the designed seal enables to reach an homogeneous fuel composition over the active area, without important internal generation of steam from parasitic combustion. This also attests of the correct assembly of the element.

In addition, the current density profiles recorded across the fuel flow direction indicate a fuel distribution which is not completely homogeneous, differing from the modeling predictions. The causes for this inhomogeneity were investigated later on by modeling, applying the exact geometry of the prototyped element. An error could be identified in the prototyping and in the model, requiring a correction of the design to improve performance. In this case again, this situation could hardly have been detected without in-situ measurements, hence giving very valuable information for the development phase of the prototype. In fact, the maximum feasible fuel utilization in this experiment was 67%, while with the correction of the anode flow distribution, fuel utilizations of 85% were later attained in a 20-element stack configuration, as shown in paragraph 3.6.

10.5 Real-time measurement of local degradation

10.5.1 Testing procedure

To avoid a pronounced overlapping effect of different operating points in the polarization history, and in particular to strengthen the link between local electrochemistry and post-experiment analyses on the segments, the operating conditions were kept constant over 1900 hours of operation. A failure in nitrogen supply caused an operation under pure (humidified) hydrogen for 130 hours (t = 220h to 350h). The average current density was kept at 0.4 Acm^{-2} before interruption of the nitrogen supply, and at 0.375 Acm^{-2} afterwards.

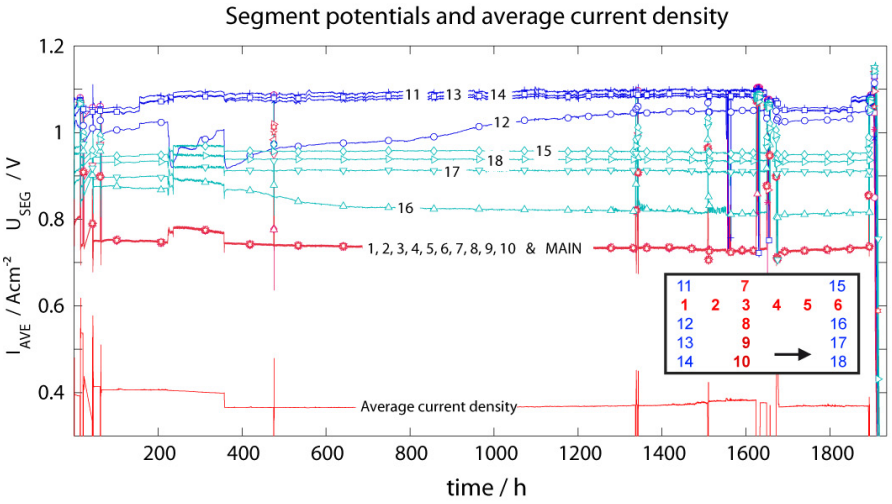

Figure 10.12: Overview of the 1900 hours of diagnostic test (segments 1-10 and main segment were polarized, 10-18 remained at OCV). Distribution of segments is recalled with indication of the flow direction.

10.5.2 Local evolution of potentials, current densities, overpotentials and ASRs

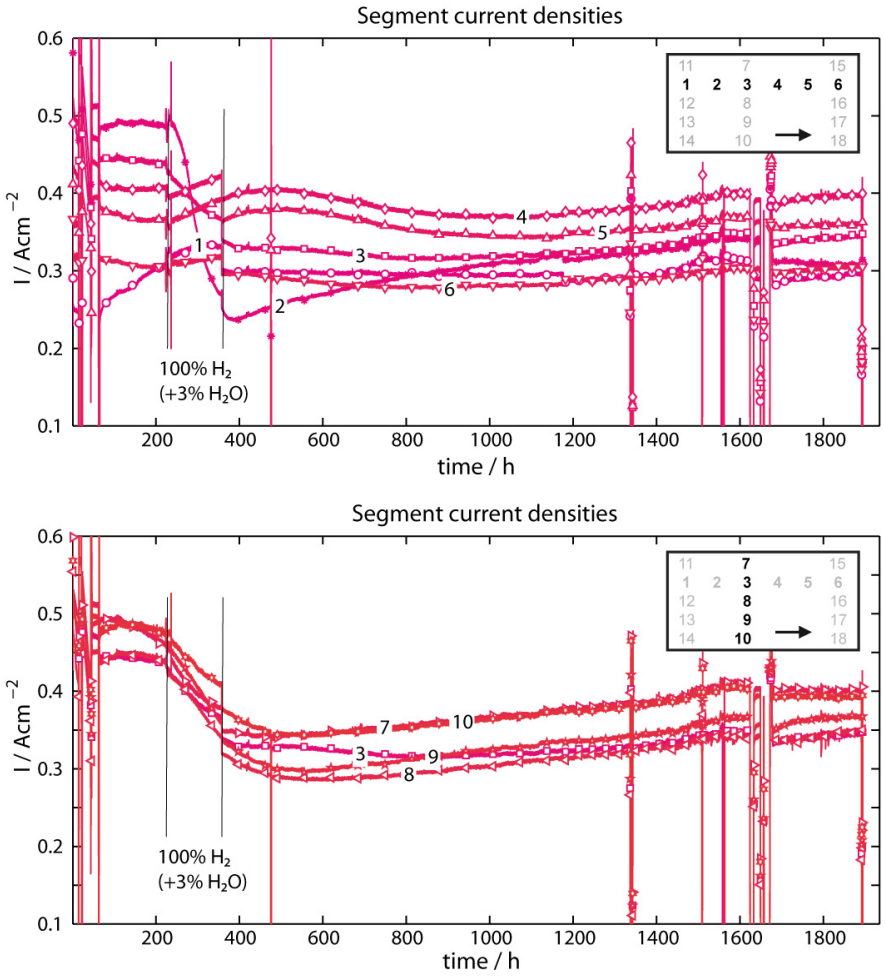

Figure 10.13: Evolution of local current densities. Top: segments disposed along the flow (1-6). Bottom: segments 2 and 7 to 10 across the flow in 3rd position

The evolution of potentials on the polarized segments (1 to 10 and MAIN) and non-polarized segments (11-18) is shown in Fig. 10.12. Apart from segment 12 at the inlet and 16 at the outlet, the potentials of the non-polarized segments remained stable. The erratic behavior of these segments, 12 and 16, originates probably from a parasitic contact with the main segment. The common operating potential of the polarized segments is visible on this figure.

Figure 10.13 shows the evolution of local current densities on the polarized segments 1 to 10. A very important reorganization of the electrochemical reaction is visible on segments 1 to 6 spaced along the flow direction. Segment 1 presents a poor performance from the beginning of the test, which was not expected from simulation results. Segment 2 presented a severe

drop of performance between t=200h to t=400h, as well as segments 3 and 7 to 10 (central segment column). These segments, placed at the same location along the flow, present a very similar behavior during the whole test. The decay of performance observed on the segments situated in the first half of the element was partly compensated by an increase in current density on the other ones (4 to 6) located downstream.

10.5.3 Evolution of local overpotentials and ASRs

The corresponding evolution in local area-specific resistances (ASR) gives a more explicit information on the degradation process (Fig. 10.14). To compute the ASRs, the Nernst potential was measured by disabling the polarization at regular intervals.

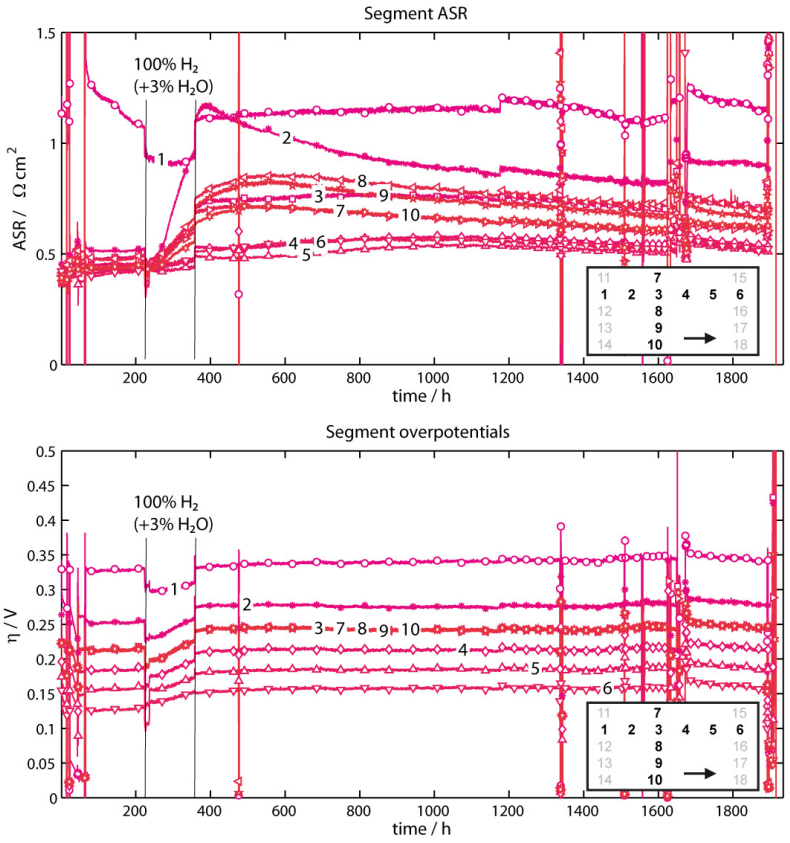

Figure 10.14: Evolution of local ASR (top) and local overpotentials (bottom).

The segment 1 at inlet presents a high ASR from the beginning of the test. Segments 2, 3 and 7 to 10 show an important increase in ASR between t=200 to 500h, followed by a long decrease with time. This decrease indicates a possible partial reversibility of at least one

degradation process, a fact that was not expected from previous results.

The extent of the rise in ASR decreases along the flow direction, and the segments 4 to 6 located in the second half of the element present remarkably stable ASRs over the whole duration of the test. ***Consequently, it can be concluded that the degradation of performance of the whole repeat-element was mainly caused by the degradation of its inlet region, while the outlet region experienced low degradation over the 1900 hours of operation.***

The sharp rise in ASR coincides with the period operating under pure, humidified hydrogen, which could lead to the hasty conclusion that the change of fuel induced an important degradation.
To look at the detail of this transition, a correction of the step of ASR resulting from the change of gases was done, by adding, respectively subtracting the amplitude of the ASR step found at t=220h and 350h to the following data. The result is shown in Fig. 10.15. On the obtained curves, the slope of the ASR curves changes before this period on some segments, and in particular on segments 3 and 7 to 1. In addition no marked change of slope at the moment of the interruption and at the moment of re-start of nitrogen supply is found. Therefore, it is concluded that both events (fuel charge and ASR evolution) are not directly related, which is confirmed afterwards by impedance spectroscopy.

With the presence of increasing ASRs in the vicinity of the gas inlets, one hypothesis could be the presence of pollutants in the gas streams, impacting first on the inlet area. However, to verify this kind of hypothesis, additional information is required. First, the affected electrodes and electrochemical processes have to be identified, and second, the obtained results have to be put in relation with post-experiment analyses. This is the object of the next paragraphs.

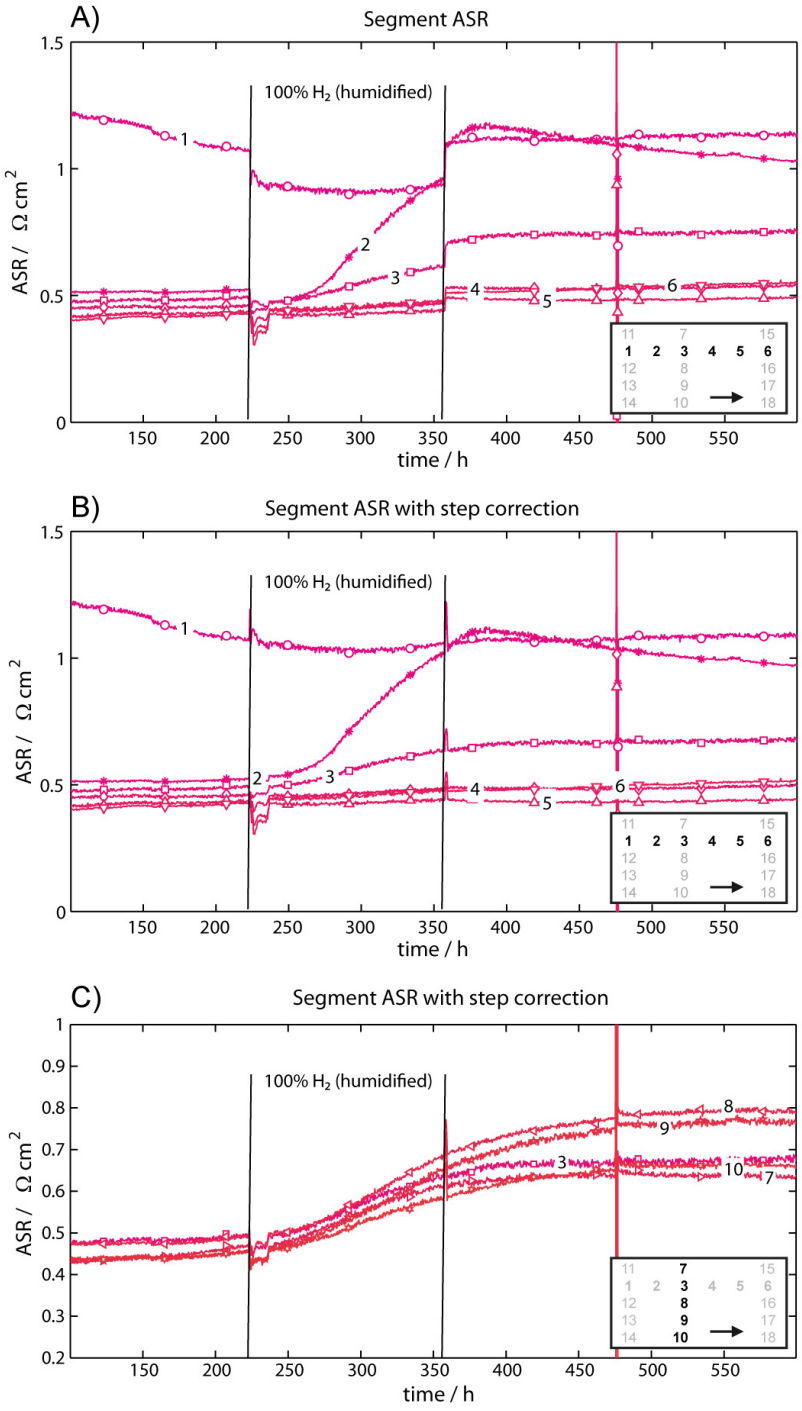

Figure 10.15: Detail of the evolution of ASRs. A) Original data on segments 1 to 6 on the horizontal row. B) The same data with a correction of ASR steps found at the change of fuel composition. C) The same step correction for the segments 3 and 7 to 10 located on the second segment column.

10.6 Analysis of the state of degradation by impedance spectroscopy

10.6.1 Methodology

After 1600 hours of operation, electrochemical impedance spectroscopy (EIS) measurements were performed on each segment to identify the extent of degradation for different electrochemical processes. The EIS measurements were performed under constant conditions for all segments. To achieve this, the polarization of all segments (including main) was stopped, in order to keep the fuel composition constant. EIS was performed with a bias current of $0.23\mathrm{A\,cm^{-2}}$ in order to include mass transport effects. First, separation of ohmic and polarization losses was performed. Next, the response of the segments over the frequency domain was analyzed to identify electrochemical processes and their level of degradation. For all contributions, the spatial distribution over the active area was studied.

Due to the absence of EIS measurements at the beginning of the test, only the relative degradation between segments could be studied at t=1600 hours. Based on the hypothesis that the cell performance was homogeneous originally and on the fact that some segments showed very low degradation over time, the relative degradation with respect to a low-degraded reference segment (i.e. n°5) can be considered as a reliable indicator.

To enable these analyses, a set of Matlab routines was written to enable batch processing of spectra, in particular for the application of the differential techniques described below. Additional routines were developed to perform fits of the recorded spectra using the equivalent circuits which are common for these types of analyses, or to perform a correction of the parasitic inductance found in the recorded data.

10.6.2 Ohmic and polarization resistance

Figure 10.16 shows the separated contributions of ohmic and polarization resistance, as well as the total ASR. The ohmic resistance map shows increased values on the polarized segments (1 to 10), and lower values on the non-polarized ones. This indicates an effect of polarization on the ohmic resistance, an observation reported in literature [68] and explained by a partial polarization-induced detachment of LSM and YSZ particles in the cathode. The polarization resistance decreases strongly from inlet to outlet ($0.8\ \Omega\,\mathrm{cm^2}$ to $0.5\ \Omega\,\mathrm{cm^2}$), indicating an important degradation of the concerned reaction steps. At the inlet, segment 1 (polarized) shows lower values than the non-polarized segments, indicating possible current-induced activation. Finally, the total resistance follows the same major trend as the polarization resistance.

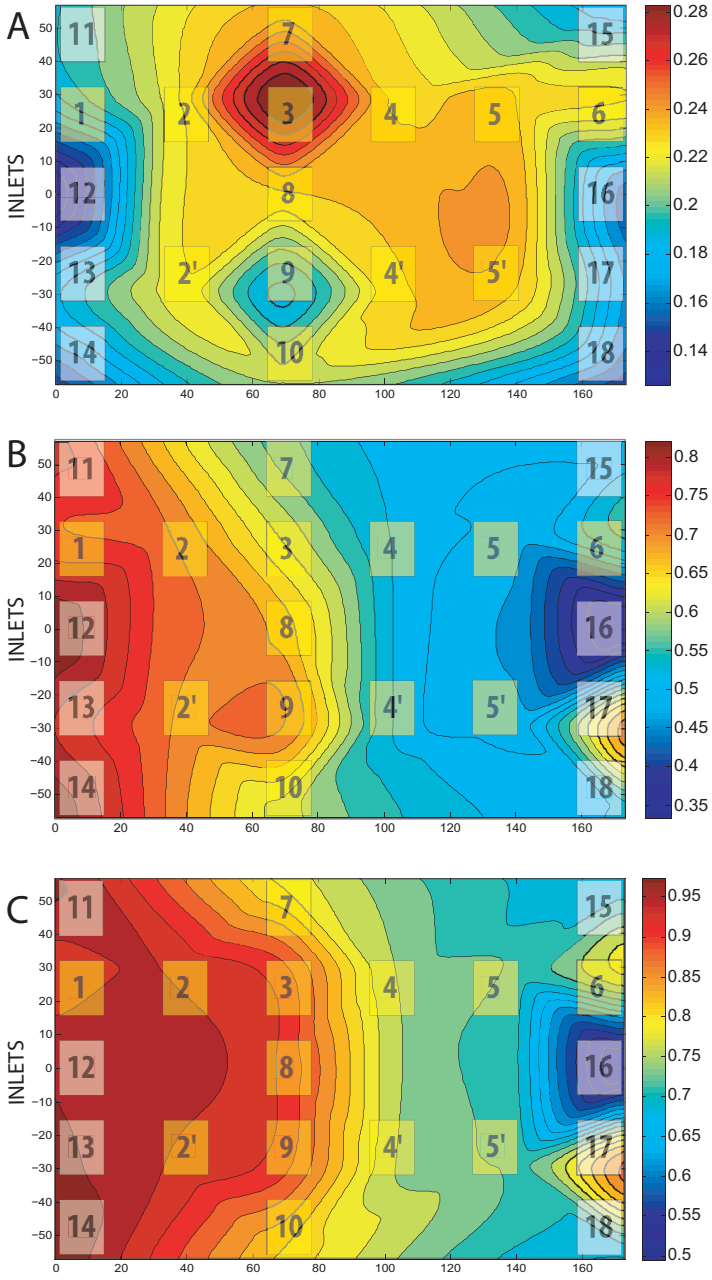

Figure 10.16: Degradation maps: projection on the active area of the local ohmic (A), polarization (B) and total resistances (C). Conditions: All segments at OCV with exception of the tested one, 6 ml min^{-1} cm^{-2}H_2 + 6 ml min^{-1} cm^{-2}N_2 (+3% H_2O), t=1600hrs.

10.7 Identification of electrochemical processes and their degradation

10.7.1 Method

The analysis of polarization losses is performed by using the differential method proposed by Jensen et al. in reference [120]. The use of differential methods presents several advantages and a particular ease of use for the large amount of recorded data. First, this method is particularly interesting in the present case, as it is the difference among the different parts of the fuel cell which is investigated to isolate the different types of degradation. Second, the use of absolute, not differential, fitting techniques in an equivalent circuit approach requires an excellent knowledge of the characteristic impedance of a specific cell type, in particular an accurate identification of the characteristic frequencies by dedicated change of operation parameters (fuel and oxidant partial pressures, current density, temperature). Else, excellent fits can be obtained, but with less physical meaning. As this data was not available for this type of the cell, this approach was abandoned. Finally, the differential technique applied in this case was found to bring the information of interest in a simpler and more direct manner.

In the approach proposed by Jensen et al., the following ***transformation*** is first applied for each spectrum :

$$\delta Z'(\omega) = -Re\left(\frac{\partial Z(\omega)}{\partial\,(ln\omega)}\right) \tag{10.2}$$

Similarly to the study of the imaginary part of impedance spectra, this function reveals electrochemical processes by the presence of peaks at distinct frequencies. *The major advantage of this function when compared to the imaginary part is that it is insensitive to parasitic inductance, as it is based on the real part of the impedance spectrum.*

Differentiation is performed for each segment j either with a reference segment k_{ref} and under the same conditions, or for the same segment under different operating conditions (ψ_2 vs ψ_1). The first differentiation is used to reveal the electrochemical processes which are more or less affected by degradation. The second differentiation is used to reveal for instance the electrochemical processes which respond to a change in fuel composition, i.e. to identify anode-related processes.
The difference function $\Delta\delta Z'$ is defined as:

$$\Delta\delta Z'_{j-k_{ref}}(\omega) = \delta Z'_j(\omega) - \delta Z'_{k_{ref}}(\omega) \tag{10.3}$$

$$\Delta\delta Z'_{\psi_2,j-\psi_1,j}(\omega) = \delta Z'_{\psi_2,j}(\omega) - \delta Z'_{\psi_1,j}(\omega) \tag{10.4}$$

In order to identify all electrochemical processes, ***summary functions*** were defined which

sum the differences functions $\Delta\delta Z$ obtained for the 18 segments under defined conditions:

$$\zeta = \sum_{k=1}^{18} (\Delta\delta Z')^2 \tag{10.5}$$

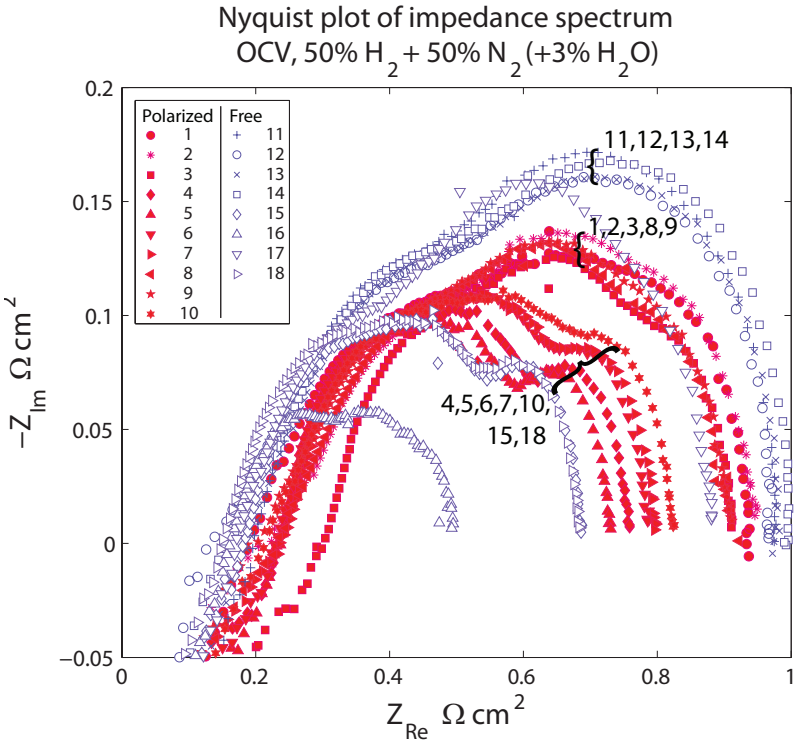

Figure 10.17: Nyquist plot of the EIS spectra recorded on all segments under constant conditions. (OCV, 50% H2-50%N2, 800°C)

10.7.2 Inspection

Nyquist plots One resulting series of spectra is given in Fig. 10.17, recorded under the nominal conditions of the test (dilute fuel) and under a constant bias current of $0.23\,\mathrm{A\,cm^{-2}}$. In this figure, the x- and y-axes are not represented using the same scale, as else it is not possible to distinguish between the different measurements. The recorded spectra show important differences between polarized (1-10) and non-polarized (11-18) segments both for ohmic and polarization losses. On the polarized segments, the higher ohmic resistances mentioned earlier are clearly visible. In the low-frequency region, the spectra present distinct features, which are studied in more detail by analyzing the corresponding $\delta Z'$ functions. Finally, a likely artifact is visible on segment 16. This segment is therefore excluded from ulterior analyses.

$\delta Z'$ transformation The corresponding transformation of the spectra in the $\delta Z'$ function is shown in Fig. 10.18. Important differences between the segments are visible over the frequency domain. As the spectra are recorded under constant parameters, the observed differences account for the alteration of the electrochemical response of the cell depending on the location of the measurement. Therefore, these differences represent different levels of response for different electrochemical processes.
In this dataset, a principal difference among the spectra is visible around 20 Hz, indicating a process heavily affected by degradation.

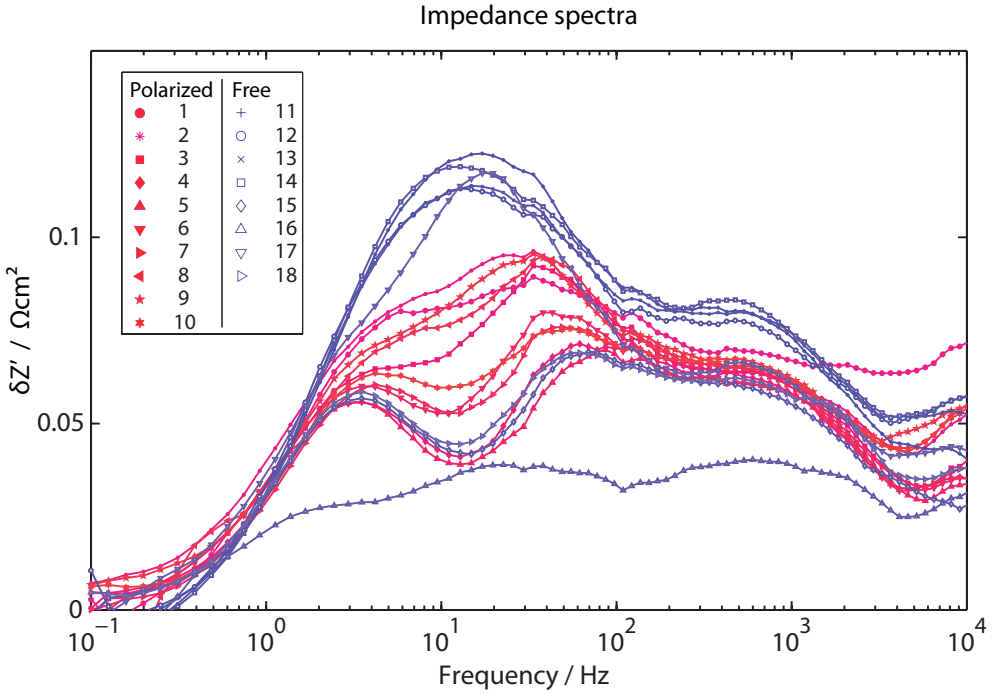

Figure 10.18: Corresponding $\delta Z'$ function computed from Eqn. (10.2). All segments at OCV, with exception of the tested one (0.21 A cm^{-2}). (50% H_2-50%N_2, 800°C)

10.7.3 Degraded processes

The identification of the degraded processes is further improved by differential methods, and in this case by subtracting the $\delta Z'$ function of the least-degraded reference segment n°5 from the $\delta Z'$ functions of all other segments (see Fig. 10.19, top right): $\Delta\delta Z'_{j-k_{ref}}(\omega) = \delta Z'_j(\omega) - \delta Z'_{k_{ref}}(\omega)$ with $k_{ref} = 5$. This is done for all segments under the same conditions, that is, the same fuel composition and bias current.
In this case, the differentiation cancels the contributions that are constant (i.e. not altered) among the segments, hence only revealing the differences in more explicit manner.

The mostly affected process is visible at 20Hz, followed by a second at 450Hz and one or several contributions above 10kHz. As shown hereafter, the contribution found at 450Hz is the only one to be sensitive to variations of fuel composition (Fig. 10.20), indicating a degradation of this anode-related process (in this case the charge transfer reaction on the anode side, as shown below).

This result of the differential method gives here a much more detailed information about the

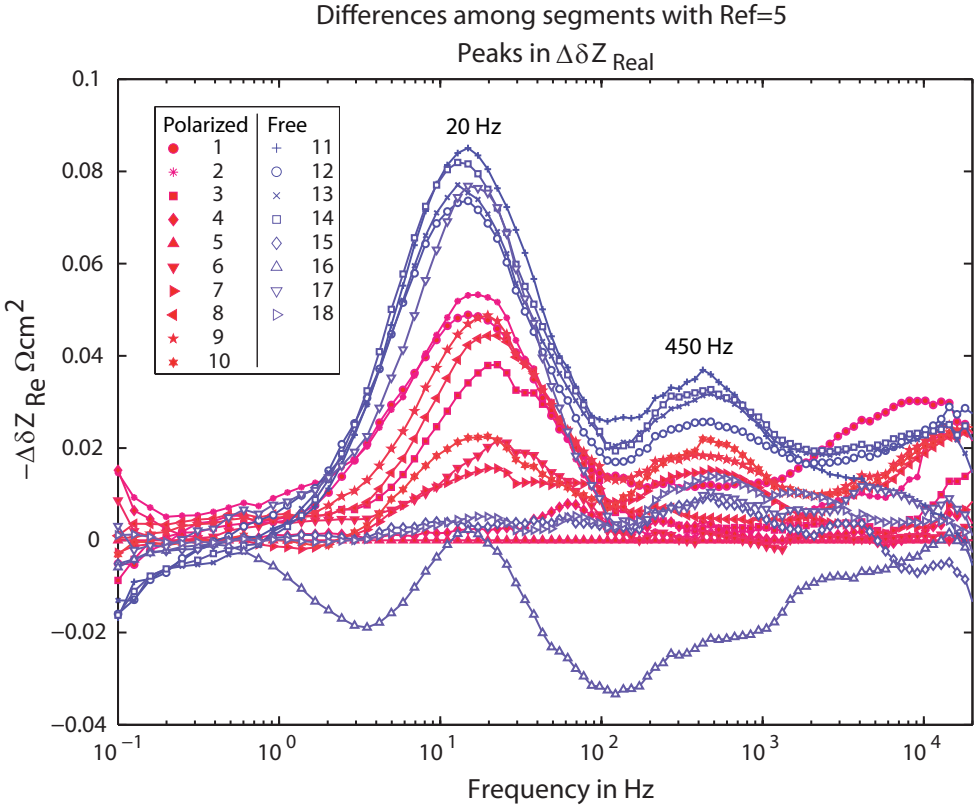

Figure 10.19: Identification of degraded electrochemical processes. Difference between individual $\delta Z'$ functions and the one of the least-degraded reference segment n°5: $\Delta\delta Z'_{j-k_{ref}}(\omega) = \delta Z'_j(\omega) - \delta Z'_{k_{ref}}(\omega)$. Recording parameters are the same for all segments (fuel composition and bias current).

already reported important inhomogeneity of the degradation over the reactive surface. In particular, it shows that the different electrochemical processes are not affected to the same extent, and also not at the same location in the fuel cell. This information can therefore be exploited to relate the degradation of a specific electrochemical process to the local operating conditions or to any other known parameter. To enable this analysis, the next steps consists therefore in the identification of the nature of the electrochemical processes, and first of the concerned electrode.

10.7.4 Identification of anode-related processes

The anode-related processes are identified by observing the variations in the spectra upon a change in the fuel composition, from dilute (50%-50% $H_2 - N_2$, humidified) to pure (humidified) hydrogen. In this case again, the differential method is applied, by computing for each segment j the difference between its own responses upon a change of fuel composition: $\Delta\delta Z'_{pure-diluteH_2,j}(\omega) = \delta Z'_{pureH_2,j}(\omega) - \delta Z'_{diluteH_2,j}(\omega)$.

The difference functions obtained for each segment are shown in Fig. 10.20, revealing three electrochemical processes with characteristic frequencies at 2Hz, 35hz and 450Hz.

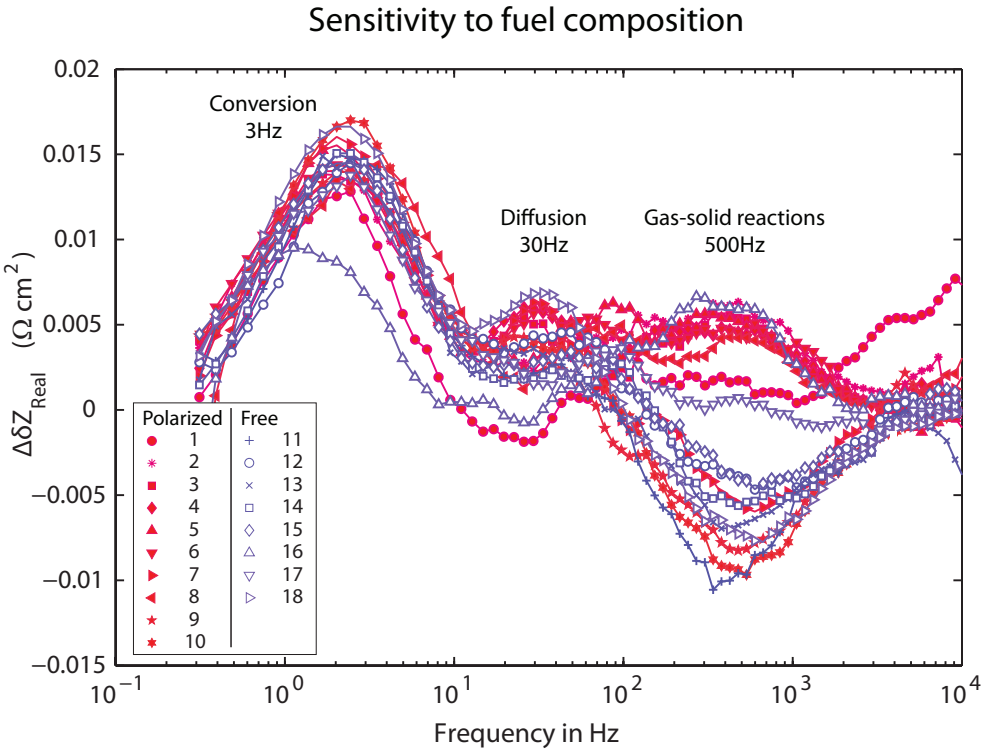

Figure 10.20: Sensitivity of the recorded spectra to changes of the fuel composition. Difference functions $\Delta\delta Z'_{pure-diluteH_2,j} = \delta Z'_{pureH_2,j} - \delta Z'_{diluteH_2,j}$ obtained for each segment upon a variation of the fuel composition (dilute vs. pure, humidified hydrogen).

Identified by their relative orders of frequency and based on literature data [121][46], it is expected that these processes correspond respectively to *gas conversion impedance, diffusion and charge transfer on the anode side.*

While, for the low-frequency conversion impedance a similar variation is observed on all seg-

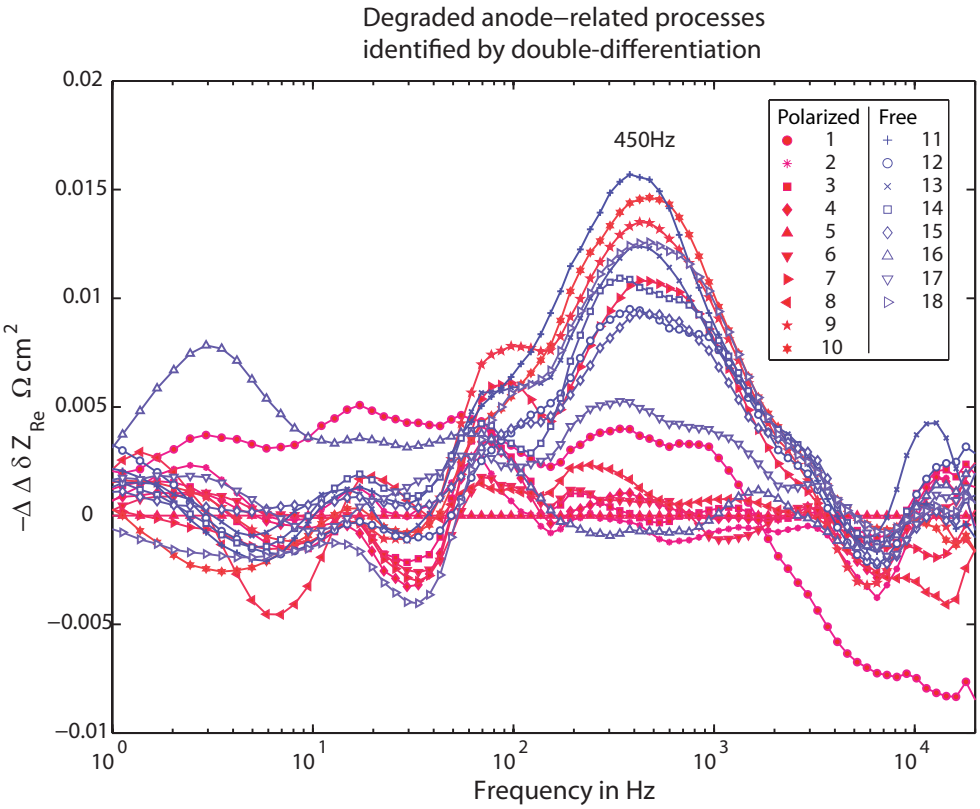

Figure 10.21: Difference among the local sensitivities to a change of the fuel composition. First, the sensitivity to the fuel composition is computed for each segment, followed by a subtraction of the sensitivity of the reference segment 5.

ments for a change of fuel composition, the contrary is true for the high-frequency process corresponding to the charge-transfer reaction. For most of the polarized segments (red), a positive variation is observed, while a negative one is affecting principally the non-polarized segments. Besides this general trend, notable exceptions exist with polarized segments (7, 9, 10) presenting a negative variation. This observation seems of particular significance, as it affects the charge transfer reaction on the anode side. To explain this observation, a particular attention was paid in the SEM-EDX analyses on possible alterations of the interfaces between nickel and YSZ particles, where the concerned reaction takes place. Unfortunately, no obvious explanation could be found.

Besides the simple differentiation described above, double differentiations can also be performed in order to study the difference among segments of the sensitivity to a specific change of parameter. For instance, the local sensitivity to the fuel composition (shown above in Fig. 10.20), can be compared to the one of the reference segment n°5 by differentiation:

$$\Delta\Delta\delta Z'^{pure-diluteH_2}_{j-5} = (\delta Z'_{pureH_2,j} - \delta Z'_{diluteH_2,j}) - (\delta Z'_{pureH_2,5} - \delta Z'_{diluteH_2,5}) \qquad (10.6)$$

The result is shown in Fig. 10.21.

While the two low-frequency processes are shadowed-out by the procedure, the details of the high-frequency contribution are emphasized. This shows that for both low-frequency processes, the sensitivity to a change of fuel composition has hardly been modified with time, and this for all segments.
For the conversion impedance, this result is expected as this term is linked to the fuel flow occurring at the cell's surface [22], and less to the intrinsic properties of the cell. For the diffusion term however, it indicates that no major change of the diffusive properties occurred.

For the high-frequency contribution, it is shown that the polarized segments 2-6 and 8 present a very low difference with respect to the reference segment 5. The only polarized segment (segment 1) on the fuel inlet line (first vertical row) presents an intermediate response. Finally, all non-polarized segments, with exception of segment 17, present a clear difference from the reference segment 5, together with the already mentioned polarized segments 7, 9 and 10.

10.7.5 Identification of cathode-related processes

Summary of observed processes Due to the absence of the possibility to dilute with nitrogen on the cathode side at the time of the experiment, it was not possible to identify the cathode-related processes in the same way as done for the anode side. It is the differences between the degraded and the anode-related processes which are used to identify the contributions from the cathode.

Figure 10.22 summarizes the processes identified previously by using the summary function defined in Eqn. (10.5). The black lines ((+) and (x)) indicate the degraded processes identified by differentiation in Fig. 10.19, which are visible both in spectra obtained under dilute and pure hydrogen (humidified).
In addition, the anode-related processes found in Fig. 10.20 are summarized by the green line (o).

From this summary, it is visible that the two degraded processes found at 20 Hz and above 10 kHz are not related to the anode-side, hence their attribution to cathode-related processes.

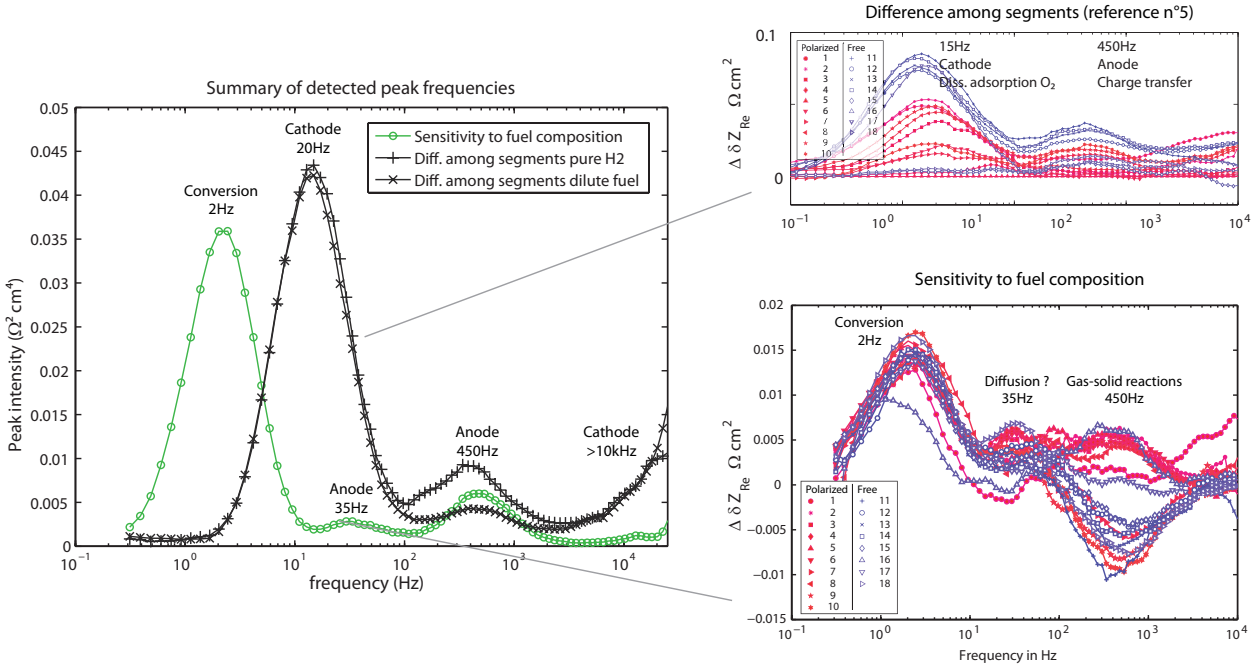

Figure 10.22: Summary functions (left) and original data (right). Green: Identification of frequency ranges affected by variation of fuel composition (50% H2 vs. 100% H2, both 3% humidified) on each segment (o). Black: Identification of degraded processes, by differentiation with segment 5 as reference ((+) and (x)).

Cathode-related processes Two principal cathode processes are expected [46] in air and under low bias current: a low-frequency process sensitive to TPB length, pO_2 and current density [44][122], and a less sensitive high frequency process corresponding to charge transfer at the interface between LSM and YSZ [46][44]. The exact mechanism underlying the low frequency process is under debate, but a certain agreement is found for oxygen dissociative adsorption, reduction and transfer to the TPB [46][44][42]. Therefore, the low-frequency process found at 20 Hz could correspond to this reaction step. However, the characteristic frequencies reported in literature are higher, in the range of 100 Hz to 1 kHz [46]. Therefore, the properties of this process have to be analyzed in more detail to confirm this possible attribution.

For the 20 Hz process, an important sensitivity on current was found in the EIS measurements as shown in Fig. 10.23. A similar sensitivity is also visible for the conversion (2 Hz) and anode charge transfer terms (450 Hz).

Additional tests performed, in our laboratory, on a button cell with similar cathode revealed a low-frequency cathode process between 10 and 26 Hz when exposed to current and pO_2 variations (see Fig. 10.24). This frequency coincides with the 20 Hz-process in the seg-

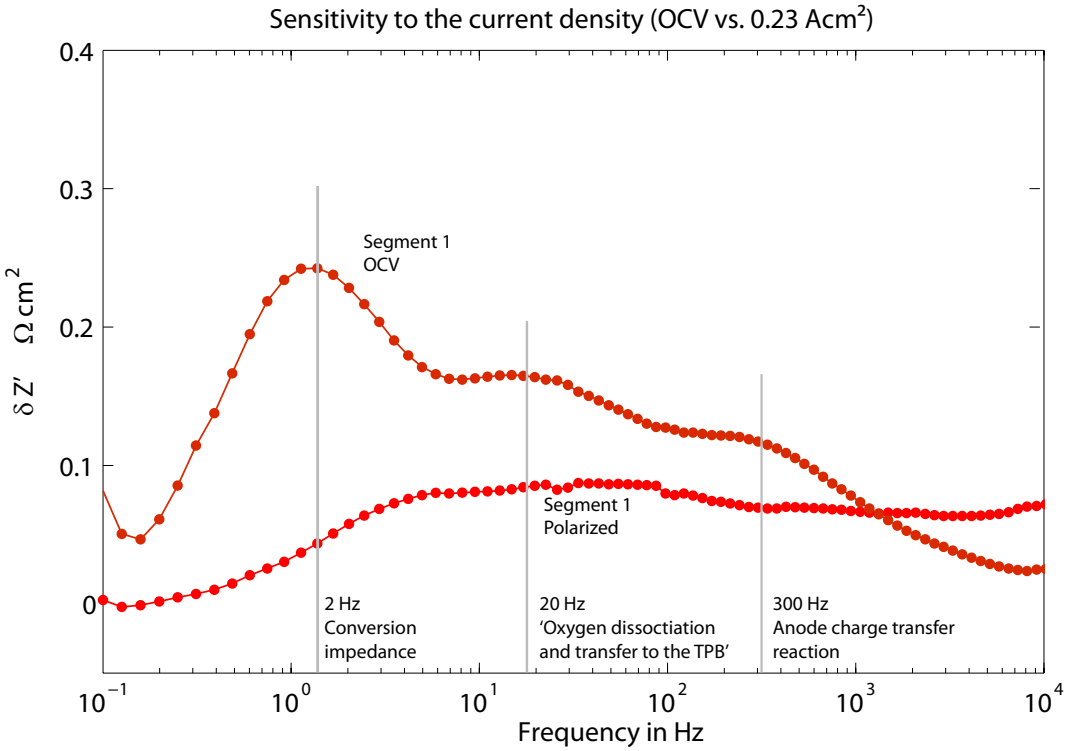

Figure 10.23: Effect on the recorded spectra of the bias current density applied in the EIS measurement (segment 1, 0.23 A cm^{-2}vs. 0 A cm^{-2}

mented case. Moreover, the button-cell test revealed a $pO_2{}^{-1/2}$ dependency of the concerned impedance (see inset), which can be expected for the above-mentioned low-frequency reaction step [44]. **Therefore, the mostly degraded process present at 20 Hz was ascribed to the low-frequency cathode reaction step *oxygen dissociative adsorption and charge transfer to the TPB* [46].**

Finally, both the segmented and the button-cell experiment reveal an electrochemical process around 10 kHz, which is attributable to the cathode, i.e. to the charge transfer between LSM and YSZ (low pO_2-dependency, as shown in the inset).

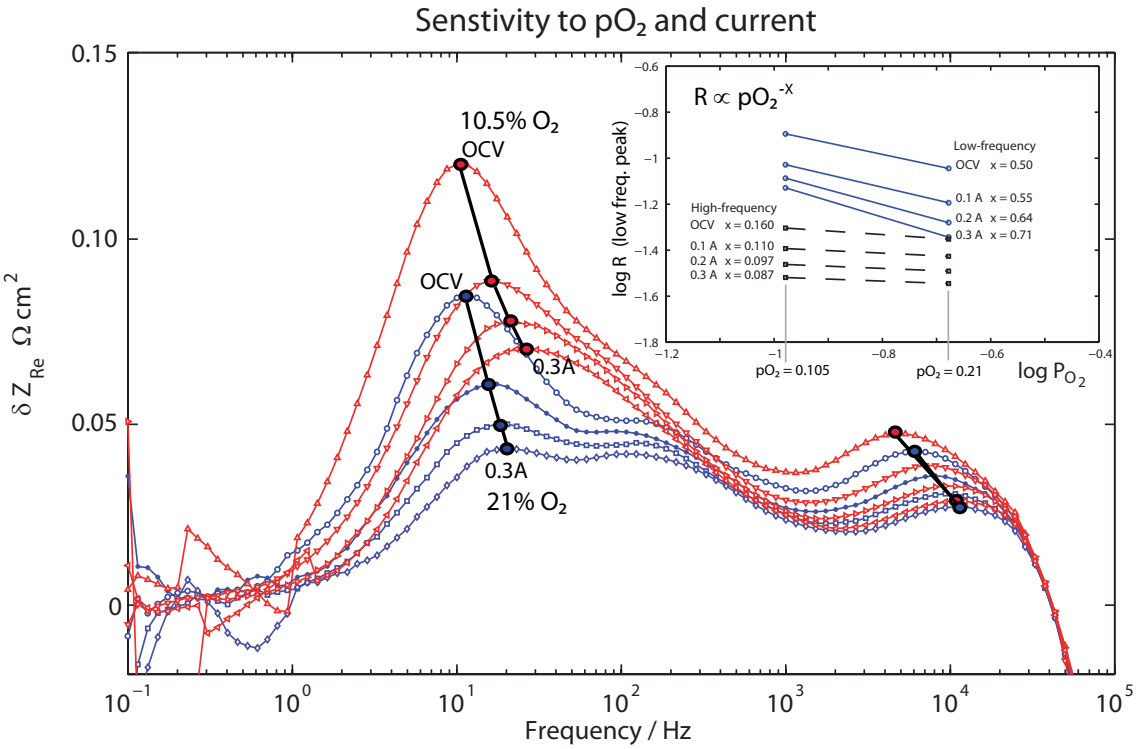

Figure 10.24: Identification of cathode-related processes in a button-cell experiment by variation of the pO_2 . Red: 10.5% O_2 . Blue: 21% O_2 . Inset: pO_2 -dependance of the low- and high-frequency impedances.

10.7.6 Summary of the identified processes

To summarize the results of the process identification procedure, the identified processes and their characteristic frequencies are shown in Table 10.1.

f / Hz	Anode	Cathode
2	Conversion	
20		**Dissociative adsorption of O_2 and transfer to the TPB**
35	Diffusion	
450	**Charge transfer**	
10'000		Charge transfer at the LSM/YSZ interface

Table 10.1: Summary of the identified electrochemical processes

With the identification of five elementary processes in the obtained dataset, which is similar to the results of other authors [46], a detailed information about degradation is obtained.

As first step towards an identification of the sources of degradation, the spatial information contained in the dataset for each electrochemical process is analyzed. This is the object of the next paragraph.

10.8 Spatial distribution of degradation

The results obtained by differentiation with a reference segment (see Fig. 10.19), which reveal the degraded processes, were projected on the active area to study the spatial distribution of degradation, as shown in Fig. 10.25. For both principally altered electrochemical processes, the inlet region is the mostly affected one. Moreover, it is clearly visible that the principal contribution to the degradation is an alteration of the electrochemical reaction on the cathode side.

On the inlet line, both processes present a lower polarization resistance solely on the only polarized segment (n°1). This observation might be compatible with a current-induced activation process, as shown hereafter. Looking at the segments that were not polarized during the test (n°11-18) located at the inlet and the outlet, a clear difference is observed which only depends on their position in the repeat-element. The polarization resistance is higher for both electrochemical processes at the inlet despite the lack of polarization in both cases. This indicates a degradation mechanism which does not depend principally on polarization.

This result shows that, using the differential methods presented above, it is possible to identify the electrochemical processes affected by degradation, but also to study their spatial distribution over the active area. Foremost, it demonstrates the intrinsically local character of degradation processes.

In the next chapter, a link is established between the features observed in the impedance spectra and the local post-experiment analysis.

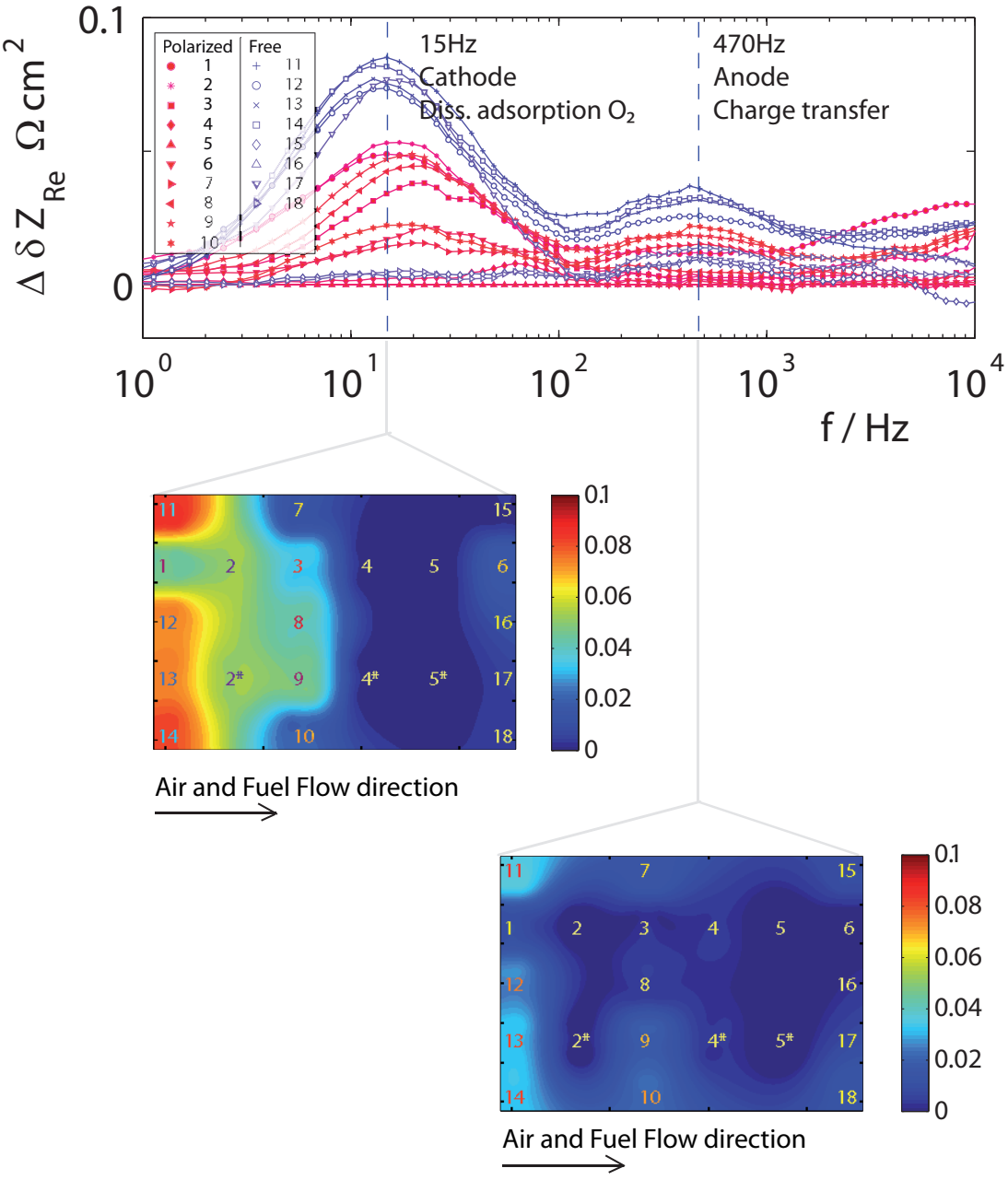

Figure 10.25: Local level of degradation after 1600 hours of operation. Top: difference plot of the $\delta Z'$ function between each segment and the reference segment n°5. Bottom: corresponding spatial distribution obtained for cathode (15Hz) and anode (470Hz) processes.

10.9 Conclusion

By using the developed diagnostic station, it was possible to reveal for the first time the local character and the highly non-homogeneous extent of degradation occurring in a real SOFC stack prototype. Using impedance spectroscopy in combination with specifically developed analysis tools, it was possible to identify the different electrochemical processes and their local level of degradation. The electrochemical reaction steps corresponding to ***oxygen dissociation and transfer to the TPB*** on the cathode side and the ***charge transfer reaction*** on the anode side were identified as the most degraded processes in this experiment.
For both processes, the spatial distribution of degradation could be established, revealing its non-homogeneous distribution over the active area. In the resulting degradation maps, it is visible that this degradation followed a consistent trend, with the main degradation located at the gas inlets. Limited degradation was recorded in the outlet region, where ASRs did not present strong variations throughout the test. This demonstrates the potential for the investigated prototype of an important reduction of its degradation .
Finally, it is shown that the global degradation of the repeat-element does not reflect the important variations of current densities or ASRs occurring internally, as balancing effects take place between more and less degrading regions. This illustrates the limited interpretation of degradation studies based on stacks or complete repeat-elements, where the measured integral indicators do not capture the internal processes accompanying the loss of performance.

Throughout this chapter, the interest of in-situ measurements of electrochemical performance and degradation has been demonstrated. In addition to the important results on degradation, a validation of the designed prototype and of the developed models could be obtained. Moreover, it was possible to control the correct assembly of the element, but also to detect a fuel distribution problem, an information that would hardly have been accessible in any other testing conditions. Thanks to this information, the fuel distribution could be corrected, enabling to reach a maximal fuel utilization of 85% and an efficiency of 53% in a 20-element stack configuration.

Beyond the already obtained results, the diagnostic station will, in the future, be completed to overcome some limitations of the present experiment. The analysis of impedance spectra will, in particular, be further enhanced by setting up a more complete characterization procedure, as well as by introducing complementary equipments to allow additional variations of parameters (for instance for modifications of the steam partial pressure).

Finally, the locally-resolved information about the degradation of the identified electrochemical processes gives a unique opportunity to selectively define the zones to be observed in the post-experiment analysis, with the underlying goal to identify possible sources of degradation. This is the object of the next chapter.

Chapter 11

Post-experiment analyses and identification of degradation sources

11.1 Introduction

In this chapter, post-experiment analyses, which were made with the purpose to identify sources of degradation in the segmented repeat-element, are presented. These analyses were obtained using scanning (SEM) and transmission (TEM) electron microscopy at the *Interdisciplinary Center For Electron Microscopy* (CIME-EPFL), operated by members of the research group working on SOFCs at EPFL.

Following persons are gratefully acknowledged for their highly valuable contribution to this project:
A.J. Schuler, PHD student, who performed numerous SEM-EDX observations on the segments selected from the analysis of impedance spectra.
A. Faes, PHD student, who spent time for sample preparation, in particular of TEM lamellae using the focussed ion beam (FIB) (Zeiss NVision 40), in addition to observation and analysis of anode samples.
C. Calderone, diploma student, who made TEM observations wit the TEM on the prepared lamellae in the frame of her diploma thesis.
Dr. S. Diethelm, Dr. A. Hessler and Dr. MER J. Van herle for their help in the interpretation of results.

To identify sources of degradation, post-experiment analyses were first performed by SEM-EDX (FEI XL30, with Oxford Instruments EDX detector). In a first step, the surface of the $(La, Sr)CoO_3$ current-collection layer of the cell was analyzed, in order to detect possible traces of pollutants. In a second step, the penetration of the identified pollutants into the LSM-YSZ cathode layer was investigated. And finally, the spatial distribution of the pollutants over the active area was studied and put in relation with the recorded degradation.

11.2 Identified pollutants

After disassembly of the repeat-element, the segments of interest were cut-out from the cell and analyzed by SEM-EDX. Due to the large degradation of the cathode in the vicinity of the air inlet, a likely contamination by pollutant species was expected.
The interface between the $(La, Sr)CoO_3$ cathode layer and the air stream was therefore analyzed first, looking for their presence. In fact, three species, known as pollutants for cathodes, were identified and quantified on the whole active area : chromium, sulfur and silicon (see Fig. 11.1).

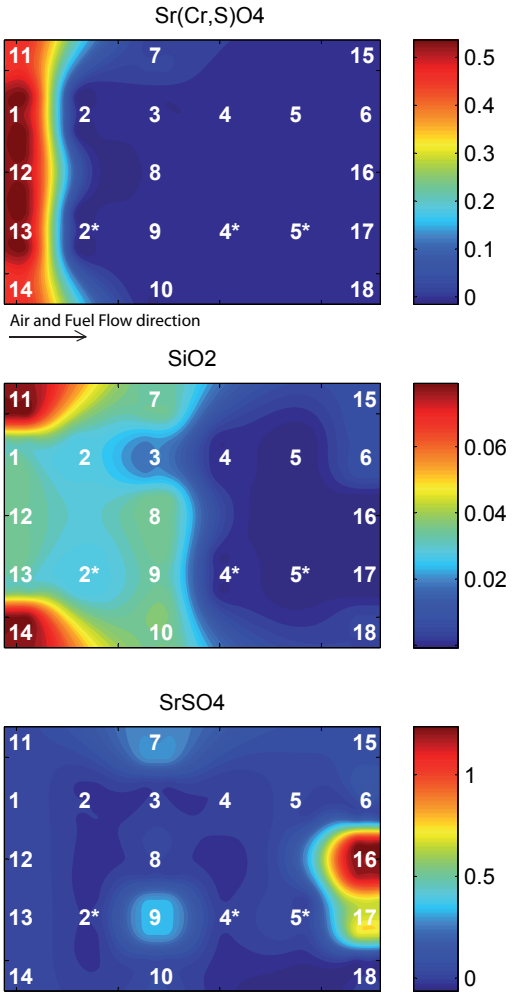

Figure 11.1: Spatial distribution of pollutants over the cathode current collection layer. Ratio of the amount of pollutant (molar %) to the amount of LSC.

Chromium ***Chromium was only found at the air inlet, with rapidly decreasing amounts along the flow.*** It forms a densified phase at the interface with the gas stream, as shown in Fig. 11.2. EDX analyses revealed a composition of 68% O, 17% Sr, 13% Cr and 2% S, indicating a sulfur-containing strontium chromate compound: $Sr(Cr_{0.85}S_{0.15})O_4$. XRD measurements showed that this compound, despite a stoichiometry close to $SrCrO_4$, presents a different crystalline structure due to the enrichment with sulfur.

As shown in Fig. 11.2, an almost dense phase is found in the direct vicinity of the air

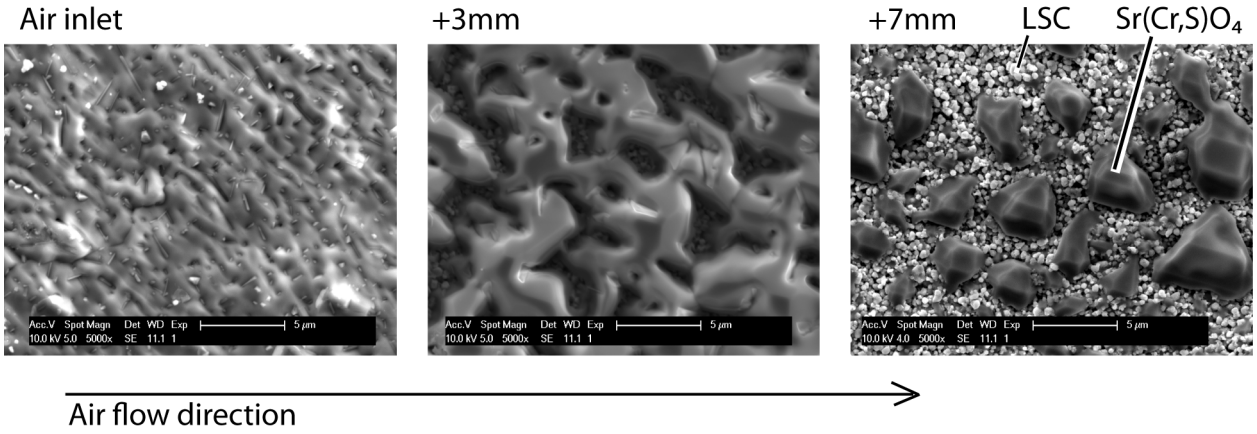

Figure 11.2: Chromium-containing phase ($Sr(Cr, S)O_4$) formed at the surface of the LSC layer. Evolution along the flow, starting from the air inlet.

inlet. Few millimeters away, the surface coverage starts to decrease, with apparition of the unaffected LSC layer. The amounts of strontium chromate continue to decrease further away, with only a few remaining spots on the surface. Finally, this phase completely disappears around the end of the first row of segments, and is not found at any other location in the element. As chromium is a known pollutant for cathodes, a link is therefore made between the poor performance of segment 1 and the presence on it of massive chromium amounts.
As chromium was not detected away from the first column of segments, it can be concluded that the main source of chromium in this experiment is located upstream of the active area, hence probably originating from system components (tubing, heaters).
Moreover, the rapid decrease of the chromium amounts on the surface indicates a trapping effect for this type of pollutant, which progressively reduces the convected and trapped amounts along the flow.

Silicon Silicon was identified as a second pollutant on top of the LSC surface. However, the exact quantification of the obtained amounts by SEM-EDX remains difficult, due to the presence of an overlap of the Kα line of silicon (1.7398 keV) and the Lα line of strontium (1.8066 keV) in the EDX spectra. The quantification of strontium was consequently performed using its Kα line found at 14.1429 keV, but the confidence in the deconvoluted amounts of silicon remains limited.

Silicon was found in the first half of the repeat-unit, with larger amounts along the inlet and in particular at its sides possibly due to the presence of sealing materials. Possible sources of silicon poisoning are consequently the seal materials, in addition to exogenous sources such as traces of silicon grease in the compressed air supply.

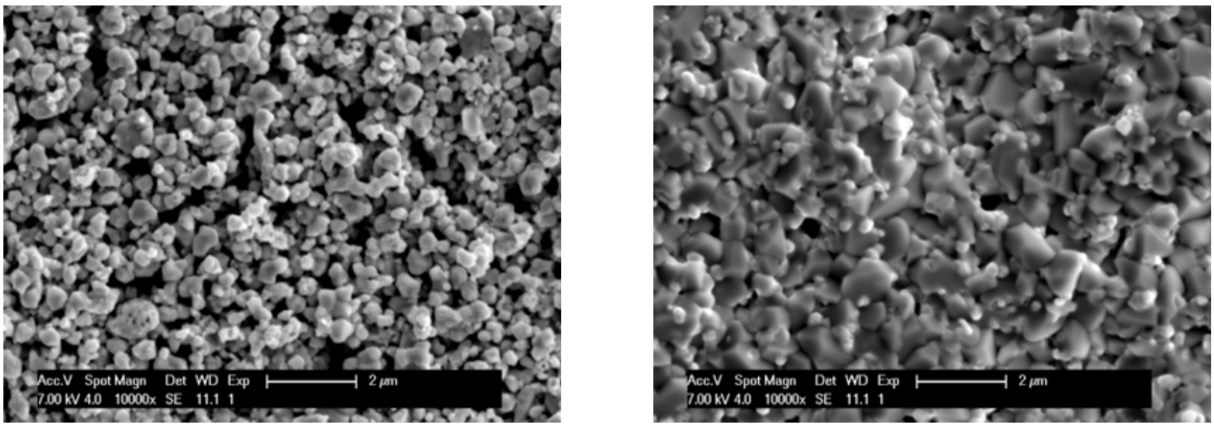

Figure 11.3: Strontium doped lanthanum cobaltite (LSC) current collector layer surface, before (left) and after (right) 1900 h exposure to sulfur-containing airflow, where strontium sulfate $SrSO_4$ is formed.

Sulfur Finally, sulfur was detected at the air inlet, and also on different spots over the active area, forming strontium sulfate $SrSO_4$ upon reaction with LSC. The resulting impact on the microstructure of the LSC surface is shown in Fig. 11.3.
While the sulfur pollution of anode materials is a known issue, the pollution of cathode materials by sulfur has received more attention recently. Yokokawa et al. identified sulfur as impurity after long-term operation of SOFC stacks in [119], and pointed out the effect of contamination on the durability of SOFC stacks [123].
Recently, Xiong et al. reported a model study of accelerated sulfur poisoning, by exposing strontium doped samarium cobaltite (SSC) and strontium doped lanthanum manganite (LSM) cathode materials to SO_2-concentrated air. While an important impact on the electrochemical performance of the SSC cathode was found, the one on the LSM cathode remained limited and was partly reversible.
In our case, a source of sulfur was found as impurity in the ceramic paste used to insulate the segments electrically. The presence at the inlet however indicates also a possible source in system components, such as the commercial polymer tubes used for air supply that were found to contain sulfur (Swagelok, Buna-N tube).

11.3 Penetration of the pollutants in the cathode layer

While the presence of the pollutants on top of the LSC layer attests of the presence of pollutants in the gas streams, only their presence in the active cathode layer (LSM-YSZ) could explain an effect on the local electrochemistry. Therefore, the penetration of pollutants into the LSM-YSZ active layer was investigated by performing EDX analyses on cell cross-sections.

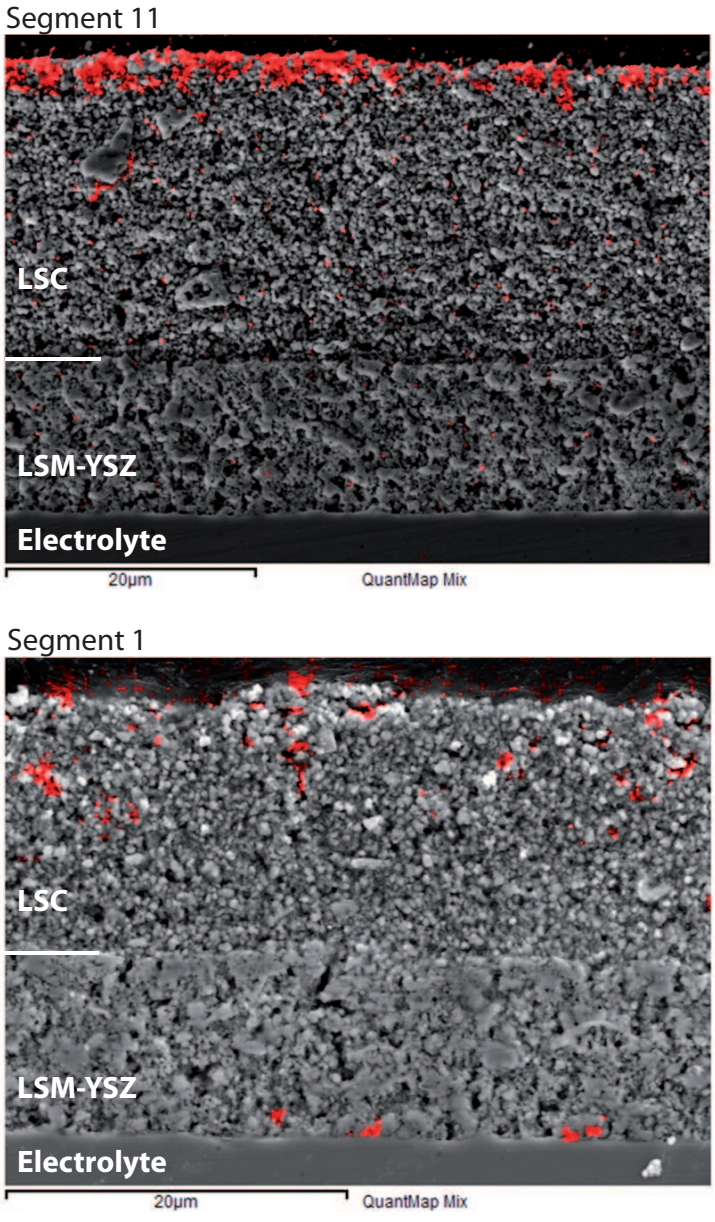

Figure 11.4: SEM cross-sections of the cathode layers on segments 11 (left) and 1 (right), with overprinted EDX mapping of Cr (red). Segment 1 was polarized during the test, segment 11 not. Top layer: LSC. Active layer: LSM-YSZ

Chromium poisoning Resulting cross-section analyses on chromium poisoning are shown in Fig. 11.4. Segment 11, located at the inlet and not polarized during the 1900 hours of operation, presents a Cr-containing layer at the top of the LSC current collection. A few Cr-containing spots are visible in the LSC, but no relevant presence can be found in the LSM-YSZ. In the segment 1, which was polarized, chromium is also found on the top of the LSC layer, but in particular also at the electrolyte. A less dense layer is found at the top of the LSC because the sample was taken a few millimeters more downstream than the one of segment 11. This result shows a probable polarization-driven deposition of chromium at the cathode/electrolyte, which can explain the poor performance of segment 1 from the beginning of the test.

To obtain more information about the nature of the chromium pollution of the LSM cathode, observations were performed with a transmission electron microscope (Philips/FEI CM300) at CIME-EPFL, as part of the diploma thesis of C. Calderone. TEM lamellae were extracted from the polluted segment 1 in close vicinity of the electrolyte, as shown in Fig. 11.5. Chromium-containing particles were identified (Fig. 11.5), whose composition was analyzed by EDX. The resulting composition was (at%) : 15.2% Cr, 2.3% S, 17.7% Sr, 58.8% O, corresponding again to a strontium chromate compound enriched with sulfur (i.e. $Sr(Cr_{0.87}S_{0.13})O_4$).

The presence of strontium chromate in a LSM-YSZ cathode is however surprising, because the formation of this compound is not expected from a thermodynamic point of view, as shown by Yokokawa et al. in [124]. Whether the simultaneous presence of chromium- and sulfur-containing species could lead to the formation of this compound remains unknown. Nevertheless, as this compound was extracted from the segment by a focused ion beam, and as the Cr-containing particle is not located near the polished surface of the sample, a contamination during the sample preparation can be excluded, which therefore excludes any artifact.

Finally, it has to be mentioned that the apparent absence of large chromium particles in segment 11 does not allow to exclude its presence. In fact, in a recent conference abstract [125], Horita et al. establish a link between the degradation of a LSM cathode and the quantified amounts of chromium evaluated by the SIMS technique. A significant effect on the performance of the cathode was observed upon pollution in their case. The corresponding concentrations of chromium quantified by SIMS were evaluated in the range of 1000ppm (0.1%), which is considered as below detection limit for TEM-EDX. Therefore, it is possible that, despite the apparent absence of chromium in the LSM-YSZ layer of segment 11, chromium was indeed present and affected the electrochemical performance. This could here possibly explain why segment 11 presents an important low-frequency contribution (20Hz), similarly to segment 1, as well as justify the difference in recorded spectra between the non-polarized segments at inlet and outlet.

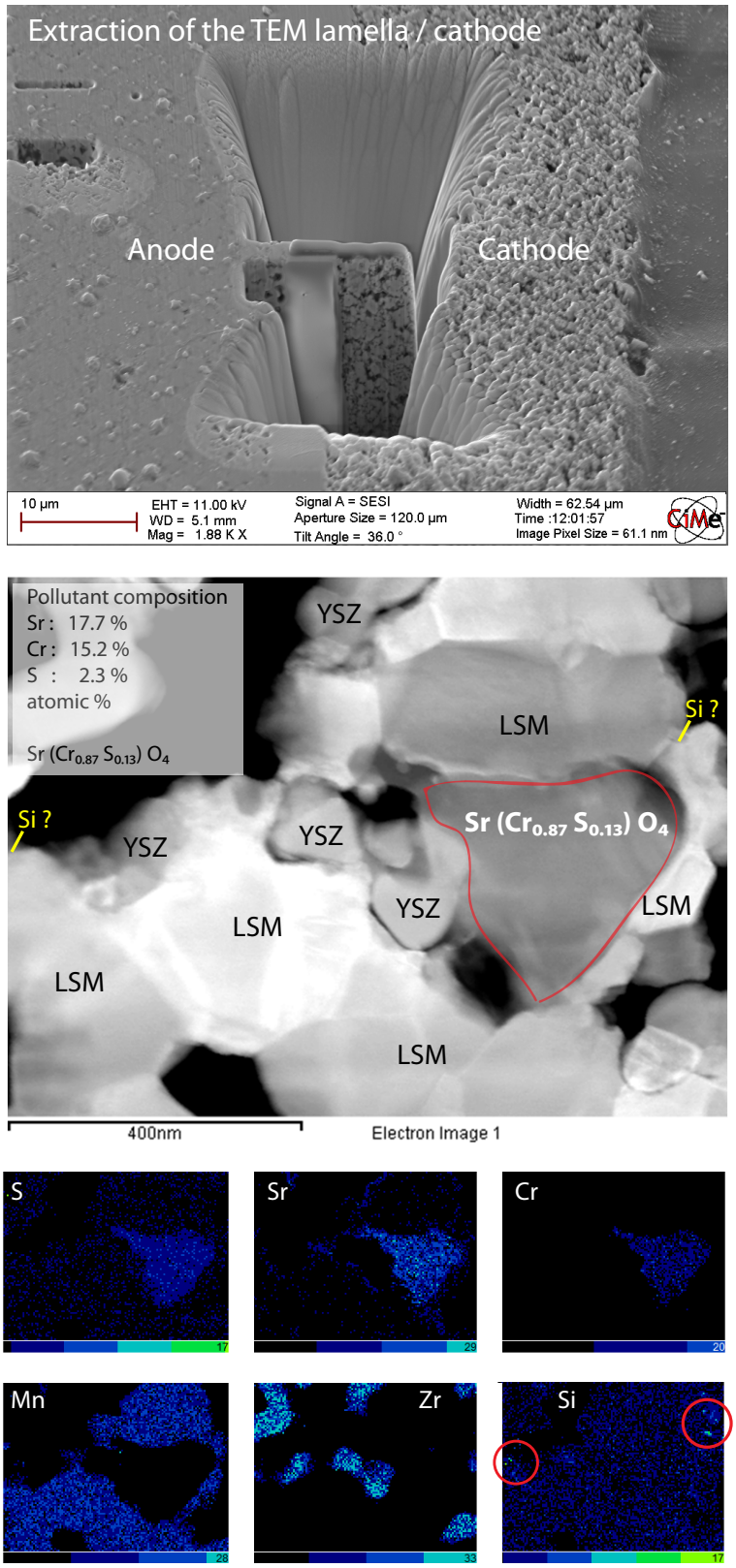

Figure 11.5: TEM observation of the chromium and silicon pollution of the LSM cathode on segment 1.

Silicon and sulfur poisoning As indicated in Fig. 11.6 for segment 1, silicon was detected in the LSC current collection layer by SEM-EDX, and also in smaller amounts in the LSM-YSZ cathode where it possibly altered the electrochemical reaction. TEM results however presented contradictory results. Using TEM-EDX, silicon was detected on several spots in the absence of strontium, as shown in Fig. 11.5, hence tending to confirm its presence. However, EELS measurements, which are not subjected to the deconvolution problem, did not confirm this observation. As the investigations area of a TEM lamella is very small, it is also very possible that the extracted specimen was void of Si contamination.

Finally, sulfur was observed in the LSC layer with which it reacted, but lay below the detection limit for SEM-EDX in the LSM-YSZ layer. In this case, the larger amount found in LSC can probably be explained by the intrinsic instability and reactivity of this material, and in particular by the activity of SrO [117][73].

As shown in the previous paragraphs, the detection and quantification of pollutants in the cathode layer is not straightforward when using EDX as detection method. Therefore, the use of other techniques such as SIMS has to be considered for future more precise and complete analyses. This technique, widely used by the group of Yokokawa et al., has shown its ability to detect and quantify pollutants at very low concentrations [123].

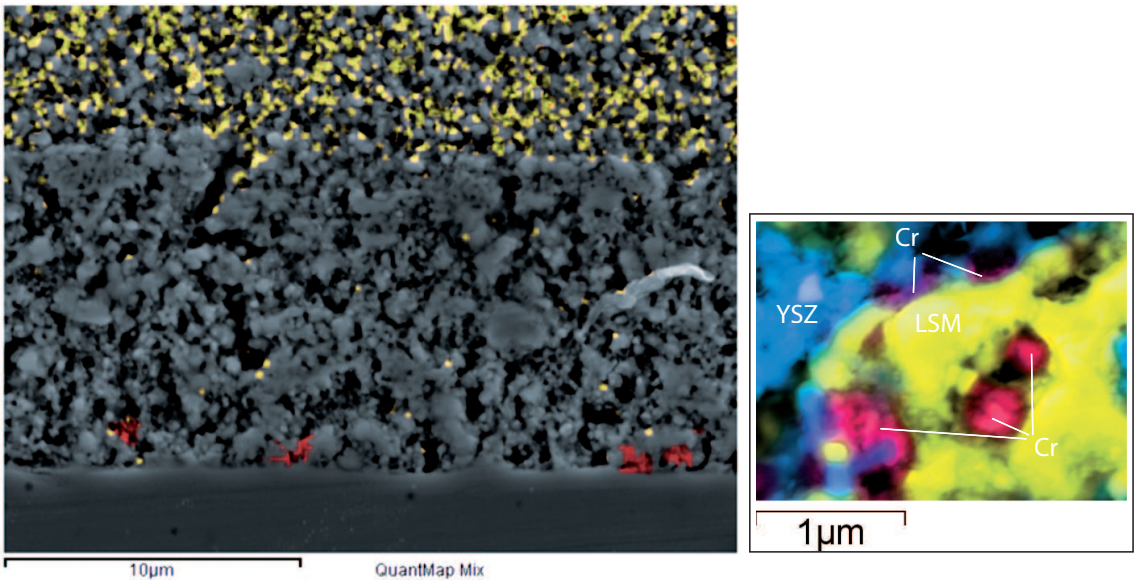

Figure 11.6: Detail of the mappings of pollutants on segment 1 (inlet). Chromium (red) and silicon (yellow). Inset: detail of a chromium-containing particle in the vicinity of the electrolyte. Top layer: LSC. Active layer: LSM-YSZ

11.4 Spatial distribution of pollutants and corresponding electrochemical performance

The electrochemical reaction is expected to take place principally in the LSM-YSZ layer, even if the distributed reaction [1] could reach the polluted LSC layer. Therefore, chromium and silicon, which were found in the LSM-YSZ and are known pollutants, most probably affected the electrochemical reaction. Recent results of Xiong and co-authors showed that a LSM/LSGMC composite cathode polluted by SOx during a short period showed a slight increase in ASR [75], but didn't presented a visibly modified microstructure or important additional phases. In addition, the effect on the performance of the electrode appears to have been partly reversible. Therefore, a limited effect of sulfur on the ASR is expected.

In fact, the comparison of the mappings of silicon and chromium poisoning in LSC (Fig. 11.1) and the level of degradation for the oxygen dissociation step on cathode side (Fig. 10.25) shows a very good match between the affected areas (segment 16 is disregarded due to artifacts in EIS). In addition, the effect of sulfur on degradation is visibly less pronounced, as the amounts found on some segments are not correlated with important local ASRs.

Therefore, it is estimated that the pollution of the cathode by Cr and Si is the probable major cause of its degradation. This conclusion is consistent with the fact that the low-frequency cathode process is mostly affected by degradation in this case, and that this process is reported to be affected by electrode pollution, shown for instance by Bentzen et al. in [126].

Nevertheless, as illustrated in the present case, a quantification of the present pollutant on the full electrode thickness and on all segments would be necessary to completely confirm this conclusion, hence requiring the use of additional analysis tools such as SIMS or GDOES.

11.5 Polarization, activation effects and microstructure

To conclude this post-experiment analysis, a final result, that further illustrates the interest of locally-resolved measurements, is presented.
As shown in the previous chapter, the segments located along the inlet of the active area presented different electrochemical responses, depending on the polarization applied during the 1900 hours of operation. To analyze this situation in more detail, the difference among the recorded impedance spectra was analyzed by differentiation, between the non-polarized segments (11 to 14) and the polarized one (1). The result is shown in Fig. 11.7.
First, it is found that the four non-polarized segments present a very similar difference with

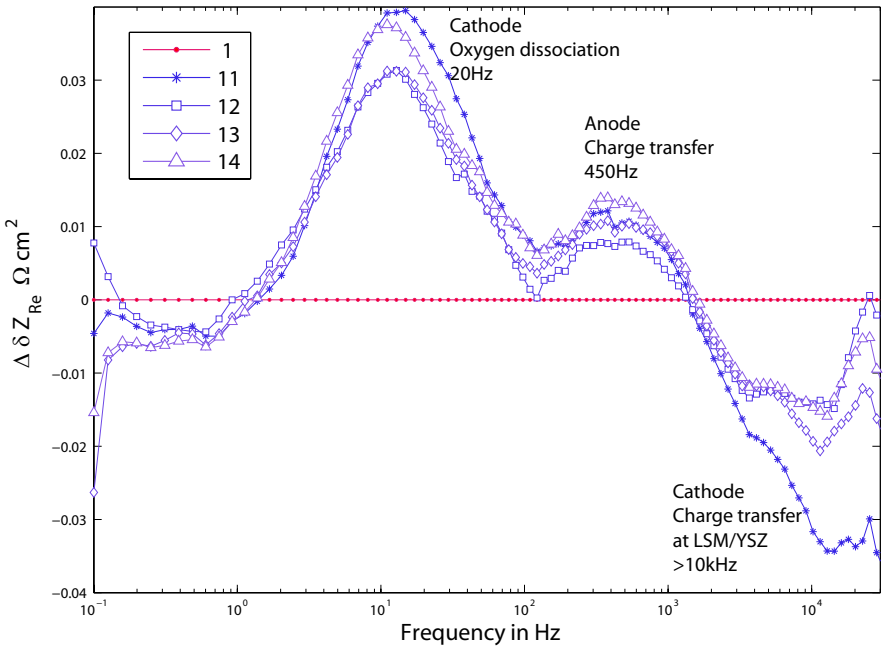

Figure 11.7: Difference in the impedance spectra between the non-polarized inlet segments 11,12,13,14 and the polarized one n°1.

respect to the only polarized segment, and this over the complete frequency domain. This attests of the consistency of the observation. In addition, no difference among the segments is observed on the low frequency process (2Hz), attributed to the gas conversion impedance. This can be expected due to the nature of this contribution.
Further, a current-induced activation is visible for the charge-transfer reaction on the anode side and for the oxygen dissociation step on the cathode side, attested by the higher impedance on the non-polarized segments. By opposition, the high-frequency contribution corresponding to the transfer of charge between LSM and YSZ presents a higher value for the only polarized segment, hence indicating a current-induced degradation.

In a review published in 2008 [66], Jiang describes different processes observed during the activation of LSM-YSZ cathodes. Besides morphological changes in the porous LSM, modifications of the interface between LSM and YSZ, which could impact on the high-frequency term, are reported. In addition, an effect of polarization is observed on SrO segregated at the surface of the LSM, whose polarization-induced removal is assumed to promote the electrochemical reaction. Finally, the formation of oxygen vacancies in LSM is reported to accompany current-induced activation.

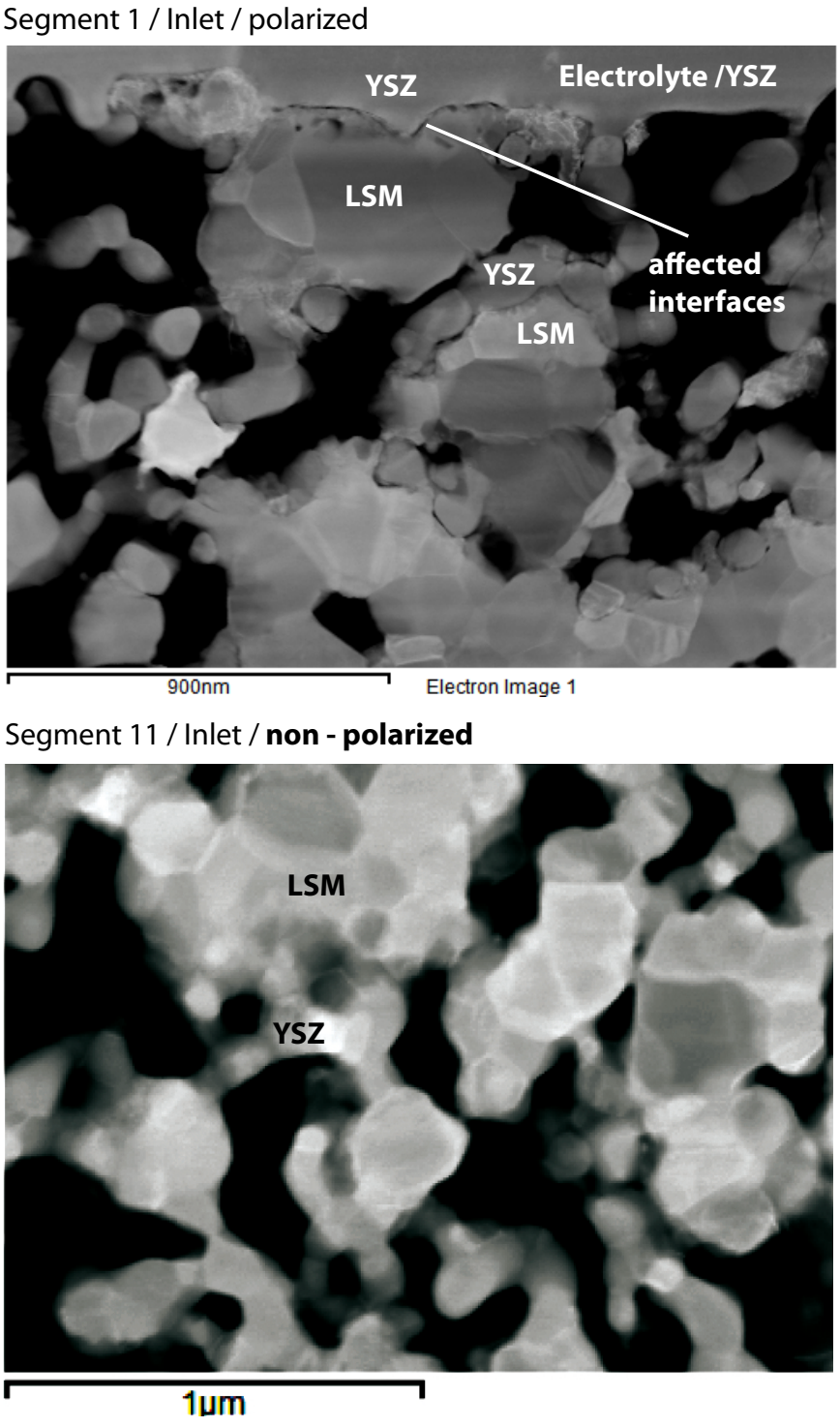

Figure 11.8: Comparison by TEM of the microstructure of segments 1 (polarized) and 11 (non-polarized) after 1600 hours of operation.

Based on the observed current-induced differences in the recorded impedance spectra, it was considered of interest to investigate whether such features could be observed on the concerned segments. This was done by observations with a transmission electron microscope. Two lamellae were extracted by focused ion beam (FIB) from the cathode of segments 1 and 11.

The resulting microstructures are shown in Fig. 11.8. The scale of the images is adapted to represent the microstructure at the same scale.

For the polarized segment (1), the interfaces between LSM and YSZ grains are clearly visible, presenting at several places an apparent detachment or partial gap between the particles. Moreover, these interfaces present 'rough' surfaces, with different topologies from the ones observed on the non-polarized segment. Whether this roughness could have contributed to an activation of the electrode by increasing the TPBS length remains unknown. Unfortunately, no additional information could be obtained about the phases found at these interfaces, where formation of $La_2Zr_2O_7$ could have been expected [68].
By opposition, on the non-polarized segment 11, the interfaces between particles of different nature are not clearly identifiable, presenting well-sintered interfaces. In addition, no additional 'roughness' of the interfaces is visible.

This result seems therefore to be in agreement with part of the phenomena associated with a current-induced degradation (process at 10 KHz). It could explain the higher impedance for the high-frequency process, attributed to the transfer of charge at the LSM-YSZ interface. In addition, this observation could also explain the differences in the ohmic resistances observed between the polarized and non-polarized segments, where the polarized ones presented higher ohmic resistances at the end of the test (see paragraph 10.6.2). However, more work is required to perform a complete analysis of the samples, in order to extract additional information.

Nevertheless, this result shows that the local EIS measurements associated with differential techniques enable to address such features, so as to identify areas of interest for the post-experiment analysis. Finally, this result shows that the presence of non-polarized segments in the fuel cell can add to the comprehension of the observed phenomena.

11.6 Conclusion

The results presented in this chapter illustrate the gain in understanding of degradation by coupling locally-resolved measurements to locally-resolved post-experiment analyses. Frequently, post-experiment analyses allow to identify, in observed samples, specific features that could have an impact on degradation, but without possessing the information whether a real impact on performance has occurred. The coupling of local measurements and observations establishes here this missing link.

The presence of at least three major pollutant species was identified on the cathode side of the tested repeat-element, i.e. on the electrode that was identified as principal source of degradation during the test.
By analyzing the spatial distribution of the pollutants over the active area, a non-homogeneous pollution of the electrodes was revealed, which, furthermore, coincides with the zones affected by degradation in the fuel cell.
Therefore, it was concluded that pollutants on the cathode side are most probably the principal source of degradation.

From a stack-developers point of view, this experiment brings a large amount of valuable information. The presence of chromium uniquely at the cathode inlet testifies for the proper protection of the interconnects against chromium evaporation. Consequently, priorities have to be set on the reduction of chromium sources in the upstream BOP components.
Silicon poisoning is estimated to be generated internally from seal materials as well as externally, requiring more investigations for dedicated adaptations of the design or of the testing conditions.
Finally, the sulfur poisoning identified in this particular test can be avoided by replacing the ceramic paste used for segmentation as well as the sulfur-containing air-supply tubes.

To conclude, the low degradation experienced by the second, less polluted half of the repeat-element, gives a perspective for possible gains in lifetime that could be achieved by a reduction of this principal source of degradation.

Chapter 12

Modeling of pollutant generation, transport and deposition

12.1 Introduction

In this last chapter, a prospective work is presented on the simulation of pollutant generation, transport and deposition in SOFC repeat-elements. Pollutants have been identified as major degradation sources by several authors, both on air and fuel side of the fuel cell.
As shown by the local measurements and local post-experiment analyses presented in the previous chapters, pollutants seem to have played a major role in the degradation of the tested prototype. Moreover, it was found that their distribution on the active area followed a consistent trend, with decreasing amounts along the flow, in addition to more polluted zones in the vicinity of the seal materials. This indicates the presence of trapping materials, such as the LSC used in the contact layer, as well as possible pollutant sources in the seal materials (silicon) or at the surface of the interconnects (chromium). Therefore, the pollution of the active area results not only from external sources, but also from stack-internal sources whose identification would help to improve the lifetime of the fuel cell. In addition, one underlying idea of this prospective work is to assess whether design options or different operating conditions could limit the emission and deposition of pollutants.
To address this question, CFD models are of particular interest, as they allow to simulate transport mechanisms in the gas phase, which is one of the principal vectors of pollutants in fuel cells. Consequently, the CFD model developed in this thesis was complemented by a pollutant emission, transport and trapping simulation module, which is presented hereafter. Using this model, it is shown that specific design options, but also testing conditions play a major role not only in the trapped amounts, but also in the location of the pollution.

12.2 Approach

The pollution by different volatile species of usual materials used in fuel cells is most often investigated in a thermodynamic approach, where equilibrium compositions are established as a function of operating conditions, gas compositions or pollutant concentrations. These thermodynamic considerations allow to identify the numerous reaction products resulting from a pollution, as for instance described by Yokokawa et al. for the case of chromium poisoning [124], or by Xiong [75] for sulfur poisoning.
Other authors focus on the pollutant release mechanisms, as well as on the quantification of the released amounts. For instance, Stanislowski et al. [127][128][5] describe an experimental method used to quantify the release of chromium from different alloys under different conditions. Besides the different rates of chromium released from different alloys, their work shows that the released amounts depend not only on the kinetics of formation of the pollutant species, but much more on the mass transport phenomena which represent a limiting factor [5], as shown in Fig. 12.1.

The same conclusion is made by Opila et al. from NASA Glenn Research Center, who

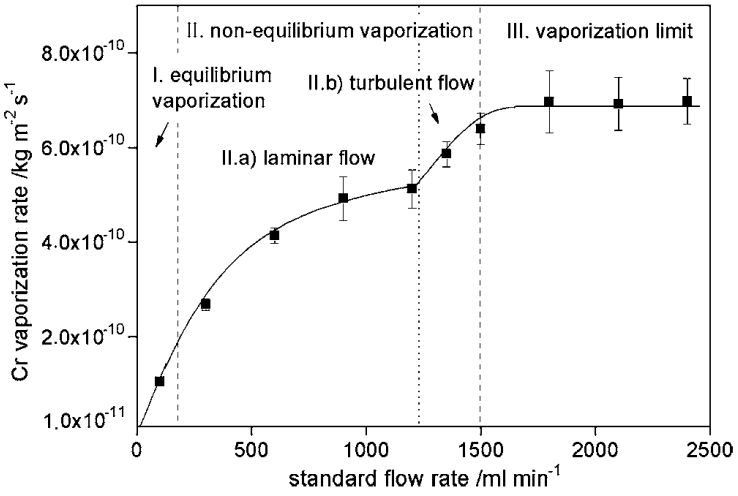

Figure 12.1: Chromium vaporization rates as a function of the flow rate for the chromia-forming alloy Ducrolloy at 800°C in air with a humidity of 1.88%. *Reproduced from Stanislowski et al. [5].*

describes the mass transport phenomena in the gas boundary layers as frequent principal rate limiting step [129]: *"In many combustion environments, volatility is limited by transport of the volatile species away from the oxide surface through a gas boundary layer. To calculate the volatility for the boundary layer limited process, the equilibrium partial pressure of the volatile species must be known, or thermodynamic data must be available to calculate this pressure."*
This property was in particular used in her group in reverse manner to estimate equilibrium partial pressures of gases on the surface of studied samples. By measuring the resulting par-

tial pressure in the gas streams and knowing the mass transfer properties in the boundary layer, the equilibrium partial pressures on the surface can be estimated [130].

As thermodynamic data about pollutant species of interest is found in literature, this approach is applied in our CFD model. The key parameters determining the evaporation rate in a boundary layer are recalled in Fig. 12.2. At the surface of the considered sample, the partial pressure of the considered pollutant specie $p_{eq,s}$ is assumed to be at equilibrium. This partial pressure depends on the local gas composition and temperature, with for instance, a strong dependance on the steam partial pressure for the evaporation of chromium. This partial pressure is estimated on thermodynamic equilibrium relations.

Away from the boundary layer, a pollutant concentration p_∞ is found in the gas stream.

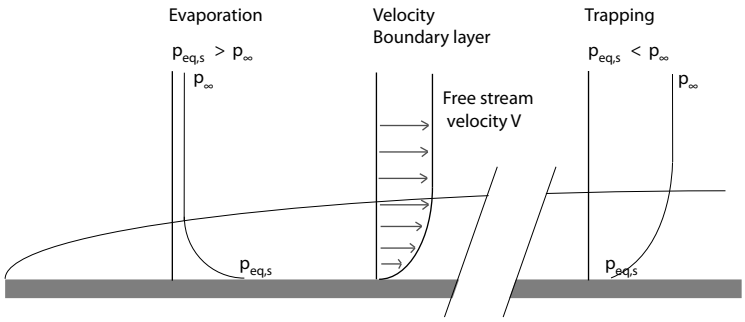

Figure 12.2: Principle of mass transfer in the boundary layer.

The difference between these two partial pressures determines the vaporization from the surface, which also depends on a mass transfer factor h_m determined by the nature of the flow.

In usual textbooks [97], mass transport is expressed in terms of difference of concentrations:

$$N''_{poll} = h_m(C_{poll,s} - C_{poll,\infty}) \tag{12.1}$$

where $C_{poll,s}$ and $C_{poll,\infty}$ are respectively the concentrations at the surface and out of the boundary layer. This relation is transformed for partial pressures as:

$$N''_{poll} = h_m(Re, Sc)\,\frac{P_{atm}}{p_0 \mathcal{R} T}\,[p_{eq,s}(T, p_j) - p_\infty] \tag{12.2}$$

with $p_0 = 1\ atm$. The mass transfer factor h_m depends on the adimensional Sherwood number Sh and on the diffusion coefficient D_{AB} for the considered specie in the present gas mixture:

$$Sh(Re, Sc) = \frac{h_m}{D_{AB}} \tag{12.3}$$

The Sherwood number depends on the local Reynolds number Re_L and Schmidt number Sc, through a relation which depends on the geometry of the flow.

$$Re_L = \frac{\rho U L}{\mu} \tag{12.4}$$

$$Sc = \frac{\nu}{D_{AB}} \tag{12.5}$$

where L is a characteristic length of the flow. In literature, relations for heat transfer are more frequently found. However, due to the analogy between mass and heat transfer, a transformation can be obtained for mass transfer. The heat transfer coefficient h_t is defined by the Nusselt number Nu, which depends on the Reynolds and Prandtl (Pr) numbers:

$$Nu(Re_L, Pr) = a \cdot Re_L^m Pr^n \tag{12.6}$$

$$= \frac{h_t\, L}{k_f} \tag{12.7}$$

with:

$$Pr = \frac{\nu}{\alpha} \tag{12.8}$$

$$\alpha = \frac{k}{\rho c_p} \tag{12.9}$$

$$\nu = \frac{\mu}{\rho} \tag{12.10}$$

The transformation from heat to mass transfer is finally given by:

$$\frac{Nu}{Pr^n} = \frac{Sh}{Sc^n} \tag{12.11}$$

where n is the exponent found in Eqn. (12.6).

Two implementation methods These standard relations are of particular interest to model the vaporization of pollutants from surfaces of known geometries, that is, for instance in tubes or heat exchangers. This type of relations can therefore be implemented in system modeling tools to simulate generation and transport of pollutants at the system level.
For internal flow in a repeat-element, this approach can be used, provided that the mass transfer coefficients can be estimated. In the computation, the equilibrium partial pressure on the surface is computed from thermodynamic data, while the partial pressure outside of the boundary layer is defined as the average partial pressure over the surface. The vaporization fluxes can then be computed from the mass transfer coefficients.
However, if a sufficient discretization of the boundary layers is possible, mass transfer can be modeled by simply imposing the equilibrium pressure on the concerned surface, while the convective and diffusive mass transfers are computed numerically. The released flux can then be computed as:

$$N''_{poll} = -D_{AB} \frac{\partial C_{poll}}{\partial z} \tag{12.12}$$

where z represents the normal direction to the surface.
To model the mass transport in the gas phase, the *User-Defined Scalar* functionalities of

FLUENT are used. The following generic equation is solved for any scalar variable ϕ_k of interest, which here represents the concentration of any pollutant :

$$\frac{\partial \rho \phi_k}{\partial t} + \frac{\partial}{\partial x_i}\left(\rho v_i \phi_k - \Gamma_k \frac{\partial \phi_k}{\partial x_i}\right) = S_{\phi_k} \tag{12.13}$$

where Γ_k and S_{ϕ_k} are respectively a diffusion coefficient and additional source term. In this case, the source term is canceled, while the diffusion coefficient of the pollutant specie is used for Γ_k.

Deposition The relations presented above are also applicable for the deposition of pollutant species on specific surfaces. In this case, the equilibrium partial pressure over the trapping surface has to be known in order to compute the resulting deposition flux.
It has to be noted that this formulation is applicable both for chemical or physical deposition processes.

12.3 Thermodynamic properties of pollutants

In the following paragraphs, the case of chromium- and silica-poisoning are investigated, as they correspond to the principal pollutants found in the segmented experiment.

12.3.1 Chromium poisoning

Vaporization As reported in literature [71][131][132], chromium poisoning occurs in SOFC atmospheres and at usual temperatures principally by the release of CrO_3 or $CrO_2(OH)_2$ from the surface of chromia-forming alloys. The second pollutant specie is found to be largely predominant even at low steam partial pressures [132].
The required thermodynamic data for both pollutant species was extracted by compiling data from Hilpert [71], Ebbinghaus [131], Gindorf [132], Stanislowski [5] and Opila [130]. As shown by Stanislowski in reference [5], considerable disagreement is found among the estimated equilibrium constants for $CrO_2(OH)_2$, as shown in Fig. 12.3.
For the evaporation of CrO_3 , the data of Ebbinghaus is used [131], as it is also close to data from Gindorf et al. [132]. The vaporization reaction is written as:

$$1/2\, Cr_2O_3(s) + \frac{3}{4} O_2(g) \leftrightarrow CrO_3(g) \tag{12.14}$$

The equilibrium partial pressure is fitted on the data extracted from the graphs of Ebbinghaus, with:

$$logK_{CrO_3} = -12235.38\, T^{-1} + 3.01 \tag{12.15}$$

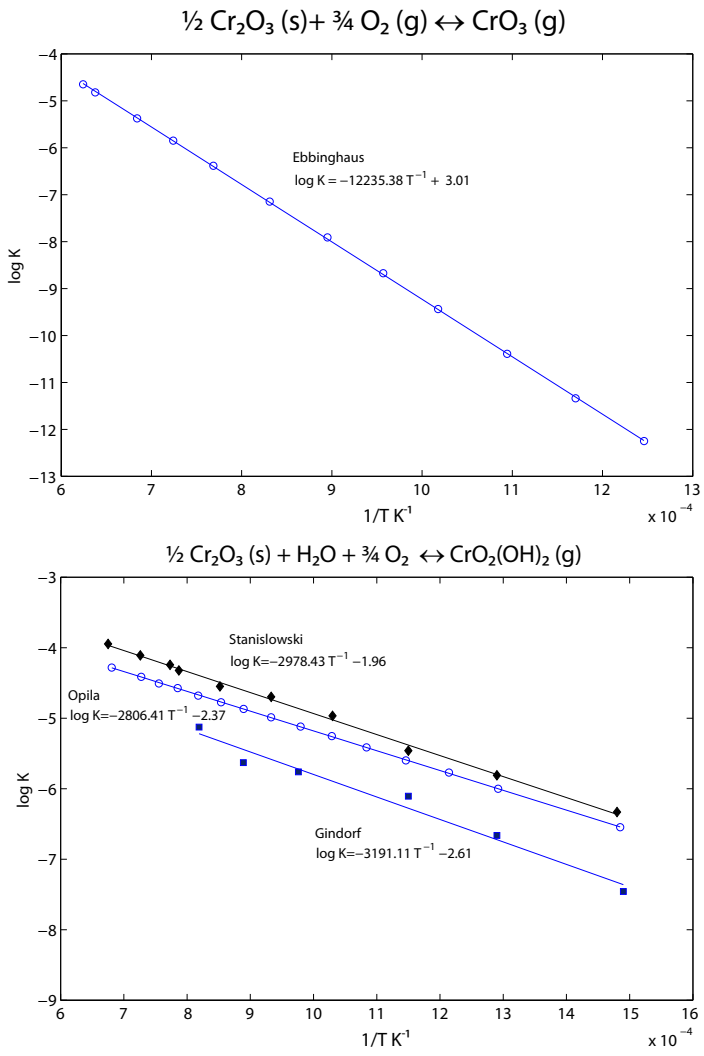

Figure 12.3: Equilibrium constants for volatile chromium species. Data by Stanislowsky, Oplia and Gindorf, extracted from Stanislowski et al. [5].

The equilibrium partial pressure on any chromia-forming surface is consequently computed as:

$$p_{CrO_3} = K_{CrO_3} \cdot p_{O_2}^{3/4} \tag{12.16}$$

For this specie, no sufficient data was found to estimate the diffusion coefficient, which was set to the same value as for $CrO_2(OH)_2$, as the molecule presents a similar radius [133].

For $CrO_2(OH)_2$, data from Stanislowski [5]is chosen arbitrarily. His data is in relative good agreement with the one presented by Opila et al [130].
The vaporization reaction involves both oxygen and steam :

$$1/2\, Cr_2O_3(s) + H_2O(g) + \frac{3}{4}O_2(g) \leftrightarrow CrO_2(OH)_2(g) \tag{12.17}$$

The equilibrium constant, fitted on the data of Stanislowski, is given by:

$$logK_{CrO_2(OH)_2} = -2978.43\ T^{-1} - 1.96 \tag{12.18}$$

And the resulting equilibrium partial pressure is estimated by:

$$p_{CrO_2(OH)_2} = K_{CrO_2(OH)_2} \cdot p_{H_2O} \cdot p_{O_2}^{3/4} \tag{12.19}$$

To compute the evaporation rates and the mass transport, the diffusion coefficient for $CrO_2(OH)_2$ in air is set to $D_{CrO_2(OH)_2} = 2.25 \cdot 10^{-5}\ m^2 s^{-1}$, taken from Nabielek et al. [134].

Known limitations In this exploratory work, several simplifications are made. For instance, only the case of a pure chromia surface is modeled. As shown by Stanislowski however, the released rates depend on the composition of the oxide scale of considered alloy. Therefore, it is a worst-case situation which is considered in the studied cases.

Deposition To model the rates at which chromium is deposited on the LSC layer, the equilibrium partial pressure of CrO_3 or $CrO_2(OH)_2$ in contact with LSC has to be known. Unfortunately, in these preliminary developments, we do not dispose of a sufficiently complete thermodynamic database to compute it reliably. In the segmented experiment however, the important presence of $SrCrO_4$ on the LSC surface at the air inlet indicates a strong reactivity with strontium. As the amounts of $SrCrO_4$ decrease rapidly along the flow and finally reach non-detectable amounts after a dozen of millimeters from the air inlet, it can be assumed that this equilibrium partial pressure is orders of magnitude lower than the partial pressure of pollutants in the gas streams. Based on this assumption, the deposition flux given by equation 12.2 is simplified to:

$$N''_{poll} = h_m(Re, Sc)\ \frac{P_{atm}}{\mathcal{R}T}\ [p_{eq,s}(T, p_j) - p_\infty] = h_m(Re, Sc)\ \frac{P_{atm}}{\mathcal{R}T}\ [0 - p_\infty] \tag{12.20}$$

In the cases where the simulation of mass transfer in the boundary layer is possible, it is the equilibrium partial pressure which is set to zero.

This formulation neglects the progressive formation of reaction products which will modify the equilibrium partial pressures with time; an unsteady formulation will be implemented in the future. The results presented below are therefore only valid for initial conditions, or for short time scales.

12.3.2 Silicon poisoning

As mentioned by Yokokawa in [73], $Si(OH)_4$ could represent one of the vectors for silica poisoning in fuel cells. As shown by Opila in [130], this specie represents the major cause of

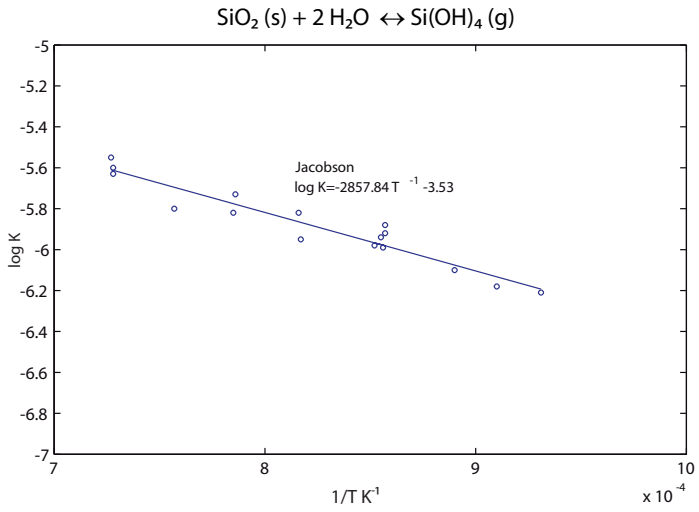

Figure 12.4: Equilibrium constant for volatile $Si(OH)_4$, extracted from data by Jacobson et al. [6].

degradation for silica-forming materials, at high temperatures and in the presence of water vapor. It is generated by the following mechanism:

$$SiO_2(s) + 2H_2O \leftrightarrow Si(OH)_4(g) \tag{12.21}$$

The extraction of data from Jacobson [6]and Opila allows to fit the temperature dependency of the equilibrium constant as (see Fig. 12.4):

$$logK_{Si(OH)_4} = -2857.84\, T^{-1} - 3.53 \tag{12.22}$$

Finally, the equilibrium partial pressure of $Si(OH)_4$ is obtained by:

$$p_{Si(OH)_4} = K_{Si(OH)_4} \cdot p_{H_2O}^2 \tag{12.23}$$

In the considered repeat-elements, the formation of $Si(OH)_4$ is assumed to take place at the surface and inside of the seal materials, where silica is found. To model its formation, a different approach is taken. As the generation occurs in a porous volume, it is the partial pressure of $Si(OH)_4$ which is directly set to its equilibrium value, depending on the steam partial pressure in the seal, which is determined by the steam partial pressures of the gases or by parasitic combustion fronts in the seal gaskets.

Deposition on the LSC surface To model the deposition of silicon on the cathode collection layer, the same assumption is made as for chromium deposition. In fact, Yokokawa et al. mention the possible reaction of $Si(OH)_4$ with SrO [73], whose reactivity with chromium-containing species has been demonstrated.

12.4 Generation of chromium-containing pollutants in a *F-design* prototype

To test the capabilities of the completed CFD model, a simulation of pollutant evaporation, transport and deposition is performed in a *F-design* repeat-element. A view of the cathode-side assembly of the element is shown in Fig. 12.5. The generation of chromium-containing pollutants occurs either on the complete surface of the interconnector, or if specified, only outside of the air channel where the presence of an effective protective coating is assumed. In this case, chromium vaporization takes place only at the interface between the interconnect and the seal materials, which are modeled as porous media. In addition, cases are considered where the incoming air is saturated with chromium, which depends on the relative humidity of the injected air.

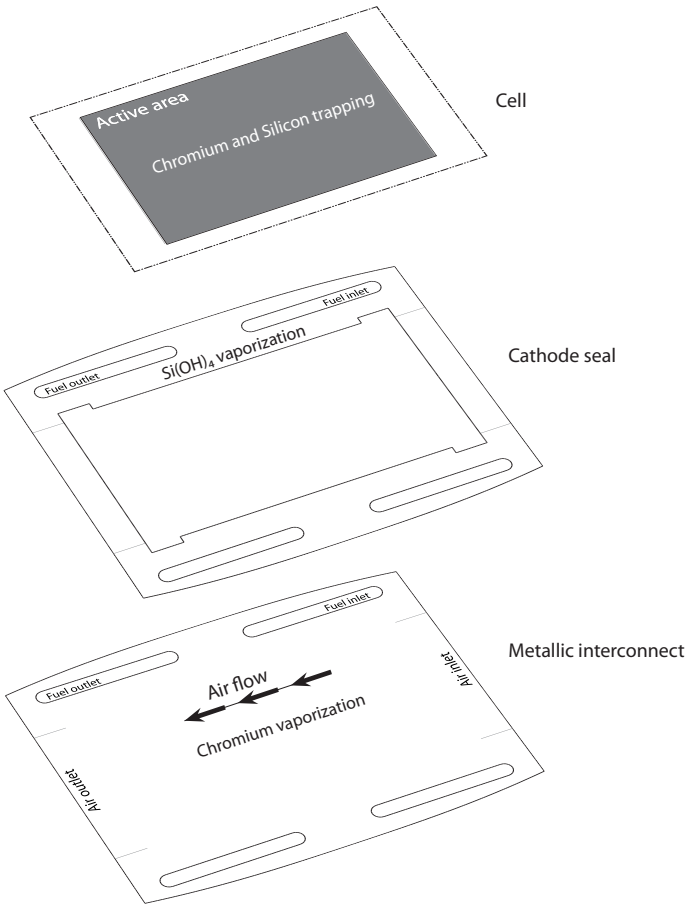

Figure 12.5: Assembly of the *F-design* stack (cathode side) and considered locations of pollutant generation and deposition.

For the generation of $Si(OH)_4$, the internal source is considered in the seal materials, where the equilibrium partial pressure is fixed, as mentioned above. In addition, some cases are considered where an external $Si(OH)_4$ source saturates the air.
For both pollutants, deposition occurs on the cathode's current collection layer. In addition, a physical re-deposition of chromium on the interconnector is possible, as described hereinafter.

12.4.1 Local generation of Cr-containing volatile species

In the following paragraphs, a fixed operating point is considered, with a fuel utilization of 60% obtained under a dilute fuel mixture (50%H_2 -50%N_2) and a lambda of $\lambda = 6$.
Figure 12.6 represents the resulting composition of the gases at the surface of the interconnector, with air and fuel inlets located on the right of the figure. Oxygen is found in the air stream and in part of the areas covered by the seal gaskets. On the sides of the element, where the fuel manifolds are located, it is principally steam and hydrogen which are found in the seals. Similarly to the case of the previous designs, a front of parasitic combustion exists in the seals, exposing the MIC on either part of it to oxidizing, resp. reducing conditions. Steam is thus present to large extents at these locations, which promotes the formation of pollutants, as shown below.

From these partial pressures and from the local temperatures, the equilibrium partial pressures of CrO_3 and $CrO_2(OH)_2$ are computed on the surface. As shown in Fig. 12.7, the places where the highest partial pressures are found differ to a large extent. CrO_3 attains highest equilibrium partial pressures in the second half of the element, where temperatures are higher, and this only in the air compartment due to lower oxygen partial pressures under the seals. The contrary is true for $CrO_2(OH)_2$, which attains maximal partial pressures at the interface between the MIC and the seals, in the vicinity of the parasitic combustion fronts. This indicates that in this case again, parasitic diffusion in seals has a negative impact on durability.

To simulate the released fluxes of chromium, the partial pressure is fixed on the MIC's surface, and the resulting mass transport is modeled numerically. The resulting fluxes are hence computed from equation 12.12. In this first case, no interconnect protection is considered, to show the potential for pollutant release in the repeat-element. Moreover, no external chromium source is considered, to investigate only stack-internal sources.

The result is shown in Fig. 12.8. $CrO_2(OH)_2$ presents by far the highest release flux, with up to $5.6 \cdot 10^{-9}\ \mathrm{kg\,m^{-2}\,s^{-1}}$, while the maximal flux of CrO_3 is limited to $9 \cdot 10^{-11}\ \mathrm{kg\,m^{-2}\,s^{-1}}$. These fluxes are always given as mass of chromium par unit area and time.
The high vaporization rates for $CrO_2(OH)_2$ are linked to the important steam partial pressures found at the surface of the MIC under the seals. Results from Stanislowski show

maximal vaporization rates of $7 \cdot 10^{-10}$ kg m^{-2} s^{-1}for water vapor mole fractions of 1.88% (corresponding to a 66% relative humidity under ambient conditions).
These results show therefore that the presence of steam in the seals results in an important source of volatile chromium in the repeat-element. Moreover, the polarization of the repeat-element, which induces larger steam partial pressure in the outlet fuel manifold, plays indirectly a role in the released amounts.

Another result of interest for the release of $CrO_2(OH)_2$ is the presence of positive *and* negative mass fluxes on its surface, accounting for places where chromium is released, and other where it is deposited. The re-deposition of chromium on the interconnect results locally from a non-equilibrium situation, where the equilibrium partial pressure on the MIC's surface is lower than the partial pressure in the gas phase. This situation occurs for instance where strong gradients of oxygen or steam partial pressure exist.
This situation principally affects $CrO_2(OH)_2$, with maximum deposition rates of $2.5 \cdot 10^{-9}$ kg m^{-2} s^{-1}, while CrO_3 is less affected.

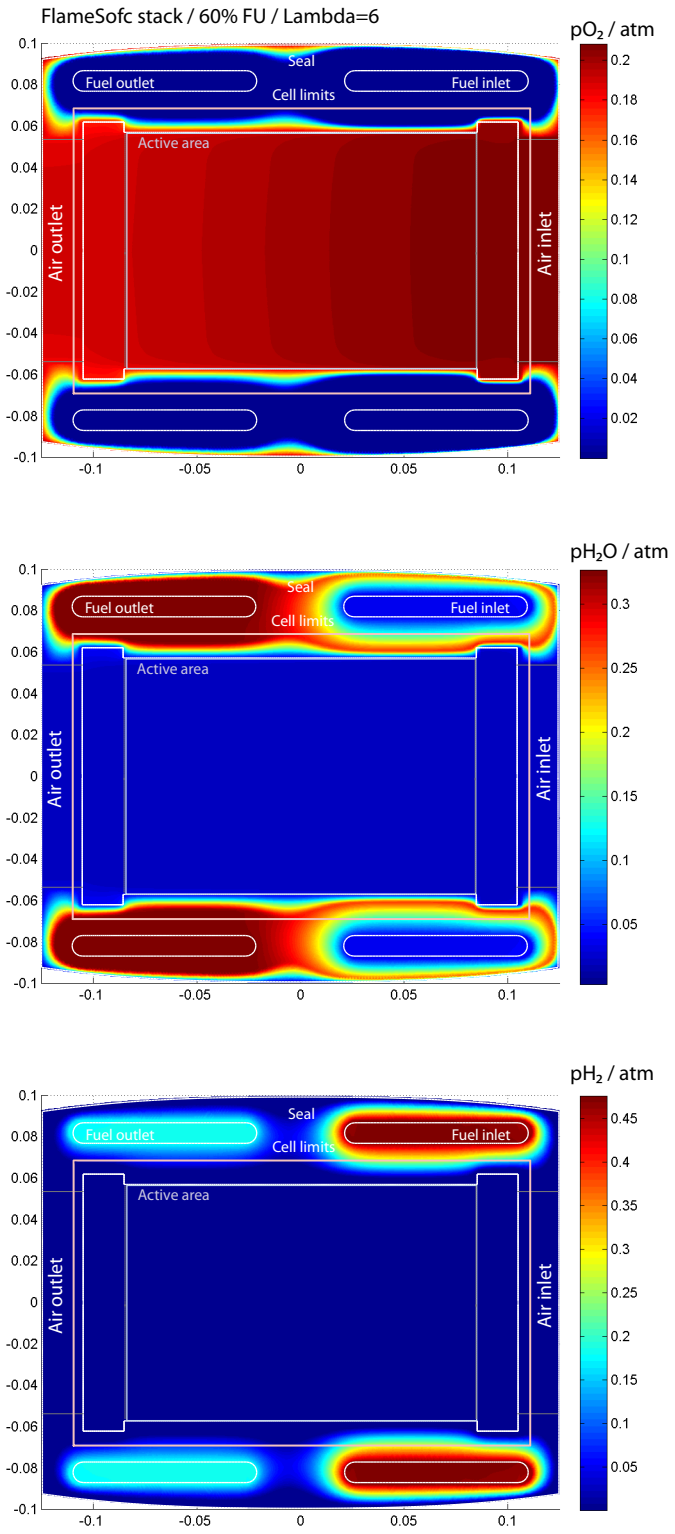

Figure 12.6: Local gas composition at the MIC surface on the cathode side of a *F-design* stack. Gas inlets are on the right. (60%FU, $\lambda = 6$, 50%-50% $H_2 - N_2$ fuel mixture)

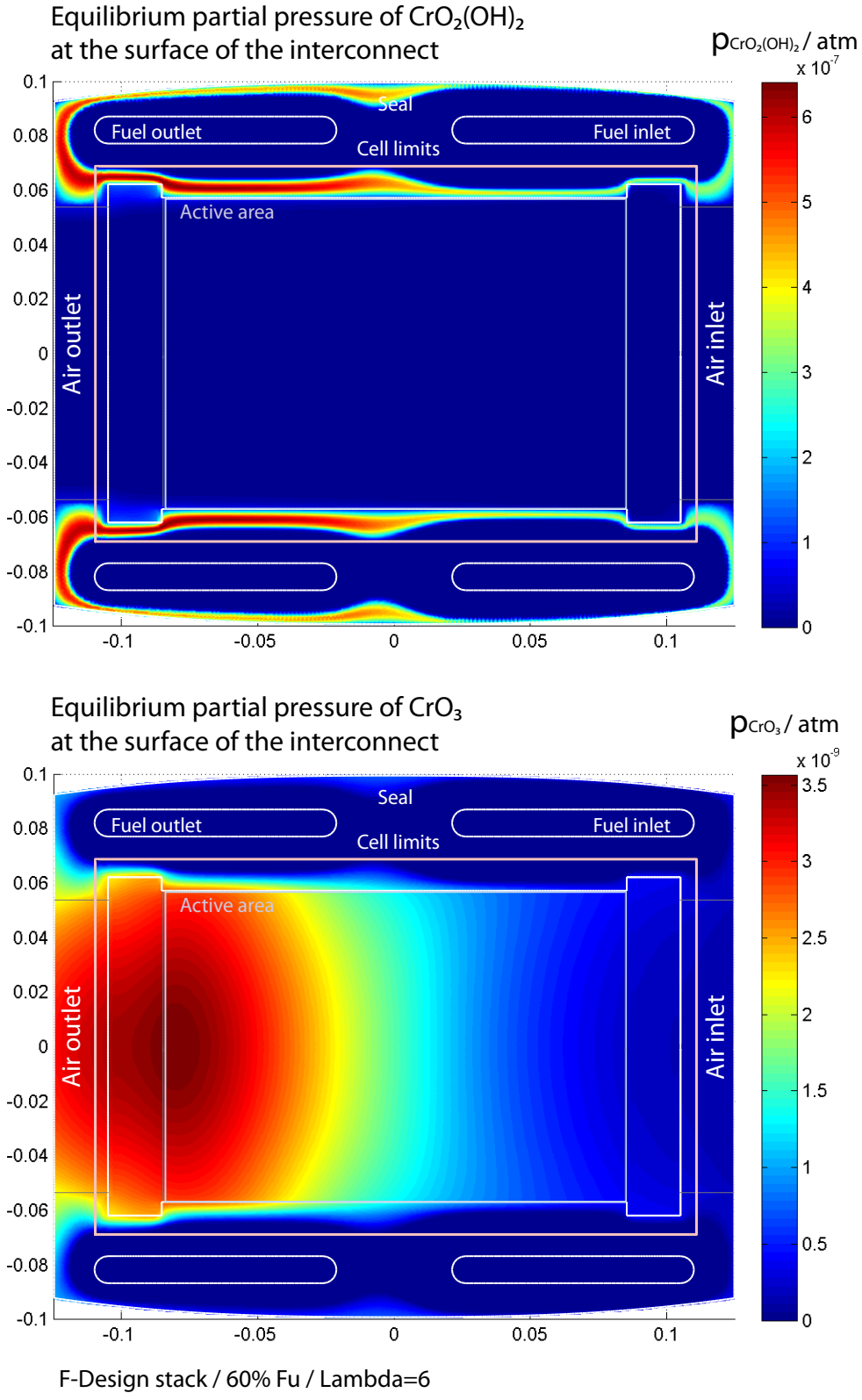

Figure 12.7: Corresponding equilibrium partial pressure of CrO_3 (g) and $CrO_2(OH)_2$ (g) at the surface of the interconnect.

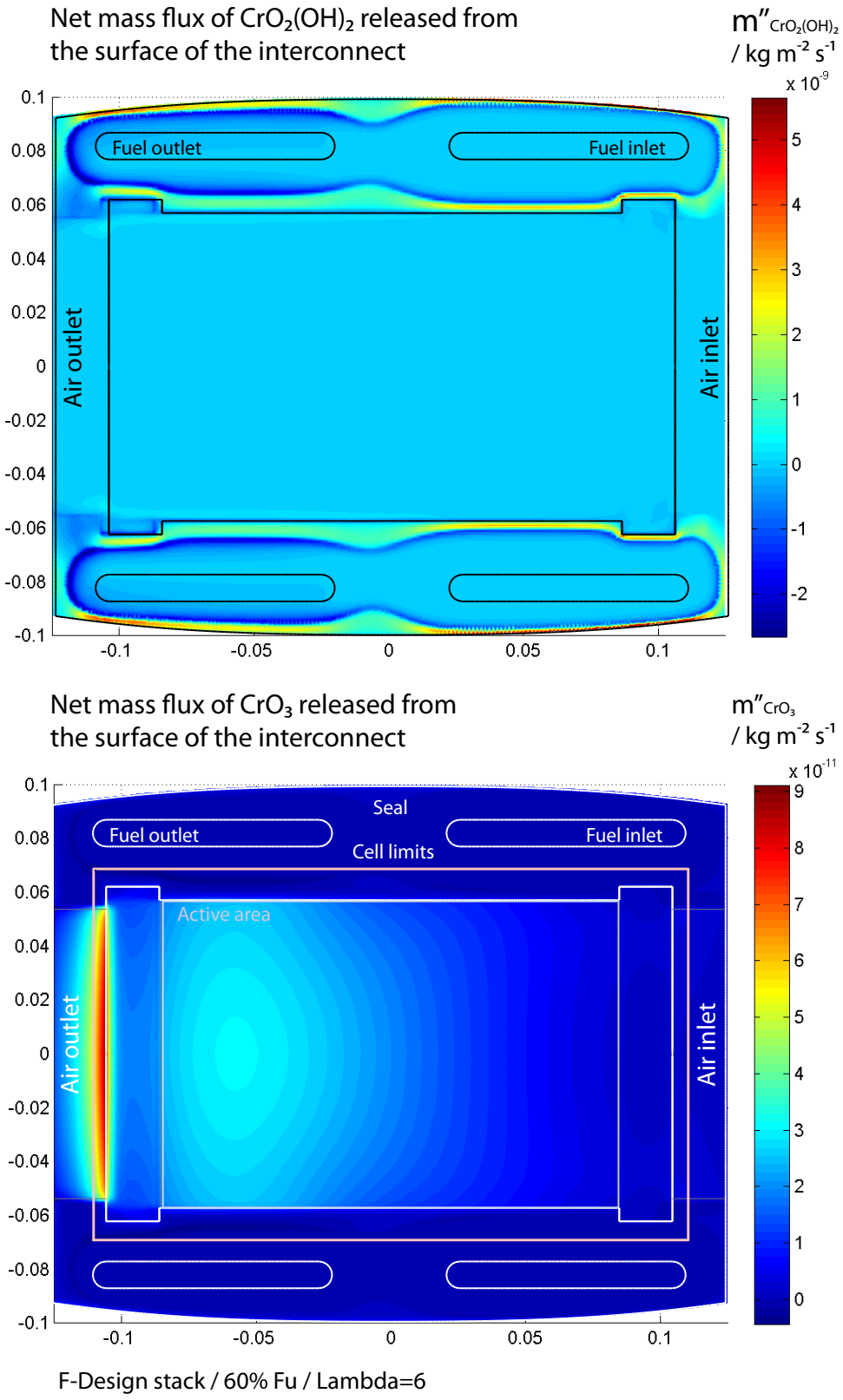

Figure 12.8: Local net mass vaporization rates of chromium from the interconnect, from the different pollutant species(CrO_3 (g) and $CrO_2(OH)_2$ (g)). No protective layer. Unsaturated, dry air (700°C).

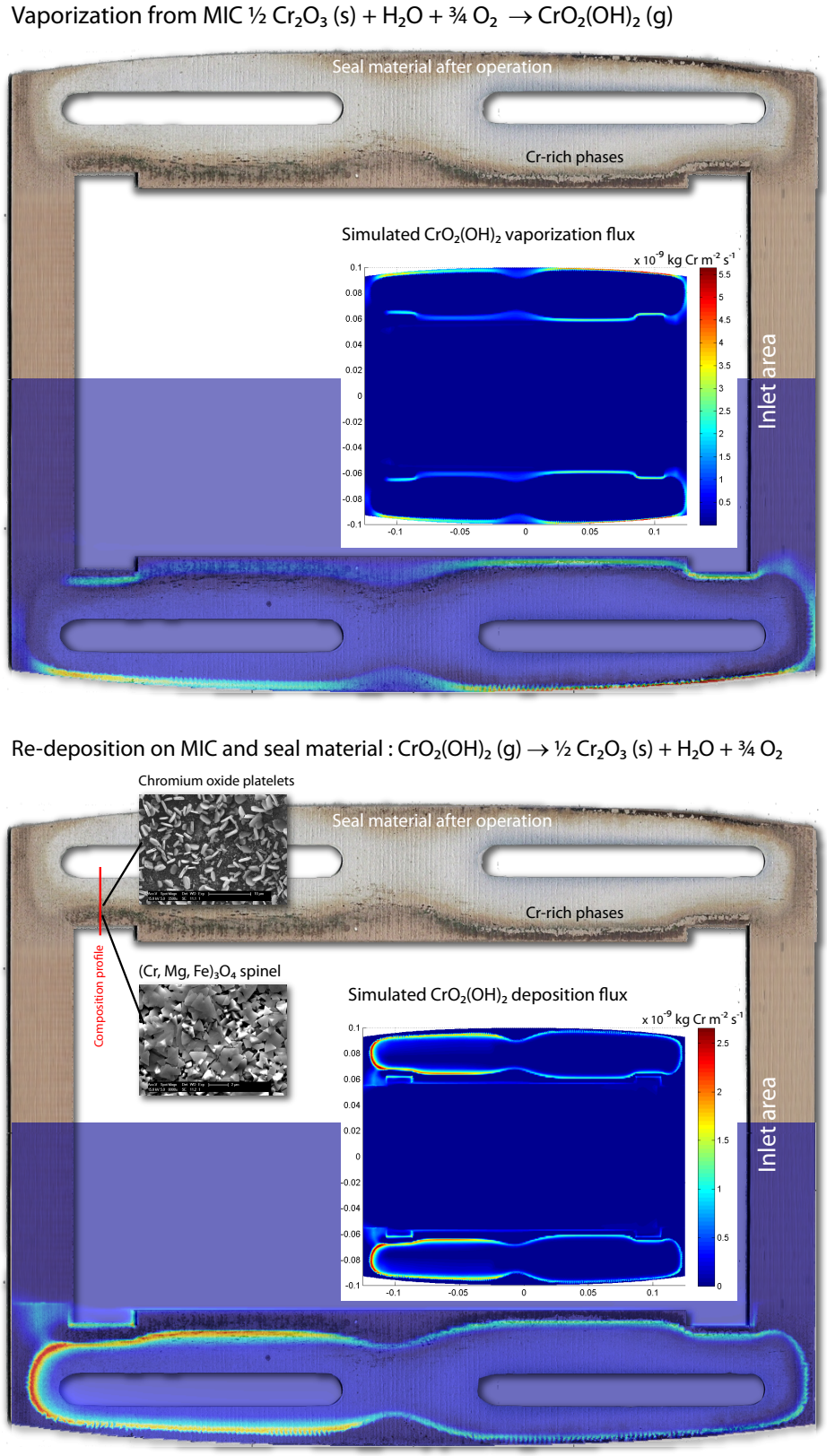

Figure 12.9: Corresponding evaporation and deposition fluxes of $CrO_2(OH)_2$ (g) at the surface of the interconnect. Comparison with profiles of chromium deposited on the surface of a seal in direct contact with the interconnect.

12.4.2 Validation

To validate these predictions, the interface between interconnect and seal was analyzed, using a disassembled seal from an experiment performed under similar operating conditions. In this case, the net mass flux of $CrO_2(OH)_2$ is separated into two distinct contributions: the positive flux corresponding to vaporization, and the negative one corresponding to deposition.
In Fig. 12.9, the simulation results are superimposed on the picture of the disassembled seal. On the seal, dark traces are observed along its internal sides. Observed by SEM-EDX, these traces are found to contain large amounts of chromium (see inset). Additional information is detailed below. Moreover the seal material presents a brownish color in the areas exposed to oxidising conditions, and a light grey coloring in reducing ones.
As shown on this figure, the simulation results are in excellent agreement with the traces of chromium deposition observed on the seal material.
In addition, it is interesting to note that the vaporization takes places on the air-side of these areas, while deposition takes places on the fuel side of it.

To investigate this process in more detail, a profile of the simulated results and of post-experiment observations is given for the red line indicated on this figure.

The result is shown in Fig. 12.10. First, the position of the air GDL and of the seal material (grey) is recalled. The simulated profiles of gas partial pressures are shown. As the profiles are taken in the vicinity of the fuel outlet manifold, high steam partial pressures are attained on the right (x=15mm), where the fuel manifold begins. At this location, a hydrogen partial pressure of 0.17 atm is found, decreasing linearly towards the place where it is burned. On the air side, a non-zero partial pressure of water vapor is found in the gas stream, due to the accumulation along the stream of steam from the parasitic combustion.
The corresponding equilibrium partial pressure of $CrO_2(OH)_2$ is recalled, attaining a maximum of $6 \cdot 10^{-7}$ atm. The corresponding net vaporization flux is shown by the green curve (x), with, as already mentioned, both positive (vaporization) and negative (deposition) fluxes along this profile.

The corresponding surface of the seal material was analyzed by SEM-EDX, which corresponds to the interface between MIC and seal. The seal material contains about 11% of Mg (atomic percent) and 17% of silicon as principal elements (after oxygen). As shown on the obtained profiles, an important amount of chromium is found on the seal, with concentrations above 13% on almost half of the width of the seal. The location of this chromium deposition on the seal matches well with the areas predicted to present high $CrO_2(OH)_2$ partial pressures.
In addition, a significant concentration of iron is also found in this area, with a peak value attained at a distance of 6mm from the air GDL.

As shown on the SEM images, the form of the deposited chromium differs depending on the location where it is observed. On the air-side of this region, a Cr_2MgO_4 spinel was identifed, presenting a characteristic spinel microstructure. This region extends from the air GDL to a distance of 4mm. Further in the direction of the fuel manifold, the form of the deposited chromium is very different. In this region, a microstructure consisting of Cr_2O_3 platelets is found at the surface of the seal material. In this case, no reaction of chromium with other species occurs.

The exact mechanism leading to these different compositions is not fully identified. In the first case, a reaction with Mg from the seal material occurs. In the second case, no chemical reaction occurs with the seal materials, indicating a possible out-of-equilibrium deposition of $CrO_2(OH)_2$ in form of Cr_2O_3 , due to the low oxygen partial pressure in the reducing atmosphere :

$$CrO_2(OH)_2(g) \leftrightarrow 1/2\, Cr_2O_3(s) + H_2O(g) + \frac{3}{4}O_2(g) \tag{12.24}$$

$$0.5O_2(g) + H_2(g) \leftrightarrow H_2O(g) \tag{12.25}$$

Summary As shown in this paragraph, the model is able to predict the location of chromium vaporization with accuracy. In fact, it is more the diffusive properties of gases in the seal materials which determine the position of the chromium vaporization, as it dictates the profiles of steam partial pressures. Nevertheless, the model is able to give an information of interest for post-experiment analyses, which in this case reveal an important release of chromium from the alloy's oxide layer. Moreover, the presence of iron at this place indicates a possible catastrophic oxidation of the interconnect, a fact that has to be further investigated.
These results show therefore the interest of this type of simulations as a support for post-experiment analyses, and possibly later for design purposes.

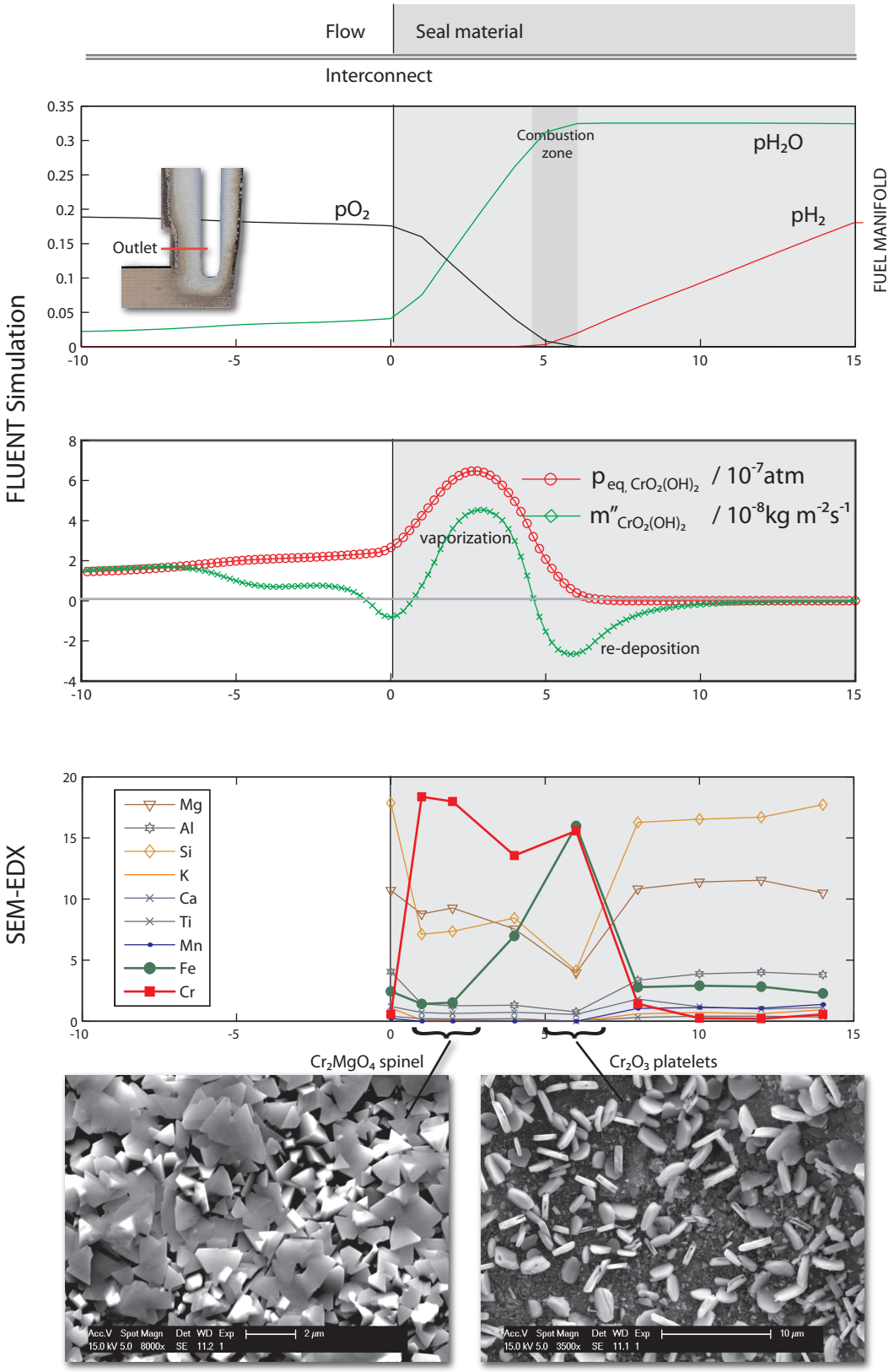

Figure 12.10: Detail of the relase/deposition profile of $CrO_2(OH)_2$ (g) at the interface of a MIC and a seal exposed to a parasitic combustion front. Corresponding SEM-EDX observations with identification of the formed phases.

12.5 Chromium poisoning of a *F-design* prototype

The simulated trapping rates on the LSC cathode layer are presented in Fig. 12.11. A logarithmic scale is used for a better visualization.

First, the situation of an unprotected interconnect is represented, allowing a release of chromium on its whole surface. Ambient air is considered, in which a steam partial pressure of 0.02 atm is imposed (66% relative humidity). Due to the length of piping in usual systems or the presence of heat exchangers, it is considered that the air is saturated with CrO_3 and $CrO_2(OH)_2$ before entering the stack. This situation is the same for all considered cases.
As shown on the first map of chromium deposition, a maximum trapping rate of $10^{-8.11}$ $kg\,m^{-2}\,s^{-1}$ is attained at the entry of the active area. The trapping rate decreases rapidly along the flow, with one order of magnitude lower attained after 35mm. A minimum trapping rate is attained approximately at half of the length of the repeat-element, before the trapping rates start to increase again. This is due to the internal generation of Cr from the MIC. In this case, the lowest trapping rate is $10^{-9.2}$ and the highest $10^{-8.11}$ $kg\,m^{-2}\,s^{-1}$. Along the sides of the active area, larger trapping rates are observed, resulting from $CrO_2(OH)_2$ released in the seals.

In a second case, the same conditions are applied to a repeat-element possessing a protection of the MIC against chromium evaporation, but only towards the air GDL (not under the seals). The same maximum trapping rate of $10^{-8.11}$ $kg\,m^{-2}\,s^{-1}$ is attained at the inlet, presenting similarly a remaining trapping rate of $10^{-9.11}$ $kg\,m^{-2}\,s^{-1}$ at about 30mm from the inlet. Unlike the preceding case, and as expected, the trapping rates continue to decrease along the flow, reaching a minimal trapping rate of $10^{-9.7}$ $kg\,m^{-2}\,s^{-1}$.
Finally, a nearly constant trapping rate of about $10^{-9.11}$ $kg\,m^{-2}\,s^{-1}$ is observed along the sides of the active area.

If the same repeat-element is considered, but using compressed air such as in the case of the segmented experiment, the apparent distribution of pollutants is modified. This results from the lower steam partial pressure, somewhat arbitrarily fixed to a value of 0.002 atm (i.e. 1/10 of the standard air humidity), which induces lower evaporation from the system components. At the inlet, a maximum trapping rate of $10^{-8.66}$ $kg\,m^{-2}\,s^{-1}$ is attained in the corners, while it is $10^{-9.11}$ $kg\,m^{-2}\,s^{-1}$ in the middle of the inlet surface. In this case, a trapping rate of $10^{-9.66}$ $kg\,m^{-2}\,s^{-1}$, that is, one order of magnitude lower than the maximum trapping rate, is attained less than 10mm from the inlet.
In this case, the relative importance of the lateral sides of the active area increases. More interesting, the maximum trapping rate along the lateral sides approaches $10^{-8.66}$ $kg\,m^{-2}\,s^{-1}$, the maximum rate found at the inlet.
In this configuration, the lowest trapping rate on the active area is $10^{-10.6}$ $kg\,m^{-2}\,s^{-1}$, which is one order of magnitude less than in the case of ambient air.

For all cases, the simulated deposition profiles present a decreasing trend from the air inlet, with more or less pronounced effects of the lateral $CrO_2(OH)_2$ generation. As shown on the maps, these lateral contributions are limited to a short distance from the seal. In the segmented repeat-element test, the amounts of chromium were quantified in the center of the segments, therefore neglecting the eventual presence of chromium in close vicinity of the seals. Nevertheless, the simulated profiles corresponding to a protected interconnect, which is the case in the segmented test, present similar profiles to those revealed by quantification in EDX. One difference exists however between the simulation and the experiment. In the simulation, the trapped amounts decrease along the flow but never reach zero values due to the intrinsic nature of the deposition law, while experimentally no chromium is detected a few dozens of millimeters away from the air inlet, which is partly due to the detection limit of the detector.

These results show that the amounts of pollutants convected by the incoming air are determining for the pollution of the repeat-element. The relatively limited difference between the protected and not-protected cases for ambient air illustrate this situation well. In this case, the evaporation of chromium from the system components presents the major source of pollution. More important in terms of testing conditions, this result shows that the effect of any protective coating becomes visible only if the air quality at the stack's inlet can be controlled. For complete systems, where ambient air is used, this result illustrates therefore the need for a development of highly effective coatings for system components.

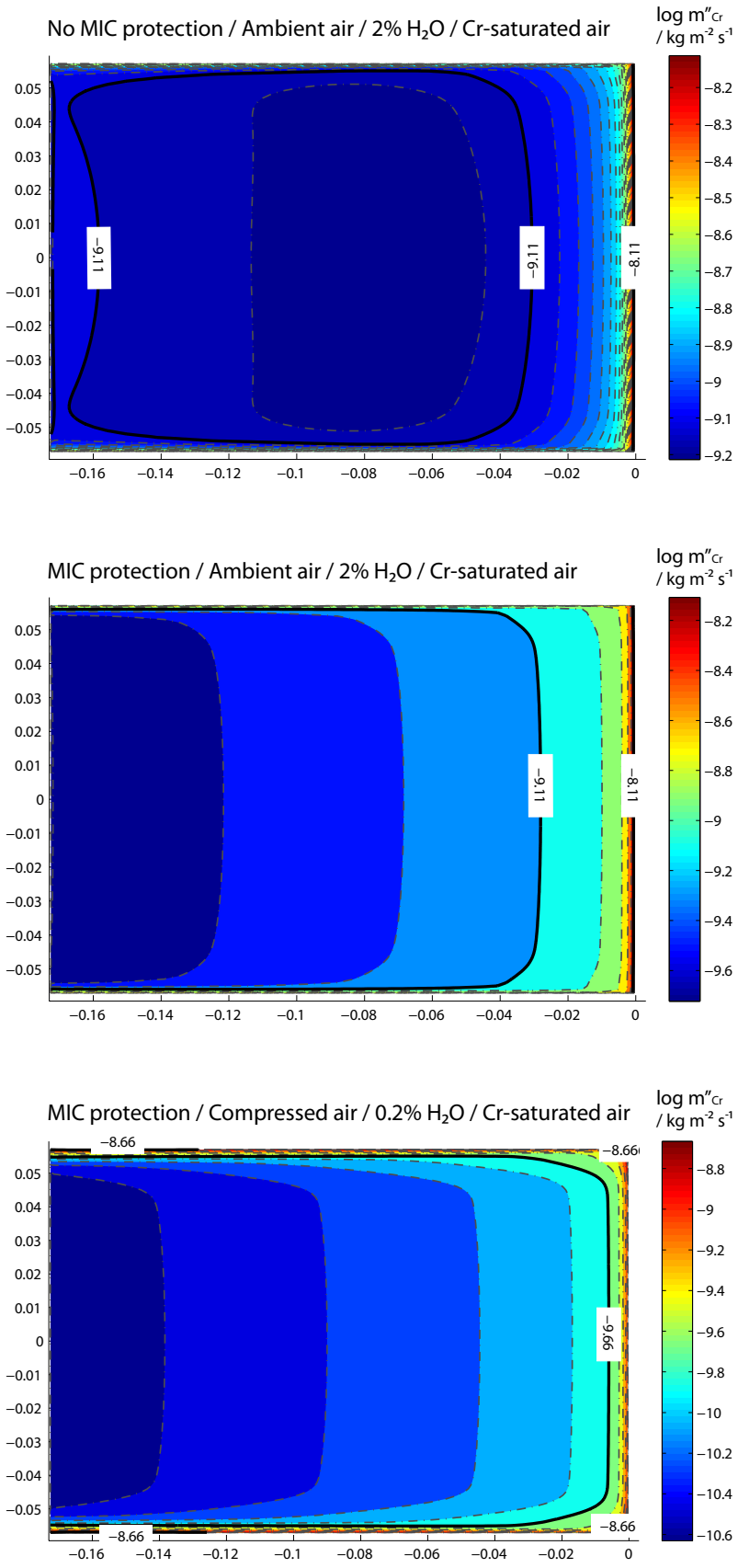

Figure 12.11: Local mass deposition rates of chromium on the cathode, from CrO_3 (g) and $CrO_2(OH)_2$ (g). Air inlet is on the right hand side. Top: no protection against Cr evaporation in the GDL, ambient air. Middle: with protection, ambient air. Bottom: situation of the segmented experiment. Compressed air with residual humidity, MIC protection.

12.6 Silicon poisoning of a *F-design* prototype

As described above, the generation of $Si(OH)_4$ from the seal material is simulated by imposing the equilibrium partial pressure in its volume. As its partial equilibrium partial pressure depends uniquely on the steam partial pressure, it is generated essentially in the vicinity of the fuel manifolds, as shown in Fig. 12.6.
The resulting deposition fluxes are depicted in Fig. 12.12, presented as function of the chosen operating conditions.
First, the case of a system configuration is illustrated, where ambient air is used (Fig. 12.12 A). It is considered that no source of volatile $Si(OH)_4$ is found before the stack. Despite this absence of source before the stack, it is in this configuration that the highest deposition rates are expected, the other cases B and C being investigated for compressed air. One notable exception exists however, with higher deposition rates attained under pure hydrogen and compressed air, as described below. Therefore, air humidity plays a major role in the internal $Si(OH)_4$ generation. This is due to the presence of seal material in contact with the entering air. In this configuration, the highest deposition rates are found along the inlet line, and especially in the corners. This profile is similar to the observations made in the segmented experiment.

When using compressed air, as illustrated in Fig. 12.12 B, C and D, it is along the sides of the element that the highest deposition rates are predicted. This observation is valid with and without $Si(OH)_4$ source before the stack (B,C). As the use of compressed air corresponds to the configuration of the segmented repeat-element, a clear difference exists between the profiles obtained by EDX and the simulated ones. Therefore, the presence of another external source of silicon can be estimated as probable, with volatile species that differ from $Si(OH)_4$.

Finally, an interesting observation is made when changing the fuel composition, from dilute to pure hydrogen (humidified) (D). In this case, the highest deposition rates of all investigated cases are attained along the sides of the active area, in the vicinity of the fuel inlet manifold. This increased trapping of silicon results from the highest steam partial pressures in the seal -resulting from parasitic combustion- due to the absence of dilution by nitrogen. This shows that variations of parameters on the fuel side can have an impact on the pollution on the cathode side.

These results show that, depending on the operating conditions, the spatial distribution of the pollution is modified. Other parameters such as the air flow rate or the temperature are consequently also expected to influence the rates of pollutant deposition, and therefore to impact on the final degradation of the prototypes.
In addition, these preliminary results show that simulation of pollutant generation, transport and deposition could help in the identification of pollutant sources by a study of the spatial distribution of deposition.

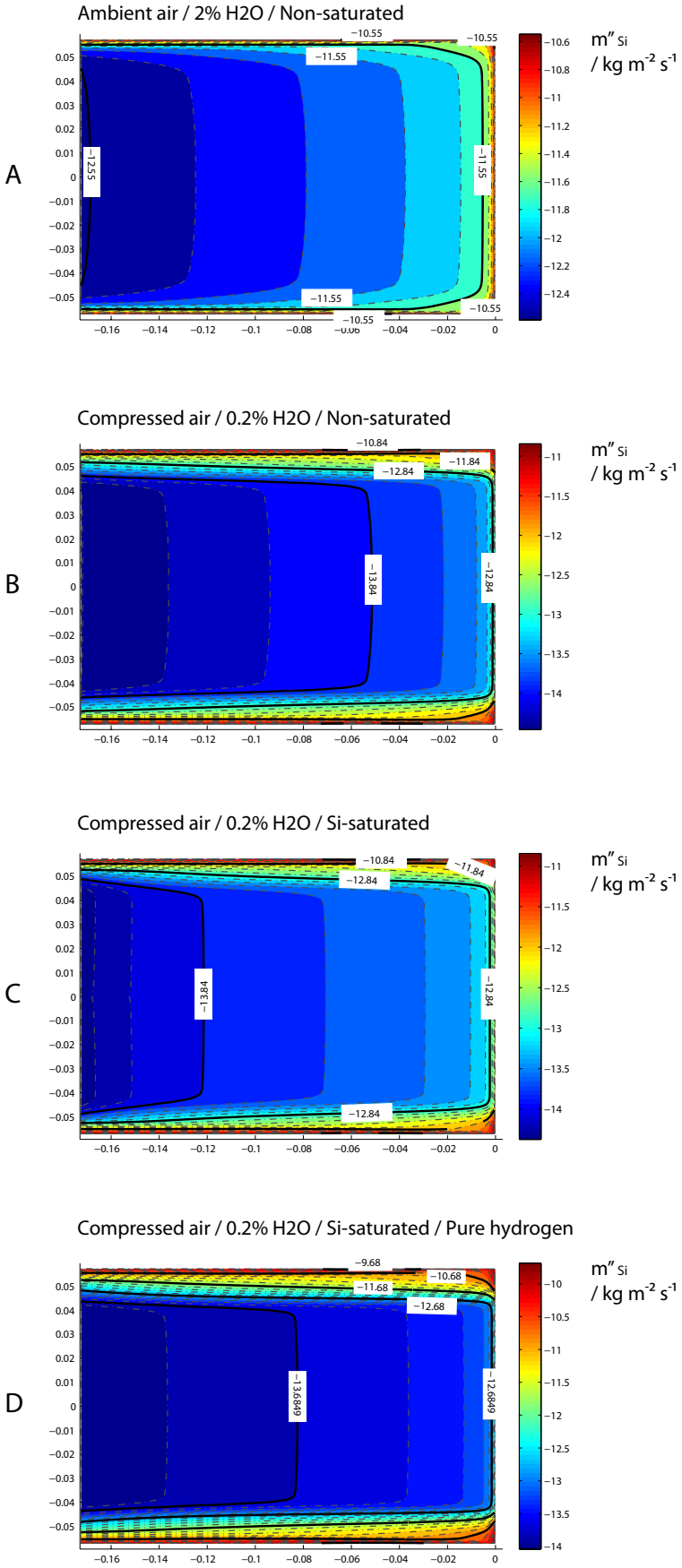

Figure 12.12: Local mass deposition rates of silicon on the cathode, from $Si(OH)_4$ (g) under different operating conditions.

12.7 Spatial distribution of pollutants and stack design

As shown in the examples presented above, the internal generation of pollutants, their transport and deposition is strongly linked to the construction of the element, and in particular to the design of the seals. As shown throughout this thesis, the design of the stack impacts on the final performance and reliability. Due to different internal sources of pollutants among the different stacks, due to their placement in the gas streams, it can therefore be expected that an impact on the degradation by pollution occurs.

In the example shown in Fig. 12.13 for the *S-design* stack, the sum of the partial pressures of CrO_3 and $CrO_2(OH)_2$ in the air stream is represented. It is clearly visible that an important generation of chromium takes place at the interface between seal and interconnect, similarly to the *F-design* case. However, the impact on the cathode is different, due to the fact that this seal is placed at the center of the active area, hence polluting the active area located downstream of it.

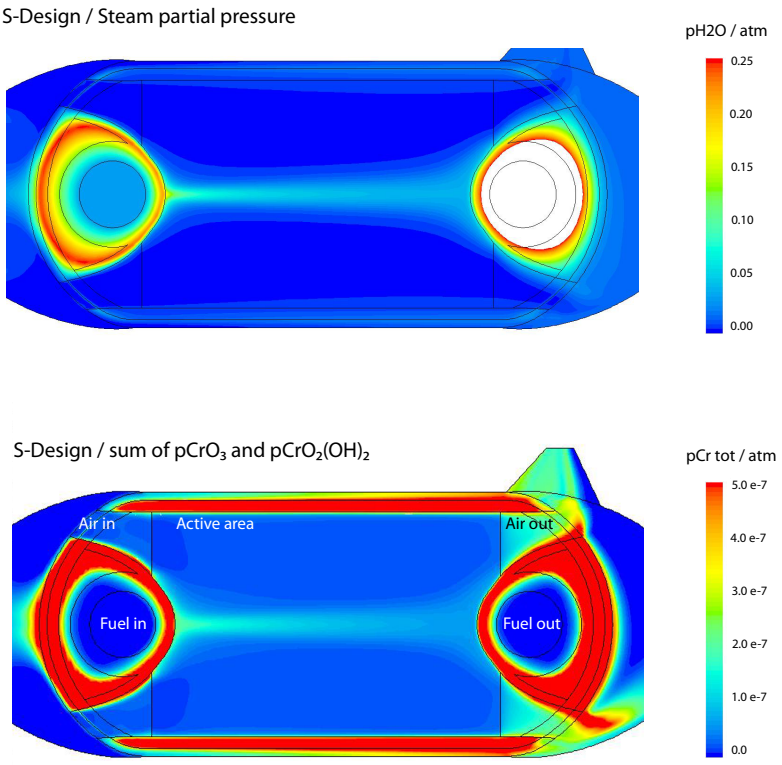

Figure 12.13: Generation of chromium-containing volatile species in a *S-design* repeat-element. Top: local partial pressures of steam on the cathode side. Bottom: total partial pressure of Cr-containing volatile species in the gas streams.

12.8 Chromium poisoning as function of the design and of the operating conditions

To conclude this chapter, a benchmark of the three investigated stack designs is given as function of the operating conditions. To compare the designs, the sole internal generation of chromium-containing volatile species is considered, where no protective coating is applied. The surface-averaged total deposition rate is given as function of the fuel flow rate, where the lambda is fixed at a value of 6 (standard operating conditions). Pure hydrogen is used in this case, as it possibly increases the vaporization rates by increasing the steam partial pressure in the seals. The result of the benchmark is shown in Fig. 12.14.

First, the average deposition rates change considerably depending on the fuel flux, which in fact dictates the air flow rate through the constant lambda. These variations in the air flow rates impact on the pollutant partial pressures by dilution, hence modifying the transport of volatile species from the MIC to the cell. For all designs, the highest pollution rates are attained at the lowest fuel flow rate. Therefore, to lower pollution, higher air flow rates would be preferred, or even higher fuel flow rates if the lambda is fixed. This represents an inverse trend from other considerations on degradation, where low current densities and power densities are preferred to limit degradation. Moreover, it has to be noted that it is the deposition rate of $CrO_2(OH)_2$ which is mostly affected by the variations of gas flows.

Second, the impact of the design on the total trapped amounts is easily visible. The *R-design* stack presents almost double deposition rates than the *S-design* stack. Even more important, for $CrO_2(OH)_2$ the *F-design* stack presents an average deposition rate which is one order of magnitude lower than in the case of the *S-design* stack. This important difference is principally explained by the absence of a seal exposed to steam in front of the flow, but also by the lower ratio of seal length to the total active area in the case of the *F-design* stack.

Finally, variations of fuel utilization have an impact on the total pollution, affecting only the specie $CrO_2(OH)_2$. This fact is linked to the displacement of the parasitic combustion fronts in the seals, which impact on the amounts of pollutants released in the flow.

This final result demonstrates, therefore, a possible link between stack pollution and stack design. To investigate the direct impact on degradation, however, a link has to be found between the deposited amounts of pollutants and the variation of area specific resistance, an information which is not available yet.

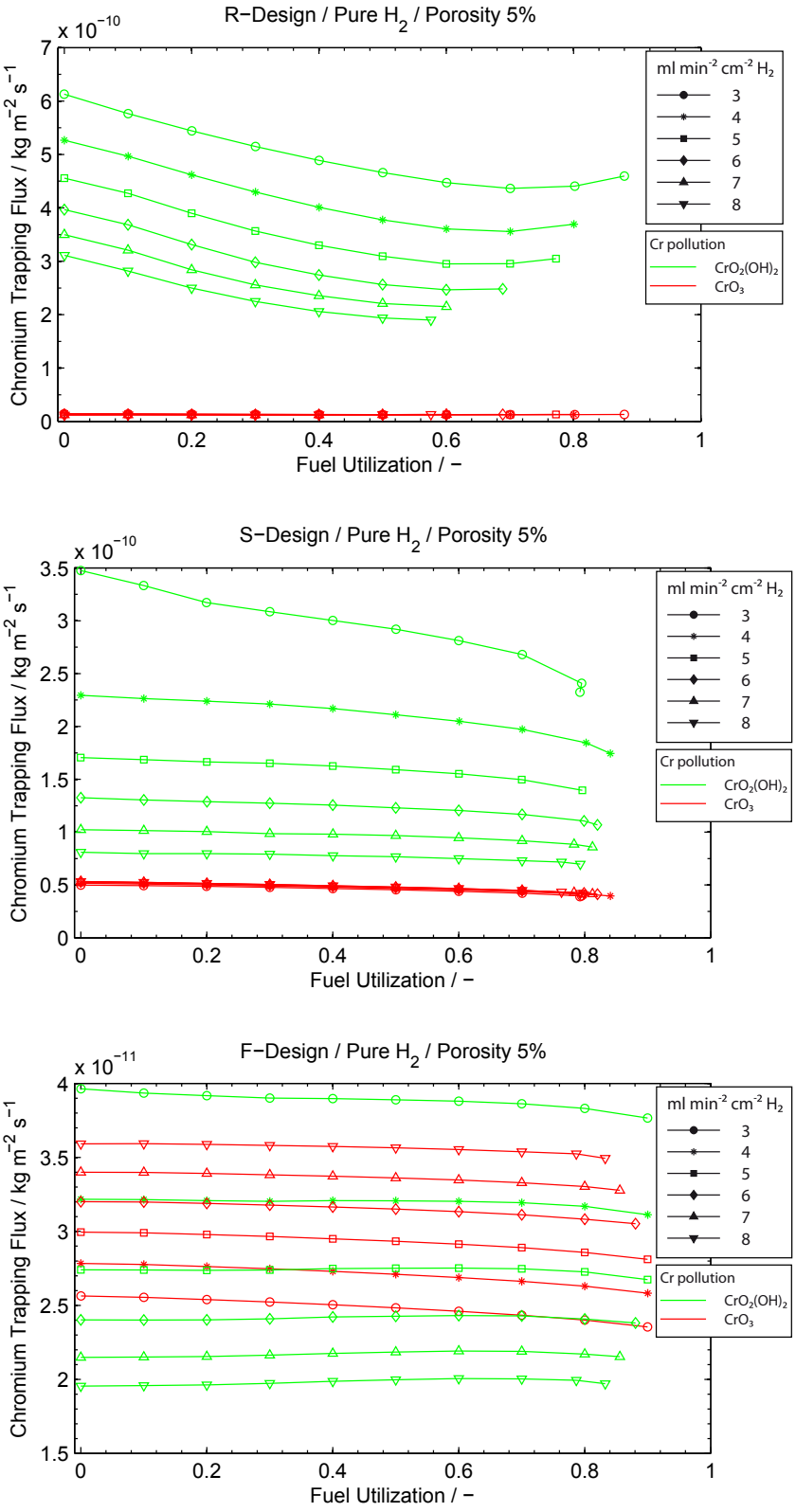

Figure 12.14: Surface-averaged total trapping rates for the three investigated stack designs, as function of the operating point. Non-protected interconnects.

12.9 Conclusion

In this chapter, it has been shown that it is possible to model the generation, transport and deposition of pollutants in SOFC repeat-element. Based on the example of the *F-design* stack, it is shown that the spatial distribution of pollutant trapping depends first on the location of its source, on the presence of protection of the components, but also principally on the operating conditions.
In particular, the humidity of the injected air represents a major factor on the deposited amounts for the considered pollutants, and this independently of the presence or not of stack-external pollutant sources.

Moreover, it was shown that the spatial distribution of pollutants differs from one stack design to the other, resulting in different total trapping rates. Besides its advantages in terms of performance and reliability, the *F-design* stack developed in this thesis shows, also in this case, a clear advantage with respect to its predecessors.
In addition, the trapped amounts were found to depend on the gas flow rates, or even indirectly on the fuel utilization. For all cases, the use of compressive seals with residual porosity induces additional chromium vaporization, an additional effect that should be taken into account in the design phases of a stack.

Finally, the simulation results could be partly validated for the *F-design* case by a correct prediction of the location where chromium generation is expected to occur. The simulated trapping profiles for chromium were analogous to the ones measured by EDX in the segmented repeat-element, where corresponding boundary conditions were applied. This illustrates the potential for model-based support in post-experiment analyses.

Despite the numerous simplifications in the evaporation and trapping model, resulting in particular from a lack of thermodynamic data, these developments show the potential for modeling-assisted diagnostics on pollution for solid oxide fuel cells.

Chapter 13

Conclusion

13.1 Overview

This thesis focuses on the study and resolution of reliability and degradation issues in solid oxide fuel cells, with a combined application of modeling and experimental tools. Besides cost, performance, reliability and lifetime are considered as the key issues for the deployment of the SOFC technology.
Starting from experimental work showing the limitations of the first-generation SOFC stack (*R-design*) prototype, this thesis aimed to develop the necessary modeling and experimental tools to provide an in-depth understanding of electrochemical performance, reliability and degradation in SOFCs. The goal was to, in particular, investigate the link between these three key issues, as well as the impact of the stack design, choice of components or operating conditions on them.
To achieve this goal, the main effort was concentrated on developing a modeling and experimental framework giving access to local properties in real or modeled repeat-elements, including local electrochemical performance, risk of failure and degradation. In addition, the second goal of this work was to propose concrete solutions for the design of stacks presenting the mandatory reliability and high performance expected from the SOFC technology.

On the experimental hand, a diagnostic test station was developed to give in-situ access to local electrochemistry in SOFC repeat-elements (Chapter 10). This test station allowed to measure the local degradation occurring in a real prototype, for the first time in SOFC research. This experiment revealed the intrinsically local character of degradation, which was expected from button-cell experiments but never verified experimentally.
A methodology was developed to analyze data obtained by impedance spectroscopy, in order to identify the different electrochemical processes and to study the spatial distribution of their degradation. This spatial information represents an advantage of core importance

for the interpretation of the results and for post-experiment analyses (Chapter 10 and 11). Finally, it is shown in Chapter 12 that the coupling of locally-resolved post-experimental analyses with locally-resolved degradation measurements enables the identification of the possible main sources of degradation, in this case in the form of pollutants.
The development of this novel tool represents the major contribution of this thesis for the research on degradation in SOFCs. Using this tool, future experiments should allow a faster and more precise evaluation of the effects of different degradation sources. In addition, the realized test station offers a platform for rapid and efficient prototype development, as well as for more fundamental experiments on segmented cells or multi-cathode experiments. Finally, this test platform offers a unique possibility to investigate the effect of stack design on degradation. At present, procedures for accelerated testing are discussed in the SOFC community, where it is suggested to modify operating conditions or to increase current and power densities to accelerate degradation. This experiment could represent an alternative, as it offers the necessary amounts of data without modifying the operating conditions.

The second developed tool is a CFD model capable of predicting performance limitations, degradation and failure issues, developed in a strong link with experimental observations. To predict perfomance limitations, (investigated in Chapter 7) the model is based on an electrochemical model, fitted on experimental data, which is able to reproduce the response of cells in situations close to limitations. In Chapter 8, it is shown that, by including the non-ideal properties of seal materials, a detailed geometry of complete repeat-elements, and indicators for the damage of electrodes, the model is able to detect and explain the major source of failure of the investigated stacks, as well as to define solutions for new stack prototypes. Finally, a complementary model allows to simulate the generation, transport and deposition of pollutants in a real repeat-element, whose outputs can be used to identify pollutant sources in conjunction with local post-experiment analyses and local measurements of degradation (see Chapter 12).

The CFD model contributes in an important manner to the knowledge of the phenomena occurring in the tested and developed stacks, their limitations and the risk associated with different operating points. Much more, it enabled the designing of prototypes while taking into account the possible weaknesses of components, hence tending to higher performance and reliability.

A validation of the combined modeling and experimental framework, developed during this thesis, is finally given by the design, the realization and validation of two prototypes (Chapter 3, 7 and 8) . The *F-design* stack, which was developed on the base of the conclusions made on performance limitations and on the identified mechanisms leading to failure, finally achieves the targeted reliability and performance which are far beyond the initial expectations of this work. Designed as a future industrial product, this stack represents the second major achievement of this thesis, offering a validation of the herein developed approach and of the model, in particular.

In the months to come, this stack will be implemented in the CHP system developed by the partners working on the FlameSOFC project. This evolution from an inital lab-style prototype to the basis of a real market product represents an important leap achieved during this thesis.

13.2 Solving Performance limitations

Initial work made on the *R-design* showed recurrent limitations in terms of performance and reliability, with efficiencies inferior to 40% and frequent failures of cells leading to premature endings of experiments. In order to understand the limitations of the design, a modeling approach was used. A CFD model, presented in Chapter 5, was developed. It includes an electrochemical model, fitted on experimental data, and allows to predict the performance of anode-supported cells in a wide range of operating conditions. The comparison with a virtual repeat-element presenting an ideal fuel distribution showed that the principal limitations of the *R-design* stack were caused by its inappropriate internal gas distribution (Chapter 7).

The identification of this problem enabled the design of a new stack (*S-design*) presenting sensibly improved performances in accordance with modeling predictions. In short stack configuration, this design attained recently a maximum efficiency of 53% LHV, operated on hydrogen. This design moreover enabled to reach an important 1-kW milestone in a 72-cell configuration.

13.3 Adressing Reliability issues

At the same time, developments were made on the CFD model to find an explanation for the recurrently low OCVs obtained with the *R-design* prototype, as well as the low performance that did not match modeling predictions, despite the electrochemical model fitted on experimental data.
Based on the inclusion of the real (and non-idealized) seal material properties and the hypothesis that diffusion in seals is important, the CFD model was now capable of reproducing the behavior of the *R-design* stack as observed in experiments. Thus, not only the low OCVs but also the low efficiencies could be explained. Furthermore, the model revealed potential severe degradation issues for the cells, occuring by local redox-cycling. Again, these predictions were found to be in excellent agreement with the experimental observations, and led to explaining the major source of failure for this type of stack. In addition, it was shown that repeated load- or thermal cycles would propagate the damaged areas until the total failure

of the cell.

On the base of these conclusions, the newly designed *S-design* stack was evaluated: it suffered from the same reliability issues as its predecessors, especially during thermal cycling. The identification of this problem, led to new technical solutions.

A new design iteration was made with intensive use of the CFD model and of its degradation sub-models. The resulting *F-design* stack, which represents the major outcome of this thesis, achieved a maximum power output of 1.84kW$_{el}$ and a maximal efficiency of 53% in a 20-cell configuration (200cm^2 cells). This result was obtained using dilute hydrogen as fuel; in other words, future operation on reformed natural gas should lead to an efficiency above 60%. Moreover, modeling and experiments show that this design not only approaches internal fuel distributions of an ideal repeat-element, but also verifies the absence of local redox-cycling of the cells, hence leading to largely improved reliability (Chapter 8).

All these developments show that the use of compressive seal materials, presenting a residual porosity, can lead to severe degradation issues or even failure, unless adaptations of the stack design are made. As shown by the *F-design* stack, solutions can be found to enable the use of such materials.

13.4 Revealing the local character of degradation

Having at least partly solved the performance and failure issues, the problem of degradation was addressed experimentally in the last part of this work (Chapters 10 and 11).

A diagnostic test station was designed and realized to perform in-situ measurements of local electrochemistry in a repeat-element and thus making the use of an instrumented interconnect in a real stack possible. A good match was found between simulation and experiment, validating both the design and the model at once. The in-situ measurements performed revealed phenomena that would have been hard to detect in any other experimental configuration, hence illustrating the interest of locally resolved information.

The intrinsically local character of degradation was revealed by the evolution of local current densities with time, as well as by impedance spectroscopy measurements. Different degradation dynamics were observed on the surface of the repeat-element, depending on their position in the element and on the local operating conditions. This shows that the degradation of a repeat-element in a real stack strongly differs from the one observed in button-cell

experiments: balancing effects take place between more and less degrading regions, modifying the distribution of the electrochemical reaction over the active area in a large extent. This result is thus of great consequence for the interpretation given to the degradation results obtained from experiments on stacks or repeat-elements.

The final state of degradation was investigated by impedance spectroscopy to identify the electrochemical processes and the level of their degradation. The analyses of the impedance spectra show a non-uniformly degraded cell, thus revealing the interest of multiple measurement points, which allow an insight in the spatial distribution of degradation for the identified degraded processes. The applied methodology allows to identify the most affected electrodes and electrochemical processes, and thereby to establish corresponding degradation maps for the first time.

The interest of a high spatial resolution was further demonstrated by the performed spatially-resolved post-experiment analyses. Chromium, silicon and sulfur were identified as principal pollutants. Their spatial distribution over the cathode surface is put in relation with data on degradation. The study of the pollutant penetration into the cathode layer, enabled chromium and silicon to be identified as probable principal causes of cathode degradation. The spatial distribution of pollutants in the end also helped identify possible contamination sources as either external or internal components.

As revealed above, this type of experiment enables to create the often missing link between usual post-experiment analyses and the effective degradation of the fuel cell. Nevertheless, it is also shown that additional experimental methods will be required to precisely quantify the amounts of pollutants, as well as an access to complete thermodynamic databases for the interpretation of the results.

Prospective work on pollutants From the conclusions above, a model for pollutant generation, transport and deposition has been included in the CFD model, as presented in Chapter 12. This model successfully predicts the location of internal generation of chromium-containing volatile species, as well as places where deposition of chromium should occur. From the results predicted by this model, it is expected that the major sources of chromium and silicon are located up stream of the stack in the segmented experiment. In addition, the model shows that the extent of pollution can be expected to depend on the stack design, as well as on the operating conditions.

The basis for additional developments is therefore set.

13.5 Future work

Based on the herein developed experimental and modeling framework, number of possibilities are offered for future investigations. New experiments with the diagnostic station will serve as basis for an improved knowledge on degradation by:

- using different cathode materials to investigate their sensitivity to pollutants
- monitoring the quality of entering air by advanced gas sampling methods
- using inert test setups to study only the intrinsic degradation of the repeat-element
- improving and automatizing the impedance measurements to investigate larger operation domains
- using reformed C-fuels to investigate their impact on the anode degradation
- using other pollutant quantification techniques such as SIMS/GDOES for more complete results
- use experiment design techniques to perform adequate parameter estimations

Concerning the modelisation work, further development in relation with the transport of pollutants would be of major interest. This, however, requires access to thermodynamic and kinetic databases, not yet available. As shown above, the choice of materials, stack design and testing conditions have significant impact on the amounts of trapped pollutants, which could be investigated using this tool. The access to locally resolved measurements of degradation associated to locally-resolved post-experiment analyses would offer a unique opportunity to validate these modelisation results.

Bibliography

[1] H. Y. Zhu and R. J. Kee. Modeling distributed charge-transfer processes in SOFC membrane electrode assemblies. *Journal of the Electrochemical Society*, 155(7):B715–B729, 2008.

[2] S. P. Simner and J. W. Stevenson. Compressive mica seals for SOFC applications. *Journal of Power Sources*, 102(1-2):310–316, 2001.

[3] T. Nakamura, G. Petzow, and L. J. Gauckler. Stability of the perovskite phase LaBO3 (B = V, Cr, Mn, Fe, Co, Ni) in reducing atmosphere I. Experimental results. *Materials Research Bulletin*, 14(5):649–659, 1979.

[4] A. Faes, A. Nakajo, A. Hessler-Wyser, D. Dubois, A. Brisse, S. Modena, and J. Van Herle. RedOx study of anode-supported solid oxide fuel cell. *Journal of Power Sources*, 193(1):55–64, 2009.

[5] M. Stanislowski, E. Wessel, K. Hilpert, T. Markus, and L. Singheiser. Chromium vaporization from high-temperature alloys I. Chromia-forming steels and the influence of outer oxide layers. *Journal of the Electrochemical Society*, 154(4):A295–A306, 2007.

[6] N. S. Jacobson, E. J. Opila, D. L. Myers, and E. H. Copland. Thermodynamics of gas phase species in the Si-O-H system. *Journal of Chemical Thermodynamics*, 37(10):1130–1137, 2005.

[7] M. Mogensen, K. V. Jensen, M. J. Jorgensen, and S. Primdahl. Progress in understanding SOFC electrodes. *Solid State Ionics*, 150(1-2):123–129, 2002.

[8] D. Larrain. *Solid oxide fuel cell stack simulation and optimization, including experimental validation and transient behavior*. Phd thesis, Ecole Polytechnique Fédérale de Lausanne (EPFL), Lausanne, CH, 2005.

[9] P. Metzger, K. A. Friedrich, H. Müller-Steinhagen, and G. Schiller. SOFC characteristics along the flow path. *Solid State Ionics*, 177(19-25):2045–2051, 2006.

[10] S. J. C. Cleghorn, C. R. Derouin, M. S. Wilson, and S. Gottesfeld. A Printed Circuit Board approach to measuring current distribution in a fuel cell. *Journal of Applied Electrochemistry*, 28(7):663–672, 1998.

[11] M. Schulze, E. Gülzow, St Schönbauer, T. Knöri, and R. Reissner. Segmented cells as tool for development of fuel cells and error prevention/prediagnostic in fuel cell stacks. *Journal of Power Sources*, 173(1):19–27, 2007.

[12] D.U. Sauer, T. Sanders, B. Fricke, T. Baumöfer, K. Wippermann, A.A. Kulikovsky, H. Schmitz, and J. Mergel. Measurement of the current distribution in a direct methanol fuel cell–Confirmation of parallel galvanic and electrolytic operation within one cell. *Journal of Power Sources*, 176(2):477–483, 2008.

[13] Mathias Reum, Stefan A. Freunberger, Alexander Wokaun, and Felix N. Buchi. Measuring the Current Distribution with Sub-Millimeter Resolution in PEFCs. *Journal of The Electrochemical Society*, 156(3):B301–B310, 2009.

[14] J. J. Hwnag, W. R. Chang, R. G. Peng, P. Y. Chen, and A. Su. Experimental and numerical studies of local current mapping on a PEM fuel cell. *International Journal of Hydrogen Energy*, 33(20):5718–5727, 2008.

[15] T. Knöri and M. Schulze. Spatially resolved current density measurements and real-time modelling as a tool for the determination of local operating conditions in polymer electrolyte fuel cells. *Journal of Power Sources*, In Press, Corrected Proof, 2009.

[16] F. Ravussin, J. Van herle, N. Autissier, M. Molinelli, D. Larrain, and D. Favrat. Local current measurement in a solid oxide fuel cell repeat element. *Journal of the European Ceramic Society*, 27(2-3):1035–1040, 2007.

[17] A. Bieberle and L. J. Gauckler. Reaction mechanism of Ni pattern anodes for solid oxide fuel cells. *Solid State Ionics*, 135(1-4):337–345, 2000.

[18] A. Bieberle and L. J. Gauckler. State-space modeling of the anodic SOFC system Ni, H2-H2O|YSZ. *Solid State Ionics*, 146(1-2):23–41, 2002.

[19] W. G. Bessler. Rapid impedance modeling via potential step and current relaxation simulations. *Journal of the Electrochemical Society*, 154(11):B1186–B1191, 2007.

[20] W. G. Bessler. Gas concentration impedance of solid oxide fuel cell anodes I. Stagnation point flow geometry. *Journal of the Electrochemical Society*, 153(8):A1492–A1504, 2006.

[21] W. G. Bessler. A new computational approach for SOFC impedance from detailed electrochemical reaction-diffusion models. *Solid State Ionics*, 176(11-12):997–1011, 2005.

[22] W. G. Bessler and S. Gewies. Gas concentration impedance of solid oxide fuel cell anodes. *Journal of the Electrochemical Society*, 154(6):B548–B559, 2007.

[23] W. G. Bessler, S. Gewies, and M. Vogler. A new framework for physically based modeling of solid oxide fuel cells. *Electrochimica Acta*, 53(4):1782–1800, 2007.

[24] W. G. Bessler, J. Warnatz, and D. G. Goodwin. The influence of equilibrium potential on the hydrogen oxidation kinetics of SOFC anodes. *Solid State Ionics*, 177(39-40):3371–3383, 2007.

[25] H. Y. Zhu and R. J. Kee. Modeling electrochemical impedance spectra in SOFC button cells with internal methane reforming. *Journal of the Electrochemical Society*, 153(9):A1765–A1772, 2006.

[26] H. Y. Zhu and R. J. Kee. A general mathematical model for analyzing the performance of fuel-cell membrane-electrode assemblies. *Journal of Power Sources*, 117(1-2):61–74, 2003.

[27] H. Y. Zhu, R. J. Kee, V. M. Janardhanan, O. Deutschmann, and D. G. Goodwin. Modeling elementary heterogeneous chemistry and electrochemistry in solid-oxide fuel cells. *Journal of the Electrochemical Society*, 152(12):A2427–A2440, 2005.

[28] H. Y. Zhu, R. J. Kee, M. R. Pillai, and S. A. Barnett. Modeling electrochemical partial oxidation of methane for cogeneration of electricity and syngas in solid-oxide fuel cells. *Journal of Power Sources*, 183(1):143–150, 2008.

[29] S. H. Chan, K. A. Khor, and Z. T. Xia. Complete polarization model of a solid oxide fuel cell and its sensitivity to the change of cell component thickness. *Journal of Power Sources*, 93(1-2):130–140, 2001.

[30] S. H. Chan and Z. T. Xia. Anode Micro Model of Solid Oxide Fuel Cell. *Journal of the Electrochemical Society*, 148(4), 2001.

[31] X. J. Chen, S. H. Chan, and K. A. Khor. Simulation of a composite cathode in solid oxide fuel cells. *Electrochimica Acta*, 49(11):1851–1861, 2004.

[32] S. B. Adler, X. Y. Chen, and J. R. Wilson. Mechanisms and rate laws for oxygen exchange on mixed-conducting oxide surfaces. *Journal of Catalysis*, 245(1):91–109, 2007.

[33] J. M. Klein, Y. Bultel, S. Georges, and M. Pons. Modeling of a SOFC fuelled by methane: From direct internal reforming to gradual internal reforming. *Chemical Engineering Science*, 62(6):1636–1649, 2007.

[34] J. M. Klein, S. Georges, and Y. Bultel. Modeling of a SOFC Fueled by Methane:Anode Barrier to Allow Gradual Internal Reforming Without Coking. *Journal of The Electrochemical Society*, 155(4):B333–B339, 2008.

[35] N. Autissier, D. Larrain, J. Van Herle, and D. Favrat. CFD simulation tool for solid oxide fuel cells. *Journal of Power Sources*, 131(1-2):313–319, 2004.

[36] D. Larrain, J. Van Herle, F. Maréchal, and D. Favrat. Generalized model of planar SOFC repeat element for design optimization. *Journal of Power Sources*, 131(1-2):304–312, 2004.

[37] D. Larrain, J. Van Herle, F. Maréchal, and D. Favrat. Thermal modeling of a small anode supported solid oxide fuel cell. *Journal of Power Sources*, 118(1-2):367–374, 2003.

[38] N. Autissier, F. Palazzi, F. Marechal, J. van Herle, and D. Favrat. Thermo-economic optimization of a solid oxide fuel cell, gas turbine hybrid system. *Journal of Fuel Cell Science and Technology*, 4(2):123–129, 2007.

[39] F. Palazzi, N. Autissier, F. Marechal, J. Van Herle, and D. Favrat. Thermo-economic optimization of a solid oxide fuel cell, gas turbine hybrid system. In *Proceedings of the 1st European Fuel Cell Technology and Applications Conference 2005 - Book of Abstracts*, volume 2005 of *1st European Fuel Cell Technology and Applications Conference 2005, EFC2005*, page 249, Rome, 2005.

[40] Arata Nakajo, Zacharie Wuillemin, Jan Van herle, and Daniel Favrat. Simulation of thermal stresses in anode-supported solid oxide fuel cell stacks: Part I: Probability of failure of the cells. *Journal of Power Sources*, In Press, Accepted Manuscript.

[41] Q. A. Huang, R. Hui, B. Wang, and J. Zhang. A review of AC impedance modeling and validation in SOFC diagnosis. *Electrochimica Acta*, 52(28):8144–8164, 2007.

[42] S. B. Adler. Factors governing oxygen reduction in solid oxide fuel cell cathodes. *Chemical Reviews*, 104(10):4791–4843, 2004.

[43] M. Mogensen, S. Primdahl, and M. Juhl. Revealing the mechanisms of SOFC electrodes using a combination of AC and DC methods. *Proceedings of the Fifth International Symposium on Solid Oxide Fuel Cells (Sofc-V)*, 97(40):385–393 1398, 1997.

[44] M. J. Jorgensen and M. Mogensen. Impedance of Solid Oxide Fuel Cell LSM/YSZ Composite Cathodes. *Journal of The Electrochemical Society*, 148(5):A433–A442, 2001.

[45] Anke Hagen, Rasmus Barfod, Peter Vang Hendriksen, Yi-Lin Liu, and Severine Ramousse. Degradation of Anode Supported SOFCs as a Function of Temperature and Current Load. *Journal of The Electrochemical Society*, 153(6):A1165–A1171, 2006.

[46] Rasmus Barfod, Mogens Mogensen, Trine Klemenso, Anke Hagen, Yi-Lin Liu, and Peter Vang Hendriksen. Detailed Characterization of Anode-Supported SOFCs by Impedance Spectroscopy. *Journal of The Electrochemical Society*, 154(4):B371–B378, 2007.

[47] S. Kakaç, A. Pramuanjaroenkij, and X. Y. Zhou. A review of numerical modeling of solid oxide fuel cells. *International Journal of Hydrogen Energy*, 32(7):761–786, 2007.

[48] K. S. Weil and B. J. Koeppel. Comparative finite element analysis of the stress-strain states in three different bonded solid oxide fuel cell seal designs. *Journal of Power Sources*, 180(1):343–353, 2008.

[49] Arata Nakajo, Zacharie Wuillemin, Jan Van herle, and Daniel Favrat. Simulation of thermal stresses in anode-supported solid oxide fuel cell stacks. Part II: Loss of gas-tightness, electrical contact and thermal buckling. *Journal of Power Sources*, In Press, Corrected Proof.

[50] R. Vassen, D. Simwonis, and D. Stover. Modelling of the agglomeration of Ni-particles in anodes of solid oxide fuel cells. *Journal of Materials Science*, 36(1):147–151, 2001.

[51] J. I. Gazzarri and O. Kesler. Non-destructive delamination detection in solid oxide fuel cells. *Journal of Power Sources*, 167(2):430–441, 2007.

[52] J. Van Herle, D. Larrain, N. Autissier, Z. Wuillemin, M. Molinelli, and D. Favrat. Modeling and experimental validation of solid oxide fuel cell materials and stacks. *Journal of the European Ceramic Society*, 25(12):2627–2632, 2005.

[53] A. A. Kulikovsky. Electrostatic broadening of current-free spots in a fuel cell stack: The mechanism of stack aging? *Electrochemistry Communications*, 8(8):1225–1228, 2006.

[54] S. J. Visco, C. P. Jacobson, L. C. De Jonghe, A. Leming, Y. Matus, L. M. Yang, I. Villareal, and L. Rodriquez-Martinez. Solid oxide fuel cells based on metal electrodes. *Ionic and Mixed Conducting Ceramics Iv*, 2001(28):368–373 428, 2002.

[55] I. Villarreal, C. Jacobson, A. Leming, Y. Matus, S. Visco, and L. De Jonghe. Metal-supported solid oxide fuel cells. *Electrochemical and Solid State Letters*, 6(9):A178–A179, 2003.

[56] G. Schiller, T. Franco, R. Henne, M. Lang, P. Szabo, O. Finkenwirth, B. Kuhn, and F. J. Wetzel. Development of thin-film SOFC for stationary and mobile application by using plasma deposition technology. *Solid Oxide Fuel Cells Viii (Sofc Viii)*, 2003(7):1051–1058 1520, 2003.

[57] H. Kurokawa, G. Y. Lau, C. P. Jacobson, L. C. De Jonghe, and S. J. Visco. Water-based binder system for SOFC porous steel substrates. *Journal of Materials Processing Technology*, 182(1-3):469–476, 2006.

[58] F. Wiener, M. Bram, H. P. Buchkremer, and D. Sebold. Chemical interaction between Crofer 22 APU and mica-based gaskets under simulated SOFC conditions. *Journal of Materials Science*, 42(8):2643–2651, 2007.

[59] J. W. Fergus. Sealants for solid oxide fuel cells. *Journal of Power Sources*, 147(1-2):46–57, 2005.

[60] A. Gubner. *Proc. 5th International Symposium on SOFC*. 1997.

[61] K. Haga, Y. Shiratori, K. Ito, and K. Sasaki. Chlorine Poisoning of SOFC Ni-Cermet Anodes. *Journal of the Electrochemical Society*, 155(12):B1233–B1239, 2008.

[62] M. Mogensen, S. Primdahl, K. V. Jensen, M. J. Jorgensen, and C. Bagger. Foreign phases and SOFC electrode kinetics. *Solid Oxide Fuel Cells Vii (Sofc Vii)*, 2001(16):521–528 1104, 2001.

[63] K. V. Jensen, S. Primdahl, I. Chorkendorff, and M. Mogensen. Microstructural and chemical changes at the Ni/YSZ interface. *Solid State Ionics*, 144(3-4):197–209, 2001.

[64] D. Waldbillig, A. Wood, and D. G. Ivey. Thermal analysis of the cyclic reduction and oxidation behaviour of SOFC anodes. *Solid State Ionics*, 176(9-10):847–859, 2005.

[65] Antonin Faes, Arata Nakajo, A. Hessler-Wyser, David Dubois, Annabelle Brisse, Stefano Modena, and Jan Van herle. RedOx study of anode supported solid oxide fuel cell. *Journal of Power Sources*, In Press, Accepted Manuscript.

[66] S. P. Jiang. Development of lanthanum strontium manganite perovskite cathode materials of solid oxide fuel cells: a review. *Journal of Materials Science*, 43(21):6799–6833, 2008.

[67] H. Yokokawa. Understanding Materials Compatibility. *Annual Review of Materials Research*, 33:581–610, 2003.

[68] A. Hagen, Y. L. Liu, R. Barfod, and P. V. Hendriksen. Assessment of the Cathode Contribution to the Degradation of Anode-Supported Solid Oxide Fuel Cells. *Journal of The Electrochemical Society*, 155(10):B1047–B1052, 2008.

[69] Steven McIntosh, Stuart B. Adler, John M. Vohs, and Raymond J. Gorte. Effect of Polarization on and Implications for Characterization of LSM-YSZ Composite Cathodes. *Electrochemical and Solid-State Letters*, 7(5):A111–A114, 2004.

[70] M.J. Heneka and E. Ivers-Tiffeée. INFLUENCE OF HIGH CURRENT CYCLING ON THE PERFORMANCE OF SOFC SINGLE CELLS. In N. Bonanos A. Hagen L. Mikkelsen K. Kammer D. Lybye P.V. Hendriksen F.W. Poulsen M. Mogensen W.G. Wang S. Linderoth, A. Smith, editor, *Risoe International Symposium on Materials Science: Solid State Electrochemistry*, pages 215–222, RisÃ¸ National Laboratory, Roskilde, Denmark 2005, 2005.

[71] K. Hilpert, D. Das, M. Miller, D. H. Peck, and R. Weiss. Chromium vapor species over solid oxide fuel cell interconnect materials and their potential for degradation processes. *Journal of the Electrochemical Society*, 143(11):3642–3647, 1996.

[72] S. P. Jiang and Y. D. Zhen. Mechanism of Cr deposition and its application in the development of Cr-tolerant cathodes of solid oxide fuel cells. *Solid State Ionics*, 179(27-32):1459–1464, 2008.

[73] Harumi Yokokawa, Hengyong Tu, Boris Iwanschitz, and Andreas Mai. Fundamental mechanisms limiting solid oxide fuel cell durability. *Journal of Power Sources*, 182(2):400–412, 2008.

[74] M. Backhaus-Ricoult. SOFC - A playground for solid state chemistry. *Solid State Sciences*, 10(6):670–688, 2008.

[75] Y. P. Xiong, K. Yamaji, T. Horita, H. Yokokawa, J. Akikusa, H. Eto, and T. Inagaki. Sulfur Poisoning of SOFC Cathodes. *Journal of the Electrochemical Society*, 156(5):B588–B592, 2009.

[76] M. de Ridder, A. G. J. Vervoort, R. G. van Welzenis, and H. H. Brongersma. The limiting factor for oxygen exchange at the surface of fuel cell electrolytes. *Solid State Ionics*, 156(3-4):255–262, 2003.

[77] E. J. Opila and R. E. Hann Jr. Paralinear oxidation of CVD SiC in water vapor. *Journal of the American Ceramic Society*, 80(1):197–205, 1997.

[78] R. C. Robinson and J. L. Smialek. SiC recession caused by SiO2 scale volatility under combustion conditions: I. Experimental results and empirical model. *Journal of the American Ceramic Society*, 82(7):1817–1825, 1999.

[79] E. J. Opila, J. L. Smialek, R. C. Robinson, D. S. Fox, and N. S. Jacobson. SiC recession caused by SiO2 scale volatility under combustion conditions: II. Thermodynamics and gaseous-diffusion model. *Journal of the American Ceramic Society*, 82(7):1826–1834, 1999.

[80] S. P. Jiang, L. Christiansen, B. Hughan, and K. Foger. Effect of glass sealant materials on microstructure and performance of Sr-doped LaMnO3 cathodes. *Journal of Materials Science Letters*, 20(8):695–697, 2001.

[81] N. Sakai, K. Yamaji, T. Horita, H. Yokokawa, T. Uehara, A. Toji, H. Kameda, K. Ogasawara, Y. Matsuzaki, and T. Sakurai. Chemical Stability of Fe-22Cr Ferritic Alloy Interconnect under SOFC Operation Conditions. In *European Fuel Cell Forum 2006*, volume B086, pages 1–9, Lucerne, Switzerland, 2006.

[82] P. Batfalsky, V. A. C. Haanappel, J. Malzbender, N. H. Menzler, V. Shemet, I. C. Vinke, and R. W. Steinbrech. Chemical interaction between glass-ceramic sealants and interconnect steels in SOFC stacks. *Journal of Power Sources*, 155(2):128–137, 2006.

[83] N. H. Menzler, P. Batfalsky, L. Blum, M. Bram, S. M. Gross, V. A. C. Haanappel, J. Malzbender, V. Shemet, R. W. Steinbrech, and I. Vinke. Studies of material interaction after long-term stack operation(x). *Fuel Cells*, 7(5):356–363, 2007.

[84] Y. S. Chou and J. W. Stevenson. Long-term thermal cycling of Phlogopite mica-based compressive seals for solid oxide fuel cells. *Journal of Power Sources*, 140(2):340–345, 2005.

[85] C. Lalanne, G. Prosperi, J. M. Bassat, F. Mauvy, S. Fourcade, P. Stevens, M. Zahid, S. Diethelm, J. Van Herle, and J. C. Grenier. Neodymium-deficient nickelate oxide Nd1.95NiO4+delta as cathode material for anode-supported intermediate temperature solid oxide fuel cells. *Journal of Power Sources*, 185(2):1218–1224, 2008.

[86] M. Bram, S. Reckers, P. Drinovac, J. Monch, R. W. Steinbrech, H. P. Buchkremer, and D. Stover. Deformation behavior and leakage tests of alternate sealing materials for SOFC stacks. *Journal of Power Sources*, 138(1-2):111–119, 2004.

[87] Y. S. Chou and J. W. Stevenson. Novel infiltrated phlogopite mica compressive seals for solid oxide fuel cells. *Journal of Power Sources*, 135(1-2):72–78, 2004.

[88] N. Autissier. *Small scale SOFC systems : design, optimization and experimental results*. Phd thesis, Ecole Polytechnique Fédérale de Lausanne (EPFL), Lausanne, CH, 2008.

[89] FLUENT. *User Manual*.

[90] R. Suwanwarangkul, E. Croiset, M. W. Fowler, P. L. Douglas, E. Entchev, and M. A. Douglas. Performance comparison of Fick's, dusty-gas and Stefan-Maxwell models to predict the concentration overpotential of a SOFC anode. *Journal of Power Sources*, 122(1):9–18, 2003.

[91] T. Ackmann, L. G. J. De Haart, W. Lehnert, and D. Stolten. Modeling of mass and heat transport in planar substrate type SOFCs. *Journal of the Electrochemical Society*, 150(6), 2003.

[92] Vinod M. Janardhanan and Olaf Deutschmann. CFD analysis of a solid oxide fuel cell with internal reforming: Coupled interactions of transport, heterogeneous catalysis and electrochemical processes. *Journal of Power Sources*, 162(2):1192–1202, 2006.

[93] E. L. Cussler. *Diffusion Mass Transfer in Fluid Systems* . Cambridge U. Press, Cambridge, UK, 1997.

[94] B. Todd and J. B. Young. Thermodynamic and transport properties of gases for use in solid oxide fuel cell modelling. *Journal of Power Sources*, 110(1):186–200, 2002.

[95] H. Yakabe, T. Ogiwara, M. Hishinuma, and I. Yasuda. 3-D model calculation for planar SOFC. *Journal of Power Sources*, 102(1-2):144–154, 2001.

[96] P. Aguiar, D. Chadwick, and L. Kershenbaum. Modelling of an indirect internal reforming solid oxide fuel cell. *Chemical Engineering Science*, 57(10):1665–1677, 2002.

[97] P. Incropera and P. DeWitt. *Fundamentals of Heat and Mass Transfer*. John Wiley & Sons, Inc., 1996.

[98] K. J. Daun, S. B. Beale, F. Liu, and G. J. Smallwood. Radiation heat transfer in planar SOFC electrolytes. *Journal of Power Sources*, 157(1):302–310, 2006.

[99] B. A. Haberman and J. B. Young. A detailed three-dimensional simulation of an IP-SOFC stack. *Journal of Fuel Cell Science and Technology*, 5(1), 2008.

[100] R. S. Barlow, A. N. Karpetis, J. H. Frank, and J. Y. Chen. Scalar profiles and NO formation in laminar opposed-flow partially premixed methane/air flames. *Combustion and Flame*, 127(3):2102–2118, 2001.

[101] B. A. Haberman and J. B. Young. Diffusion and chemical reaction in the porous structures of solid oxide fuel cells. *Journal of Fuel Cell Science and Technology*, 3(3):312–321, 2006.

[102] A. Nakajo, Z. Wuillemin, J. Van Herle, and D. Favrat. Simulation of thermal stresses in anode-supported solid oxide fuel cell stacks. Part II: Loss of gas-tightness, electrical contact and thermal buckling. *Journal of Power Sources*, 193(1):216–226, 2009.

[103] A. Nakajo, Z. Wuillemin, J. Van Herle, and D. Favrat. Simulation of thermal stresses in anode-supported solid oxide fuel cell stacks. Part I: Probability of failure of the cells. *Journal of Power Sources*, 193(1):203–215, 2009.

[104] J. Fleig, H. L. Tuller, and J. Maier. Electrodes and electrolytes in micro-SOFCs: A discussion of geometrical constraints. *Solid State Ionics*, 174(1-4):261–270, 2004.

[105] P. Metzger, K. A. Friedrich, G. Schiller, and C. Willich. Spatially Resolved Measuring Technique for Solid Oxide Fuel Cells. *Journal of Fuel Cell Science and Technology*, 6(2):–, 2009.

[106] Daniel Beckel, Ulrich P. Muecke, Thomas Gyger, Guillaume Florey, Anna Infortuna, and Ludwig J. Gauckler. Electrochemical performance of LSCF based thin film cathodes prepared by spray pyrolysis. *Solid State Ionics*, 178(5-6):407–415, 2007.

[107] V. Dusastre and J. A. Kilner. Optimisation of composite cathodes for intermediate temperature SOFC applications. *Solid State Ionics*, 126(1-2):163–174, 1999.

[108] A. Bieberle, L. P. Meier, and L. J. Gauckler. The Electrochemistry of Ni Pattern Anodes Used as Solid Oxide Fuel Cell Model Electrodes. ECS, 2001.

[109] Manabu Ihara, Takeshi Kusano, and Chiaki Yokoyama. Competitive Adsorption Reaction Mechanism of Ni/Yttria-Stabilized Zirconia Cermet Anodes in H[sub 2]-H[sub 2]O Solid Oxide Fuel Cells. *Journal of The Electrochemical Society*, 148(3):A209–A219, 2001.

[110] E. Achenbach. Three-dimensional and time-dependent simulation of a planar solid oxide fuel cell stack. *Journal of Power Sources*, 49(1-3):333–348, 1994.

[111] P. Aguiar, C. S. Adjiman, and N. P. Brandon. Anode-supported intermediate temperature direct internal reforming solid oxide fuel cell. I: Model-based steady-state performance. *Journal of Power Sources*, 138(1-2):120–136, 2004.

[112] P. Costamagna and K. Honegger. Modeling of solid oxide heat exchanger integrated stacks and simulation at high fuel utilization. *Journal of the Electrochemical Society*, 145(11):3995–4007, 1998.

[113] Olivier Bucheli, Michele Molinelli, Thomas Zahringer, Emily Thorn, Stefan Diethelm, Zacharie Wuillemin, Arata Nakajo, Nordahl Autissier, and Jan van Herle. Design of 500 W Class SOFC Stack with Homogeneous Cell Performance. *ECS Transactions*, 7(1):123–132, 2007.

[114] M. Molinelli, D. Larrain, N. Autissier, R. Ihringer, J. Sfeir, N. Badel, O. Bucheli, and J. Van Herle. Dynamic behaviour of SOFC short stacks. *Journal of Power Sources*, 154(2):394–403, 2006.

[115] Y. S. Chou, J. W. Stevenson, and P. Singh. Thermal cycle stability of a novel glass-mica composite seal for solid oxide fuel cells: Effect of glass volume fraction and stresses. *Journal of Power Sources*, 152(1):168–174, 2005.

[116] S. Le, K. Sun, N. Zhang, Y. Shao, M. An, Q. Fu, and X. Zhu. Comparison of infiltrated ceramic fiber paper and mica base compressive seals for planar solid oxide fuel cells. *Journal of Power Sources*, 168(2):447–452, 2007.

[117] H. Yokokawa, N. Sakai, T. Horita, K. Yamaji, M. E. Brito, and H. Kishimoto. Thermodynamic and kinetic considerations on degradations in solid oxide fuel cell cathodes. *Journal of Alloys and Compounds*, 452(1):41–47, 2008.

[118] Zacharie Wuillemin, N. Autissier, A. Nakajo, M. Luong, J. Van herle, and D. Favrat. Modeling and Study of the Influence of Sealing on a Solid Oxide Fuel Cell. *Journal of Fuel Cell Science and Technology*, 5(1):011016–9, 2008.

[119] Harumi Yokokawa, Takao Watanabe, Akira Ueno, and Koji Hoshino. Investigation on Degradation in Long-Term Operations of Four Different Stack/Modules. *ECS Transactions*, 7(1):133–140, 2007.

[120] Soren Hojgaard Jensen, Anne Hauch, Peter Vang Hendriksen, Mogens Mogensen, Nikolaos Bonanos, and Torben Jacobsen. A Method to Separate Process Contributions in Impedance Spectra by Variation of Test Conditions. *Journal of The Electrochemical Society*, 154(12):B1325–B1330, 2007.

[121] S. Primdahl and M. Mogensen. Oxidation of Hydrogen on Ni/Yttria-Stabilized Zirconia Cermet Anodes. *Journal of The Electrochemical Society*, 144(10):3409–3419, 1997.

[122] X. J. Chen, K. A. Khor, and S. H. Chan. Identification of O2 reduction processes at yttria stabilized zirconia|doped lanthanum manganite interface. *Journal of Power Sources*, 123(1):17–25, 2003.

[123] H. Yokokawa, Horita T., Yamaji K., H. Kishimoto, X. P. Xiong, and M. E. Brito. Effect of Contamination on the Durability of SOFC Stacks and Modules in Real Operation Condition. In *European Fuel Cell Forum*, volume B1004, pages 1–12, Lucerne, Switzerland, 2008.

[124] H. Yokokawa, T. Horita, N. Sakai, K. Yamaji, M. E. Brito, Y. P. Xiong, and H. Kishimoto. Thermodynamic considerations on Cr poisoning in SOFC cathodes. *Solid State Ionics*, 177(35-36):3193–3198, 2006.

[125] T. Horita, Y. Xiong, M. Yoshinaga, T. Kishimoto, K. Yamaji, M. E. Brito, and H. Yokokawa. ACCELERATED DEGRADATION OF SOFC CATHODES BY Cr VAPORS. *ECS Transactions*, vol. 25 (2), In press., 2009.

[126] J.J. Bentzen, J.B. Bilde-Soerensen, Y.B. Liu, and M. Mogensen. Chromium Poisoning of Composite LSM/YSZ. *Proceedings of the 26th Risoe International Symposium on Materials Science*, 2005.

[127] M. Stanislowski, U. Seeling, D. H. Peck, S. K. Woo, L. Singheiser, and K. Hilpert. Vaporization study of doped lanthanum gallates and Ga2O 3(s) in H2/H2O atmospheres by the transpiration method. *Solid State Ionics*, 176(35-36):2523–2533, 2005.

[128] M. Stanislowski, J. Froitzheim, L. Niewolak, W. J. Quadakkers, K. Hilpert, T. Markus, and L. Singheiser. Reduction of chromium vaporization from SOFC interconnectors by highly effective coatings. *Journal of Power Sources*, 164(2):578–589, 2007.

[129] E. J. Opila. Volatility of common protective oxides in high-temperature water vapor: Current understanding and unanswered questions. In *Materials Science Forum*, volume 461-464, pages 765–774, 2004.

[130] Elizabeth Opila, Nathan Jacobson, Dwight Myers, and Evan Copland. Predicting oxide stability in high-temperature water vapor. *JOM Journal of the Minerals, Metals and Materials Society*, 58(1):22–28, 2006.

[131] B. B. Ebbinghaus. Thermodynamics of gas phase chromium species: The chromium oxides, the chromium oxyhydroxides, and volatility calculations in waste incineration processes. *Combustion and Flame*, 93(1-2):119–137, 1993.

[132] C. Gindorf, L. Singheiser, and K. Hilpert. Vaporisation of chromia in humid air. *Journal of Physics and Chemistry of Solids*, 66(2-4):384–387, 2005.

[133] A. Zwetanova, A. Machkova, and M. Christov. Modelling of chromium contamination of sofc cathodes from metallic interconnects. *Journal of the University of Chemical Technology and Metallurgy*, 42(1):89–92, 2007.

[134] H. Nabielek. *Correlation between Chromium Evaporation from SOFC Ferritic Steel Interconnects and Cell Degradation Proceedings 7th European SOFC Forum.* 2006.

Zacharie WUILLEMIN

04 dec. 1977
Ch. de Lallex 6, 1091 Grandvaux, Switzerland
zacharie.wuillemin@epfl.ch

Education

2003 **Master of Sciences: Graduation as Mechanical Engineer**
Ecole Polytechnique Fédérale de Lausanne (EPFL), Lausanne, Switzerland

Bombardier Transport-Vevey Technologies S.A. Award.
Best 2nd cycle average mark including the Master Thesis

Master Thesis on the development of an interactive online simulation environment for the numerical modeling of compressible flows around wing profiles

1997 **Maturité C (scientific)**
Collège de Staël, Carouge, Switzerland

Employment experience

2003-2009 **Laboratory for Industrial Energy Systems**
Ecole Polytechnique Fédérale de Lausanne (EPFL), Lausanne, Switzerland
PhD Student in the Solid Oxide Fuel Cells group.

- Developement of 2 stack prototypes in collaboration with HTCeramix SA-SOFCPower S.p.A., Yverdon, Switzerland and Trento, Italy
- Modeling performance and degradation of repeat-elements an stacks
- Developement of a diagnostic test station for in-situ measurements

Thesis director : Prof. D. Favrat
Thesis co-director : Dr. Jan Van herle

2003 **Laboratory for Computational Engineering (LIN)**
Ecole polytechnique fédérale de Lausanne (EPFL), Lausanne, Switzerland
Research assistant.
Developement of an online simulation environment to be used for teaching purposes.

Skills

CFD tools : Fluent™ with programming of User Defined Functions for control, and postprocessing, Gambit
CAD tools : Solidwork, I-deas, Catia
Electronics : LTspice /SwitcherCAD
Programming : C, Matlab, LabWindows/CVI, LabView
Office : MS Office, LaTex,
Multimedia : Photoshop, Illustrator, Premiere
Laboratory : Mechanical construction, Advanced prototyping, Instrumentation, Electronics

Languages

French: mother tongue
English: fluent
German: fluent

Publications

Journal Articles

Simulation of thermal stresses in anode-supported solid oxide fuel cell stacks.
Part II: Loss of gas-tightness, electrical contact and thermal buckling
Nakajo, A ; Wuillemin, Z ; Van herle, J ; Favrat, D
In: Journal of Power Sources, vol. 193, num. 1, 2009, p. 216-226

Simulation of thermal stresses in anode-supported solid oxide fuel cell stacks.
Part I: Probability of failure of the cells
Nakajo, A ; Wuillemin, Z ; Van herle, J ; Favrat, D
In: Journal of Power Sources, vol. 193, num. 1, 2009, p. 203-215

Impact of Materials and Design on Solid Oxide Fuel Cell Stack Operation
Diethelm, Stefan ; Van herle, Jan ; Wuillemin, Zacharie ; Nakajo, Arata et al.
In: Journal of Fuel Cell Science and Technology, vol. 5, num. 3, 2008, p. 0310031-0310036

Modeling and Study of the Influence of Sealing on a Solid Oxide Fuel Cell.
Wuillemin, Zacharie ; Autissier, Nordahl ; Nakajo, Arata ; Luong, Minh-Tam et al.
In: Journal of Fuel Cell Science and Technology, vol. 5, num. 1, 2008, p. 011016-9

Modeling and experimental validation of solid oxide fuel cell materials and stacks
Van herle, Jan ; Autissier, Nordahl ; Favrat, Daniel ; Larrain, Diego et al.
In: Journal of the European Ceramic Society, vol. 25, num. 12, 2005, p. 2627-2632

Conference Papers

Locally-Resolved Study of Degradation in a SOFC Repeat-Element
Z. Wuillemin, A. Nakajo, A. Müller, A.J. Schuler, S. Diethelm, J. Van herle, D. Favrat
To be presented at : 216th ECS meeting, Vienna, Austria, October 2009
In : ECS Trans., vol. 25 (2), 2009, in press

Sulfur as Pollutant Species on the Cathode Side of a SOFC System
J. Schuler, Z. Wuillemin, A. Hessler-Wyser, J. Van herle
To be presented at : 216th ECS meeting, Vienna, Austria, October 2009
In : ECS Trans., vol. 25 (2), 2009, in press

Investigation of Local Electrochemical Performance and Local Degradation in an Operating Solid Oxide Fuel Cell
Wuillemin, Zacharie ; Müller, Andres ; Nakajo, Arata ; Autissier, Nordahl et al.
Presented at: 8th EUROPEAN FUEL CELL FORUM 2008, Lucerne, June 30 - July 4, 2008.
In: Proceedings of the 8th EUROPEAN FUEL CELL FORUM 2008, vol. B1009, 2008, p. 1-20,

Modeling of Local Cell Degradation in Solid Oxide Fuel Cells: Cumulative Effect of Critical Operating Points
Wuillemin, Zacharie ; Faes, Antonin ; Diethelm, Stefan ; Nakajo, Arata et al.
Presented at: 8th EUROPEAN SOLID OXIDE FUEL CELL FORUM 2008, Lucerne, June 30 - July 4, 2008 .
In: Proceedings of the 8th EUROPEAN SOLID OXIDE FUEL CELL FORUM 2008, vol. A0224, 2008, p. 1-12

Design of 500 W Class SOFC Stack with Homogeneous Cell Performance
Bucheli, Olivier ; Molinelli, Michele ; Zähringer, Thomas ; Thorn, Emily et al.
Presented at: 10th International symposium on Solid Oxide Fuel cells, Nara, Japan, June 3-7, 2007.
In: Electrochemical Society Transactions, vol. 7, num. 1, 2007, p. 123-132

Progress in Stack Power Density using the SOFConnex™ Concept
Diethelm, Stefan ; Tagliaferri, Enrico ; Ihringer, Raphaël ; Molinelli, Michele et al.
Presented at: 9th International Symposium on Solid Oxide Fuel Cells, Quebec (CAN), May 15-20 2005.
In: Proceedings of the 9th International Symposium on Solid Oxide Fuel Cells, vol. PV2005-SOFC9, 2005, p. 147-157

Presentations & Talks

Locally-Resolved Study of Degradation in a SOFC Repeat-Element
To be presented at : 216th ECS meeting, Vienna, Austria, October 2009 (Oral)

Measurement and Analysis of Local Degradation in a Solid Oxide Fuel Cell
Presented at : Diagnostic Tools for Fuel Cell Technologies, Trondheim, Norway, June 23-24 2009 (Oral)

Investigation of local electrochemical performance and local degradation in an operating Solid Oxide Fuel Cell
Presented at : Scientific Advances in Fuel Cell Systems, Fuel Cells Science and Technology 2008, Copenhagen, Denmark, 8 – 9 October 2008 (Poster)

Investigation of Local Electrochemical Performance and Local Degradation in an Operating Solid Oxide Fuel Cell
Presented at: 8th EUROPEAN FUEL CELL FORUM 2008, Lucerne, June 30 - July 4, 2008. (Poster)

Modeling of Local Cell Degradation in Solid Oxide Fuel Cells: Cumulative Effect of Critical Operating Points
Presented at: 8th EUROPEAN SOLID OXIDE FUEL CELL FORUM 2008, Lucerne, June 30 - July 4, 2008 . (Poster)

In-situ measurements in a Solid Oxide Fuel Cell under varying operating conditions
Workshop on modeling and validation. 2006. Winterthur, Switzerland, 2008. (Oral)

Modeling of critical operating points and study of their effects on long term degradation of Solid Oxide Fuel Cells
International Workshop on Degradation Issues in Fuel, Crete, Greece, 19 - 21 September 2007 (Poster)

Modelling and study of the impact of diffusive transport in compressive seal materials for solid oxide fuel cells
3rd Real-SOFC Workshop on « Modelling and understanding degradation in SOFCs » 2-3 july 2006. Hertenstein, Switzerland, (Oral)

Modelling and study of the impact of diffusive transport in compressive seal materials for solid oxide fuel cells
3rd FUEL CELL RESEARCH SYMPOSIUM on MODELLING AND EXPERIMENTAL VALIDATION, *16-17 March 2006*, Dübendorf, Switzerland, (Oral)

Modeling and study of the influence of sealing on a solid oxide fuel cell
Presented at: ASME 2005 First European Fuel Cell Technology and Applications Conference, Rome, Italy, 14-16,december 2005. (Oral)

Representation of LENI / EPFL at the Hannover Fair (D)
Hannover (D), 2004

Coached Semester Projects & Diploma Theses

Optimization of the anode flow field for a SOFC stack
T. Cornu, Master Thesis, 2009

Modélisation CFD de l'enceinte haute température d'une pile à combustible SOFC
T. Cornu, Semester Project, 2009

Numerical study of a tubular Solid Oxide Fuel Cell and its electrochemical phenomena
M. Reclari, Minor Project, 2009

In-situ investigation of the local electrochemical and physical properties in a Solid Oxide Fuel Cell under varying operating conditions
A. Müller, Master Thesis, 2008

Validation d'un modèle CFD de pile à combustible SOFC par la mesure et l'analyse de champs de température en opération
Y. Pellegrinelli, Master Thesis, 2008

Conception d'un stand d'essais pour la mesure et l'analyse locale dans une pile à combustible SOFC
P. Oberholzer, Master Thesis, 2007

Mesures locales de température dans un repeat-element de pile à combustible SOFC
A. Servonet, Semester Project, 2007

Résolution spatiale des réactifs gazeux dans une pile à combustible de type SOFC
M.T. Luong, Master Thesis, 2005